

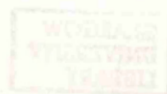
AN ELECTRON-OPTICAL STUDY OF IRON OXIDE PHASES PRODUCED IN
ALKALINE AND ACIDIC FERRIC SOLUTION IN THE PRESENCE OF
SELECTED ADDITIVE SPECIES.

by

IAN DAVID HANNAH

A Thesis submitted for the Degree of Ph.D. in the University
of Glasgow.

c I.D. Hannah 1994



ProQuest Number: 13834027

All rights reserved

INFORMATION TO ALL USERS

The quality of this reproduction is dependent upon the quality of the copy submitted.

In the unlikely event that the author did not send a complete manuscript and there are missing pages, these will be noted. Also, if material had to be removed, a note will indicate the deletion.



ProQuest 13834027

Published by ProQuest LLC (2019). Copyright of the Dissertation is held by the Author.

All rights reserved.

This work is protected against unauthorized copying under Title 17, United States Code
Microform Edition © ProQuest LLC.

ProQuest LLC.
789 East Eisenhower Parkway
P.O. Box 1346
Ann Arbor, MI 48106 – 1346

ACKNOWLEDGEMENTS

I would like to express my thanks to my supervisor, Dr. Tom Baird, for his advice during the course of my research work, and to my parents for their support.

The project was partly funded by Johnson-Matthey Colour, based at Cresswell, Stoke-On-Trent. My grateful thanks go to Mr. J.P. MacDonald and the Cresswell Technical Services staff for making my brief stay there so enjoyable.

Lastly, I would like to extend my thanks to my colleagues in the Electron Microscopy group and technical staff members Davi Thom and Eoin Robertson.

SUMMARY

The presence of foreign ions (both anionic and cationic species) has been found to exert a profound influence on the composition and morphology of crystalline products formed on ageing the unstable ferric oxide-hydrate ferrihydrite. In the present work, electron-optical techniques have been used to study the effect of Zn(II) and Ni(II) species on the above transformation. The results obtained have been compared with previous studies on the influence of Mn(II), Co(II) and Cu(II) ions.

Depending on the growth conditions, the uncontaminated oxide-hydrate transforms to hematite ($\alpha\text{-Fe}_2\text{O}_3$), by a largely solid-state rearrangement, and/or goethite ($\alpha\text{-FeOOH}$) through a dissolution/reprecipitation mechanism. Zinc species adsorb strongly on ferrihydrite and were found to strongly inhibit the rate of dissolution, thereby promoting hematite formation. Although data indicated that as much as 9-10 mol% zinc had been incorporated in the hematite structure, the additive species were not found to be associated with goethite. This was in accord with a situation in which readsorption of zinc on undissolved ferrihydrite was favoured over release into solution. By contrast, the less strongly-adsorbing nickel species did not promote formation of hematite at high pH and, since readsorption on ferrihydrite was less favoured, as much as 8-9 mol% of the additive was found to be incorporated in goethite.

These transition metal cations appeared to direct the composition and morphology of goethite/hematite-containing products through two extreme types of behaviour:- ions such as Cu(II) and Zn(II) which interact strongly with ferrihydrite will block the release of soluble ferric species, thereby influencing hematite development directly and goethite formation indirectly. By contrast, species such as Mn(II) are more easily released into solution and interact directly with the oxyhydroxide. Co(II) and Ni(II) may show intermediate behaviour. A number of other factors, including the amphoteric behaviour of the additive hydroxides, should also be considered when discussing the action of these additives.

Spinel phases formed in the presence of divalent cationic additives were thought to nucleate either in solution or on the surface of ferrihydrite. In the present work, results pointed to a mechanism by which spinel crystals nucleated on the precursor and were fed by soluble species during growth. The proportion of additive required to induce spinel formation at high pH was found to be lowest for zinc and copper. Growth of goethite crystals in precipitates which had been "seeded" with species capable of acting as goethite nuclei was strongly inhibited, while spinel formation was not retarded to a great extent.

Data indicated that many of the spinel crystals contained insufficient additive ions to give a fully-substituted stoichiometry. Some evidence for extended ordering was obtained for defect zinc-magnetites.

CONTENTS

Summary

Chapter 1

Page

1	Introduction.
3	1.1 Structural Aspects of the Iron Oxides and Oxyhydroxides.
3	1.1.1 Goethite (α -FeOOH).
5	1.1.2 Hematite (α -Fe ₂ O ₃).
6	1.1.3 Lepdocrocite (γ -FeOOH).
7	1.1.4 Akaganeite (β -FeOOH).
8	1.1.5 Ferrite Phases.
12	1.2 Hydrolysis Reactions in Ferric Salt Solution.
12	1.2.1 Initial Hydrolysis Equilibria.
14	1.2.2 Formation and Composition of High Molecular Weight Polynuclear Species.
16	1.2.3 Development of Crystalline Iron Oxide and Oxyhydroxide Phases.
19	1.3 Formation of Crystalline Phases from Aqueous Mn(II), Co(II), Ni(II), Cu(II) and Zn(II) Salt Solution.
21	1.4 Formation of Crystalline Products from the Poorly-Ordered Ferric Oxide-Hydrate Ferrihydrite.
21	1.4.1 Proposed Structures for Ferrihydrite.
25	1.4.2 Nucleation and Growth of Goethite and Hematite in Ferrihydrite Gels.

30	1.4.3 Effect of Growth Conditions on Product Morphology.
32	1.5 Effect of Foreign Ions on the Transformation of Ferrihydrite.
33	1.5.1 Adsorption of Ionic Species on Ferrihydrite and Ferric Oxides/Oxyhydroxides in Solution.
34	1.5.2 Effect Of Additives on Product Composition.
34	1.5.2 a) Adsorbing Ligands.
36	1.5.2 b) Cationic Species.
39	1.5.3 Effect of Additives on Product Morphology.

Chapter 2: Experimental

Page

44	Introduction.
45	2.1 The Transmission Electron Microscope.
47	2.1.1 Image Formation in the TEM.
47	2.1.2 Beam Interaction with the Specimen:- The Weak Phase Approximation.
52	2.1.3 The Multi-Slice Model.
54	2.1.4 The Effect of the Electron-Imaging System:- Factors Affecting Retrieval of Information.
60	2.2 Electron and X-Ray Diffraction Techniques.
60	2.2.1 Diffraction Theory:- The Bragg Law.
60	2.2.2 Powder X-Ray Diffraction.
61	2.2.3 Electron Diffraction.

63	2.2.4 Interpretation of Electron Diffraction Patterns.
63	2.2.4 a) Systematic Absences.
65	2.2.4 b) Extended Ordering.
66	2.2.4 c) Double Reflection.
67	2.2.4 d) Possible Errors Arising from Geometric Effects.
68	2.3 X-Ray Microanalysis in the TEM.
68	2.3.1 Theoretical Considerations for Quantitative EDX Analysis.
71	2.3.2 Sample Preparation,Analyser Calibration and Accuracy of Results.

Chapter 3: Results

Page

74	3.1 Characterisation of Ferrihydrite and Zinc-Ferrihydrite Gels.
78	3.2 Initial Determination of Product Composition from X-Ray Powder Diffraction Data.
82	3.3 TEM Analysis of Products:- Effect of Zinc on the Morphology of Goethite and Hematite.
82	3.3.1 Hematite.
85	3.3.2 Goethite and Twin Crystals.

- 96 3.4 Development of Zinc-Magnetite in Ferrihydrite Gels.
- 97 3.4.1 Transformation at pH 9-12.
- 97 3.4.1 a) Characterisation of Spinel Crystals.
- 105 3.4.1 b) Characterisation of 'amorphous' background
Material in Transformation Products.
- 109 3.4.2 Transformation at Neutral pH.
- 111 3.5 Zinc Distribution in Transformation Products.
- 116 3.6 The Effect of Zinc on the Development of
Crystalline Phases Formed on Addition of Excess
Base to Partially-Hydrolysed Ferric Solution.
- 117 3.6.1 Ageing in the Absence of Additive.
- 121 3.6.2 Goethite and Spinel Formation in the Presence of
Zinc Species.
- 126 3.7 The Effect of Nickel (II) Species on the Trans-
Formation of Ferrihydrite.
- 126 3.7.1 Characterisation of Precipitates.
- 127 3.7.2 Transformation at pH 12.
- 130 3.7.3 Transformation at Neutral pH.
- 132 3.8 Transformation of Ferrihydrite in the Presence of
both Nickel (II) and Zinc (II) Species.
- 132 3.8.1 Characterisation of Products.
- 133 3.8.2 Incorporation of Additive Species.

135 3.9 Effect of Beam Damage on TEM Observation and
Characterisation of Ferric Oxides and Oxyhydroxides.

135 3.9.1 Beam Damage in Goethite.

136 3.9.2 Beam Damage in Spinel Crystals.

Chapter 4: Discussion.

Page

138 4.1 Influence of Foreign Cations on the Development of
Goethite and Hematite from Ferrihydrite.

138 4.1.1 Changes in Product Composition.

142 4.1.2 Additive Incorporation in Goethite and Hematite.

148 4.1.3 The Effect of Additives on the Final Morphology
of Goethite and Hematite.

149 4.1.3 a) Goethite and Twin Crystals.

153 4.1.3 b) Hematite Crystals.

155 4.2 Formation and Composition of Spinel Phases Induced
by the Presence of Additive Species.

155 4.2.1 Probable Mechanisms for Spinel Nucleation and
Growth in Ferrihydrite Gels.

159 4.2.2 Composition of Ferrite Phases.

163 References.

CHAPTER 1. DEVELOPMENT OF SOLID OXIDE AND OXYHYDROXIDE PHASES
IN AQUEOUS FERRIC SALT SOLUTION.

The enormous importance of iron behaviour in industrial, geological, environmental, metallurgical and biological applications makes the elemental chemistry of fundamental significance today.

In the present study, the ageing of aqueous ferric salt solutions in basic and, to a lesser extent, acidic media in the presence of selected cationic impurities (specifically zinc and nickel) has been investigated. Some of the crystalline products obtained, such as goethite (α -FeOOH) and hematite (α -Fe₂O₃), have specific applications in the pigments industry (in woodstains, automotive paints, etc). These forms are precursors of maghemite (γ -Fe₂O₃), a ferric oxide which is widely used in the production of magnetic tapes. The iron oxides are also an important component of soils. Since these crystals are amongst the smallest particles present, they may contribute considerably to the total surface area even if their proportion amounts to only a few percent.

In the following introductory chapter, the results of previous studies on the hydrolysing behaviour of ferric species in solution and the formation of crystalline phases from disordered "iron hydroxide" will be summarised. In acidic media, hydrolytic polymerisation reactions in ferric salt solution are found to start almost immediately (except at very low pH). Depending on the ageing conditions, the process will usually proceed via a mechanism involving the formation of high molecular weight polynuclear species from low weight

precursors. The polymers are then found to coalesce gradually (over periods ranging from weeks to years) by a process which eventually leads to the precipitation of a range of crystalline ferric oxide and oxyhydroxide phases, including goethite, hematite, lepidocrocite (γ -FeOOH) and akaganeite (β -FeOOH). The composition of the products so formed is mainly determined by parameters such as the solution concentration, the nature of the anions present, and the ageing temperature.

The rate of hydrolysis in ferric salt solution is found to be enhanced by addition of base. However, if excess base is added such that the OH:Fe ratio is greater than 2.5-3, the hydrolysis stage is bypassed and an unstable disordered precipitate (named "ferrihydrite" after the corresponding mineral form) is formed immediately. Transformation of this solid will result in the formation of at most only two crystalline products, goethite and hematite. Again, the product composition can be controlled by fixing experimental parameters such as the gel pH or concentration, or by introducing foreign ions to the system.

The presence of additive species, both anionic (ligands) and cationic (potential substituents), has been found to exert a profound influence on the composition and morphology of crystalline products formed on ageing ferrihydrite. This effect is of special importance in the manufacture of pigments, where particle size and morphology must be strictly controlled, and in soils, where the iron oxides are found together with many organic and inorganic contaminants.

1.1 STRUCTURAL ASPECTS OF IRON OXIDES AND OXYHYDROXIDES.

In the following section, the structures of a number of ferric oxides and oxyhydroxides are discussed. The phases shown have been selected so as to cover the range of crystalline products which may develop either through ageing of ferrihydrite (with or without the presence of additives) or by extended hydrolysis of ferric salt solution.

The structures of most of the iron oxides and oxyhydroxides can be described in terms of essentially close-packed anion layers stacked one on top of the other, with Fe^{3+} occupying octahedral or sometimes tetrahedral interstices. The stacking sequence in the third dimension can give rise to either hexagonal (ABABA...) or cubic (ABCABC...) packing. Often both cubic and hexagonal polymorphs exist.

1.1.1. GOETHITE ($\alpha\text{-FeOOH}$)

Goethite is the most common form of the iron (III) oxyhydroxides, and is the polymorph to which most other FeOOH phases eventually revert on ageing. The structure has been determined as isostructural with the manganese minerals ramsdellite ($\alpha\text{-MnO}_2$) and groutite ($\alpha\text{-MnOOH}$), and with the aluminium oxyhydroxide, diasporite ($\alpha\text{-AlOOH}$). These structures consist of double chains of connected $[\text{M}(\text{O},\text{OH})_6]$ units, in which hydrogen bonding plays an important role (Fig. 1.1). The octahedra are linked together to form single chains parallel to $[001]$, through sharing of opposite edges. Two such chains are then crosslinked by edge sharing, with one displaced $c/2$ with respect to the other. The resulting double chains are

then further crosslinked together through corner sharing to produce the orthorhombic symmetry associated with goethite.

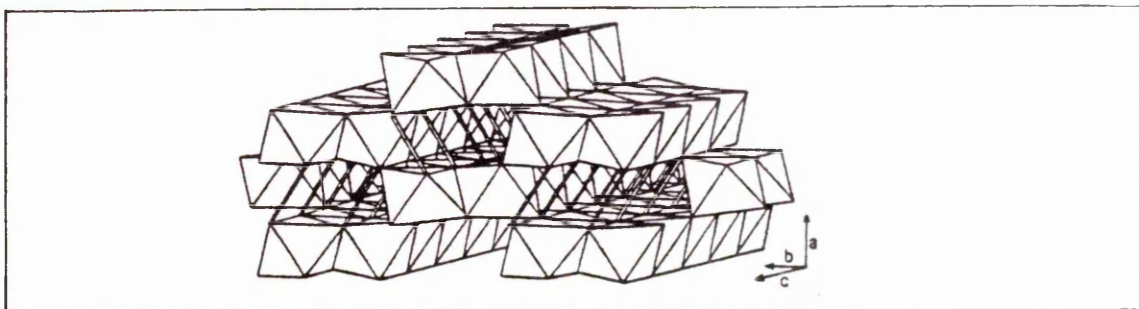


Fig.1.1:- A model of the goethite structure based on octahedral units. Hydrogen bonds are represented by small bars.

Alternatively, goethite can be viewed as a hexagonal close-packed lattice of hydroxyl and oxygen anions, with stacking of oxygen planes along $[100]$ in an -AB-AB-AB- sequence. The ferric ions are then distributed in an ordered array amongst only the octahedral sites (Fig.1.2).

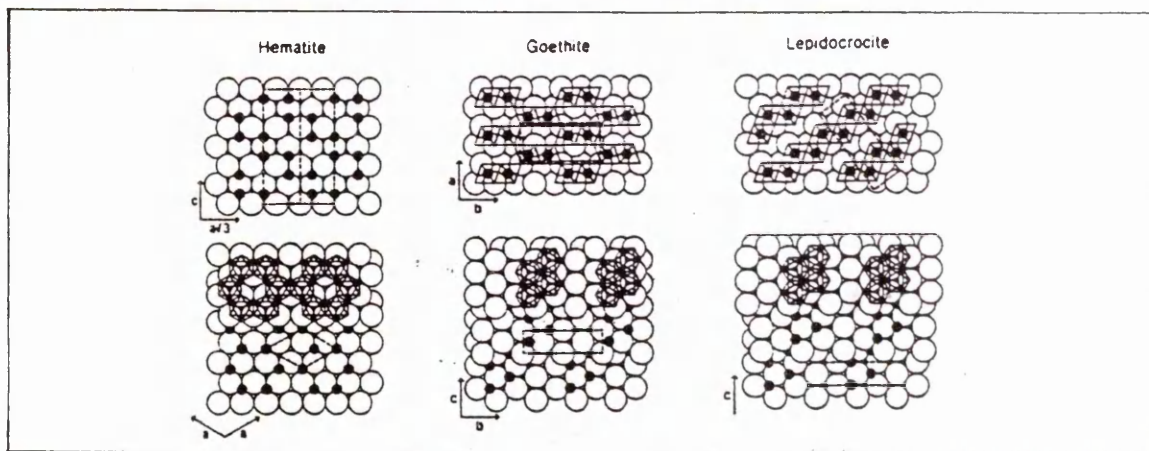


Fig.1.2:- Close-packed models of the ideal hematite, goethite and lepidocrocite structures. Large open circles are O atoms, small black circles are Fe atoms. Selected octahedra are outlined with thin solid lines, unit cells are outlined with dashed lines (taken from Eggleton *et al* [1]).

1.1.2. HEMATITE (α -Fe₂O₃)

The hematite structure was one of the first mineral structures to be determined by X-ray diffraction [2]. The original model put forward was later confirmed by Pauling and Hendricks [3] and refined by Blake *et al* [4]. Although hematite is commonly produced from ferrihydrite (as is goethite), it is normally only observed as a hydrolysis product in high temperature preparations.

The basic structural model is of a hexagonal close-packed array of oxygen anions stacked along [00.1] in which 2/3 of the octahedral sites in every layer are occupied by Fe³⁺. Each Fe(III) ion is surrounded by 6 oxygen atoms and each oxygen is shared by 4 Fe(III). The planes of Fe atoms are shifted by one octahedral site in each successive layer along [00.1]. Each FeO₆ octahedron shares three edges with three neighbouring octahedra in the same [00.1] plane, and shares one face with a similar grouping in an adjacent layer either above or below it.

The O and Fe sublattices are, however, both distorted from the idealised arrangement described above. In the left half of Fig. 1.3, the strain in the Fe sublattice is illustrated. Iron atoms in adjacent octahedra which share a face are sufficiently close that they are repelled from one another. In this way, the cations lie closer to the unshared faces of the octahedra than the shared faces. The subsequent distortion of the oxygen sublattice is shown in the right half of the figure. Circles representing the O atoms are drawn large enough so that the 3 spheres defining the shared face just touch one

another. When this is the case, the three spheres defining the unshared face of the adjacent octahedron are separated from one another. The unshared face is therefore larger in size.

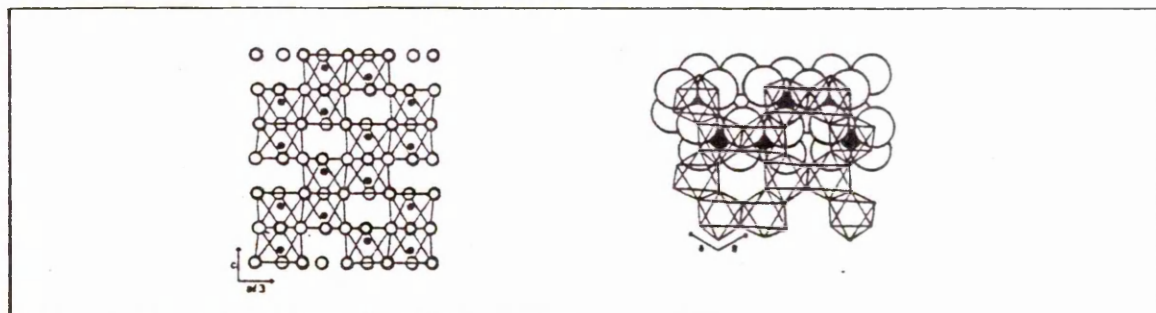


Fig.1.3:- The hematite structure. O atoms are represented by open circles, Fe by solid circles. Left: projected onto $[11.0]$. Solid circles are in the plane, thin open circles are below the plane and thick open circles are above the plane of the paper. Right: projection onto $[00.1]$.

1.1.3. LEPIDOCROCITE (γ -FeOOH)

Lepidocrocite (the second most common polymorph of FeOOH) is thought to develop directly from low molecular weight species during hydrolysis of ferric salt solution, but only in cases where the gel concentration is relatively low. In contrast to goethite and hematite, this form has not been observed as a potential product which can be produced on ageing ferrihydrite.

The crystal structure was first determined by Ewing [5], and later re-examined by Christensen [6]. The proposed model comprises planes of O atoms stacked in a cubic sequence along $[150]$. The Fe(III) atoms occupy octahedral sites and are arranged in double rows along $[001]$ (Fig.1.2). Like goethite, the structure can then be viewed as comprising chains of

linked $\text{Fe}(\text{O},\text{OH})_6$ octahedra, but in this case the double chains are crosslinked by edge rather than corner-sharing. Thus, the lepidocrocite structure consists of individual corrugated layers (Fig.1.4). The hydroxyl groups are located between each double layer, with H-bonding holding the overall structure together.

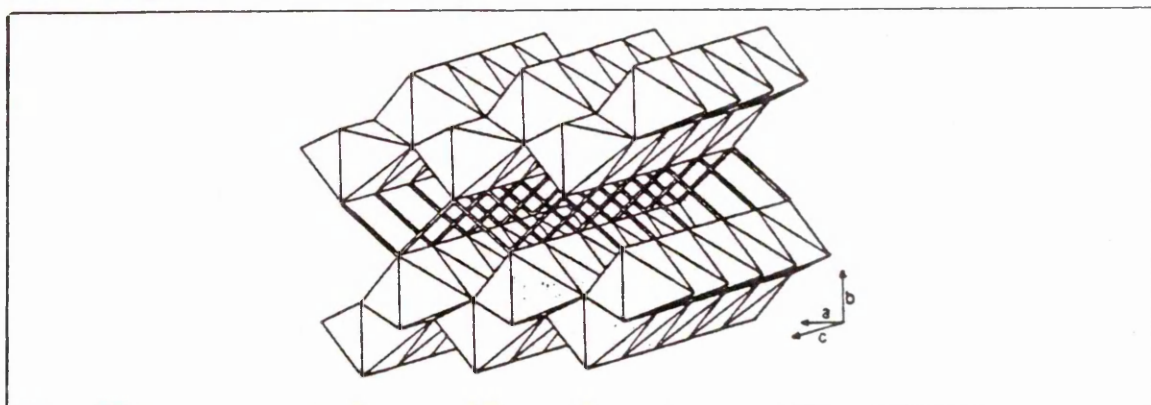


Fig.1.4:-The lepidocrocite structure.H-bonds are represented by open tubes.

1.1.4. AKAGANEITE (β - FeOOH)

As is the case for γ - FeOOH , the β - FeOOH polymorph is not observed as a product formed on ageing ferrihydrite. It is only found to develop through the slow hydrolysis of ferric chloride solution.

The basic building blocks of the structure are $[\text{FeO}_6]$ units which share edges and form double chains parallel to $[001]$. These double chains are further linked, with the octahedra sharing corners with adjacent double chains to give a three-dimensional framework. The result is a body-centred tetragonal cell having an open structure (Fig.1.5). Akaganeite is uniquely characterised by the presence of tunnels, parallel to the extended c-axis, which run the length of the crystals.

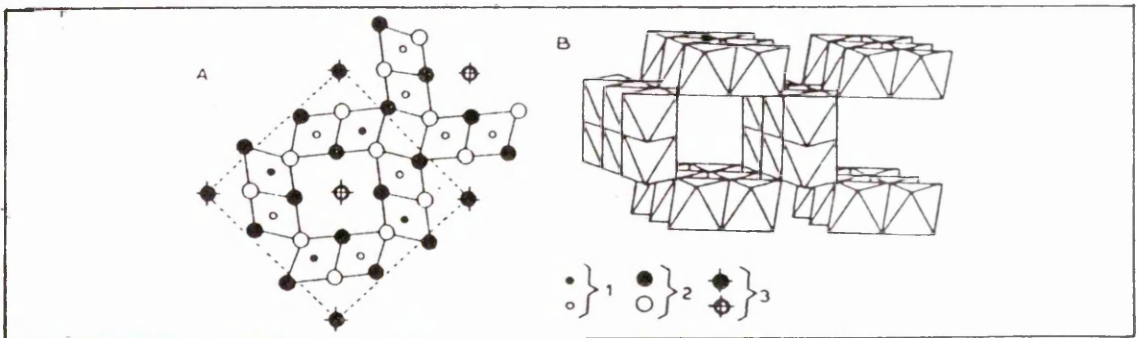
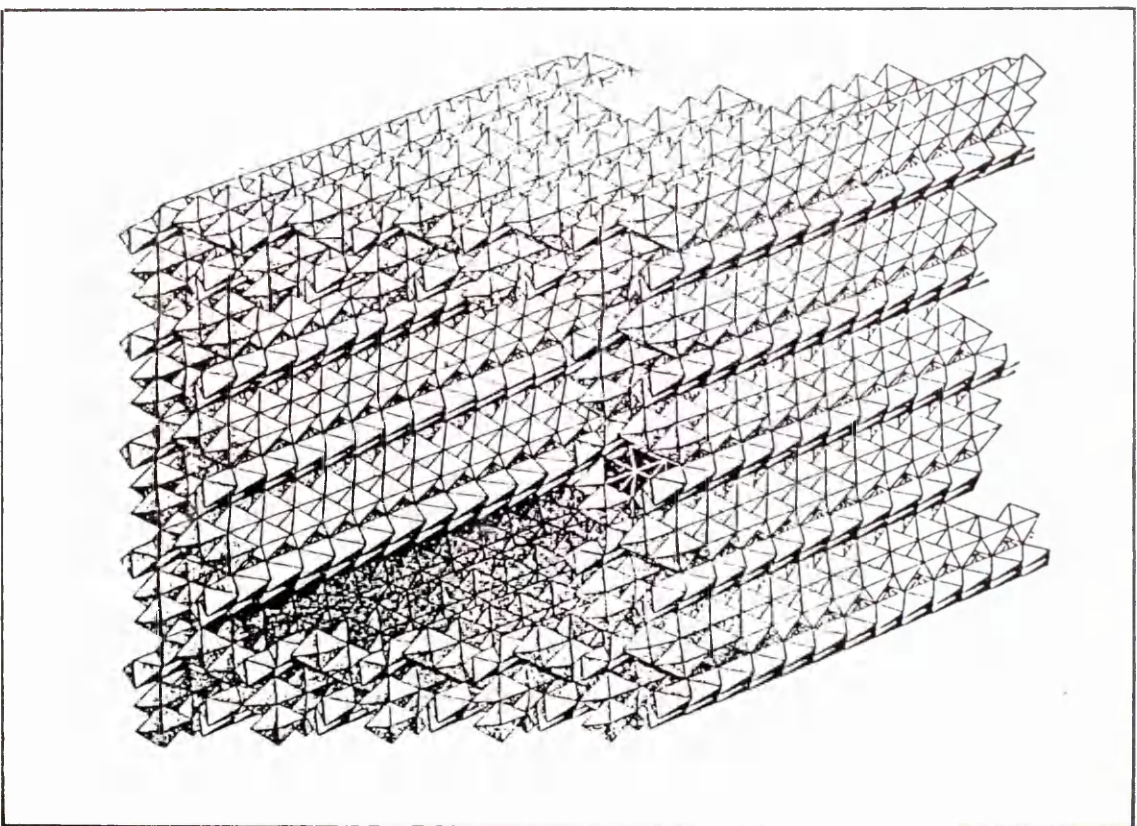


Fig.1.5:- The β -FeOOH structure, viewed as double chains of linked octahedra projected onto [001] (above, left). White circles represent atoms at zero level, black circles correspond to atoms at $c/2$ (1=Fe, 2=O, 3=Cl). Above, right:- the framework structure showing development of tunnels parallel to [001]. Below:- proposed atomic superstructure of a singular crystal of β -FeOOH.



These tunnels, one of which is present per unit cell, are square (0.5nm per side), bounded by two rows of octahedra, and can accommodate water molecules as well as hydroxyl, chloride, fluoride, sulphate and nitrate anions. Larger anions such as Cl^- are essential for the tunnel structure to develop. Ellis *et al* [7] showed that Cl^- is specifically adsorbed on $\beta\text{-FeOOH}$ and cannot be fully eluted either by washing, or by exchange with inert (NO_3^-) or specifically interacting anions (eg F^-). The oxyhydroxide is isostructural with the hollandite group ($\alpha\text{-MnO}_2$), with OH^- replacing half of the O^{2-} . However, in the case of the hollandites it is the presence of Ba^{2+} , Pb^{2+} , K^{2+} and Na^+ that is essential to the structure.

$\beta\text{-FeOOH}$ has previously been prepared by a variety of methods, but the only essential requirement appears to be the presence of Cl^- (or F^-) during hydrolysis or precipitation. The characteristic small crystal size and the structural cavities present mean that $\beta\text{-FeOOH}$ presents a large proportion of its ions to the surface. It would thus be expected to be especially effective as an ion exchanger.

1.1.5. FERRITE PHASES.

The formation of doped ferric oxides having a spinel structure has previously been found to be induced by the presence of divalent cations in ferrihydrite gels. Of interest in the present work are the metals of the first transition series, especially Mn, Co, Ni, Cu and Zn. The spinel crystals formed have a nominal stoichiometry MFe_2O_4 , with structures mainly based on that of magnetite (Fe_3O_4).

The spinel unit cell is face-centred, cubic and contains 32 oxygen anions forming a nearly close-packed framework as viewed along the [111] diagonals (Fig.1.6). There are 16 possible octahedral and 8 tetrahedral sites available for cation occupation, giving a general chemical formula for ideal spinels XY_2O_4 ($X_8Y_{16}O_{32}$ in the normal unit cell), where X and Y are cations of different valence.

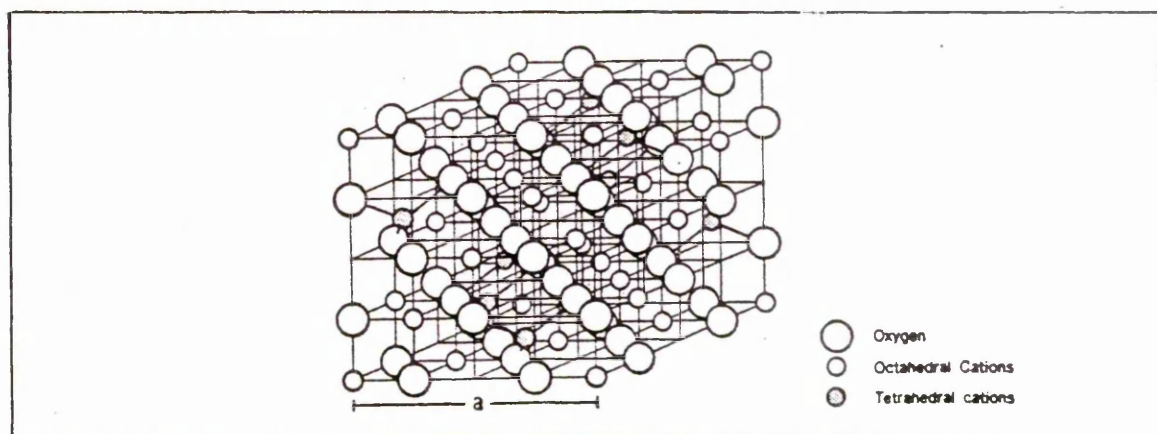


Fig.1.6:- The spinel unit cell, oriented to emphasise the stacking of [111] planes.

However, there is a complicating factor, in that the cation distribution over the available interstitial sites may vary. The two extreme types of behaviour result in the normal structure (described above) or the inverse structure. Magnetite adopts the inverse spinel structure, in which the cations occupy the interstitial sites such that the eight Fe^{2+} ions are distributed in octahedral vacancies and the sixteen Fe^{3+} are shared evenly between octahedral and tetrahedral positions. By convention, the chemical formula can then be written as $(Fe^{3+})_{tet}[Fe^{2+}Fe^{3+}]_{oct}O_4$. Magnetite is a defect structure with a narrow range of composition, having an Fe:O ratio between 0.750 and 0.744 (depending on the cation impurities and

methods of preparation).

If Fe(II) is replaced by one of Cu(II), Ni(II), Co(II) or Mn(II), the resultant spinels still exhibit the inverse form [8]. However, in zinc-magnetite the situation is reversed. The cation distribution can be influenced by a number of factors which should be considered together. These include ionic size, covalent bonding effects, and the crystal field stabilisation energy. Goodenough and Loeb [9] suggested that cations which form sp^3 hybrid orbitals are favoured in tetrahedral sites. In the present work, the formation zinc and nickel-ferrites has been examined, and a variable composition observed for both phases. The stoichiometries can be considered as a solid solution series which would have limiting parameters $\gamma\text{-Fe}_2\text{O}_3$ (the unsubstituted oxide) and $M\text{Fe}_2\text{O}_4$ (fully-substituted).

Maghemite ($\gamma\text{-Fe}_2\text{O}_3$) is so named because it has an identical chemical composition to hematite. Unlike hematite, however, it is strongly magnetic and has a pseudo-spinel crystal structure similar to that of magnetite. In maghemite, 1/9 of the metal atom sites are vacant. These unoccupied positions may be distributed in one of two ways; either evenly through octahedral and tetrahedral sites or confined only to octahedral sites. It is a defect structure with an Fe:O ratio between 0.67 and 0.72, and can be formed by the low temperature oxidation of magnetite. This reaction proceeds by a topotactic process which leaves the oxygen sublattice unchanged but involves the diffusion of Fe^{2+} ions to the surface of a grain, where they are oxidised to Fe^{3+} (leaving cation vacancies). If diffusion can proceed unhindered, one

microcrystal of magnetite can be completely transformed to maghemite without formation of a new crystal. For each Fe^{2+} diffusing to the surface, two more must be oxidised to maintain the total cationic charge balance within the bulk structure (which becomes $\text{Fe}^{3+}_{8/3} \square_{1/3}\text{O}_4$, where \square denotes an interstitial vacancy). In this way, 32 oxygen anions are associated with only 21.33 cations, making 2.67 vacancies available for each unit cell. Maghemite could then be described by the formula $\text{Fe}_{21.333} \square_{2.667}\text{O}_{32}$. The vacancies are thought to be preferentially located at octahedral interstices, and X-ray/neutron diffraction studies have concluded that only four particular sites per unit cell could be occupied [10]. However, powder diffraction data obtained by Takei *et al* [11] indicated that the vacancies were randomly distributed, with nearly 20% of the total number occupying tetrahedral sites.

There is also evidence that the maghemite structure is not exactly that of a spinel, in that many preparations have shown the presence of faint reflections that could arise from a tetragonal unit cell (in which case the vacancies are ordered along a particular [100] axis). This would result in a repeat distance three times the cubic edge, and the chemical formula could be rewritten as $\text{Fe}[(\text{Fe}_{1/6} \square_{1/3})\text{Fe}_{1.5}]\text{O}_4$ where the round brackets indicate the iron-vacancy ordering along [001]. In each tetragonal unit cell, 4 iron atoms and 8 vacancies lie on a fourfold screw axis. Braun [12] and Von Sinha *et al* [13] suggested that light atoms such as hydrogen were trapped in the cation vacancies, giving rise to a highly ordered superstructure.

1.2. HYDROLYSIS REACTIONS IN FERRIC SALT SOLUTION.

The Quantification of the mechanisms by which crystalline phases are precipitated from solutions of transition metal salts is subject to a multitude of experimental and conceptual difficulties concerning multiple reaction pathways that occur simultaneously and are difficult or impossible to separate [14].

In the case of ferric species, Flynn [15] combined previous hydrolysis schemes proposed by De Bruyn [16-20] and Spiro *et al* [21-24] into a four stage ageing process depicted below.

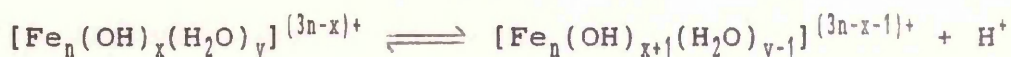
- 1) Formation of low molecular weight species, leading to development of polymer spheres.
- 2) Hardening of the spherical polymer.
- 3) Gradual aggregation to rods and rafts.
- 4) Precipitation of crystalline phases.

1.2.1. INITIAL HYDROLYSIS EQUILIBRIA.

The eventual conversion of the hexa-aqua ion $\text{Fe}(\text{H}_2\text{O})_6^{3+}$ into crystalline oxide/oxyhydroxide phases during ageing can be viewed as a polymerisation reaction, initiated by proton loss. The liberation of H^+ ions into solution leads to a gradual decrease in the gel pH as hydrolysis proceeds. Previous studies [16,17] have shown that there is a pH value (pH_0) above which the pH decrease will start immediately after preparation. At $\text{pH} < \text{pH}_0$ the polymerisation begins only after an induction period.

A range of possible reactions which may be involved at the initial stages of polymerisation is illustrated in Fig. 1.7. A limited number of species are shown, including only hydroxo-bridged oligimers or polymers. The $\text{Fe}(\text{OH})_2^{2+}$ and $\text{Fe}(\text{OH})_2^+$ species formed by deprotonation of the hexa-aqua ion are expected to possess the structures $[\text{Fe}(\text{OH}_2)_5(\text{OH})]^{2+}$ and *cis-* or *trans-* $[\text{Fe}(\text{OH}_2)_4(\text{OH})_2]^+$ respectively. The dimeric species $\text{Fe}_2(\text{OH})_2^{4+}$ or Fe_2O^{4+} has been structurally characterised only in the form of complexes with organic ligands, e.g. in $[\text{L}_5\text{FeOFeL}_5]$ where L is the pentadiene amine. This process of hydroxo-bridge formation is known as *olation*.

Fig. 1.7 can be compared to an organic polymerisation reaction, where it is often enough to use one rate constant for chain initiation, one describing chain lengthening, and some form of termination step. However, the hydrolysis of ferric solution is very different. As the charge per unit iron decreases, reactions involving water displacement become faster. Consequently, the rate of polymerisation increases from left to right across the reaction scheme. Similarly, the rate increases going from top to bottom since the acidity of a polymer is noticeably higher than that of the corresponding monomer, due to the charge effect on the protolytic equilibrium:



Studies have shown that the *olation* process predominates in the early stages of hydrolysis. Experimental data from de Bruyn supported the notion that *olation* is reversible, and depolymerisation is easily achieved by acidification.

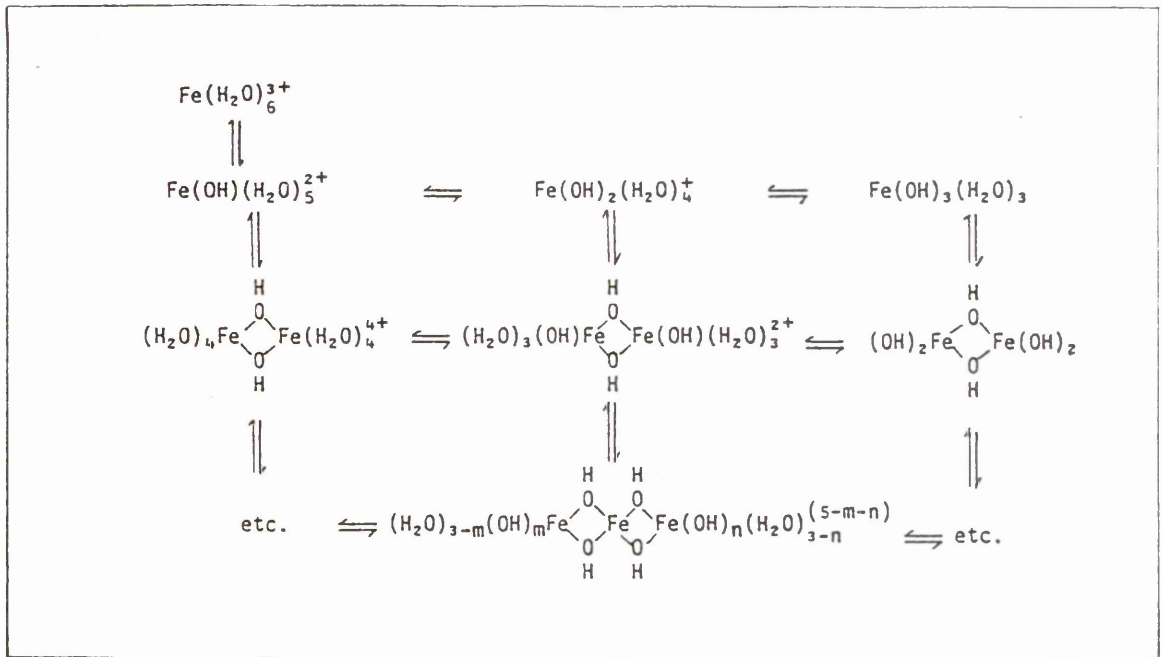


Fig.1.7:- Olation reaction matrix at the initial stages of polymerisation.

The second process required for polymerisation involves formation of oxo-bridges from two hydroxide ligands through loss of water. This is known as *oxolation*:



where the reactants are polymers of variable size. De Bruyn considered that oxolation is essentially irreversible: acid addition will not restore initial conditions, even after a considerable time.

Since the development of polynuclear species is accompanied by a continuous fall in the pH of the ferric solution, this characteristic can be utilised to follow the kinetics of polymer growth. De Bruyn *et al* [17] studied the reaction in the pH range 1.7-2.5, and found that there was a preliminary induction period, increasing indefinitely at progressively lower initial pH (keeping $C_{\text{Fe(III)}}$ constant) during which critical nuclei having 16-32 Fe atoms were formed. Growth was thought to proceed via addition of an unspecified polymeric unit.

1.2.2. FORMATION AND COMPOSITION OF HIGH MOLECULAR WEIGHT POLYNUCLEAR SPECIES.

The equilibria leading to the low molecular weight hydrolysis products illustrated in Fig. 1.7 are established rapidly and are well understood. Of interest here are the species Fe^{3+} , $\text{Fe}(\text{OH})^{2+}$, $\text{Fe}(\text{OH})_2^+$ and $\text{Fe}_2(\text{OH})_2^{4+}$ or Fe_2O^{4+} . If the solutions are aged at $\text{pH} < 2.8$, both the time elapsing prior to precipitation and whether the precipitate is amorphous or crystalline is dependent on the molar ratio $\text{OH}^-:\text{Fe}^{3+}$ of excess

base added. If this value, termed a , is greater than a critical value a_{min} (which lies between 0.5 and 1.0) then a crystalline precipitate will form in an ageing time of anything from minutes to hours. For reliable characterisation of the hydrolysis process, it is necessary to add base such that localised precipitation does not occur immediately. At $a < a_{min}$ a microcrystalline precipitate forms directly from a solution of low molecular weight species (where large polynuclears are absent). On addition of sufficient base giving a ratio $a_{min} < a < 2.8$, the pale yellow ferric solution will take on a red-brown colour as colloidal polynuclear species form and slowly transform (over a period of weeks to months at room temperature) to give either an amorphous precipitate or crystalline oxide/oxyhydroxide phases. Spiro *et al* [23] and Quirk *et al* [25] isolated the hydrolytic polymer from ferric nitrate and chloride solutions as an amorphous solid. The OH:Fe mole ratios they derived indicated that the polymer was cationic, and evaluation of structural data indicated that the iron atoms had co-ordination number 6, giving a basic $Fe(O, OH, H_2O)_6$ structural unit. Infra-red spectra for the isolated polymer obtained by Spiro *et al* [23] indicated that NO_3^- was not coordinated to Fe, while corresponding powder diffraction data suggested the possibility of tetrahedral co-ordination of iron by oxygen, with an Fe-O distance 0.21nm and nearest Fe-Fe separation 0.35nm. Alternatively, better-resolved XRD data obtained for hydrolysed ferric nitrate solution by Magini [26] was interpreted in terms of octahedral co-ordination of Fe(III), with Fe-O measured at 0.20-0.21nm and Fe-Fe at 0.34-

0.35nm. However, Spiro found that his optical data suggested in favour of octahedral rather than tetrahedral co-ordination in the polymer. Further comparison of the observed Fe-O separation in polynuclears with values for crystalline phases also supported an octahedral environment (with Fe-O distances 0.20 to 0.21nm for octahedral and 0.18-0.19nm for tetrahedral Fe).

The postulated $\text{Fe}(\text{O}, \text{OH}, \text{H}_2\text{O})_6$ octahedra in the polymers are likely to be joined by sharing vertices and/or edges. For octahedra sharing edges the expected Fe-Fe distance is 0.30nm while corner-sharing gives a 0.38-0.41nm spacing. Spiro *et al* [23] deduced a minimum Fe-Fe distance of 0.34-0.35nm. However, Fe-Fe interactions were not well-resolved from those only involving oxygen. The data are therefore inconclusive as to the mode of linking the octahedra in the polymers; both edge and vertice sharing may be present.

1.2.3. DEVELOPMENT OF CRYSTALLINE FERRIC OXIDE AND OXY-HYDROXIDE PHASES.

A diagram of the proposed mechanism by which crystalline solids are eventually deposited from ferric nitrate or perchlorate solution through hydrolysis is shown in Fig.1.8. Spiro *et al* [21,24] suggested a two-step ageing process for the initial polymer spheres which were first formed from solution. This consisted of a "hardening" stage, followed by agglomeration. De Bruyn *et al* [16-19] inferred a three-step approach consisting of formation of polymer spheres from low molecular weight species, aggregation and subsequent precipitation.

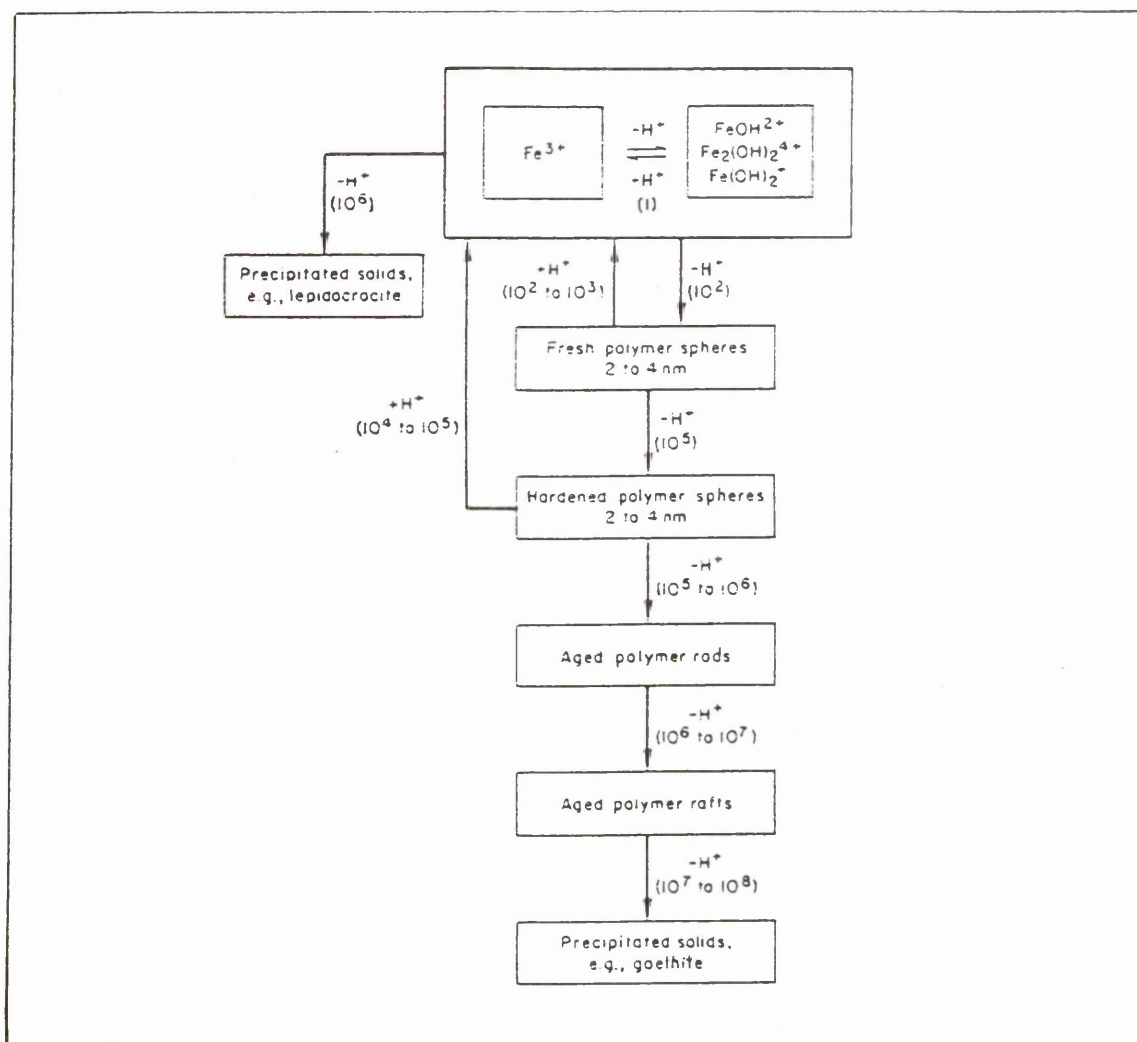


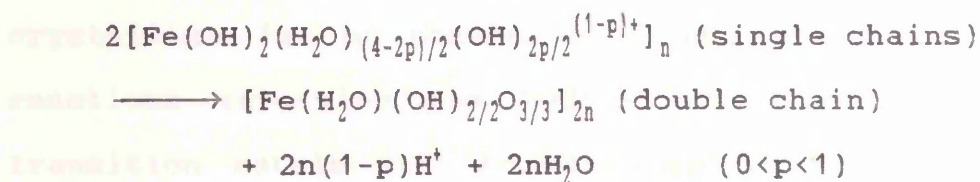
Fig.1.8:- Hydrolysis processes in Fe(III) solution. Numbers in brackets give reaction times (s) at 25°C.

The nature of hydrolysed ferric salt solutions has been extensively studied by Quirk *et al* [25,27a)-c)] and De Bruyn *et al* [16] using a combination of ultracentrifugation and TEM. If the solution pH was greater than pH_p , then small polymeric species were found to have developed after 24 hours ageing. TEM examination of aged nitrate, perchlorate or chloride solutions showed that the hydrolytic polymer present in the gels comprised spheres, 2-4nm in diameter, having a molecular weight of the order 10^4 . On the basis of a monomer of formula $\text{Fe}(\text{OH})_{2.5}^{0.5+}$, the number of iron atoms per polymer particle is about 10^2 .

The polynuclear species were found to aggregate to form rods and rafts over a period of 1 to 10 days. Individual spheres gradually lost their identity, and after weeks to months ageing the rafts slowly flocculated to form a crystalline precipitate. In the case of nitrate or perchlorate solutions, the solid product was found to comprise α -FeOOH (or γ -FeOOH if the ferric ion concentration and OH:Fe ratio were low) [28-32]. The oxide phase, hematite, was generally observed only in high temperature preparations, while β -FeOOH was only produced in gels containing chloride ions [16,33-39].

The possible condensation reactions by which monomeric $[\text{Fe}(\text{H}_2\text{O})_{6-n}(\text{OH})_n]^{(3-n)+}$ combines to form polymers comprising -Fe-OH-Fe- and -Fe-O-Fe- linkages (through ololation and oxolation respectively) have already been described. A more plausible description of the irreversible oxolation reaction mechanism can be made by considering the process not in terms of a simple deprotonation step (which should be fast and revers-

ible), but as a condensation-deprotonation of two single chains of edge-linked $\text{Fe}(\text{OH}, \text{H}_2\text{O})_6$ octahedra to form double chains having composition $\text{Fe}(\text{O}, \text{OH}, \text{H}_2\text{O})_6$. This can be expressed by



The low rate for the oxolation reaction is therefore not surprising, due to the probable displacement of co-ordinated H_2O , OH^- or other ligands, and the necessary steric requirements.

The eventual deposition of solid phases from ferric salt solution can be explained using this scheme if further condensation of the above double chains is now considered. If chain-linking proceeds solely through corner-sharing, it can be seen how the α - FeOOH or, if Cl^- is present, β - FeOOH structures could arise (Section 1.1). By contrast, development of γ - FeOOH requires formation of double layers of octahedra solely connected through edge-sharing, with H-bonding holding these layers together. Such a structure cannot easily develop via a mechanism involving formation of double chains [15]. It is not clear whether the processes by which α - Fe_2O_3 is formed involve the polymer or only low molecular weight species. If the oxide does develop directly from solution, then the formation of kinked chains is necessary, as the structure cannot be constructed using straight single or double chains (Section 1.1).

1.3. FORMATION OF CRYSTALLINE PHASES FROM AQUEOUS Mn(II), Co(II), Ni(II), Cu(II) AND Zn(II) SALT SOLUTIONS.

Before the formation of synthetic ferrihydrite (the unstable "iron (III) hydroxide") and its conversion to crystalline ferric phases are considered, the comparable reactions involving the hydroxides of other first row transition metals will be discussed. If these species are introduced to alkaline ferrihydrite gels, the presence of totally separate crystalline additive phases is often observed in products formed where the foreign ions are present in large quantities. The solubility of the relevant additive hydroxides may also influence the final product composition, and should be considered.

In contrast to the behaviour of ferric species, most other first row transition metal cations undergo only a low degree of hydrolysis prior to precipitation. In acid media, hydrolysis of Zn^{2+} leads to formation of only low molecular weight polynuclears, of which $Zn(OH)^+$ is the best established. At neutral pH, these species are soon precipitated [40]. In basic media, $Zn(OH)_4^{2-}$ and possibly $Zn_2(OH)_6^{2-}$ are present. The hydroxide is readily soluble in concentrated base (Table 1.1). Gubeli et al [41] calculated the solubility of zinc hydroxide ($Zn(OH)_2$) as a function of pH. A plot of $[Zn_{tot}]$ vs pH gave a curve with maxima at pH 7 and 12 and minimum values about pH 9.6-10.0. $Zn(OH)^+$, $Zn(OH)_2$ and $Zn(OH)_3^-$ were detected at about pH 7.5, with $Zn(OH)_4^{2-}$ dominating at pH > 11.

Zinc hydroxide shows a complicated system of solid phases [40]. Precipitates formed from salt solutions where

OH:Zn < 1 usually comprise active forms, eg amorphous Zn(OH)_2 or $\alpha\text{-Zn(OH)}_2$ which transform to more stable forms on ageing. Sometimes, mixed precipitates are produced. In Zn(II)-water systems, the distinct solid phases are amorphous Zn(OH)_2 , α , β_1 , β_2 , γ , δ and $\epsilon\text{-Zn(OH)}_2$, active ZnO and inactive ZnO. The oxide is the most stable phase at ambient temperature.

Copper(II) and cobalt(II) species also undergo only slight hydrolysis prior to precipitation. In alkaline media, both the hydroxides exhibit amphoteric behaviour, yielding Cu(OH)_4^{2-} and Co(OH)_4^{2-} respectively in strongly alkaline solution. By contrast, Mn(II) is only slightly amphoteric. The predominant species released into solution is thought to be Mn(OH)_3^- . In this case, the hydroxide is the stable phase relative to MnO . The hydroxide of nickel is insoluble [40, 42]. In acidic media, the solubility decreases linearly as the pH increases. At a point just below pH 7, the value then curves asymptotically. In alkaline media the hydroxide is effectively insoluble, and will age to form crystalline Ni(OH)_2 .

CATION	HYDROXIDE SOLUBILITY	CRYSTALLINE PRODUCT
Mn(II)	slightly soluble, probably giving Mn(OH)_3^- in solution	Mn(OH)_2 is stable relative to the oxide, MnO
Co(II)	Co(OH)_4^{2-} in solution	Co_3O_4 , CoOOH
Ni(II)	insoluble	Ni(OH)_2
Cu(II)	Cu(OH)_4^{2-} in solution	CuO
Zn(II)	Zn(OH)_4^{2-} in solution	mainly ZnO

Table 1.1:- Additive hydroxide solubilities and potential transformation products.

1.4. FORMATION OF CRYSTALLINE PRODUCTS FROM THE POORLY-ORDERED OXIDE-HYDRATE FERRIHYDRITE.

1.4.1. PROPOSED STRUCTURES FOR FERRIHYDRITE.

Addition of excess base to ferric salt solution, such that the ratio of hydroxyl to iron species exceeds 2.8, will result in the immediate formation of a red-brown precipitate. The first worker to obtain distinct X-ray diffraction patterns for such a gel was Van Der Geissen [43], who prepared the hydrous oxide by precipitating ferric nitrate solution at room temperature using ammonia. The solid was isolated by freeze-drying and characterised. TEM showed masses of poorly-defined platelets about 3nm in diameter. XRD patterns were obtained using $Mo_{K\alpha}$ radiation rather than $Co_{K\alpha}$ which had previously suggested that the precipitate was amorphous. Der Geissen indexed the observed reflections (Table 1.2) in terms of a cubic unit cell having $a_0 = 0.837\text{nm}$, a value quite close to the unit cell dimension of magnetite and maghemite. Soon afterwards, Towe and Bradley [44] obtained XRD data for a hydrolysate formed by heating ferric nitrate solution at 80°C without introducing base to the system. In this study, the powder diffraction data suggested that the solid contained hexagonally close-packed anion layers, with lattice parameters $a_0 = 0.508\text{nm}$ and $c_0 = 0.94\text{nm}$. The proposed structure was essentially equivalent to that of hematite, but with all lines and amplitudes derived from the ordered rhombohedral cation arrangement missing (including 0.368nm (01.2) and 0.267nm (10.4), the two strongest low-angle spacings).

hkl	GEISSEN, 1966		TOWE, BRADLEY, 1967		CHUKHROV, 1971	
	d(nm)	I	d(nm)	I	d(nm)	I
110	0.252	vs	0.254	s	0.250	m
112	0.225	s	0.224	ms	0.221	mw
113	0.197	s	0.198	m	0.196	vw
114	0.172	s	0.172	w	0.172	vw
115	not found		0.152	m	0.151	m
300	0.148	vs	0.147	s	0.148	m

Table 1.2:- powder diffraction spacings obtained for synthetic and natural ferrihydrites in previous studies.

Chukhrov *et al* [45] and Schwertmann [46] later carried out studies of naturally-occurring "amorphous" ferric oxide-hydrates. The former workers were the first to propose the name "ferrihydrite" for the mineral having composition $5\text{Fe}_2\text{O}_3 \cdot 9\text{H}_2\text{O}$. The solid contains 15-25% water, and infrared studies by Russell [47] showed that the concentration of structural OH may lie between one third and one half that in crystalline ferric oxides. Towe and Bradley [44] suggested the formula $\text{Fe}_5\text{HO}_8 \cdot 4\text{H}_2\text{O}$ for the synthetic polymer hydrolysate, while Russell proposed $\text{Fe}_2\text{O}_3 \cdot 2\text{FeOOH} \cdot 2.6\text{H}_2\text{O}$ for the mineral, in order to indicate the presence of OH groups as well as water in the structure.

The hematite-like model proposed by Towe and Bradley [44] is shown in Fig.1.9 a). The ferrihydrite structure is shown in projection on the plane (11.0), and comparison with hematite (Fig.1.9 b)) shows that displacements are ordered such that the repeat period covers four successive close

packed $O^{2-}/OH^-/H_2O$ anion layers. This is less than the six-layer repeat unit for hematite. In four successive layers the octahedral cation sites occupied should be $2/3, 1/3, 1/3, 1/3$.

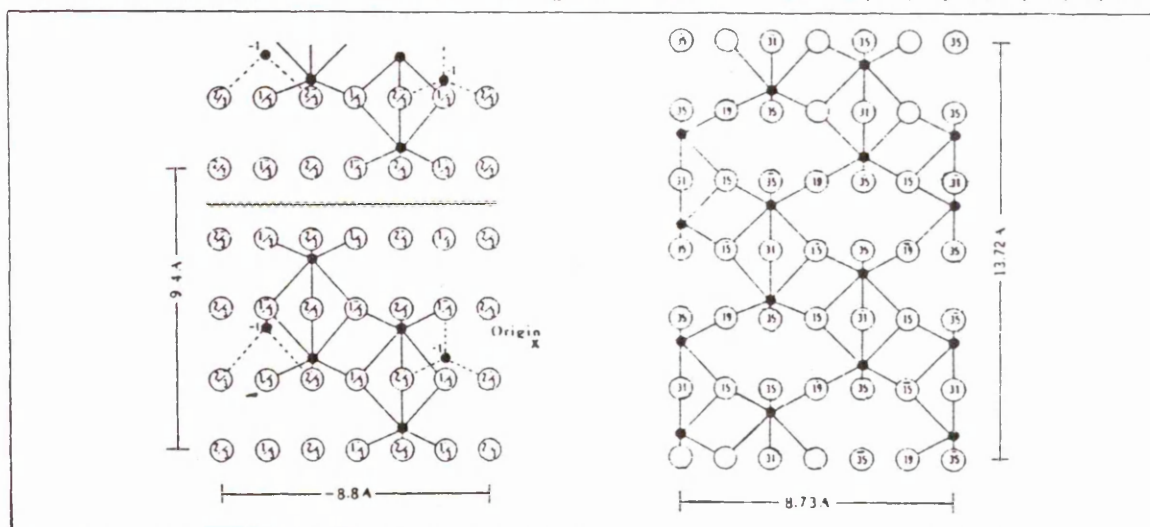


Fig.1.9:- possible hematite-like structure for ferrihydrite. a) projection of ferrihydrite on $[11.0]$. Idealised detail of Fe octahedra are shown. Lateral displacements are optional at the horizontal line. b) projection of hematite on $[11.0]$ (from Towe and Bradley [44]).

Chukhrov *et al* [45] suggested that since the diffraction data for ferrihydrite is limited, the above structural model should be taken as tentative. Atkinson *et al* [48] examined synthetic precipitates obtained by addition of strong base to ferric nitrate, and suggested that the principal diffraction lines observed, at 0.252nm, 0.148nm and 0.127nm, could be derived from a combination of goethite reflections (for which $d(021)=0.258\text{nm}$, $d(040)=0.249\text{nm}$, $d(002)=0.151\text{nm}$, $d(042)=0.129\text{nm}$ and $d(080)=0.125\text{nm}$). The remaining lines associated with ferrihydrite can also be attributed to goethite. However, comparison of calculated and observed XRD intensities by Van der Giessen [43] suggested that neither a hexagonal nor a

cubic unit cell adequately described the structure.

The degree of ordering in the solid has been found to be dependent both on the method of preparation and the degree of ageing. A maximum of six lines have been observed for the most highly-ordered solids, but ferrihydrite obtained by rapid neutralisation of ferric solutions generally shows only two broad bands at 0.25 and 0.15 nm with $\text{MoK}\alpha$ radiation. These lines were thought to correspond to diffraction by (11.0) and (30.0) planes within the hexagonal anion layer. Feitknecht *et al* [49] proposed that the basic structural unit in this material is a tetramer composed of four planar $\text{Fe}(\text{O},\text{OH})_6$ units. It has also been suggested that the spacings at 0.25 nm and 0.15 nm, present for most of the iron oxyhydroxide phases, are characteristic of a ferrihydrite precursor called "proto-ferrihydrite". Burns [50] thought that the mineral ferrihydrite could merely arise from a poorly ordered arrangement of FeO_6 octahedra.

Only recently, Manceau *et al* [51] proposed a new model for ferrihydrite based on local structure measurements made by EXAFS, and a comparison of experimental and calculated XRD profiles. Two and six-line solids precipitated from ferric salt solutions were both found to be short-range ordered, consisting of Fe octahedra linked by corners, edges and faces. The structures were found to be related to well-crystallised oxides/oxyhydroxides, and the absence of definable hkl reflections in some samples was found to be caused by the small size of the coherent scattering domains (csd). The measured Fe-Fe distances and static disorder implied that ferrihydrite

has similarities to both hematite and $\alpha/\beta/\gamma$ -FeOOH polymorphs. The local structure differs from the aqueous polymers formed by hydrolysis of ferric salt solutions (Section 1.2).

The ordered six-line ferrihydrite was found to comprise a mixture or fine intergrowth of three components:-periodic and non-periodic alternations of hcp and ccp packings and ultradispersed hematite (2nm wide by 1.4nm thick). Ferrihydrite proper then consists of ABA and ACA fragments with ferric ions only occupying octahedral interstices. In most of the individual particles, ABACAB.... packing forms a 3D structure. In some cases the fragments alternate randomly. The 3D model allows for the presence of cavities or channels inside ABA and ACA fragments. Anions in A sites form continuous 2D planes, while an island-like structure (nano-porosity) can develop, since only 85% of B and C positions are occupied (water can be accommodated by the remaining 15 %). However, due to the absence of any long-range Fe distribution, the structure can still be described as possessing a hexagonal sublattice.

1.4.2. NUCLEATION AND GROWTH OF GOETHITE AND HEMATITE.

The "amorphous" ferric oxide-hydrate described in the previous section is thermodynamically unstable, and will transform in time to produce the more stable crystalline phases hematite (α -Fe₂O₃) and goethite (α -FeOOH). The composition of the products so formed is found to be highly dependent on the ageing conditions [48,52-57], with goethite formation promoted where dissolution of ferrihydrite is at

a maximum, and hematite produced where the solid precursor is most stable. It is therefore proposed that these crystalline phases are formed by two competing mechanisms: -hematite nucleation and growth occurring within the particles of ferrihydrite, while goethite nucleates solely in the bulk solution, without any direct interaction with the solid.

Reaction kinetics have mainly been followed using a method developed by Schwertmann [58], which involved measurement of the level of unconverted ferrihydrite as an indicator of the extent of reaction. Results have shown that the transformation proceeds in two stages. An initial slow stage, termed the induction period, is followed by a much more rapid reaction. The induction period, which corresponds to the time during which crystal nucleation occurs, can be extended by altering the solution conditions. Increasing the ionic strength or the concentration of hydroxyl ions, or lowering the temperature all serve to retard the transformation [57]. Once the second stage of the transformation is under way, the overall rate of conversion can be expressed as the sum of the rates for goethite and hematite, i.e. $R_{\text{total}} = R_{\text{H}} + R_{\text{G}}$. A plot of $-\ln[\text{ferrihydrite remaining}]$ vs time for this stage of the reaction is linear, indicating a first order reaction with respect to the amount of ferrihydrite remaining.

The master variable governing the composition of the products is pH. Schwertmann and Murad [53] precipitated ferrihydrites from ferric nitrate solution at pH 7-8 and held the resultant gels in solutions at pH 2.5-12 for up to three years at room temperature. Characterisation of products showed

that hematite formation was at a maximum at pH 7-8, while the sole product at pH 4 and 12 was goethite. The relative proportions of each phase produced appears to depend on the activity and nature of the ferric species present in solution. The point of zero charge for ferrihydrite is approximately 7.5, and at pH 7-8 the aggregation of ferrihydrite under the influence of Van der Waals forces is at a maximum. Similarly, the activities of aqueous ferric species, Fe(OH)_2^+ and Fe(OH)_4^- are maximised at pH 4 and 12 respectively [40]. Schwertmann and Fischer [55] followed the conversion of ferrihydrite to hematite at pH 6 by TEM, and found that the small precipitate particles gradually coalesced to form larger, more dense aggregates which eventually transformed into single, highly defect crystals of hematite. X-ray diffraction/on-line neutron diffraction studies on the hydrothermal growth rate of goethite/hematite have shown that the gel acidity increased as ferric species liberated protons from water as hematite formed [56]. Combes *et al* [59] used X-ray absorption spectroscopy (EXAFS) to quantify changes in the local structure of ferrihydrite as transformation to hematite proceeded at neutral pH. They found that, during the early stages of reaction, a significant increase in the localised ordering occurred. Fe-Fe distances became shorter and FeO_6 octahedra adopted the distorted habit associated with hematite. Since ferrihydrite and hematite both share a similar hexagonally-packed anion sublattice, nucleation of hematite might require only that ordered regions within ferrihydrite are formed. The aggregation stage observed by Schwertmann

and Murad [53] may promote ordering. From the experimental observations, nucleation and growth is thought to proceed by a combination of dehydration and condensation reactions. Once nucleation has occurred, growth would continue until the local supply of growth units is exhausted. The mechanism of growth may involve loss of a proton from a structural hydroxyl group present in ferrihydrite, followed by migration of the proton to combine with another OH group, leading to elimination of a water molecule and formation of an oxo linkage [60]. The local charge imbalance caused by proton loss is then compensated for by migration and redistribution of Fe^{3+} within the cation sublattice. However, if the ferrihydrite model proposed by Manceau [51] is employed it is likely that some degree of dissolution-reprecipitation operates, with the channels in the solid precursor possibly allowing migration of ions and lateral displacement of cubic layers to hcp.

Formation of goethite from ferrihydrite in both acidic and alkaline media is dependent on the rate of dissolution of ferrihydrite. Exact details of the mechanism by which crystal nucleation and growth occurs have not been established, but a reconstructive transformation by which goethite nuclei, formed during the induction period, are fed by soluble ferric species is thought to operate. In alkaline media the growth unit is thought to be $\text{Fe}(\text{OH})_4^-$, which is the predominant ferric species present in solution at up to pH 12-13 [57]. It is a suitable growth unit both for ease of rearrangement at the crystal surface and because it need only lose

one unit of charge upon incorporation into the crystal lattice. The exact point at which hematite ceases to form with increasing pH is subject to disagreement in the literature, where values between 10 and 12 are quoted [48,57,61]. Ferrihydrite transforms solely to goethite in the range 12 to 14, but Cornell and Giovanoli [57] found that hematite reappeared in products formed at $\text{pH} > 14$. The proportion of hematite present increased with hydroxyl ion concentration, and comprised 95% of the product at 6M $[\text{OH}^-]$. Similarly, raising the suspension concentration and reaction temperature both promote hematite formation. According to Lengweiler *et al* [62], dissolution of ferrihydrite may involve interaction of hydroxyl ions with the ferrihydrite surface. In this way, where hydroxyl concentrations are high enough, the surface may become saturated with base and the rate of dissolution may reach a limiting value. The rate of nucleation of goethite and hence the rate of growth depends on the free energy of nucleation, which in turn depends on the supersaturation of the solution with respect to goethite. The rates of nucleation and growth of both goethite and hematite are retarded at very high pH, but the effects are much greater for goethite. As described above, the dissolution of ferrihydrite may reach a limiting value, while at the same time nucleation and growth of goethite may also be retarded in solution as the predominant soluble ferric species ($\text{Fe}(\text{OH})_4^-$ [62]) is replaced at high pH by another ion that requires greater modification to form a critical nucleus or become incorporated at the crystal surface. At high pH, TEM studies have shown long, thin goethite

crystals with numerous surface imperfections. This observation is consistent with the idea that species less favourable for goethite formation are present. Possible anions which have been suggested are $\text{Fe}(\text{OH})_5^{2-}$ and $\text{Fe}(\text{OH})_6^{3-}$ [53,63], but there is no hard evidence that they actually exist.

1.4.3. EFFECT OF GROWTH CONDITIONS ON THE MORPHOLOGY OF TRANSFORMATION PRODUCTS.

A variety of experimental conditions can affect the nature of the crystalline phases which develop during the transformation of ferrihydrite. Temperature, ionic strength, hydroxyl ion concentration and pH are all capable of altering not only the product composition, but also the crystal morphology.

In most preparations, single crystals of goethite adopt a characteristic acicular morphology, where extension of the c-dimension relative to a and b results in the formation of long, needle-like crystals. Hematite produced at pH 7 typically grows as plate-like crystals which show hexagonal symmetry [48,54]. In products where both phases occur together, epitaxial twinning is found to be common [48,57].

Goethite crystals are often found to be multi-domainic, comprising several intergrowths running parallel to the c-axis. These are thought to arise due to secondary nucleation on (010) faces, where active hydroxyl groups can act as a template for epitaxis to proceed [57,64]. Since the process is relatively slow, interfacial irregularities are relaxed and the resultant intergrowths are largely coherent. Cornell and

Giovanoli [57] found that increasing the hydroxyl ion concentration inhibited goethite formation and gave rise to crystals which were free from intergrowths. Partial dissolution in acid showed that numerous structural defects were present. Similarly, increasing the ionic strength resulted in the formation of crystals with surface irregularities, ragged edges, etc. This observation suggested that some interference due to anion adsorption had occurred during crystal growth. Raising the ionic strength was also found to promote intergrowth formation, independent of pH. Schwertmann *et al* [65] studied the effect of temperature on the crystallinity of goethites formed from ferrihydrites stored between 4 and 90°C. Raising the temperature was found to increase particle size and reduce the domainic character of the crystals. A combination of XRD, IR and dehydroxylating temperature data suggested that a low temperature (low a -dimension, a_0 about 0.463nm) and a high temperature (high a -dimension, a_0 about 0.461nm) goethite had been produced. A narrow transition range was observed where the transformation temperature was in the region 40-50°C.

Variations in hematite morphology due to solution conditions are less apparent and subject to little discussion, although studies have indicated that crystal regularity improved with increasing temperature, while raising ionic strength produced crystals having a distorted morphology [57].

1.5. EFFECT OF FOREIGN IONS ON THE TRANSFORMATION OF FERRIHYDRITE.

Previous laboratory studies have, to varying extents, considered the effects of phosphate, silicate species, simple sugars, organic acids and metal cations such as Al, Ti, Mn, Co, Ni, Cu and Zn on the transformation of ferrihydrite. Products have been formed under a wide variety of growth conditions, with gels held at pH values ranging from slightly acidic (pH 6) to strongly alkaline (pH 12) and at temperatures between 25 and 90°C. The majority of additives have been found to retard the crystallisation and frequently give rise to an increase of the proportion of hematite in the products. Their effectiveness increases with additive concentration and decreases with rising pH.

Generally, the additives can be divided into four groups, depending on how they influence the kinetics and products of transformation:-

- 1) Those that *strongly retard* the reaction and promote formation of $\alpha\text{-Fe}_2\text{O}_3$ *indirectly*, e.g. citric acid, phosphates, silicates, glucose, maltose and *meso*-tartaric acid [51, 61, 66-68, 69-72].
- 2) Those that *weakly retard* the transformation and promote formation of $\alpha\text{-Fe}_2\text{O}_3$ *indirectly*, e.g. lactic acid and sucrose [61, 68].
- 3) Those that *accelerate* the transformation and *directly* promote nucleation of $\alpha\text{-Fe}_2\text{O}_3$, e.g. oxalic acid and 1-tartaric acid [54, 67].
- 4) Cations that weakly or moderately retard the trans-

formation, can be incorporated into the lattices of goethite and hematite, and induce formation of other crystalline phases, e.g. Al, Mn, Co, Ni, Cu and Zn [73-80].

Alternatively, the additives can be grouped as those which are not incorporated into the crystalline phases, i.e. *ligands*; and those which are, i.e. *substituents*.

1.5.1. ADSORPTION OF IONIC SPECIES ON FERRIHYDRITE AND FERRIC OXIDES/OXYHYDROXIDES IN SOLUTION.

The extent of interaction of additive species at a metal oxide-solution interface should be considered in terms of electrostatic forces, chemical considerations and the nature of the cationic species in solution.

The surface charge of hydrated metal oxides is found to arise through the removal from solution of protons, hydroxyl ions or water to complete the co-ordination sphere of the surface metal ions [81]. The -M-OH groups so formed are involved in acid-base reactions, resulting an overall positive, negative or neutral surface charge:-



Dissociation gives



The zero point of charge (zpc) will lie at the pH value for which equal numbers of positive and negative surface groups are present (the pH(zpc)). In the absence of specific adsorbing ions, the value is intrinsic for each oxide (Table

1.3) and depends on the acidity of the metal plus the electrostatic field of the solid. The $\text{pH}(\text{zpc})$ is generally found to be inversely proportional to the metal charge:radius ratio and also to the size of the unit cell.

ferrihydrate	7.6-8.1	$\gamma\text{-Fe}_2\text{O}_3$	6.7
$\alpha\text{-FeOOH}$	5.9-7.2	Fe_3O_4	6.5
$\alpha\text{-Fe}_2\text{O}_3$	5.2-8.6		

Table 1.3:- points of zero surface charge for selected ferric oxide phases in solution (from Riley [82]).

The discussion is further complicated, since adsorption can be affected by more than electrostatic forces, eg phosphate, arsenate and selenite anions are known to adsorb on negatively charged iron oxide surfaces [82]. The interaction of metal ions is therefore best explained in terms of both chemical and coulombic attraction.

1.5.2. EFFECT OF ADDITIVES ON PRODUCT COMPOSITION.

1.5.2.a) ADSORBING LIGANDS.

Many ligands adsorb on the surface of ferrihydrate and can stabilise the precipitate against both internal rearrangement and dissolution, thereby potentially hindering nucleation and growth of hematite and goethite. In addition, a variety of ligands can hinder nucleation and growth of goethite in solution. Those additives that adsorb on ferrihydrate have a much greater retarding effect than those which act only in solution.

Adsorbing ligands retard the formation of $\alpha\text{-FeOOH}$ by hindering dissolution of ferrihydrate, thereby reducing

the supply of soluble ferric species available for nucleation and growth of the oxyhydroxide phase. It is found that the most strongly adsorbing ligands are those which retard the transformation to the greatest extent. Little is known about the mechanism by which ligands prevent dissolution, but it is assumed that they act by blocking specific surface sites from which the release of soluble ferric species proceeds. Rubio and Matijevic [83] suggested that phosphate and silicate species, which form multi-nuclear surface complexes, stabilise an oxide while polydentate mono-nuclear surface species withdraw electron density from the metal-oxygen bonds in the lattice, so promoting dissolution.

Two possible mechanisms have been suggested by which aggregation of ferrihydrite is retarded by adsorbing ligands. In the first case, two or more particles may be linked to form an immobile network by a polydentate ligand. A stabilising effect is often observed for a level of adsorption giving much less than a monolayer coverage. Alternatively, the negative surface charge may be increased through formation of surface complexes by anionic species at pHs above the z.p.c. of ferrihydrite, thereby inhibiting particle aggregation. This mechanism is supported by the observation that in systems containing silicate species, increasing ionic strength promotes formation of hematite at pH values where only goethite is expected to form.

Oxalate and 1-tartrate, which directly promote formation of hematite, are thought to operate by directing the formation of ordered regions, which have Fe-Fe distances comparable to

those in hematite, within the ferrihydrite precursor. These areas may then act as nuclei for growth of the oxide. Fischer and Schwertmann [54] found that at pH 6 in the presence of oxalate the rate of transformation was increased, while the intermediate aggregation step was absent, i.e. particles of the amorphous precipitate coalesced directly into single crystals of $\alpha\text{-Fe}_2\text{O}_3$. These ligands adsorb on ferrihydrite through functional groups (COOH and/or OH) which are separated by one C-C bond, forming binuclear ferric-organic surface complexes.

In solution, ligands such as lactose and sucrose, which adsorb weakly or not at all on ferrihydrite, retard the transformation by interfering with nucleation of goethite. Competition for sites on subcritical nuclei between the organic ligand and $\text{Fe}(\text{OH})_4^-$ probably retards formation of stable goethite nuclei. This effect increases with rising additive level, but can be eliminated by seeding with crystals of $\alpha\text{-FeOOH}$. Additives that do adsorb on ferrihydrite also retard formation of goethite in solution, but in cases where the ligand adsorbs strongly, interference in solution is outweighed by the retardation in the release of soluble ferric species and seeding has little effect.

1.5.2.b) CATIONIC SPECIES.

Previous studies have considered the effects of Al^{3+} , Mn^{2+} and Cu^{2+} on the transformation of ferrihydrite in detail, while the influence of Co^{2+} , Ni^{2+} and Zn^{2+} has thus far only been considered briefly. The presence of the above species

has been found to direct the reaction in a manner similar to that of many anions, in that adsorption will retard the rate of dissolution of the disordered precursor. However, in contrast to most anionic species, the cations are easily incorporated in the crystalline phases formed (the main requirements for substitution being a reasonable match between the radii and charges of Fe^{3+} and the substituent cation). They will also induce formation of products other than goethite and hematite.

The extent to which the transformation of ferrihydrite is affected by the presence of these additive species is dependent on the nature of the ion present. The metal cations are typically found to promote formation of hematite at a higher pH than would otherwise be expected, since extending the induction period and retarding the overall rate of dissolution is effectively comparable to carrying out the reaction at lower pH. The only species previously found to deviate from this behaviour is Mn(II) [75]. Formation of hematite was found to be suppressed by manganese, even at low levels of addition, although formation of hematite containing up to 5 mol% Mn could be induced to form at pH 8 where oxalate species (which will directly promote formation of the oxide) were introduced to the system.

The additional crystalline products formed in additive-ferrihydrite gels which are of primary interest in the present work are the ferrite phases (nominally MFe_2O_4 , where M is the substituent ion). MnFe_2O_4 , CoFe_2O_4 , NiFe_2O_4 , CuFe_2O_4 and ZnFe_2O_4 have all been identified from powder diffraction data for

products formed in ferrihydrite gels held at pH 12. However, under equivalent conditions, the proportion of additive required to induce spinel formation varies from species to species [80]. The mechanism by which the spinel phase develops is not fully understood, but it is generally thought that growth proceeds through the dissolution-reprecipitation of soluble ferric and additive species. Crystal nucleation may occur in solution or may require a degree of interaction with the ferrihydrite precursor. The mechanism will be discussed in detail in Chapter 4.

At high levels of addition, the formation of a totally separate additive oxide phase is also usually observed (e.g. Mn_3O_4 , Co_3O_4 , CuO , etc).

1.5.3. EFFECT OF ADDITIVES ON PRODUCT MORPHOLOGY.

Although synthetic goethite crystals are found to display a multitude of shapes and sizes, the only two basic morphologies which have previously been characterised are acicular and twin forms. As described in Section 1.4.3, acicular crystals are elongated along [001] and typically comprise several well-formed intergrowths. Twin crystals often exhibit a pseudo-hexagonal symmetry, and may comprise either a plate-like hematite centre with outgrowths of goethite on the (11.0) faces (ie epitaxial twins), or consist of up to three acicular goethite outgrowths mutually rotated 120° and meeting on (021) planes (without a hematite centre). The latter, composite twins, show a variety of habits and are therefore classified as twin pieces, dendritic twins or star-shaped crystals.

The presence of an organic ligand is generally found to promote intergrowth formation in goethite. Temporary adsorption of the ligand on the surface of the growing crystal is thought to interfere with the surface mobility of growth units, causing a slight misalignment in ordering.

The only additives studied to date which have been found to produce a complete alteration in the characteristic acicular goethite morphology are silicate species. At lower levels of addition, the ligand appears to improve the crystallinity of goethite and induced formation of shorter, wider crystals which often display well-developed (021) faces. The presence of silicates will, in addition, reduce the

average number of domains per crystal to two or three well-defined intergrowths. These observations suggested that, where goethite is grown in glass vessels under alkaline conditions, silicate contamination may actually improve the crystallinity of the product. In the presence of higher silicate levels, goethite grows as pseudo-hexagonal plates or, at the highest concentration, as bipyramidal crystals bounded by well-formed (021) or (121) and (111) faces which develop at the later stages of transformation. The pseudo-hexagonal plates in the product were at first thought to be crystals of hematite, but were found to be very short, thick laths with enhanced development of the terminal (021) planes. The change in morphology appears to arise due to preferential adsorption of silicate species on these terminal faces of the crystals (which have a high Fe density), thereby retarding growth in that direction. Development of crystals with different habits at different stages of the transformation was thought to occur due to the increase in Si concentration in solution as the reaction proceeds. The pseudo-hexagonal crystals were usually found to be single-domain, and typically darker along the c-axis, suggesting that they are bounded by a few well-formed (110) faces.

As noted above, synthetic goethite crystals usually retain a more or less acicular shape despite the presence of additives. A common influence of those cationic species which have previously been studied, and those that are of interest in the present work, is to increase the length to width ratio of the crystals. As the proportion of additives such as Mn

or Co in the system increases, growth of very long, thin crystals (often exhibiting many surface imperfections) is induced. For those species already studied, this is attributed to adsorption rather than incorporation of the additives into the crystal lattice. Under conditions unfavourable for growth, such as the presence of temporarily adsorbing species, addition of growth units proceeds most readily at the ends of the crystals, reducing intergrowth formation and leading to formation of the elongated crystals observed.

Hematite crystals grown from ferrihydrite at pH 7-11 are typically observed as irregular or hexagonal plates 100-300nm in diameter. At pH > 14, the oxide forms as large plates with diameters between 1 and 3 μm .

In contrast to goethite, the morphology of hematite is readily modified by the presence of foreign species. The effects of organic ligands are well documented in the literature, but the morphologies of crystals grown in the presence of cationic species have not generally been described in detail.

Simple sugars such as maltose and glucose and citrate species are found to produce elongated rods up to 350nm in length. These rod-like crystals were found to be hematite which had grown preferentially in the [00.1] direction, with enhanced development of (11.0) planes probably arising due to preferential adsorption of the foreign ligand on these faces. In alkaline media, glucose and maltose are partially converted to a mixture of different sugars and hydrocarboxylic acids. The observed modification in the hematite morphology is probably due more to these species than to the

presence of the original sugars. The presence of oxalate or silicate species can produce very thick ellipsoidal crystals of hematite having an internal laminar or chain structure. The individual particles which made up these crystals exhibited an appearance reminiscent of ferrihydrite, but had developed a hexagonal morphology during crystallisation. It has been suggested that the shape of these crystals was due to adsorption of the ligand on the parent ferrihydrite, rather than on the growing crystal. If the products formed in the presence of silicates contained both hematite and goethite, then the oxyhydroxide was mainly present as outgrowths from the oxide. The number of outgrowths was found to decrease as pH of transformation increased; at or above pH 11, only two needles formed on either side of a hematite nucleus. Giovanoli noted that buserite grown in the presence of SiO_2 exhibited outgrowths that nucleated only on certain areas of the parent crystal: the other sites are presumably blocked by adsorbed silicate. This mechanism may also apply to the goethite-hematite system. Addition of maltose and glucose has been found to induce formation of a new epitaxial twin comprising acicular goethite outgrowths on prismatic hematite, usually perpendicular to the (11.0) faces. The outgrowths on these twins were typically found to number two or three (much lower than the six observed for twins having a plate-like centre of $\alpha\text{-Fe}_2\text{O}_3$). The outgrowths appeared to nucleate and grow on opposite sides of the prismatic oxide, and were often completely overgrown across the central area. The outgrowths were often narrower and thicker than

those on comparable single acicular crystals, an effect which could be accounted for if the twins were viewed with [010] perpendicular to the electron beam.

The morphology of hematite grown in the presence of cationic species may be influenced not only by adsorption effects, but also by any structural modifications induced by incorporation of the substituents. In the presence of Cu, rhombohedral crystals of hematite bounded by (10.2) faces were produced [79]. These were found to be well-developed in all three crystallographic directions relative to comparable control samples, and showed a narrow size distribution. The shape of the crystals could be caused by preferential adsorption of Cu on the (10.2) planes during growth, but it is equally likely that the modification arises due to the incorporation of Cu in the crystal structure. In octahedral lattice sites, the Cu^{2+} ions (being a d^9 species) induce a Jahn-Teller distortion which results in the elongation of the octahedra along a trigonal axis. Such a distortion could then account for the adoption of a rhombohedral habit by the oxide crystals.

CHAPTER 2: EXPERIMENTAL.

The present study is concerned with changes in the nature and morphology of crystalline ferric oxide and oxyhydroxide phases formed on ageing ferrihydrite or partially-hydrolysed ferric salt solutions in the presence of cationic impurities.

During the course of the work, products were routinely characterised using a combination of X-ray powder diffraction and TEM analyses. The degree of additive incorporation in each of the crystalline phases formed was determined quantitatively *in situ* in the TEM using an electron probe microanalysis (EPMA or EDX) facility. The effect of impurities on the local crystal structures was examined by imaging particles at high-resolution, using JEOL 1200 and Akashi 002B transmission electron microscopes operating at, respectively, 120 and 200kV.

In the following chapter, the general physical theories behind the analytical techniques described above will be set out, and the limitations of each method discussed. Factors which will be considered include; parameters affecting resolution in the TEM; the limitations in interpreting powder diffraction data; the influence of physical and geometrical effects on the interpretation of electron diffraction patterns, and the variety of errors which may arise in microanalysis (eg due to detector inefficiency, the nature of the elements present, inaccuracy in integral measurement, etc).

2.1. THE TRANSMISSION ELECTRON MICROSCOPE.

In 1926, the German physicist Hans Buch demonstrated the ability of axially symmetric electrostatic or magnetic fields to focus electron beams. Louis de Broglie [84] had already in 1924 put forward the hypothesis that matter, as well as light, might show both wave and particle aspects. He suggested that any particle travelling with a momentum p should have an associated wavelength given by

$$\lambda = h/p \quad (2.01)$$

where h is Planck's constant. The above relationship was confirmed by electron diffraction experiments by Davisson and Germer in 1927 [85], and by G.P. Thomson, son of J.J. Thomson (who had discovered the electron in 1897), in 1928. By the early 1930's, construction of the first electron microscope by Ruska and Knoll was under way. This instrument was capable of magnification $\times 12,000$ using two magnetic lenses. The resolution attained was far higher than was possible using a light microscope, by virtue of the very short wavelength of an electron beam. An approximation, accurate to a few percent, can be developed for the wavelength as a function of the microscope accelerating voltage, using the De Broglie relationship between the electron wavelength and momentum. This is expressed as

$$\lambda = 1.2V^{-1/2} \quad (2.02)$$

where V is the accelerating voltage in kV. For an instrument operating at 100kV, the calculated wavelength is 0.37nm (and 0.18nm at 400kV). These wavelengths are five orders of magnitude smaller than that of visible light.

The basic design of a transmission microscope is shown in Fig.2.1. A cathode emitter, typically a heated tungsten hairpin filament, produces a fine beam of electrons which is then accelerated across a potential of up to several hundred kV, and collimated by the Wehnelt cylinder at the anode. Increased brightness and coherency can be attained with the use of single-crystal filaments, such as lanthanum hexaboride (LaB_6) [86]. The divergent beam is then focused to a spot of diameter 2-3 μm on the specimen stage by a series of condenser lenses. An aperture situated below the condenser lens can be inserted into the beam path. By reducing the diameter of this condenser aperture the coherency can be increased (although a subsequent reduction in image brightness is also observed).

On passing through the specimen, the incident beam is altered in such a way that the exit wave carries structural information. The image formed by the objective lens is then enlarged by further intermediate and projector lenses, and can subsequently be viewed at the base of the column on a fluorescent screen or recorded on a photographic plate. The observed image contrast can be varied by insertion of an objective aperture (Section 2.1.2).

Since the modified beam leaving the specimen is transmitted by the objective lens, its performance is critical and largely determines the resolution limits of the instrument. Inaccuracies in the manufacture of the iron pole-pieces and inhomogeneities in composition will limit this. For high resolution imaging, a good quality objective lens is therefore essential. Since the other lenses in the magnification system,

Key to Fig.2.1 (over):-

A:- Schematic outline of a typical Transmission Electron Microscope (TEM).

B:- Ray diagram showing image formation.

F:- electron-emitting filament

WC:- Wehnelt cylinder

A:- anode

C1:- first condenser lens

CA1:- first condenser aperture (fixed)

C2:- second condenser lens

CA2:- second condenser aperture (variable)

S:- specimen stage

O:- objective lens

OA:- objective aperture (variable)

SA:- area selection aperture

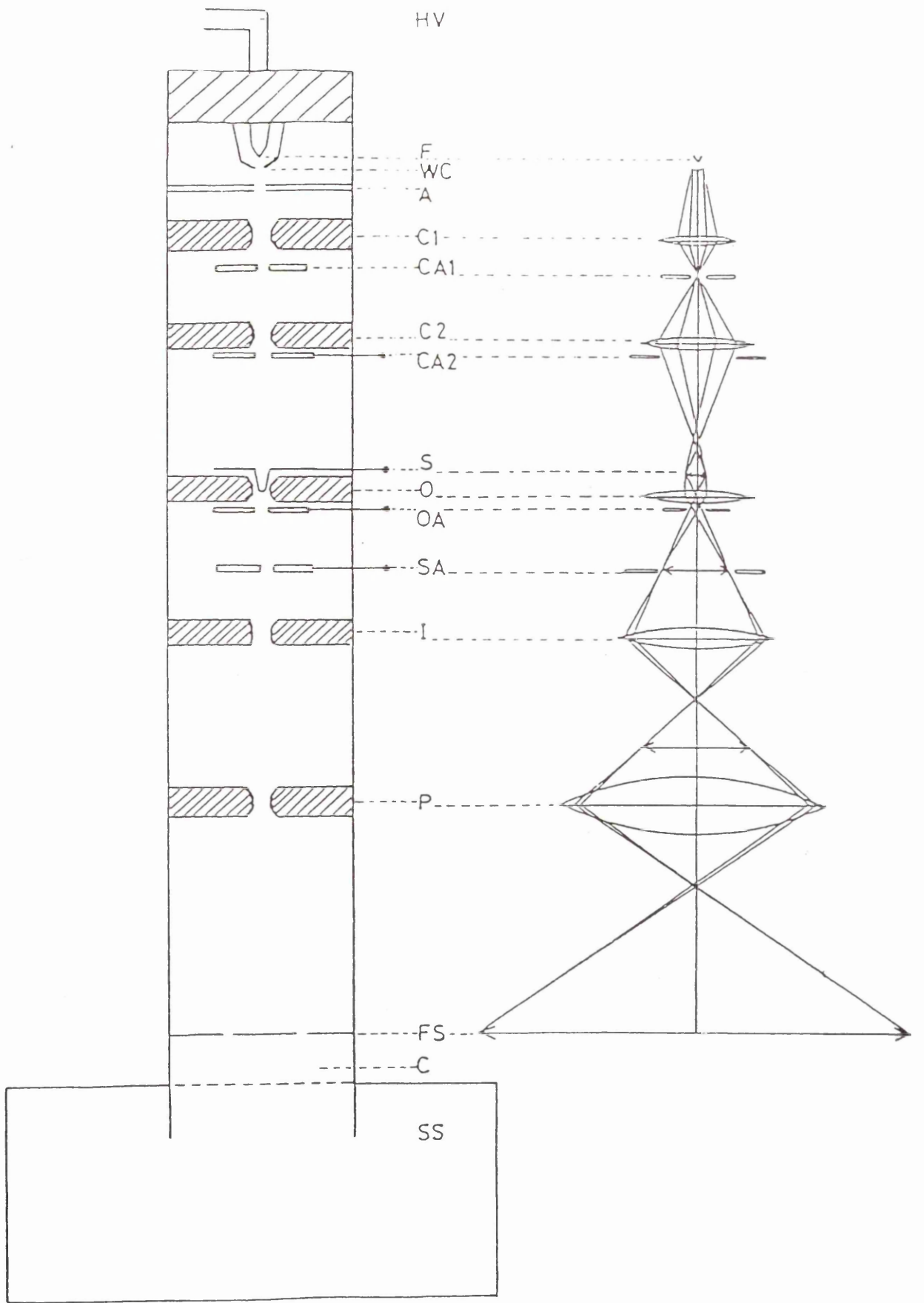
I:- intermediate lens

P:- projector lens

FS:- fluorescent viewing screen

C:- camera

SS:- electronics and high vacuum systems



A

B

the intermediate and projector lenses, simply magnify the image and thus the aberrations caused by the objective lens, they are of less importance.

2.1.1. IMAGE FORMATION IN THE TEM

An image recorded in the TEM (whether on photographic film or TV camera/computer) is essentially brought about by a complicated interference pattern, the nature of which is dependent on the potential distribution (i.e. atomic positions) in the specimen, and the effect of the lens system on the transmitted signal. Lenz [87] showed that, under certain conditions, the TEM imaging system can be described by linear transfer theory. If we know the manner in which the specimen interacts with the incident beam, a correspondence can be drawn between the signal exiting the specimen and the final output signal observed. Under ideal conditions, the image in the viewing plane of the TEM would constitute a direct mapping of the projected specimen structure, with columns of atoms viewed as low intensity dark spots. A direct linear relationship between spot intensity and the amount of scattering material present would then be obtained.

2.1.2. BEAM INTERACTION WITH THE SPECIMEN:- THE WEAK PHASE APPROXIMATION

The processes by which electron waves interact with a specimen in the microscope column can be described in terms of either elastic or inelastic scattering events. The first case to consider is that of a thin specimen, where single-

scattering conditions can be applied. In such a specimen little or no absorption will occur, and the majority of the incident electrons are transmitted. The remaining scattered waves, the proportion of which is dependent on the thickness and appropriate cross-sections of the specimen, can either be recombined with the undeviated waves or physically excluded by the insertion of apertures into the column, selected in order to vary the contrast in the final image.

Elastic scattering will occur where electrons passing through a specimen encounter, or come very close, to an atomic nucleus, and are deflected from the beam path without loss of energy. Alternatively, the incident electron waves may undergo any one of a number of processes resulting from direct interaction with orbital electrons in the specimen. These are inelastic collisions which lead to deflection with loss of energy, and include the emission of secondary electrons, which is the basis of the analytical techniques Auger and Electron Energy Loss Spectroscopy (EELS).

To determine the effect of interaction with the specimen on the incident beam, it is useful to describe the electron motion in terms of a wave function. Boersch [88] considered that a wave formulation could replace the notion of electrons being scattered by the specimen. The function for an electron having total energy E travelling in three dimensions can be obtained by solving the following form of the Schrodinger equation

$$\nabla^2 \psi^2 + (2m/\hbar^2)[E - V(r)]\psi = 0 \quad (2.03)$$

where ψ is the wave function for an electron having

associated probability distribution $|\psi|^2$, ∇^2 is the second order derivative in three dimensions ("del squared"), E is the single energy of the electrons, m is the mass, h is the modified Planck constant (where $h = \hbar/2\pi$), and $V(r)$ is the potential energy.

From equation (2.03), the refractive index (n) for electrons having energy E much greater than $V(r)$ can be derived as

$$n(r) = 1 - [V(r) / 2E] \quad (2.04)$$

which has a near unitary value for a thin specimen. If we consider two waves at a point r , one of which has passed through a specimen of thickness dz , the other of which has traversed the same distance in a vacuum, then the former will have experienced a phase modulation during its passage. This will result in a phase difference $\Theta(r)$ between the two waves. This can be expressed by

$$\Theta(r) = 2\pi/\lambda [n(r) - 1] dz \quad (2.05)$$

and can be rewritten as

$$\Theta(r) = -\sigma V(r) dz \quad (2.06)$$

where $\sigma = \pi/(\lambda.E)$ is the extent of interaction. Since the scattering value is in the order of 10^6 times larger for electrons than for X-rays, a large phase shift can be induced in waves passing through a specimen comprising even a monolayer of molecules (c.f. a few tens of microns required for the corresponding X-ray situation).

The effect of traversing the specimen then results in a modification in the phase of the incident beam according to the potential distribution encountered. The wavefunction

exiting the specimen can therefore be expressed in terms of the incident wavefunction ψ_0 combined with a transmission function $q(r)$, given by

$$q(r) = \exp\{-i\sigma V(r)\} \quad (2.07)$$

where i is the complex identity ($i^2 = -1$), denoting the phase nature of the object, and $V(r)$ is the potential distribution in the object if projected onto a plane normal to the beam direction. The variable r denotes 3-dimensional co-ordinates. The transmitted function is then

$$\psi_e(r) = \psi_0(r) \cdot q(r) \quad (2.08)$$

The power of the scattering interactions experienced by a wave passing through a specimen is dependent on the atomic number of the nuclei present and the path length travelled in the sample. In some cases, electrons are deflected so far away from the path of the incident beam that they are physically removed, either through interaction with the objective aperture or the microscope column. Alternatively, the degree of spherical aberration experienced may be so large that the electrons do not contribute to the final image. This type of scattering from points in the specimen produces incoherent elastic scattering. In a specimen having a periodic structure the scattering occurs in accord with the Bragg Rule, in which case the beams are scattered coherently. Elastic scattering of both the above types gives rise to "amplitude contrast" in the image, since the final wave amplitude is affected. The extent of this effect is dependent on the size of objective aperture used, since this is largely responsible for removing scattered electrons from the image. In a periodic specimen

this is known as "diffraction contrast". Decreasing the aperture diameter will increase the contrast. Areas from which elastically-scattered electrons have been removed are subsequently imaged as dark regions.

In the case of inelastic scattering effects, the energies (and consequently the wavelengths) of electrons will be altered. Recombination of these waves with transmitted and elastically-scattered electrons will result in either diminished or reinforced image intensity, depending on the relative phases of the interacting waves. This mechanism gives rise to "inelastic phase contrast". Similarly, "elastic phase contrast" can be obtained if the objective aperture size allows transmission of elastically-scattered electrons. If the focus conditions are such that recombination of these waves with the transmitted beam is possible, the end result is again increased or decreased wave amplitude.

The retrieval and interpretation of information obtained by phase contrast is severely affected by lens aberrations, since any small periodicities in the specimen which might lie parallel to the direction of the incident beam will produce a wide elastically-scattered range of electrons. If a large objective aperture is used, these waves will be transmitted, but will be focussed onto the image by off-axis areas of the objective lens.

2.1.3. THE MULTI-SLICE MODEL

The phase contrast effects described in Section 2.1.2. can only be interpreted in simple terms for very thin specimens (less than 10nm) for which only single-scattering events occur and kinematic approximations hold. In most cases, however, electrons which have already been deviated on entering a sample having a periodic structure can subsequently encounter further lattice planes which will further scatter the waves. For this reason, a more rigorous dynamical treatment is necessary in order to account for the final amplitudes and phases.

Cowley and Moodie [89] originally detailed an approach by which propagation of a wave incident on a specimen could be broken down by repeated application, for each of the layers encountered, of the changes caused by interaction with individual atomic planes (Fig. 2.2). A scheme by which the final wavefunction exiting the specimen can be determined is now available. A mathematical treatment of the above model can be illustrated using the integral theorem of Helmholtz and Kirchoff [90], which took boundary conditions equivalent to those applied for propagation of a wave field between two points across an aperture. They obtained a general formula which expressed the amplitude at a point P' in terms of the value at an initial point P .

If the wavelength of the radiation is considerably larger than the object dimensions (i.e. the scattering angles are small) then (knowing that the wave function at a particular plane is $\psi(x,y,z)$) it is possible to determine an

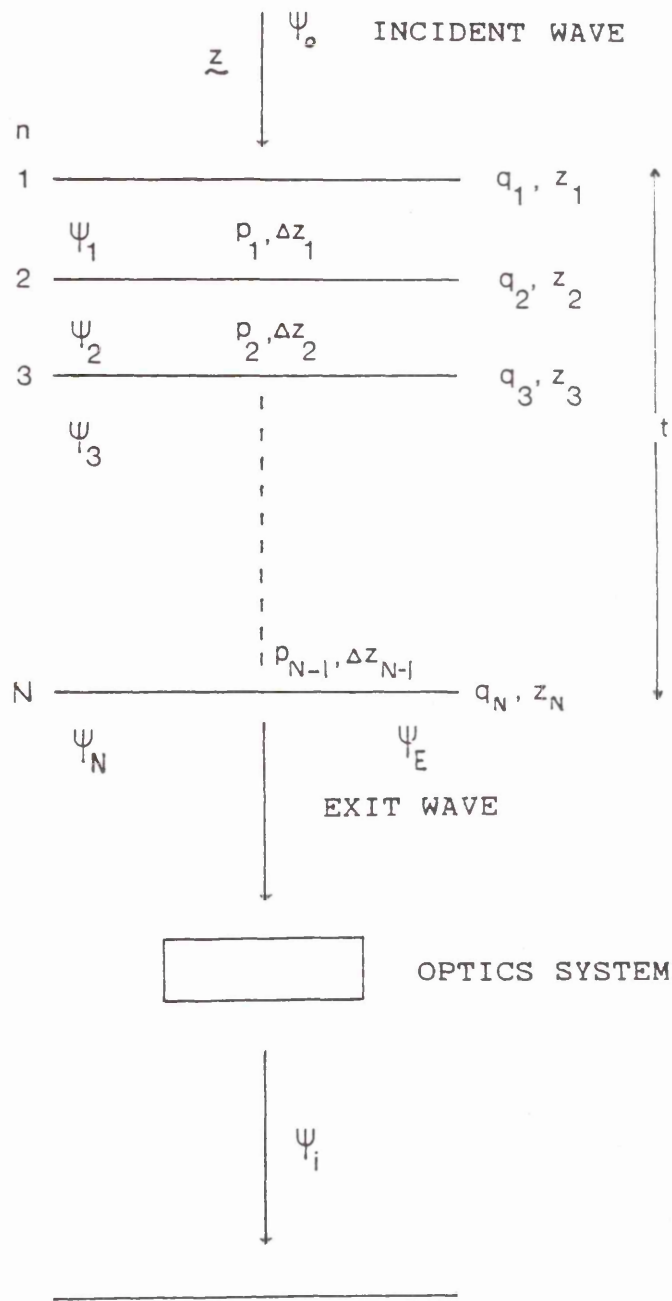


Fig.2.2:- Multi-slice model, showing incident wave propagation through both the specimen and the lens imaging system.

expression for the wave $\psi'(x,y,z)$ on any plane which is separated from the first by a distance Δz . This can be expressed by the equation

$$\psi'(x,y,z) = [i \exp(-2\pi i k \Delta z) / \Delta z \cdot \lambda] \iint \psi(x,y,z) * \exp[-2\pi i k [(x-X)^2 + (y-Y)^2] / 2\Delta z] dx \cdot dy \quad (2.08)$$

where $k = 1/\lambda$ and the double integral is taken over the XY plane with a closing surface at infinity.

In a crystalline specimen, the atoms or molecules are arranged in regular well-defined sequences, stacked in prominent planes which define the periodicity. The passage of the beam through the specimen is calculated by repeated application of the single-slice approximation for each plane of atoms encountered ($z_1 \dots z_n$). Lastly, neighbouring planes are separated by a region of free space, propagation through which must also be taken into account.

For an incident beam ψ_0 , the wave arriving at the second plane z_2 is given by

$$\psi_1(x,y,z_1) = [\psi_0(x,y,z_0) \cdot q_1(x,y,z_1)] * P_1(x,y,\Delta z_1) \quad (2.09)$$

where P_1 is the Fresnel propagator from the first to the second slice, such that

$$P_1 = [i \exp(-2\pi i k \Delta z_1) / \Delta z_1] \exp\{-2\pi i k (x^2 + y^2) / 2\Delta z_1\} \quad (2.10)$$

where Δz_1 is the separation between planes 1 and 2. The wave emerging from the second plane is given by

$$\psi_2(x,y,z_2) = [\psi_0(x,y,z_0) \cdot q_1(x,y,z_1)] * P_1(x,y,\Delta z_1) \cdot q_2(x,y,z_2) \quad (2.11)$$

and the general case can be expressed as

$$\psi_{n+1}(x,y,z_{n+1}) = [\psi_n(x,y,z_n) * P_1(x,y,\Delta z_n)] \cdot q_{n+1}(x,y,z_{n+1}) \quad (2.12)$$

If the summation is made over N , the total number of slices, then

$$\sum_{i=1}^N \Delta z_i = t \quad (2.13)$$

where t is the specimen thickness in the z -direction. The wavefunction exiting the crystal is then $\psi_N(x, y, z_N)$, which can be determined by repeated application of the above process by computer. The image viewed on the image plane of the TEM is then obtained by propagation of ψ_N through the optical system.

If an interpretation of the intensities observed on the image plane in terms of the crystal structure is required, detailed calculations are necessary. However, simplifying approximations are available. As a simple case, the effect of ignoring propagation through the specimen is equivalent to cancelling the wave spread caused by Fresnel diffraction. This estimation involves allowing the phase factor to have value x . The spread then simplifies to a value x , such that

$$x = (t\lambda)^{1/2} \quad (2.14)$$

where t is the specimen thickness.

2.1.4. EFFECT OF THE ELECTRON IMAGING SYSTEM:- FACTORS AFFECTING RETRIEVAL OF INFORMATION.

A wave-mechanical treatment of electron optics shows that the limits of resolution in the TEM are dependent both on the nature of the incident wave interaction with the specimen and the subsequent effects of the electron imaging system in transferring the resultant exit wave to the image plane. This can be explained by application of Transfer Theory.

The weak phase approximation can be used to calculate the final image intensities by considering the effect of the lens system on the specimen exit wave. In the case of a perfect imaging system, the wavefunction on the image plane, $\psi_i(x', y')$, is a scaled version of the wave exiting the specimen, $\psi_e(x, y)$, such that $x'/x = y'/y = M$ (the magnification factor of the system).

However, magnetic lenses are not perfect, and degradation in image quality must be considered. The formation of an image from the wave exiting the specimen can be split into two parts. Firstly, a Fourier transform takes this modified wave to the back focal plane (from which the diffraction pattern is derived). This can be expressed as

$$\psi(u, v) = F[\psi_e(x, y)] \quad (2.15)$$

where u and v are reciprocal-space co-ordinates, and F denotes a Fourier operation. A second, inverse, transform onto the image plane is then given by

$$\psi_i(x, y) = F^{-1}[\psi(u, v)] \quad (2.16)$$

The limitations of the lens system must also be incorporated. The effects of spherical aberration (expressed as a constant, C_s), and the lens aberration defect (Δf) are accounted for with the inclusion of a phase modulator, $X(u, v)$.

Spherical aberration is defined as the inability of a lens to focus all incident electron waves emanating from a point source to a point focus. Every region of the lens does not have the ability to focus electrons equally. The outer zones have greater strength, and waves interacting with these areas will come to focus before those encountering regions

closer to the axis. The net result is to produce a spreading of the beam, forming a "disc of least confusion" having diameter

$$d_s = 0.5C_s \cdot \alpha^3 \quad (2.17)$$

where α is the semi-angular aperture of the lens. The effect of spherical aberration can be reduced to some extent by insertion of a limiting aperture into the back focal plane of the objective lens. However, image interpretation is then further complicated by the resultant interference or diffraction effects produced. Information will also be lost through exclusion of scattered electrons.

The above deviations are now included through multiplication by a transfer function $T(u,v)$ given by

$$T(u,v) = A(u,v) \exp[iX(u,v)] \quad (2.18)$$

where $A(u,v)$ reflects use of an objective aperture in the back focal plane. The function has value 1 at all points inside the aperture and 0 outside. The phase adjustment factor $X(u,v)$ is defined as

$$X(u,v) = 2\pi/\lambda [1/2 \Delta f \alpha^2(u,v) - 1/4 C_s \alpha^4(u,v)] \quad (2.19)$$

where (u,v) are the co-ordinates in the back focal plane such that $(u^2+v^2)^{1/2} = \alpha/\lambda$ (α is the scattering angle), and Δf is the defocus distance in the object plane. The wave function in the back focal plane can then be written as

$$\psi(u,v) = F[\psi_o(x,y)] \cdot T(u,v) \quad (2.20)$$

If a further approximation is made to the weak phase object model for the specimen applied in Section 2.1.2., so that $\sigma V(r) \ll 1$, the transmission function shown in equation

(2.07) can be expanded using only zero and first order terms for the exponential series. The amplitude distribution in the back focal plane is then given by

$$\begin{aligned}\psi(u,v) &= F[q(x,y)] \\ &= \delta(u,v) - [\sigma V(r)\sin X(u,v) - i\sigma V(r)\cos X(u,v)]\end{aligned}\quad (2.21)$$

in which the two terms correspond to, respectively, a central beam unaffected by the specimen (undeviated wave amplitude) and the distribution arising from elastically scattered electrons.

If the above function is then projected onto the image plane, a further (inverse) transform gives

$$\psi_i(x,y) = 1 - F^{-1}[\sigma V(r)\sin X(u,v) - i\sigma V(r)\cos X(u,v)]\quad (2.22)$$

and intensity, $I(x,y)$, is given by

$$\begin{aligned}I(x,y) &= 1 + 2\sigma V(x,y)*F[A(u,v)\sin X(u,v)] \\ &\quad - 2\sigma V(x,y)*F[A(u,v)\cos X(u,v)]\end{aligned}\quad (2.23)$$

where * represents a convoluted integral. The three terms of Equation (2.23) correspond to, respectively, a uniform bright background, the superimposed phase contrast image and, lastly, the absorption contrast contribution.

The observed image contrast can be explained qualitatively by considering diffracted beams in the back focal plane. At low values of spatial resolution, $\sin X \rightarrow 0$ and $\cos X \rightarrow 1$. The image obtained is then dark in regions of higher mass thickness (corresponding to maximum absorption). As resolution increases, $\sin X \rightarrow 1$ and $\cos X \rightarrow 0$, so that absorption contrast plays little part. The image intensity can then be written as

$$I(x,y) = 1 + 2\sigma V(x,y)*F[A(u,v)\sin X(u,v)] \quad (2.24)$$

The wavefunction $\sin X(u,v)$ is called the Phase Contrast Transfer Function (PCTF), the importance of which lies in the influence it exerts over the transfer of information from the object to the image plane. If the PCTF has zero value then the second term in Equation (2.24) disappears, and no contrast is observed in the image. Conversely, object detail is transferred with maximum contrast where the function holds a unitary value. In this case,

$$I(x,y) = 1 - 2\sigma V(x,y) \quad (2.25)$$

which indicates a linear relationship between object and image.

The final contrast is therefore dependent on the oscillating PCTF, which is itself dependent on spatial frequency (and hence the scattering angle for each frequency), the defocus value and the spherical aberration constant, C_s . Fig. 2.3. shows a plot of the PCTF vs $1/d$ (nm^{-1}), the spatial resolution, over a range of defocus values assuming coherent illumination. The resolution is limited by the fall-off in transfer efficiency at high spatial frequencies. Before this limit is reached, the transfer function will generally have gone through several oscillations, so that different spatial frequencies will be imaged in reverse contrast. To overcome the problems in image interpretation caused by this effect, it is necessary to choose an operating region where the transfer function has similar values, and extends over a good range of spatial frequencies prior to reversal. A defocus value can be chosen, where

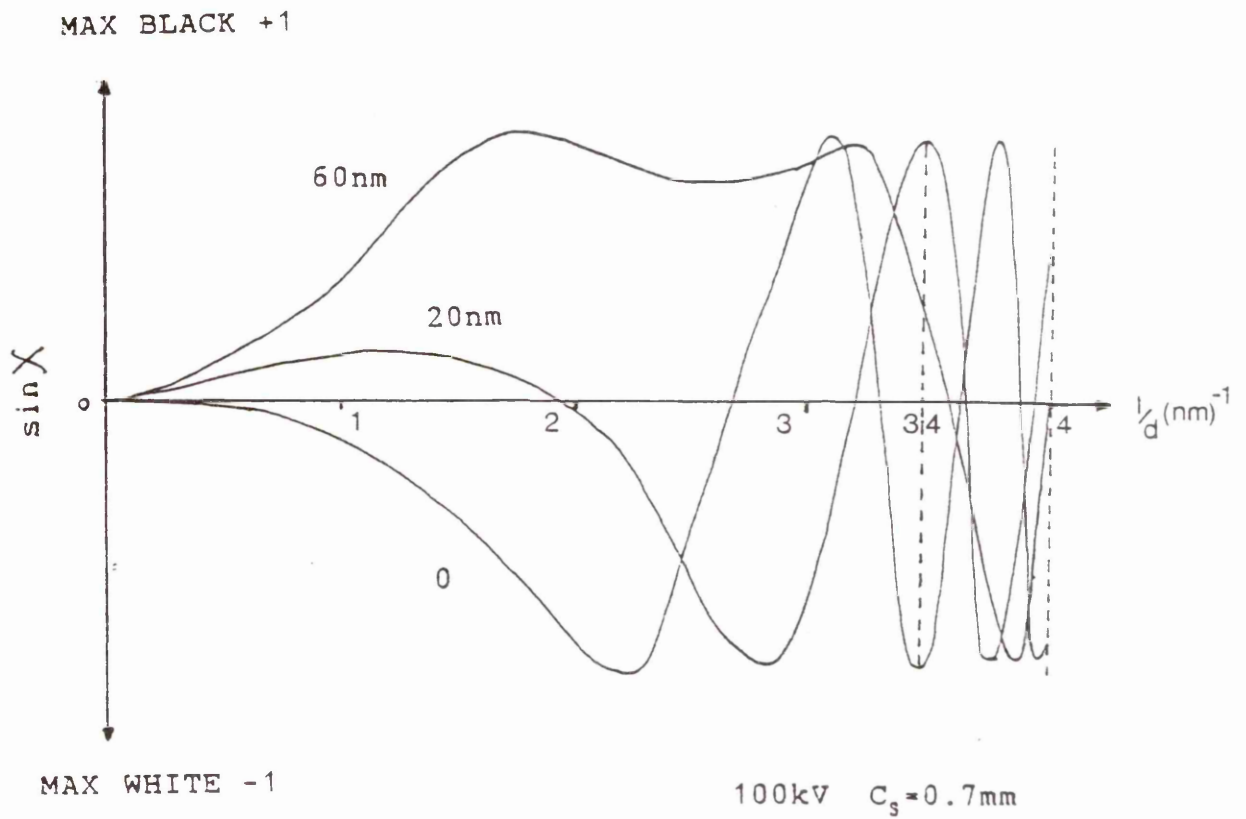


Fig.2.3:- Phase Contrast Transfer Function (PCTF) for a range of defocus values (50 micron aperture cut-off).

$$\Delta f_n = \{C_s \lambda (4n + 1.5)\}^{1/2} \quad (2.26)$$

if n is an integer. In order to maximise the contrast in a high-resolution image, an "optimum defocus" value, Δf_0 , can be chosen such that

$$\Delta f_0 = 1.22(C_s \cdot \lambda)^{1/2} \quad (2.27)$$

However, even with the optimum defocus conditions applied, a loss in resolution will be observed with an increased spherical aberration contribution. If the value of C_s is reduced, the flat region of the PCTF curve at Δf_0 (see Fig. 2.3) is broadened, and the point-to-point resolution limit (d_{\min}) is improved. The limiting value is given by

$$d_{\min} = 0.65 \cdot C_s^{1/4} \cdot \lambda^{3/4} \quad (2.28)$$

Smaller structure can also be resolved in good contrast, if an appropriate defocus value is chosen. In Fig. 2.3, a 0.29 nm spacing ($1/d = 3.4 \text{ nm}^{-1}$) can be imaged at high contrast where $\Delta f = 20 \text{ nm}$, and at high reverse contrast at $\Delta f = 0$.

The treatment of Transfer Theory described so far has assumed a perfectly coherent electron source. However, the source is of finite size (affecting spatial coherence) and is not completely monochromatic (inducing chromatic aberration). The latter effect will result in an energy spread in electrons passing through the objective lens. Lower energy electrons will then be brought to focus first, forming a disc rather than a point on the image. The PCTF can, however, be further modified to account for these contributions.

Lastly, the effects of astigmatism should be considered. Defects in the objective lens magnetic field arising from asymmetry due to manufacture or charge build-up in the column

will induce a directional smearing in the image. Fortunately, the effect can be corrected with the use of compensating lens fields which are easily adjusted while the instrument is in use.

2.2. ELECTRON AND POWDER X-RAY DIFFRACTION TECHNIQUES.

2.2.1. DIFFRACTION THEORY:- THE BRAGG LAW.

Consider a set of crystallographic planes having interplanar spacing d and associated Miller indices (hkl) . A parallel beam of radiation meeting these planes at an incident angle θ will undergo constructive interference under conditions where the difference in path length ($AB+AC$) between rays encountering successive planes is equal to an integral number of wavelengths (Fig.2.4). This requirement can be expressed in terms of the Bragg Law

$$n\lambda = 2d\sin\theta \quad (2.29)$$

This is the relationship on which the following diffraction techniques are based.

2.2.2. POWDER X-RAY DIFFRACTION.

Routine methods for the identification of iron minerals in soils are included in Klug and Alexander [91], Brindley and Brown [92] and Nemezc [93]. The primary technique used for the investigation of these minerals is that of X-ray powder diffractometry, developed by Debye and Scherrer. X-rays are found to exhibit wavelengths similar to the atomic spacing in crystals, and are therefore capable of undergoing diffraction. In the above technique, the sample is prepared as a powder. Since

this will comprise a random arrangement of crystals, it is certain that a proportion will satisfy the Bragg condition, even though monochromatic incident radiation is employed. In the present work, products comprising mixtures of synthetic oxides and oxyhydroxides were initially characterised from powder XRD data in order to gain an idea of the overall composition prior to examination in the TEM.

Samples were sent for analysis to the Geology Department at Glasgow University, where the pressed powder mounts were scanned using CoK_α radiation (wavelength 1.7902Å) at a rate of 2 or 4°/min to resolve the necessary diffraction peaks. However, the uses of this technique were found to be limited, since many of the ferric oxides and oxyhydroxides exhibit a similar range of peaks (eg goethite and hematite), and phases which were present in low proportions could often not be identified without TEM analysis. In addition, many of the particles in these samples were of such a size (down to 10-40nm) that the effects of line broadening made accurate measurement of peak positions impossible.

2.2.3. ELECTRON DIFFRACTION.

Modern electron microscopes enable us to observe the diffraction pattern formed in the back focal plane of the objective lens when a specimen having a periodic structure is imaged. Alteration of the lens currents will focus the pattern down onto the fluorescent viewing screen, where it can be recorded using photographic film. Use of a selected-area aperture, inserted into the first plane of the objective

lens, allows identification of small areas in a sample (limited by the aperture size).

If we consider the Bragg condition where $n = 1$. Equation (2.29) rearranges to

$$1/d = (2/\lambda)\sin\theta \quad (2.30)$$

If Fig.2.4 is now redrawn, with a sphere of radius $1/\lambda$ inserted which intersects the transmitted and diffracted beams at, respectively, O' and P (Fig.2.5a)), then the distance $O'P$ is given as $(2/\lambda)\sin\theta$, i.e. equal to $1/d$ (equation (2.30)). This "sphere of reflection" or "Ewald Sphere" is a common device used in the interpretation of electron diffraction patterns [94-98].

Suppose then that the diffracted ray proceeds along OP , past P' , and makes a spot P'' on the viewing screen (Fig.2.5b). The transmitted beam similarly proceeds along OO' and meets the image plane at the origin O'' . Triangle $OO''P'$ is similar to $OO'P$, so that the transmitted beam following the line OO'' passes through a distance L (the camera length) which is equal to $M.(1/\lambda)$ where M is a magnification factor. $O''P'$ is then equal to $M(1/d) = Md^*$ where d^* is the reciprocal lattice vector. Simple geometry gives the result $\tan 2\theta = D/2L$

Since the wavelength of the radiation is small, the angle θ is also very small (less than 3°), in which case $\tan 2\theta$ is approximately equal to $2\sin\theta$ or simply 2θ . Combining this result with the Bragg equation gives

$$Dd/2 = \lambda L \quad (2.31)$$

where λL is known as the Camera Constant, the value for which is dependent on the operating conditions and the camera

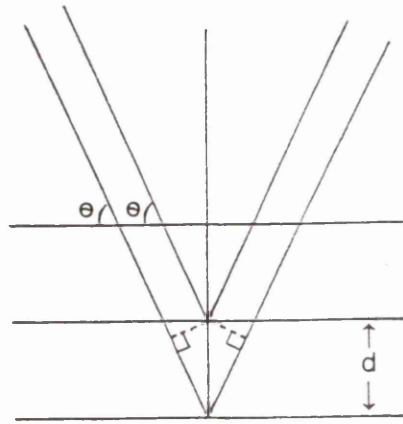


Fig.2.4:- Diffraction of incident radiation by a set of lattice planes having periodicity $d(\text{nm})$.

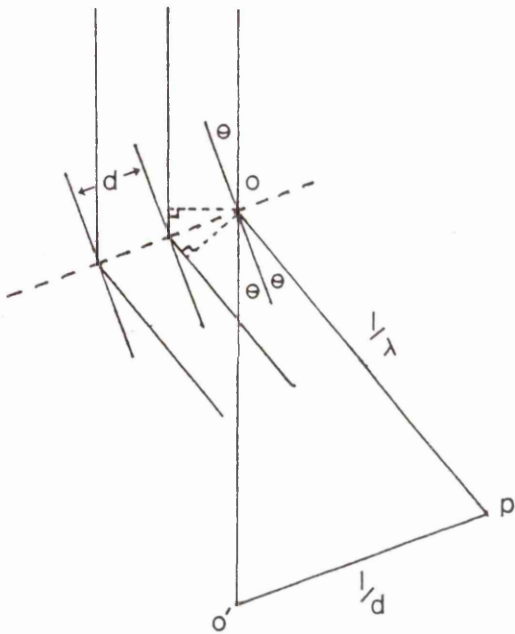


Fig.2.5.a):-The Ewald Sphere.

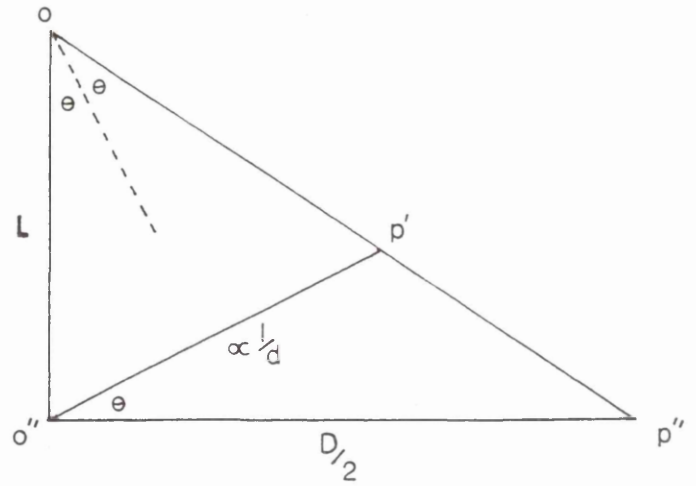


Fig.2.5.b):- Formation of a diffraction spot P'' on the viewing screen.

length L , and can be determined using a diffraction pattern having known spacings.

Variations in instrumental parameters will usually prevent a very accurate determination of results in electron diffraction work. However, if care is taken, spacings measured to within 0.1-0.5% of actual values can be obtained. The proportional error in camera length is given by

$$dL/L = df_0/f_0 + dm/m + dM/M \quad (2.32)$$

where f_0 is the focal length of the objective lens, m is the magnification of the intermediate lens, and M is the magnification factor for the projector lens.

2.2.4. ANALYSIS OF ELECTRON DIFFRACTION PATTERNS.

Although powder diffraction data gave an idea of the bulk composition of samples, it was necessary to examine selected-area diffraction patterns for individual crystals if further information on crystal orientation, local structure, twinning, etc was required. However, in order to avoid inaccuracies in the results, factors affecting the appearance of diffraction patterns should first be considered. In the following sections, the appearance of forbidden reflections, observation of extended ordering/double diffraction, and the effect of slight crystal tilting are all detailed.

2.2.4.a) SYSTEMATIC ABSENCES.

If we consider a unit cell having atoms arranged at points (x, y, z) , then electrons meeting the atomic planes at any one Bragg angle will be scattered such that a phase

difference between waves is created, the magnitude of which is dependent on the set of planes (hkl) which are encountered.

The intensity I of a diffraction spot is dependent on the square of the structure factor F , which is obtained by adding together the amplitudes of the scattered waves:-

$$\begin{aligned} |F|^2 &= [\sum f \cos 2\pi(hx+ky+lz)]^2 + [\sum f \sin 2\pi(hx+ky+lz)]^2 \\ &= (A+iB)(A-iB) \\ &= A^2 + B^2 \quad (2.33) \end{aligned}$$

where

$$F = \sum f \exp 2\pi i(hx+ky+lz) \quad (2.34)$$

then

$$|F|^2 = FF^* = A^2 + B^2 \quad (2.35)$$

where

$$F = (A+iB), F^* = (A-iB) \quad (2.36)$$

In a body-centred lattice, the atomic positions for identical atoms are $(0,0,0)$ and $(1/2,1/2,1/2)$. This gives a structure factor

$$\begin{aligned} F &= f \exp(2\pi i \cdot 0) + f \exp[2\pi i(h/2+k/2+l/2)] \\ &= f(1 + \exp[\pi i(h+k+l)]) \\ &= f[1 + \cos \pi(h+k+l)] \\ &= 2f \cos^2[\pi/2(h+k+l)] \quad (2.37) \end{aligned}$$

F is then zero at $n\pi/2$ when n is odd (ie $(h+k+l)$ is odd), and $2f$ where the sum is even. This is the basis for the extinction of intensity in bcc unit cells. In the case of an ordered material with stoichiometry AB , the mean atomic scattering factor is given by $f = (f_A + f_B)/2$, and

$$F = f_A + f_B \exp \pi i(h+k+l) \quad (2.38)$$

which gives a value of $(f_A + f_B)$ for an even sum and $(f_A - f_B)$ where it is odd.

2.2.4.b) EXTENDED ORDERING.

The occurrence of ordering in a structure may result in the appearance of certain simple geometrical effects in a diffraction pattern. For example, forbidden reflections may be observed faintly in an ordered pattern, diffraction spots may appear at positions corresponding to fractional co-ordinates where ordering involves more than one unit cell, and patterns may exhibit discrete satellite spots around those at integral indice values.

In cases where ordering cannot be developed from one unit cell (for example the stoichiometry A_2B cannot be derived from a single body-centred unit, where there are only two atoms present), larger multiples must be involved. In the above case, a cubic unit cell of double edge gives 8 original cells, equivalent to 16 atoms. Absent diffraction spots can then be observed, with additional spots halfway between. Doubling the unit cell makes these fractional spots integral values. If the origin is set at a B atom, there are then

- a) $4x_B$ at $(0,0,0)$, $(0,1/2,1/2)$, $(1/2,0,1/2)$ and $(1/2,1/2,0)$
- b) $4x_A$ at $(1/2,1/2,1/2)$, $(1/2,0,0)$, $(0,1/2,0)$ and $(0,0,1/2)$
- c) $8x_A$ at $(1/4,1/4,1/4)$, $(1/4,3/4,3/4)$, $(3/4,1/4,3/4)$, $(3/4,3/4,1/4)$, $(3/4,3/4,3/4)$, $(3/4,1/4,1/4)$, $(1/4,3/4,1/4)$ and $(1/4,1/4,3/4)$

The structure factor F can then be calculated by inserting the co-ordinates in equation (2.34). For h, k, l all odd,

this simplifies to

$$F=4(f_B-f_A) \quad (2.39)$$

and for h,k,l all even there are two possible cases,

$$1) F = 4(f_A+f_B) + 8f_A$$

if $h=4h',k=4k',l=4l'$ or if only one is a multiple of 4

$$2) F = 4(f_A+f_B) - 8f_A$$

if $h=2h',k=2k',l=2l'$ with $h'k'l'$ all odd or one odd

2.2.4.c) DOUBLE REFLECTION

The above effects are concerned with the appearance of lattice spots at positions which should have zero intensity or at points between. Double diffraction will also give finite intensity at integral points on single-crystal patterns which would otherwise have zero intensity. This arises where a ray diffracted by one set of planes ($h_1k_1l_1$) with spacing d_1 is further scattered by a second set ($h_2k_2l_2$) (Fig.2.6.a)). As shown in Fig.2.6.b), point P_1 on the diffraction pattern will arise from the singly-scattered ray. P_2 lies at a distance d_2^* from O and is caused by double diffraction. It should be noted that the angles involved are generally in the order of 2° . P_3 , a point having non-zero intensity could then also arise from double diffraction, such that

$$d_3^* = OP_1 + OP_2 \quad \text{and} \quad h_3=h_1+h_2, k_3=k_1+k_2, l_3=l_1+l_2$$

(all + or all -). Finally, P_3 will only be finite if P_2 is finite. If P_2 should be systematically absent, then P_3 will not have finite intensity. In this way, a face or body-centred case will not be affected.

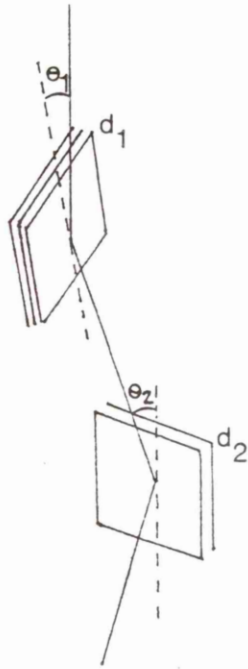


Fig.2.6.a):- Scattering of an incident beam by two different sets of lattice planes, (h_1, k_1, l_1) and (h_2, k_2, l_2) .

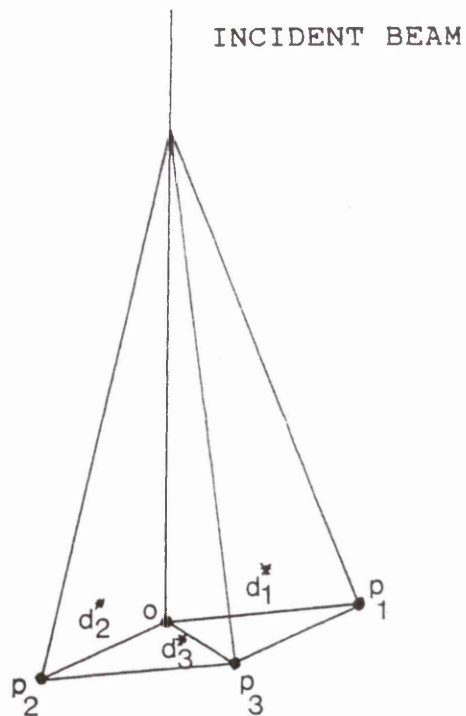


Fig.2.6.b):- Formation of extra spots on a diffraction pattern due to double reflection.

2.2.4.d) POSSIBLE ERRORS IN MEASUREMENT DUE TO GEOMETRICAL EFFECTS

Ambiguous results are often obtained where specimens contain stacking faults or have very small dimensions in one direction (e.g. platelets). Here, elongation of the observed spots occurs in a direction perpendicular to the fault or plate. Since each point on the reciprocal lattice can be regarded as a sphere having a fixed diameter, the spots recorded in a diffraction pattern are dependent on the way in which the sphere of reflection cuts these small spheres.

Fig. 2.7 shows a specimen plane tilted so that the apparent spot radius r_1' for spot P_1 is smaller than the actual radius r_1 . For rotation through an angle ρ about OX,

$$\cos \rho = S_1 Q_1 / S_1 P_1 = OS_1 \tan \phi_1' / OS_1 \tan \phi_1 = \tan \phi_1' / \tan \phi_1 \quad (2.40)$$

then $\tan \phi' = \tan \phi \cdot \cos \rho < \tan \phi$ and $\phi' < \phi$, in which case the point moves towards the axis of rotation. If $\phi = 0$ then the axis of rotation coincides with OP. Similarly, at $\phi = 90^\circ$ the displacement is also zero.

We now want to know how the angle between OP_1 and OP_2 is affected by a small rotation, ie the change $(\phi_2 - \phi_1)$

$$\begin{aligned} \tan(\phi' - \phi) &= (\tan \phi - \tan \phi') / (1 + \tan \phi \cdot \tan \phi') \\ &= \tan \phi (1 - \cos \rho) / (1 + \tan^2 \phi \cdot \cos \rho) \end{aligned} \quad (2.41)$$

this is at a maximum value where

$$\tan(\phi - \phi') \rightarrow \infty \text{ ie } 1 + \tan^2 \phi \cos \rho \rightarrow 0 \text{ where } \tan^2 \phi = 1 / \cos \rho$$

The value for $\tan(\phi - \phi')$ is then

$$\tan(\phi - \phi') = 1/2 \tan \phi (1 - \cos \rho) \quad (2.42)$$

the magnitude of which is relatively unimportant.

It is also possible to determine the apparent change in the interplanar d-spacing in a similar manner.

2.3. X-RAY MICROANALYSIS IN THE TEM.

2.3.1. THEORETICAL CONSIDERATIONS FOR QUANTITATIVE EDX ANALYSIS.

Some TEM instruments have the valuable additional feature of providing a facility for elemental analysis of sample composition. Various names can be used to describe the technique, including Electron-Probe Microanalysis (EPMA), Energy-Dispersive X-Ray Microanalysis (EDX) or Analytical Electron Microscopy (AEM). The basic mode of operation makes use of the fact that bombarding a specimen in the TEM with high-energy electrons results in the generation of certain X-rays which are characteristic of each element present in the sample [99,100]. Inner shell electrons may be ejected from atoms through interaction with the electron beam, and outer shell electrons subsequently drop into the resulting vacancies. The excess energy is then released as electro-magnetic radiation, often in the form of X-rays which can then be picked up by a detector inserted into the microscope column above the specimen stage. The facility for microanalysis installed on the Akashi 002B (Link Analytical QX2000) is illustrated in Fig. 2.8. This system employed a windowless detector consisting of a Si(Li) crystal surrounded by a gold electrical contact layer (about 150 \AA^0) and a thin dead layer of Si.

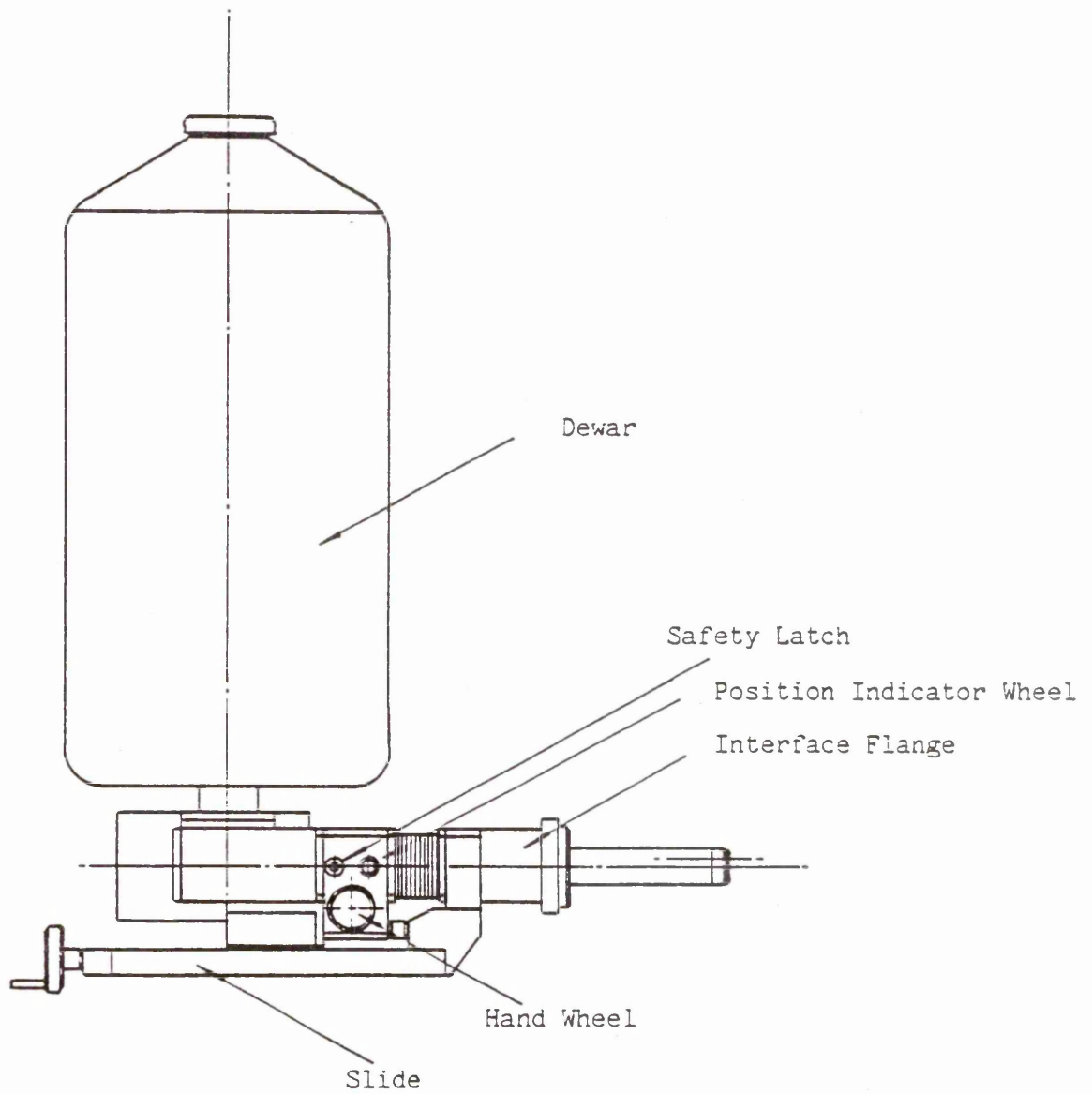


Fig.2.8:- Schematic diagram of the detector used in the present work.

In order to record an EDX profile, the electron beam is first focussed onto the desired area of the specimen, using a probe diameter between 5.6 and 56nm in the present work. The detector is then inserted into the column and, once a sufficient number of counts have been obtained, the energies of the X-rays in the resulting spectrum are measured in order to characterise the atoms present. The relative amounts of each element in the specimen can be calculated quantitatively by comparing the relative integral areas of comparable peaks. In the present project, it was then possible to determine the extent of additive incorporation in particular ferric oxides/oxyhydroxides in products which comprised several phases. In previous studies, bulk atomic adsorption spectroscopy could only be applied to samples in which one phase was present.

The number of ionisations per primary beam electron with energy E_0 on a sample containing element A is given by

$$n = (N_A \cdot c_A \cdot \rho / A_A) \int_{E_0}^{E_c} Q_A / (dE/dx) \quad (2.43)$$

where N_A is Avagadro's number, A_A is the atomic weight of element A, ρ is the sample density, c_A is the concentration of A, E_c is the critical energy for excitation of K, L or M characteristic X-rays, Q_A is the ionisation cross-section (the probability per unit path length of an electron of given energy causing ionisation in a particular shell of an atom A in the specimen), and dE/dx is the mean change in energy of an electron travelling a distance x through the sample.

There are several problems associated with analytical microanalysis, one of which is generation of spurious X-

rays. The characteristic X-ray intensity in photons per incident electron generated in a sample is given by

$$I_A = (\text{const.} \cdot c_A \cdot w_A \cdot a_A \cdot R) / A_A \int_{E_0}^{E_c} [Q_A / (dE/dx)] \cdot dE \quad (2.44)$$

where w_A is the fluorescence yield corresponding to electrons which are backscattered and do not generate ionisation, a_A is the fraction of total K or L intensity which is measured as K_α or L_α radiation, and R is the backscatter factor.

If the specimen is assumed to be infinitely thin (the Thin Film Criterion), then the effects of fluorescence and absorption of electrons by the sample can be ignored. Few electrons are backscattered, and thus only a fraction of the total energy is lost. The trajectory of an electron can be assumed to be the same as the film thickness, t . Generated X-ray intensity is then equal to the intensity leaving the sample, giving

$$I_A = \text{constant} \cdot c_A \cdot w_A \cdot a_A \cdot Q_A \cdot (t/A_A) \quad (2.45)$$

However, calculating the value of the constant and other terms is difficult since many of the geometric factors and other constants cannot be evaluated exactly. The value for t also varies from one point in the specimen to another.

Consider a sample comprising two elements, A and B. It is possible to express relative intensity values for the elements present in the form of the mass concentration ratio c_A/c_B , where

$$c_A = A_A \cdot I_A / \text{const.} \cdot w_A \cdot Q_A \cdot a_A \cdot t \quad (2.46)$$

and

$$c_B = A_B \cdot I_B / \text{const.} \cdot w_B \cdot Q_B \cdot a_B \cdot t \quad (2.47)$$

then

$$c_A/c_B = K_{AB} \cdot I_A/I_B \quad (2.48)$$

where

$$K_{AB} = A_A(Q.w.a)_B/A_B(Q.w.a)_A \quad (2.49)$$

The values for K_{AB} vary with operating voltage, but are independent of sample thickness and composition if the two intensities are measured simultaneously and the thin film criteria are satisfied. This is known as the Ratio or Cliff-Lorimer method.

2.3.2. SAMPLE PREPARATION, ANALYSER CALIBRATION AND ACCURACY OF QUANTITATIVE CALCULATIONS

Standard synthetic ferrihydrite samples were made up by fast addition of 1M NaOH to 0.1M ferric nitrate solution. Analar grade chemicals were weighed out on an analytical balance, with the required additive:iron mole fractions calculated as molar percentage additive present = moles additive/(moles additive+moles iron)x100. The final gel pH was measured using a pH meter, and samples were then aged at 70°. The above parameters were chosen to facilitate simple comparison with previous studies. Unless stated otherwise, it should be taken that each of the products described in Chapter 3 were formed under the above conditions.

In order to calibrate the analyser, it was necessary to examine samples which comprised known quantities of zinc and nickel. The system software was first used to calculate a range of additive:iron mass concentration ratios from profiles for individual untransformed zinc and nickel-ferrihydrite precipitates. Comparison of the relative integral

areas for Zn, Ni and Fe K_{α} peaks gave a readout of both gross and, with background noise removed, net integrals. These values were then further compared with integral areas determined manually.

From these ratios, a range of mole percentage zinc to iron ratios could be obtained using equation (2.49), with K_{Zn-Fe} taken as 1.23, and K_{Ni-Fe} as 1.05. A typical calculation is shown below:-

measured integral areas: Zn=1111, mol.wt.=65.38

Fe=3081, mol.wt.=55.84

then

$$C_{Zn}/C_{Fe} = 1.23 \times 1111 / 3081$$

$$= 0.444$$

so that

$$(\% \text{age mass Zn}) / (\% \text{age mass Fe}) = 0.444$$

If the crystal contained 1 mole Fe, then the proportion of Zn can be calculated as

$$\text{moles Zn} = 55.84 \times 0.444 / 65.38$$

$$= 0.379 \text{ moles}$$

and the molar %age additive present is then

$$Zn / (Zn + Fe) = 0.379 / (1.379)$$

$$= 27.5 \text{ mol}\%$$

Samples required for TEM examination were first dispersed in ethanol or water under ultrasonics and dried down onto carbon-coated grids. If the specimens were mounted on copper grids, it was often found that the close proximity of the Zn K_{α} and Cu L_{α} peaks caused some disagreement between net integral measurement by the system software and manual

integral calculations. The latter values were found to be identical to the computer-determined gross integrals. These values were then compared with calculations for specimens dried onto gold grids, where peak interference should not occur. In this case manual gross and net values were found to be equal. Using results from gross and manual integrals, it was therefore unnecessary to use gold grids on a day-to-day basis. Similar interference problems were not encountered with Ni.

Comparison of experimentally-measured concentration ratios with values calculated from the total weights of additive and ferric species present in the standards gave a good level of agreement, but the accuracy of the results are dependent on a variety of factors, including errors in preparation and integral calculations, and detector inefficiency (due to possible errors arising from incomplete charge collection, signal pile-up and generation of spurious x-rays in the microscope column). The widest range of divergent values should be obtained for precipitates in which additive distribution is not even throughout the specimen (an effect which was amplified in precipitates containing low levels of additive). However, mixing equal proportions of each required element (where the most even distribution would be expected) gave results showing good agreement with calculated values.

Although the precision of measurement for any one analysis was quite high (ie readings effectively became constant after a sufficient counting time), the actual accuracy of results could be as low as 15-20%.

CHAPTER 2:- MATERIALS

2.1. INTRODUCTION

2.2. EXPERIMENTAL PROCEDURE

2.3. RESULTS AND DISCUSSION

2.4. CONCLUSION

CHAPTER 3:- RESULTS

3.1. INTRODUCTION

3.2. EXPERIMENTAL PROCEDURE

3.3. RESULTS AND DISCUSSION

3.4. CONCLUSION

3.5. REFERENCES

3.6. APPENDIX

3.7. BIBLIOGRAPHY

3.8. SUMMARY

3.9. ACKNOWLEDGEMENTS

3.10. REFERENCES

3.11. APPENDIX

3.12. BIBLIOGRAPHY

3.13. SUMMARY

3.14. ACKNOWLEDGEMENTS

3.15. REFERENCES

3.16. APPENDIX

3.17. BIBLIOGRAPHY

3.18. SUMMARY

3.19. ACKNOWLEDGEMENTS

3.20. REFERENCES

3.21. APPENDIX

3.22. BIBLIOGRAPHY

3.23. SUMMARY

3.24. ACKNOWLEDGEMENTS

3.1. CHARACTERISATION OF FERRIHYDRITE AND ZINC-FERRIHYDRITE PRECIPITATES.

Addition of base to freshly-prepared ferric nitrate solution led to immediate formation of a red-brown solid. Samples prepared for TEM examination directly after precipitation showed aggregates of material comprising small platelets about 5-10nm in diameter (Plate 1). Selected-area diffraction patterns obtained showed three broad rings, with spacings measured at 0.25nm (strongest intensity), 0.22nm (weak) and 0.15nm (medium) (Plate 2). These values are consistent with, respectively, (110), (112) and (300) reflections for the disordered ferric oxide-hydrate ferrihydrite (Table 1.2). Similar results for base-precipitated ferrihydrite were quoted by Towe and Bradley [44], who observed two broad lines at 0.255nm and 0.147nm which they correlated with hexagonal close-packing of oxygen atoms. However, according to Manceau *et al* [51] the 2-line ferrihydrite may contain both short range ordering and a proportion of cubic close-packed layers. For convenience, the spacings measured for the synthetic precipitates obtained in the present work have been indexed in accord with a hexagonal unit cell having dimensions $a_0=0.508\text{nm}$, $c_0=0.94\text{nm}$ [44].

In previous studies [46,101], the least crystalline ferrihydrites (so-called "two line" samples) have been imaged as almost featureless platelets similar in morphology to the solids observed here. Fitzpatrick [102] showed that more ordered areas gave evidence for spherical structures with more strongly diffracting margins than cores. In the same

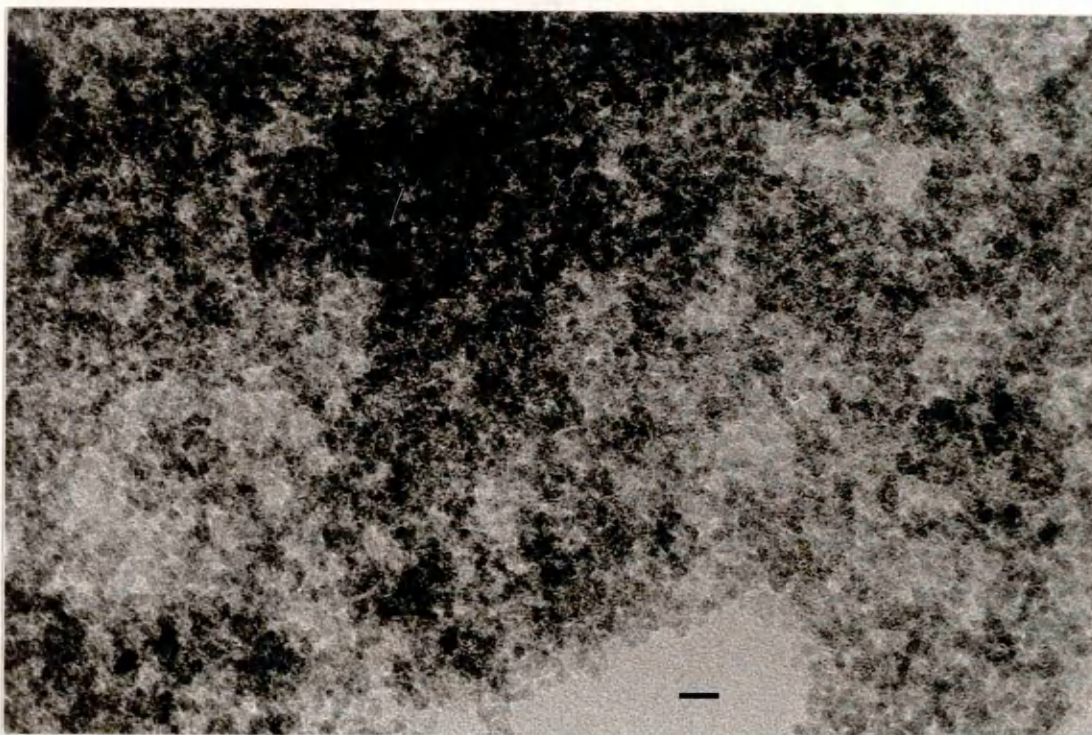


Plate 1:- Ferrihydrite platelets, shown immediately after precipitation from ferric nitrate solution at pH 12. Scale bar represents 10nm.



Plate 2:- Selected-area diffraction pattern obtained for the precipitate shown in Plate 1.

study the most ordered samples, "six line" ferrihydrites, showed a clear domain texture, with some faceted edges at about 120° and short perpendicular lattice fringes (showing multiple defects) measured at 0.26nm and 0.22nm. In the present work, clear resolution of lattice fringes was not observed, either on the fresh precipitates or on ferrihydrite platelets that were aged but did not transform to a recognisably crystalline phase. Imaging at high magnification showed that the particles exhibited a rounded morphology.

Base was next added to ferric salt solutions containing various proportions of zinc nitrate (up to a mole percentage ratio $Zn/(Zn+Fe)$ equal to 80%). The brown-yellow solids thus formed were found to be lighter in colour than precipitates produced in the absence of additive, becoming increasingly pale when precipitation was carried out in the presence of high levels of zinc. This observation suggested that, rather than all the additive species being directly associated with ferrihydrite, some proportion of (white) zinc hydroxide may have been present in many of the gels.

TEM examination of these solids showed masses of small platelets having a morphology similar to that of precipitates produced in the absence of additive. Plates 3 and 4 show, respectively, a selected area and corresponding diffraction pattern from a sample precipitated at pH 12 from a nitrate solution containing 30 mol% zinc. The observed diffraction spacings are again consistent with ferrihydrite. The EDX profile shown (Fig. 3.1) was obtained for a section of the above area using a 44nm probe. Measurement of the relative

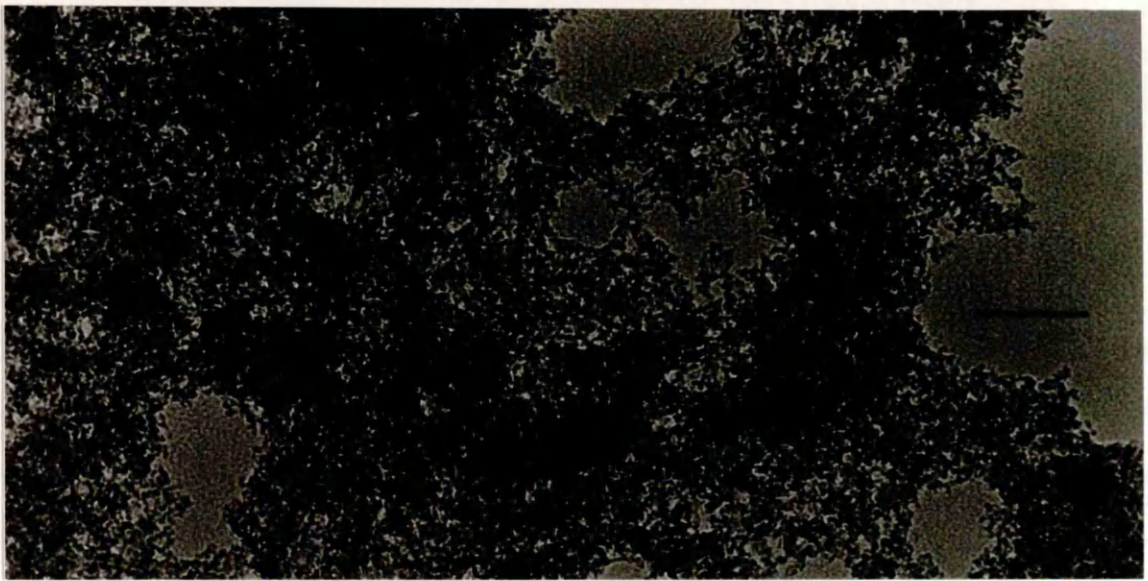


Plate 3:- Precipitate formed at pH 12 on addition of base to ferric salt solution containing 30 mol% zinc. Scale bar represents 100nm.

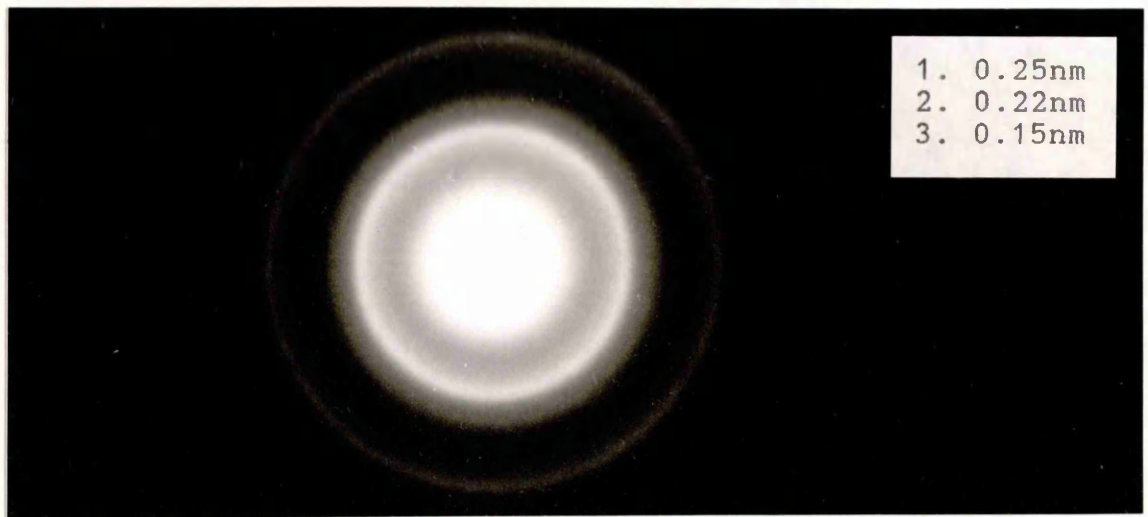


Plate 4:- Selected-area diffraction pattern for Plate 3.

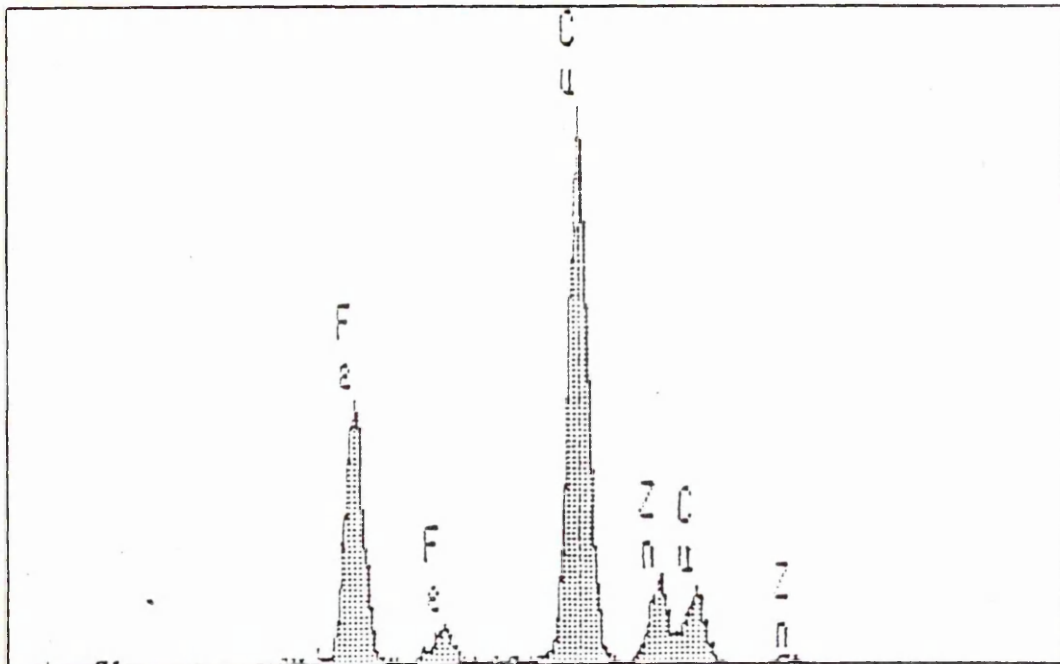


Fig.3.1:- Typical EDX profile for the above precipitate.

integral areas gave a zinc:iron mass concentration ratio $C_{Zn}/C_{Fe} = 0.44$, corresponding to approximately 27 mol% additive associated with the solid.

Plate 5 shows a precipitate obtained on addition of excess base to a nitrate solution containing 80 mol% zinc. In this case, EDX data (Fig.3.2) indicated that the sheet-like material shown comprised a separate additive phase distinct from ferrihydrite. The spacings measured from the corresponding diffraction pattern (inset) were consistent with a zinc hydroxide. After placing the precipitate in an oven at 70°C the amorphous hydroxide quickly transformed, yielding poorly-defined crystals up to about 500nm in length. Plate 6 shows a subsample taken from the same product 30 minutes after precipitation. Spacings measured from the corresponding diffraction pattern (Plate 7) were consistent with zinc oxide (ZnO). A similar product was obtained on heating zinc nitrate solutions precipitated at pH 7, and 12 in the absence of ferric species.

The methods used to characterise the precipitates are somewhat artificial, in that the results (e.g. extent of additive association with ferrihydrite) may be affected by the method of specimen preparation, which involved removal, dispersion and drying down of subsamples from each gel onto carbon-coated grids prior to TEM/EDX analyses. However, even if the above factors are taken into account, the presence of appreciable levels of a totally separate zinc hydroxide phase in any of the samples should have been reflected in the rapid development of ZnO on heating the gels. The actual results

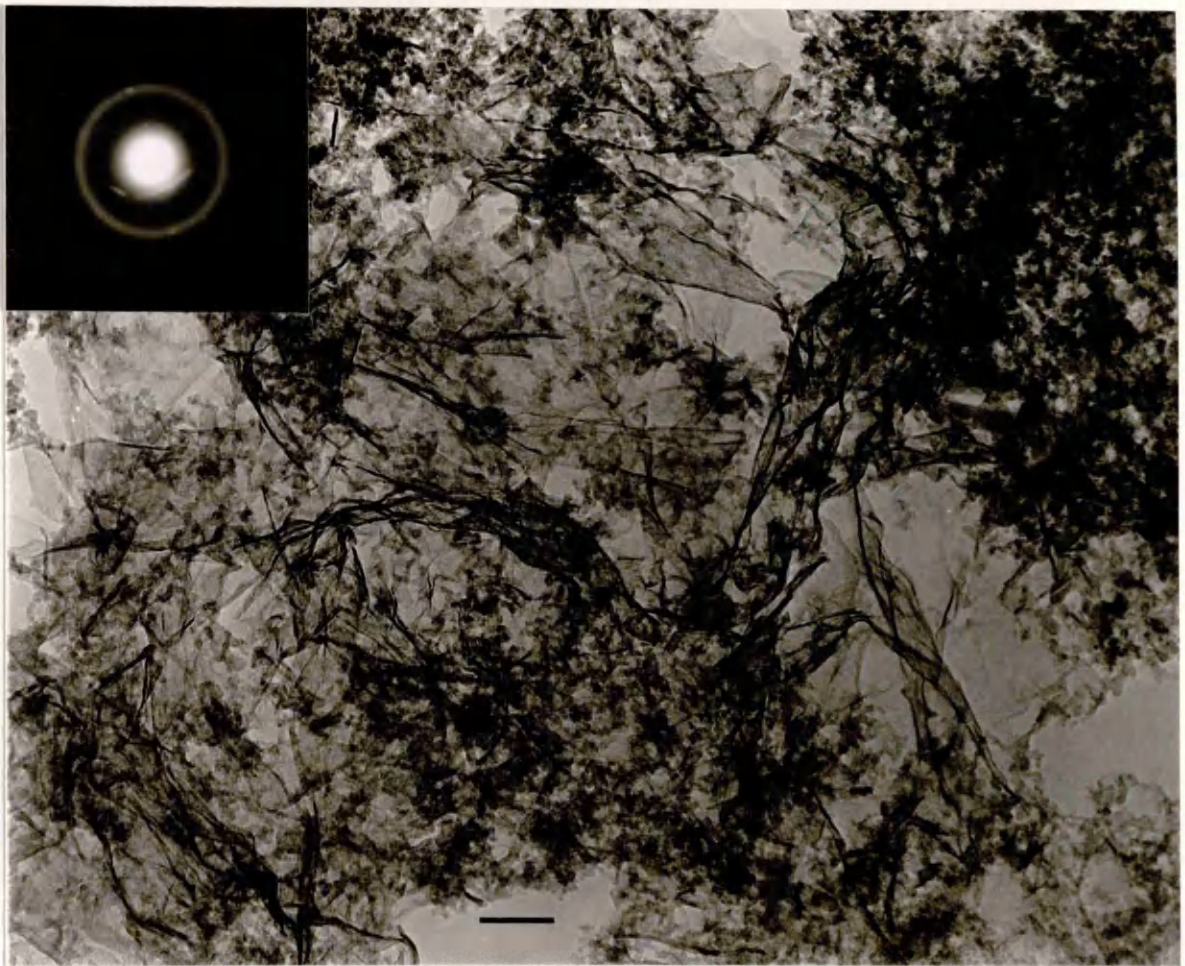


Plate 5:- Precipitate comprising ferrihydrite and sheet-like zinc hydroxide, formed at pH 12 on addition of base to 80 mol% zinc/20 mol% ferric nitrate solution. Scale bar represents 50nm.

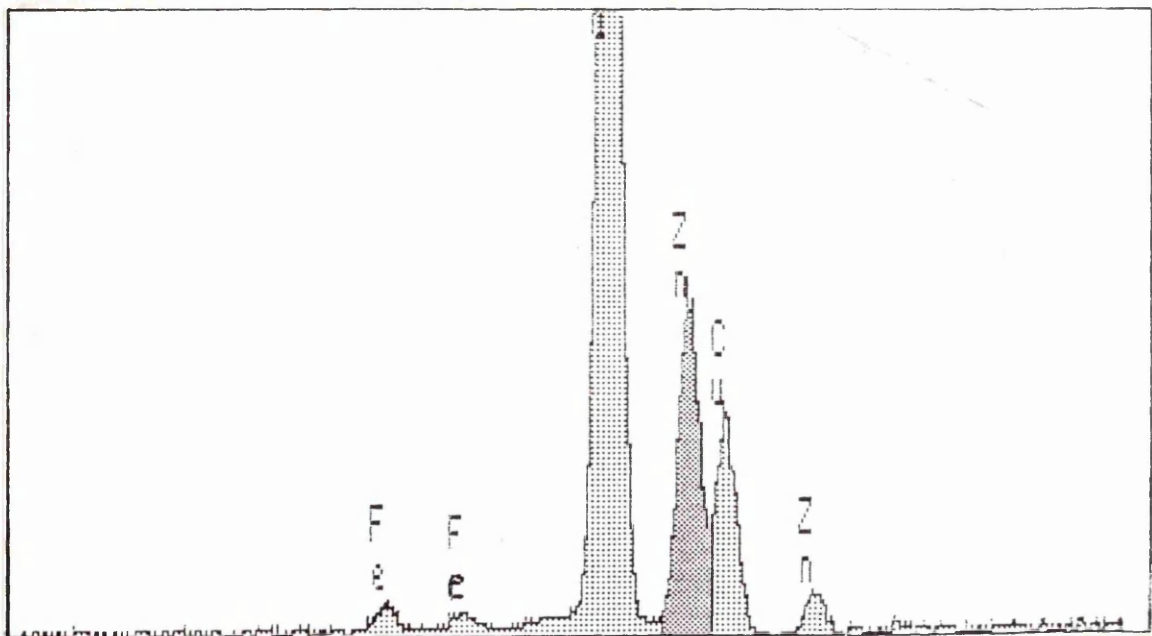


Fig.3.2:- Typical EDX profile obtained for the above precipitate, showing the predominance of zinc in the gel.

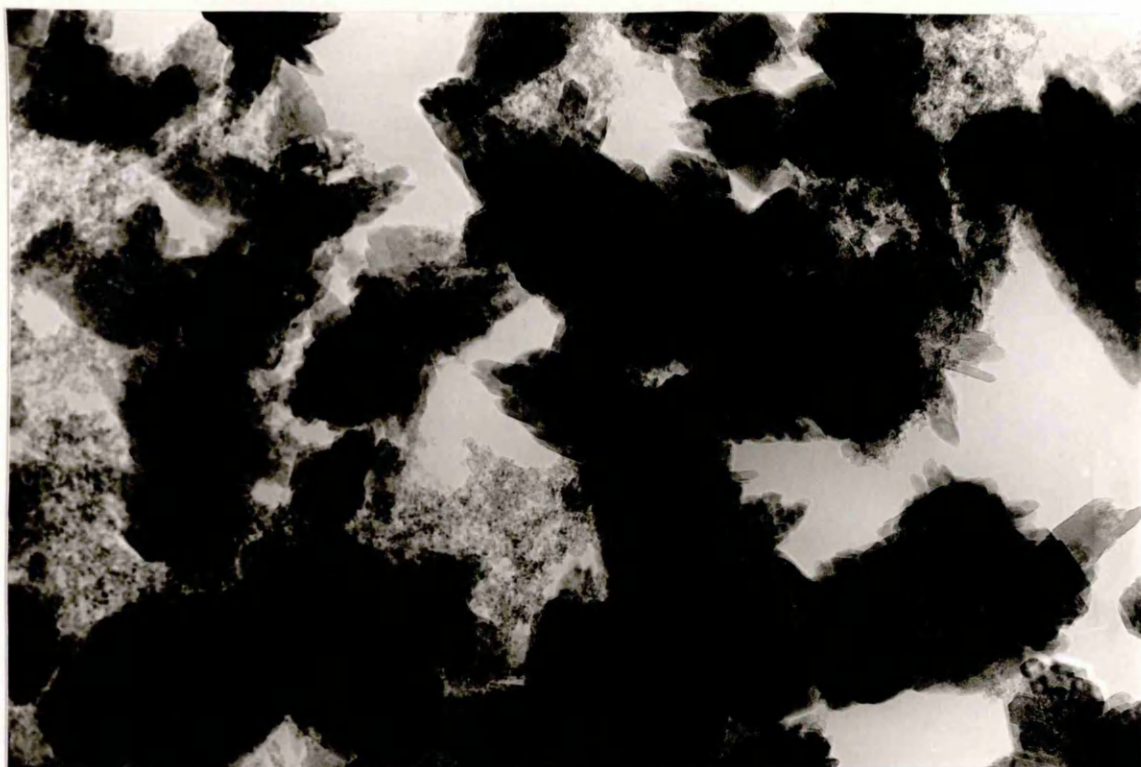


Plate 6:- 80 mol% zinc gel (Plate 5), 30 minutes after precipitation. A separate crystalline zinc phase has already developed. Scale bar represents 100nm.

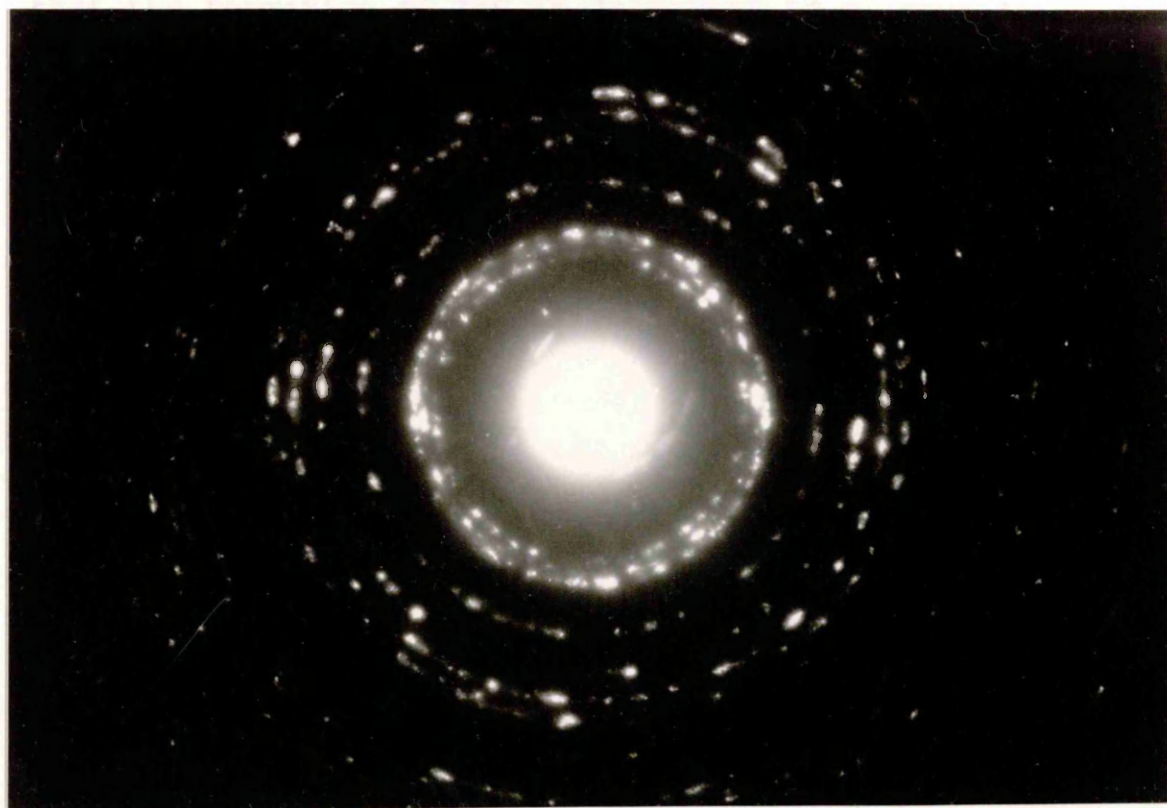


Plate 7:- Diffraction pattern for the crystals shown in Plate 6. The spacings are consistent with ZnO.

obtained from electron diffraction and TEM data indicated that zinc oxide was generally absent from transformation products formed at less than 30 mol% addition, suggesting that any additive hydroxide had dissolved before crystallisation occurred. It is then likely that the substituent was directly associated with ferrihydrite, either adsorbed as distinct species or as a "coating" of hydroxide. In the latter case, $\text{Zn}(\text{OH})_2$ will probably act as a reservoir for the release of soluble zinc.

The range of separate additive oxide/oxyhydroxide phases previously identified in products formed on ageing Mn(II), Mn(III), Co(II) and Cu(II)-ferrihydrite precipitates at pH 12 is summarised in Table 3.1. The present work has indicated that the formation of ZnO is dependent to a large extent on the initial presence of zinc hydroxide in the gels. It might be expected that the proportion of an additive hydroxide remaining in the gels would be related to the amphoteric behaviour in alkaline media (Section 1.3).

ADDITIVE	SEPARATE PHASE(S) PRODUCED
Mn(II)	none at up to 50 mol% addition
Mn(III)	$\text{Mn}_2\text{O}_4, 7\text{A}^0$ phyllomanganate at 30 mol% addition
Co(II)	none at up to 50 mol% addition. 100% Co(II) gave Co_3O_4 and CoOOH
Cu(II)	CuO at 33 mol% addition

Table 3.1:- Separate additive oxide/oxyhydroxide phases previously found in transformation products formed at pH 12.

Due to the large surface area and proposed porosity of ferrihydrite, the precipitates are thought to be capable of accommodating quite high levels of adsorbed species. In coprecipitated samples, some proportion of additive species may be present in internal sites [103]. However, electron diffraction data in the present work gave no evidence that the presence of zinc led to an immediate ordering in the structure of individual ferrihydrite platelets (eg inducing spinel formation).

3.2. INITIAL DETERMINATION OF PRODUCT COMPOSITION FROM X-RAY POWDER DIFFRACTION DATA.

In accord with the results of previous studies [48,53,55], ageing of ferrihydrite gels at elevated temperature in the absence of additive led to development of products which, depending on the growth conditions, were found to comprise either goethite, hematite or a mixture of the two phases (Table 3.2). Examination of XRD profiles obtained for products formed on ageing ferrihydrite at pH 12 indicated that the only crystalline phase present was goethite. Lowering the pH at which the gels were held was found to retard the transformation and so promote formation of hematite, until at neutral pH goethite was absent from the product.

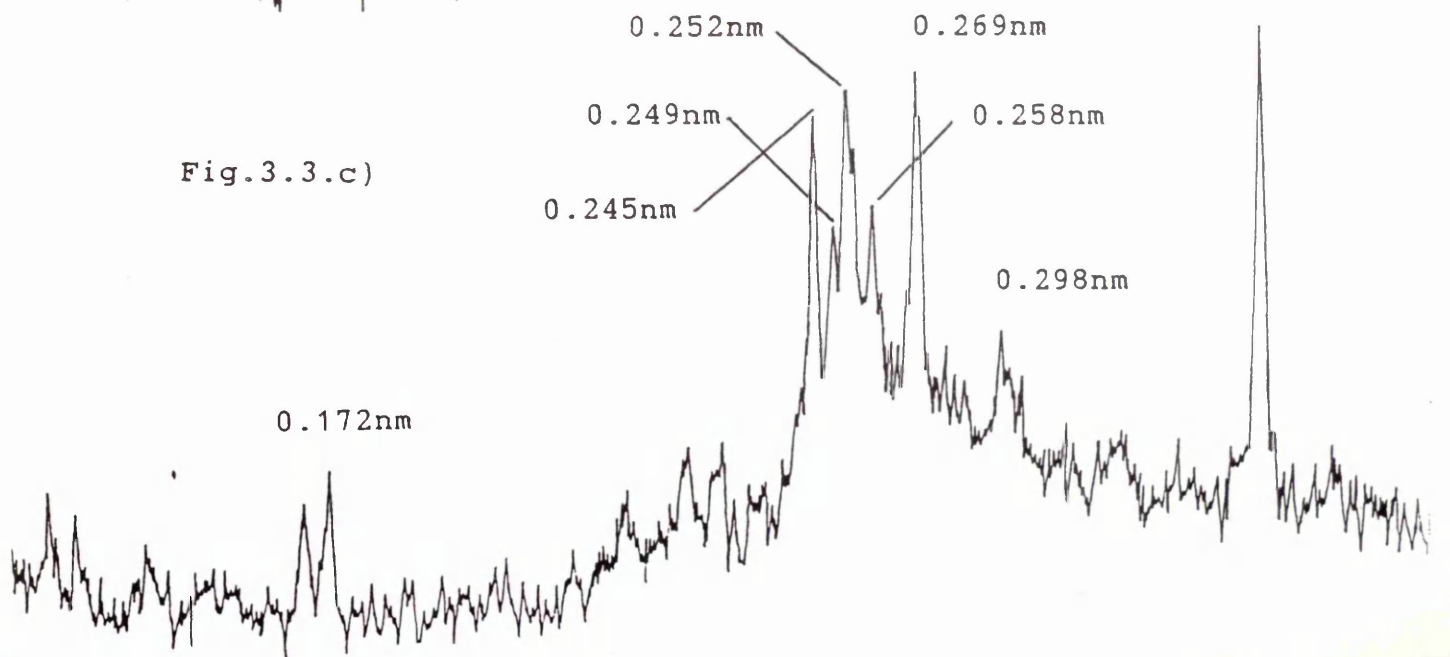
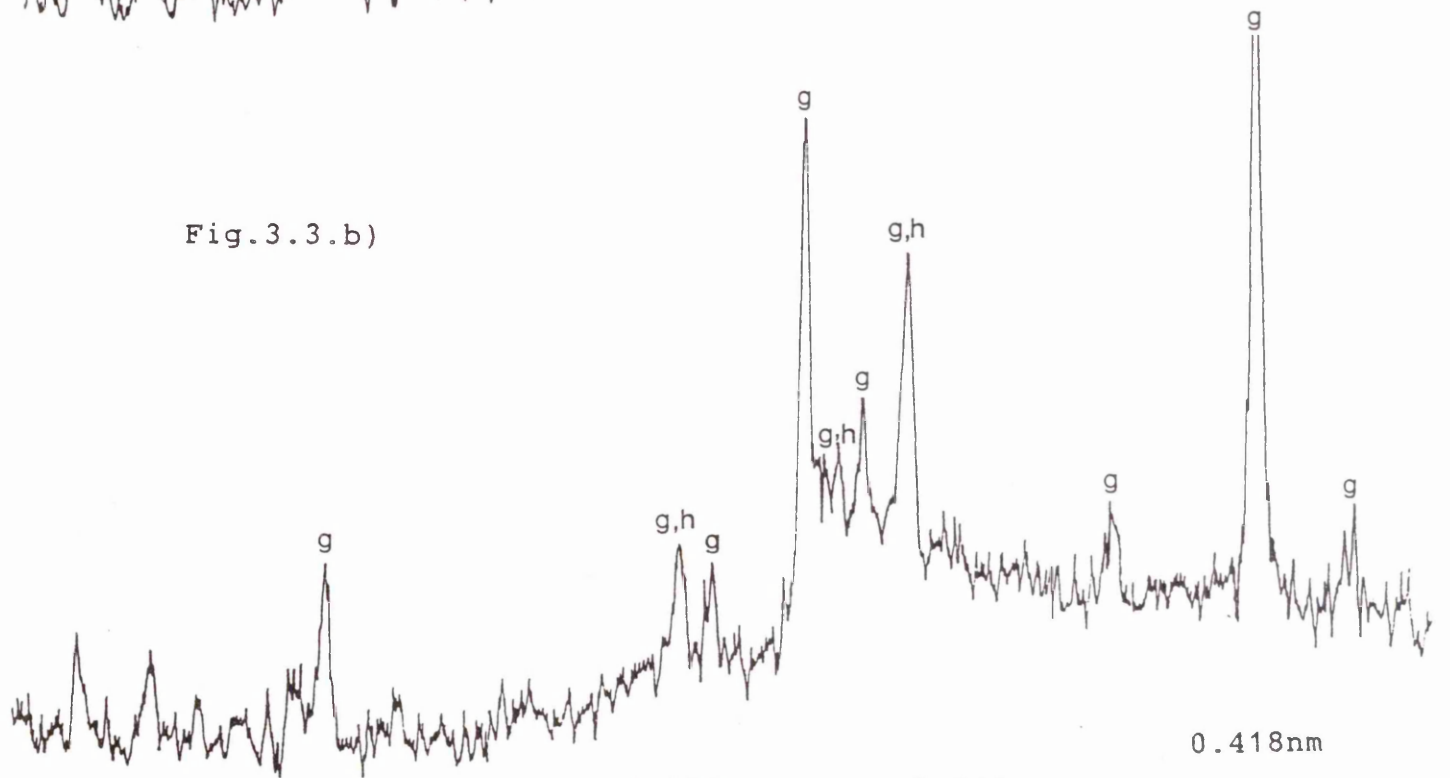
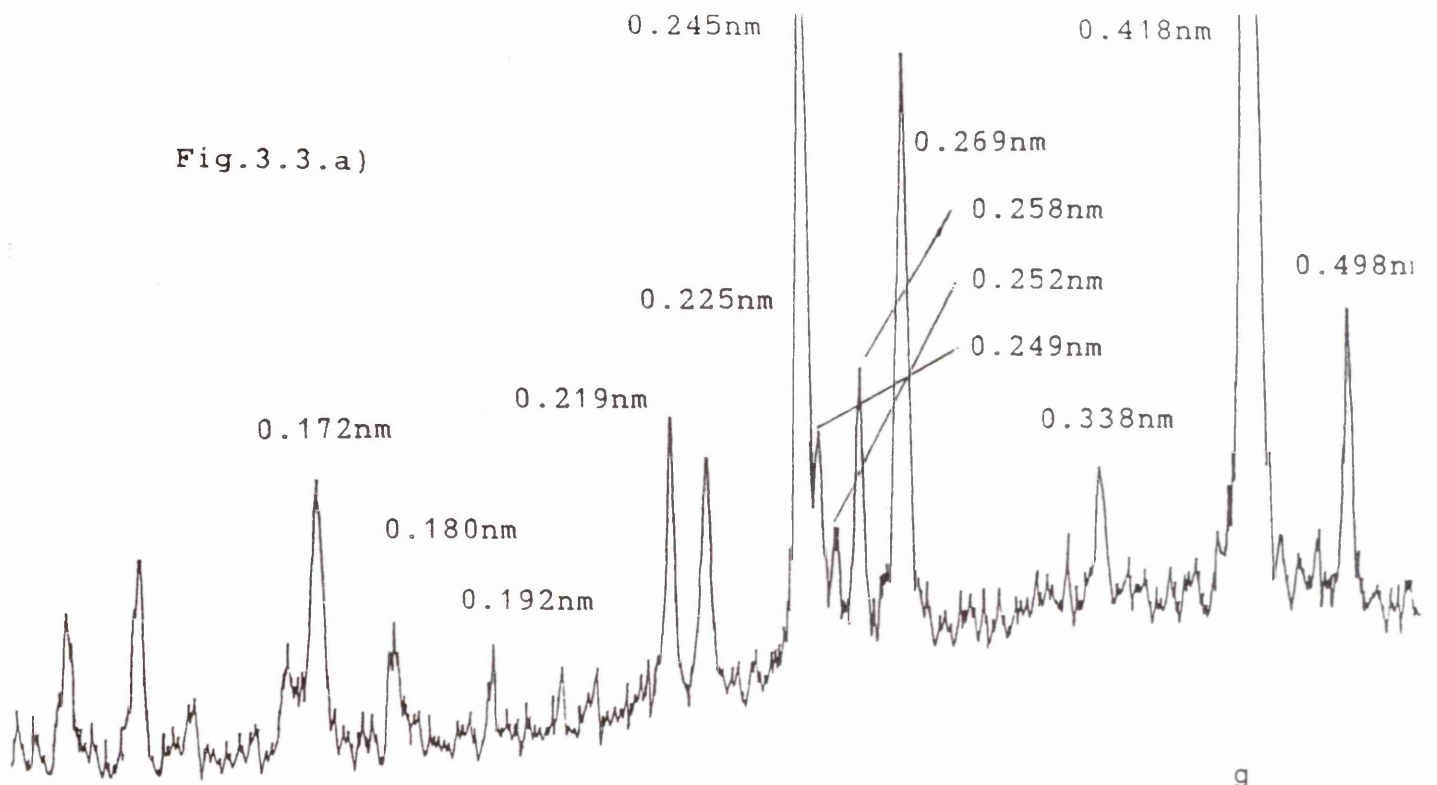
As expected, the relative amounts of goethite and hematite produced in samples which were formed on ageing gels containing a proportion of zinc were found to be dependent on the transformation pH and the level of additive associated with ferrihydrite (Table 3.2).

pH 12			
ADDITIVE LEVEL	<5 mol%	10 mol%	15 mol%
PRODUCTS	G	G,H,S	S
pH 9			
ADDITIVE LEVEL	0	5 mol%	15-20 mol%
PRODUCTS	G,H	H	H,S
pH 7			
ADDITIVE LEVEL	<5 mol%	8-10 mol%	15 mol%
PRODUCTS	H	H,S	S

Table 3.2:- Influence of zinc species on the formation of oxide phases in transformation products. In the presence of high levels of additive, the sole ferric oxide produced was the spinel phase (G=goethite, H=hematite, S=spinel phase).

XRD data quoted previously for samples produced at pH 12 in the presence of 9 to 18 mol% zinc [80] indicated that the formation of hematite had been promoted. However, in the present study the presence of the oxide could not definitely be confirmed from powder diffraction data alone. Figs. 3.3 a)-c) show XRD profiles obtained for products formed at pH 12 in the presence of, respectively, 0, 5 and 10 mol% additive. Signals corresponding only to hematite were absent from the control sample, and the only spacing observed in the other profiles which was not consistent with goethite was a peak at 0.30nm (Fig. 3.3.c) which corresponded to the (220) reflection for the spinel phase. However, comparison of the relative heights of the peaks at 0.418nm (goethite d_{110} , 100% intensity) and 0.269nm (hematite d_{104} , 100% intensity) did suggest that formation of the oxide phase was promoted as the level of additive increased. The range of measured spacings,

Fig 3.3 a)-c) (over):- XRD profiles obtained for transformation products formed at pH 12 in the presence of, respectively, 0, 5 and 10 mol% zinc (g=goethite, h=hematite).



together with values expected for goethite and hematite are summarised in Table 3.3.

Powder diffraction data did, however, show that goethite formation was strongly inhibited at pH 9 in the presence of even low levels of additive (2.5-3.5 mol%). If the transformation was carried out at pH 7, the product composition was limited to at most two phases; hematite and the spinel.

As indicated in Table 3.2, the extra spacings observed for products containing in excess of 7-8 mol% additive were found to be consistent with zinc-magnetite, $ZnFe_2O_4$. If the level of zinc added initially was raised further, the dark red spinel phase became the dominant product. This was the only crystalline material observed in samples formed at pH 7, 9 and 12 in the presence of between 20 and 40 mol% additive (at which point zinc oxide could be detected).

Figs. 3.4 and 3.5 show profiles obtained for samples produced at pH 12 in the presence of, respectively, 20 and 50 mol% additive. The extra spacings indicated in Fig. 3.5 are consistent with expected values for zinc oxide, ZnO (as identified by TEM, Section 3.1).

Assuming uniform additive distribution throughout the products, the proportion of zinc which was present initially in the 20 mol% sample is insufficient to give a stoichiometry $ZnFe_2O_4$ (requiring 33 mol% additive). It is then possible that individual crystals may be defective with respect to the substituent cation, which would in turn affect the average unit cell dimension. However, due to the broad nature of the peaks in each of the samples studied it was not possible to

GOETHITE			HEMATITE			EXPTL
d(nm)	(hkl)	I/I ₀	d(nm)	(hkl)	I/I ₀	d(nm)
0.498	020	10				
0.418	110	100				0.418
			0.368	012	25	
0.338	120	10				0.339
0.269	130	30	0.269	104	100	0.269
0.258	021	8				0.259
0.252	101	4	0.251	110	50	0.252
0.249	040	16				0.250
0.245	111	25				0.245
0.225	121	10	0.229	006	2	0.225
0.219	140	20	0.220	113	30	0.220
0.192	041	6	0.207	202	2	
0.180	211	8	0.184	024	40	
0.172	221	20				0.173

Table 3.3:- Comparison of expected powder diffraction spacings for goethite and hematite with experimental results for products formed at pH 12 in the presence of up to 10 mol% zinc.

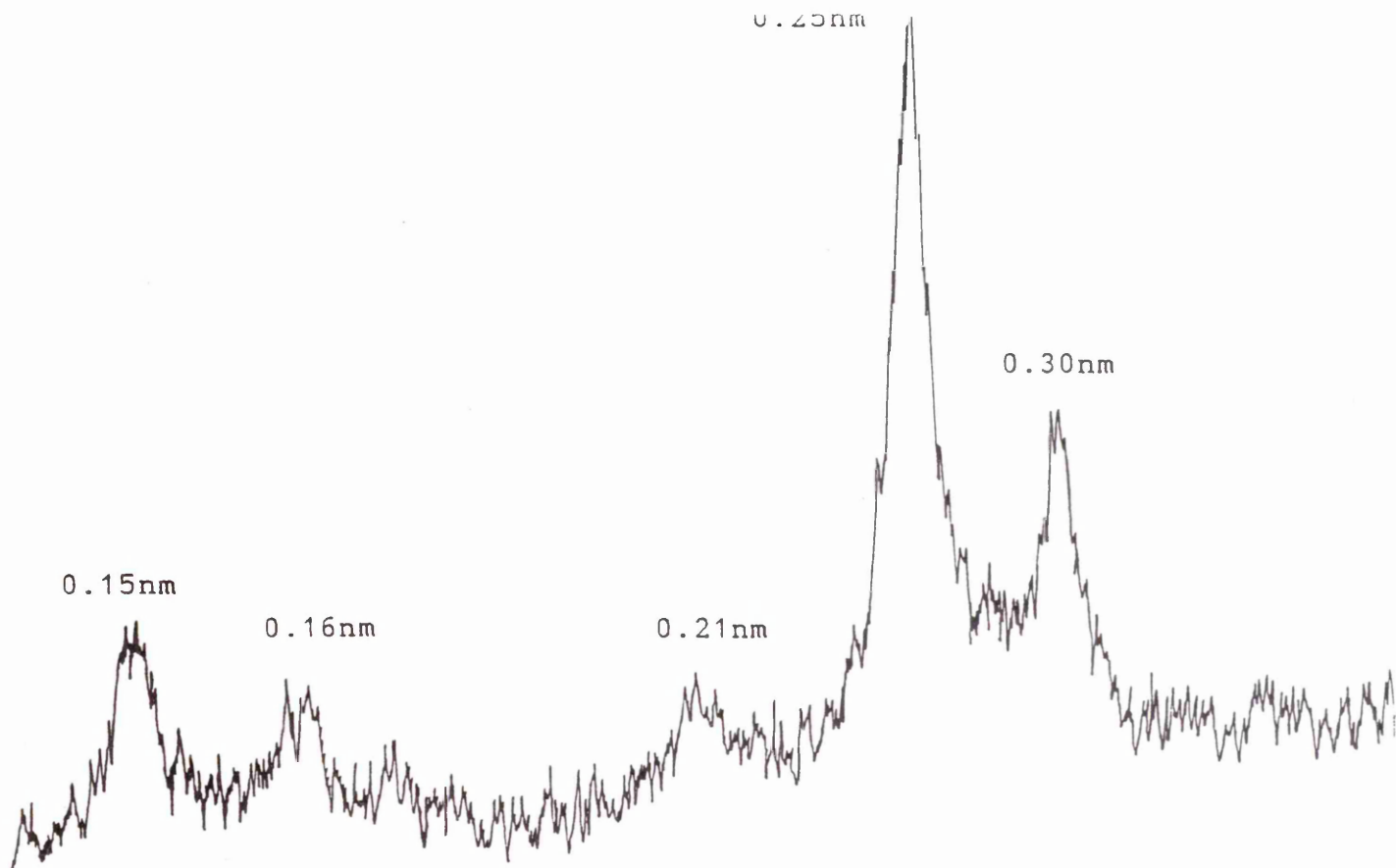


Fig.3.4:- Spinel phase formed at pH 12 in the presence of 20 mol% zinc.

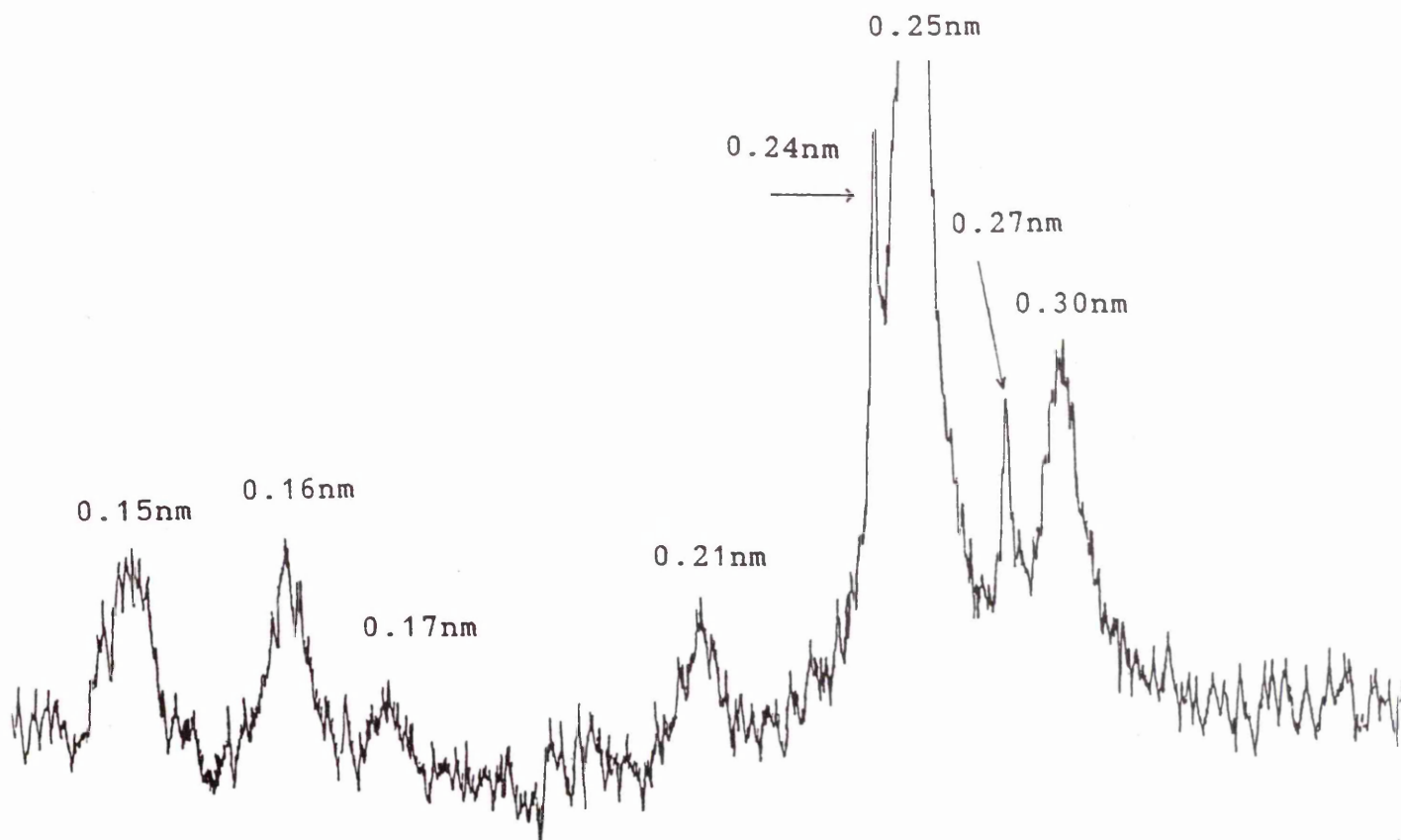


Fig.3.5:- Product formed at pH 12 in the presence of 50 mol% zinc. Extra peaks (arrowed) are consistent with ZnO.

measure d-spacings accurately, so that any variations in unit cell parameter could not be determined. Table 3.4 shows the range of experimentally-measured spacings obtained, together with corresponding values for stoichiometric zinc-magnetite. Peaks measured at 0.295-0.30nm, 0.25-0.255nm, 0.21-0.215nm, 0.16-0.165nm and 0.145-0.15nm were indexed as, respectively, (220), (311), (400), (333)/(511) and (440) reflections for a face-centred cubic spinel structure. Signals at 0.48nm (corresponding to (111) spacing, 20% intensity) and 0.243nm ((222) spacing, 10% intensity) were absent from each of the spectra studied, while the expected peak at 0.172nm (corresponding to (422) spacing, 40% intensity) was often of minimal intensity. The relative peak intensities for those signals which were common to every XRD profile were also found to vary quite widely over the range of products examined.

ZINC-MAGNETITE			EXPTL XRD DATA
d(nm)	I/I ₀	(hkl)	d(nm)
0.485	20	111	ABSENT
0.299	50	220	0.30
0.254	100	311	0.25
0.243	10	222	ABSENT
0.210	40	400	0.21
0.172	40	422	0.17
0.162	70	333	0.16
0.149	80	440	0.15

Table 3.4:- Comparison of measured spinel spacings with expected values for zinc magnetite.

3.3. TEM ANALYSIS OF PRODUCTS:- THE EFFECT OF ZINC ON THE FORMATION AND MORPHOLOGY OF GOETHITE AND HEMATITE.

In order to identify variations in goethite and hematite morphology induced by the presence of zinc, the transformed samples were next prepared for TEM examination. Additive incorporation levels were determined by EDX analysis.

3.3.1. HEMATITE.

At neutral pH, TEM showed gradual aggregation of ferrihydrite into dense masses which transformed with time into plate-like crystals up to approximately 100-200nm in diameter (Plate 8). In accord with powder diffraction results, selected-area electron diffraction data for these products indicated that the only crystalline phase present was hematite.

Indexing of patterns obtained for individual crystals showed that most were singly-diffracting in nature. A fairly wide range of zone axes were identified, suggesting that most of the hematite plates tended to be well-developed in all three crystallographic directions. However, a large number of wide crystals were found to be imaged in $[00.1]$, suggesting that growth in the c-direction may have been restricted.

The presence of up to 8 mol% zinc in precipitates formed at pH 7 retarded the rate of transformation, and led to a slight decrease in the average crystal size (Plate 9). Raising the level of additive to 10 mol% strongly promoted formation of the spinel phase (Section 3.4.). In this case, development of hematite was inhibited, and only a low proportion of small oxide particles could be identified.

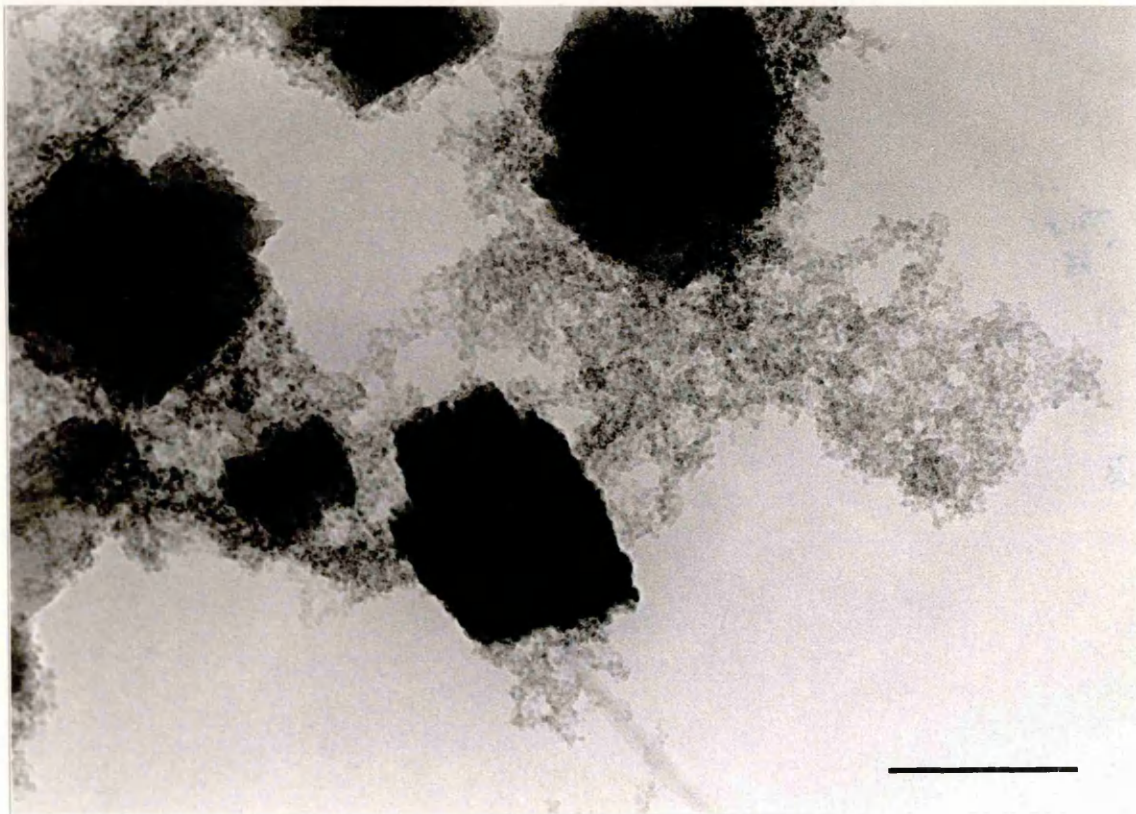


Plate 8:- Hematite crystals formed at neutral pH in the absence of zinc. Scale bar represents 100nm.

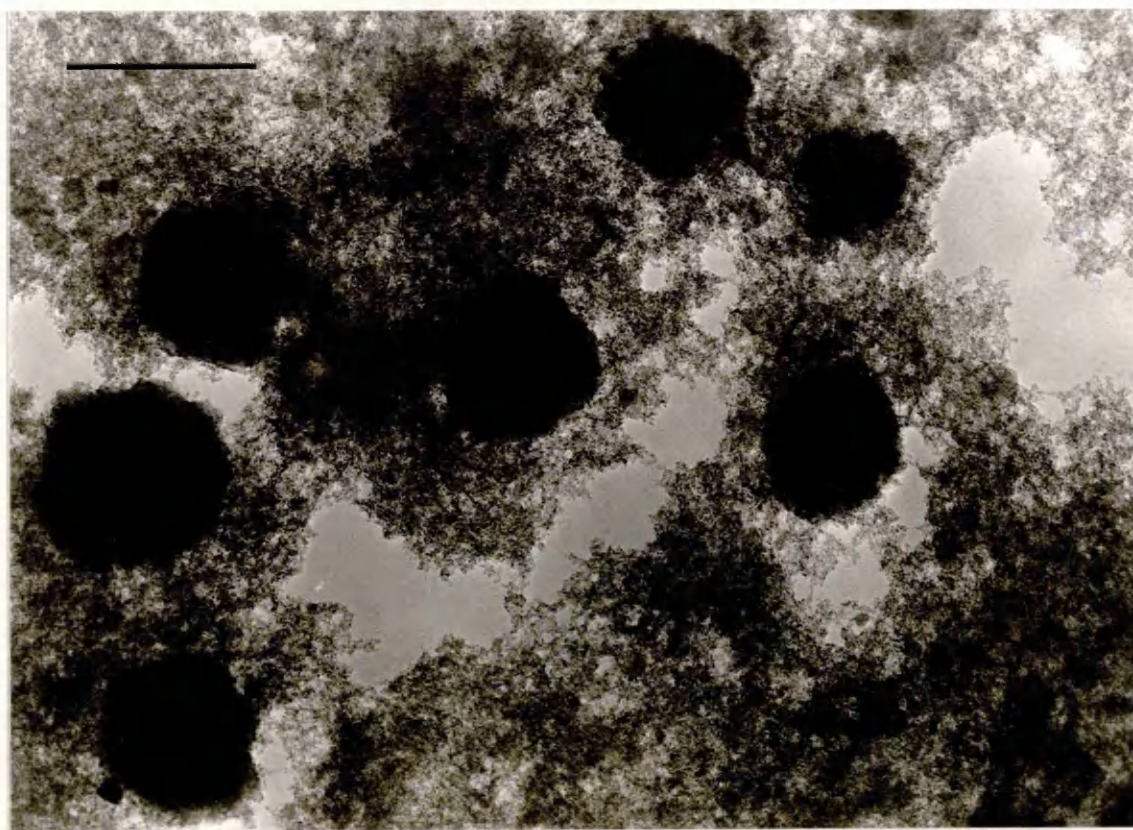


Plate 9:- Hematite formed at neutral pH in the presence of 8 mol% zinc. Scale bar represents 100nm.

If the initial gel pH was raised to 9, the presence of 2.5-5 mol% additive strongly inhibited development of goethite. These products were found to comprise hematite plates and some twin crystals showing short outgrowths (Section 3.3.2.). Raising the proportion of additive above 7-8 mol% was again found to promote formation of zinc-magnetite, but hematite nucleation and growth did not appear to be as strongly inhibited as at pH 7; large hematite crystals could still be detected in products formed in the presence of up to 15-20 mol% additive. The average crystal dimensions, which did not vary significantly with the level of zinc present, were larger than those of the plate-like crystals observed in control samples formed at pH 7 (300-400nm by 100-200nm compared to 100-200nm diameter).

In contrast to oxide particles formed in the absence of additive, these crystals were often found to be poorly-defined in nature. Plate 10 shows a hematite crystal formed at pH 9 in the presence of 12.5 mol% zinc. At high magnification (as shown) the surface can be seen to comprise individual platelets similar in size to the ferrihydrite precursor (although faceting at each particle edge appeared to have occurred during crystallisation). It was not possible to index the corresponding diffraction pattern (Plate 10, inset) so that a single zone could be identified. This suggested that the above domains were misaligned. Such an incoherent structure could arise if growth was inhibited. The effect was frequently observed for hematite formed in the presence of higher levels of additive. The EDX profile obtained (Fig. 3.6) gave a mass

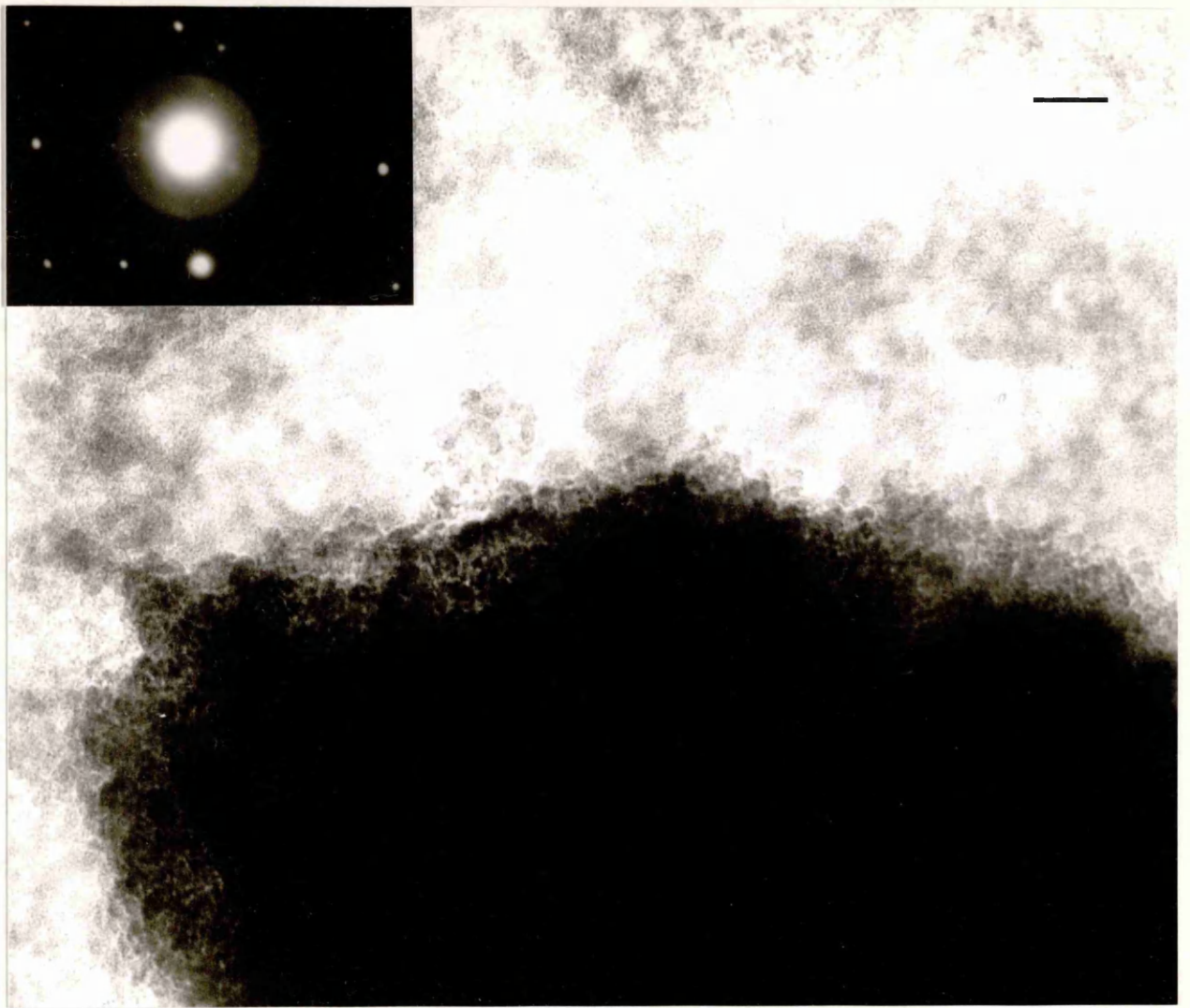


Plate 10:- Multi-domainic hematite crystal formed at pH 9, showing granular character induced by the presence of zinc. Scale bar represents 20nm.

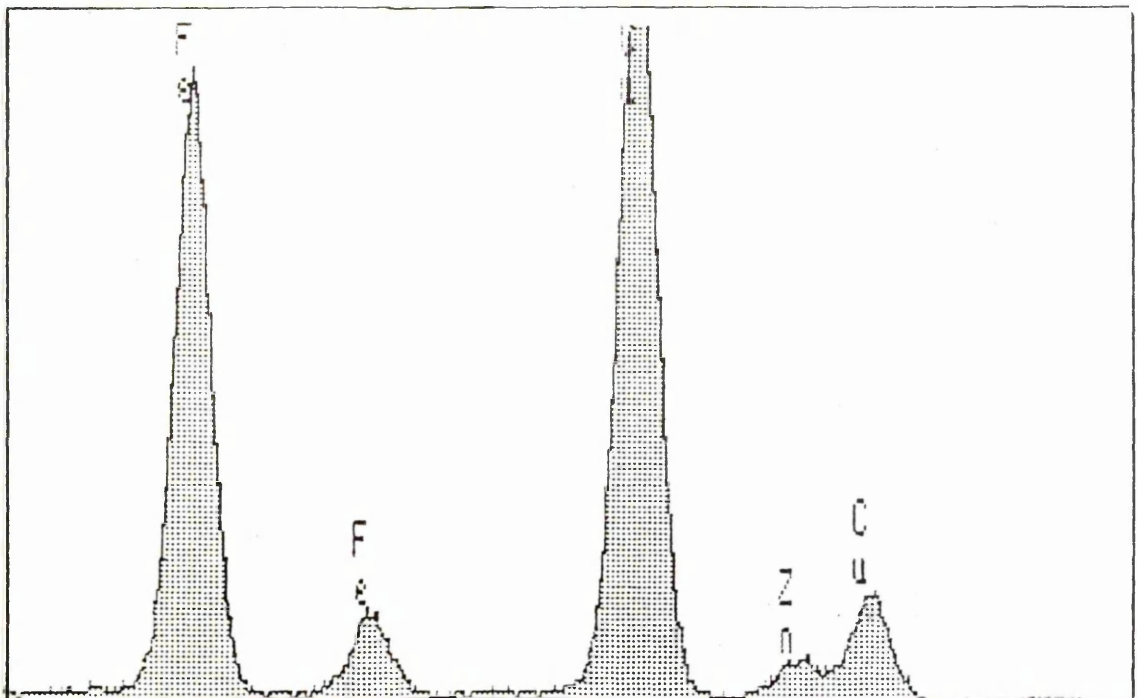
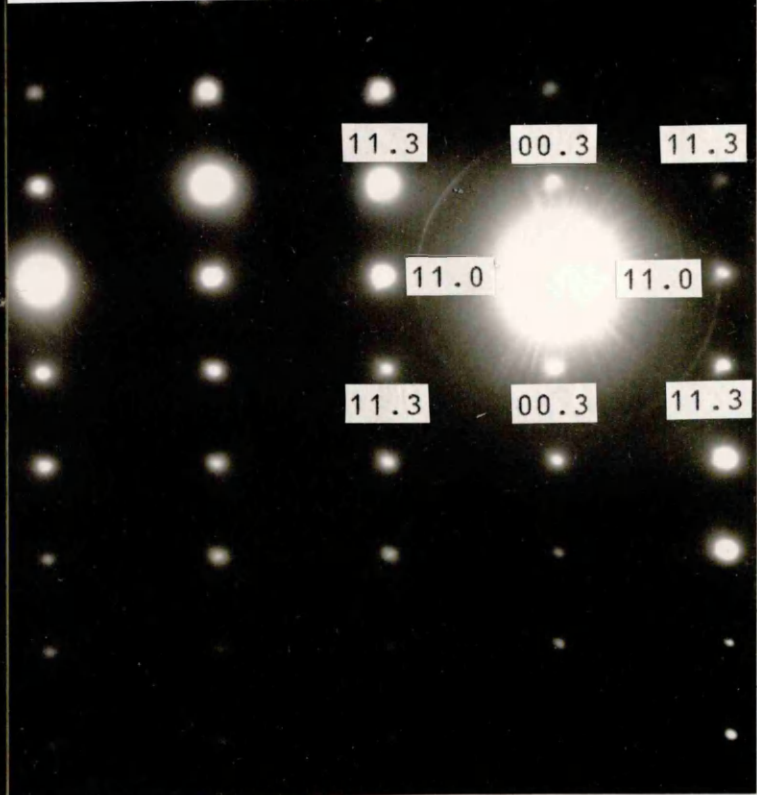
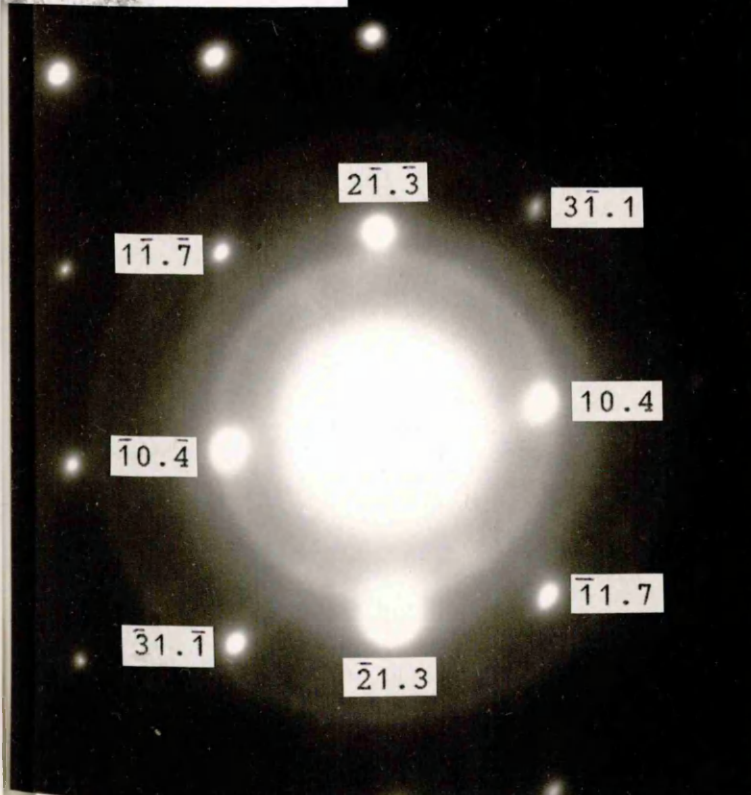
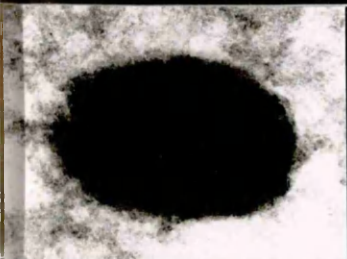
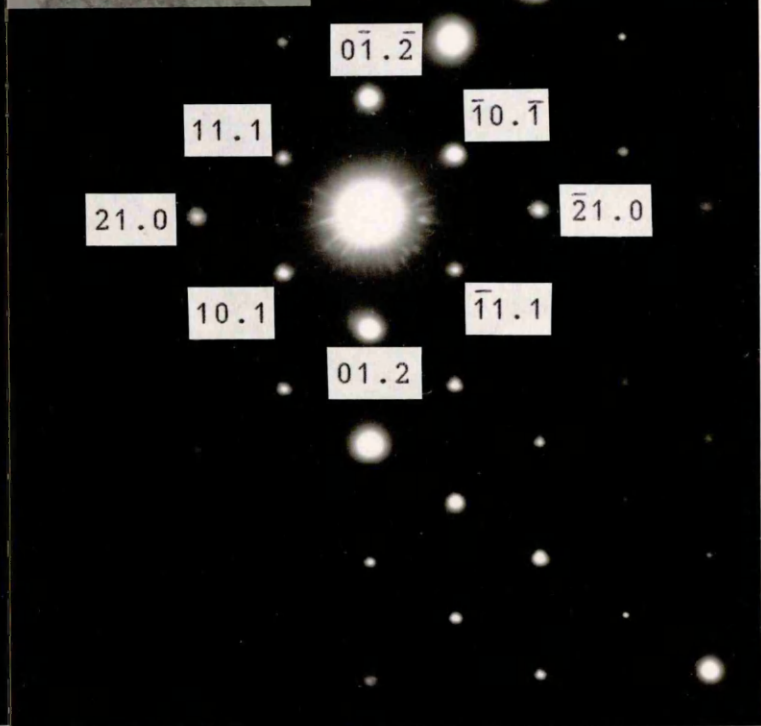
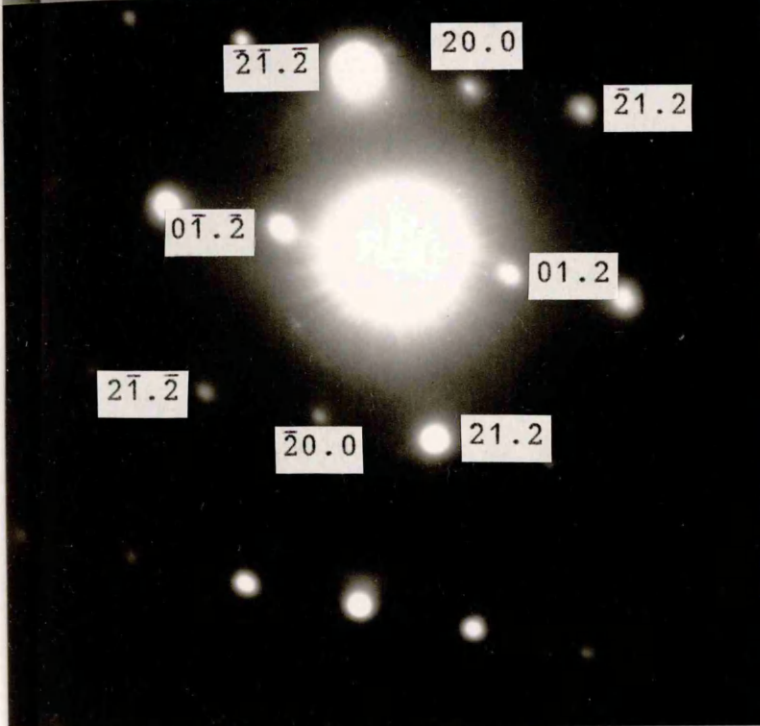
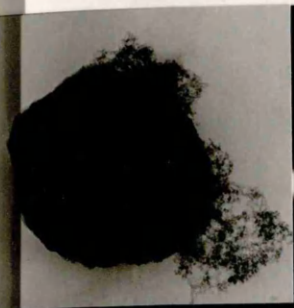


Fig.3.6:- EDX profile obtained for the above crystal.

concentration ratio $C_{Zn}/C_{Fe} = 0.11$, corresponding to 8.6 mol% additive incorporation in the crystal lattice. Each of the hematite crystals examined was found to have taken up some proportion of the additive during growth. A full treatment of the levels of zinc incorporated in the oxide is given in Section 3.5.

Cornell and Giovanoli [79] found that hematite formed in copper-ferrihydrite systems at pH 12 exhibited a rhombohedral morphology which was thought to arise from preferential adsorption of additive species on (10.2) faces. EDX data has shown that zinc was also adsorbed or incorporated in the oxide structure. This was found to induce development of a prismatic or pseudo-rhombohedral morphology in the hematite crystals, especially at pH 9. Indexing of diffraction patterns obtained for single-domain zinc-hematite particles showed that, as with oxide plates formed at pH 7, the crystals had adopted a wide variety of orientations relative to the electron beam direction. Although the presence of additive was found to modify the hematite morphology, the crystals were not uniform (in contrast to goethite and spinel crystals). However, the zone axes most commonly observed were of the form $[XY.1]$, where the crystals were tilted away from $[00.1]$. Plates 11 a)-c) (inset) show typical crystals produced at pH 9 in the presence of zinc. The corresponding diffraction patterns have been indexed as hematite imaged in $[02.1]$, $[12.1]$ and $[4\ 11.1]$. A $[00.1]$ zone axis was rarely identified. Plate 11d) shows a hematite crystal imaged in $[11.0]$. In these cases, growth in the c-direction does not appear to be restricted.

Plates 11 a)-d) (over):- Selected single-domain hematite crystals formed in the presence of zinc, shown together with the corresponding diffraction patterns.



Due to the relative thickness and uneven surface character of the hematite plates, crystals were generally found to be unsuitable for high-resolution imaging. It was therefore difficult to obtain information on the localised structure around the individual grains from which most of the zinc-hematite particles were comprised. Plate 12 (inset) shows a crystal formed at pH 9 in the presence of 15 mol% zinc, which EDX analysis showed to contain about 7 mol% additive. The corresponding diffraction pattern (main Plate) could be indexed in accord with an essentially singly-diffracting hematite crystal imaged in [62.1]. Plate 13 shows an enlarged area (arrowed). Lattice fringes could only be resolved at the edges of the crystal, which are staggered and terminate in lattice planes measured at 0.37nm. This value is consistent with the (10.2) reflection for hematite. Although a large number of apparent defects were observed in the bulk crystal, the lattice fringes were generally coherent at the crystal edges. It was not possible to determine whether the defects were intrinsic to the crystal structure or arose due to focal conditions or beam damage.

3.3.2. GOETHITE AND TWIN CRYSTALS.

TEM examination of products formed at pH 12 in the absence of zinc showed a predominance of large single crystals, typically 300-500nm in length. These were found to exhibit the characteristic acicular morphology associated with goethite, with growth extended in the [001] direction relative to [100] and [010] (Plate 14). Spacings measured from

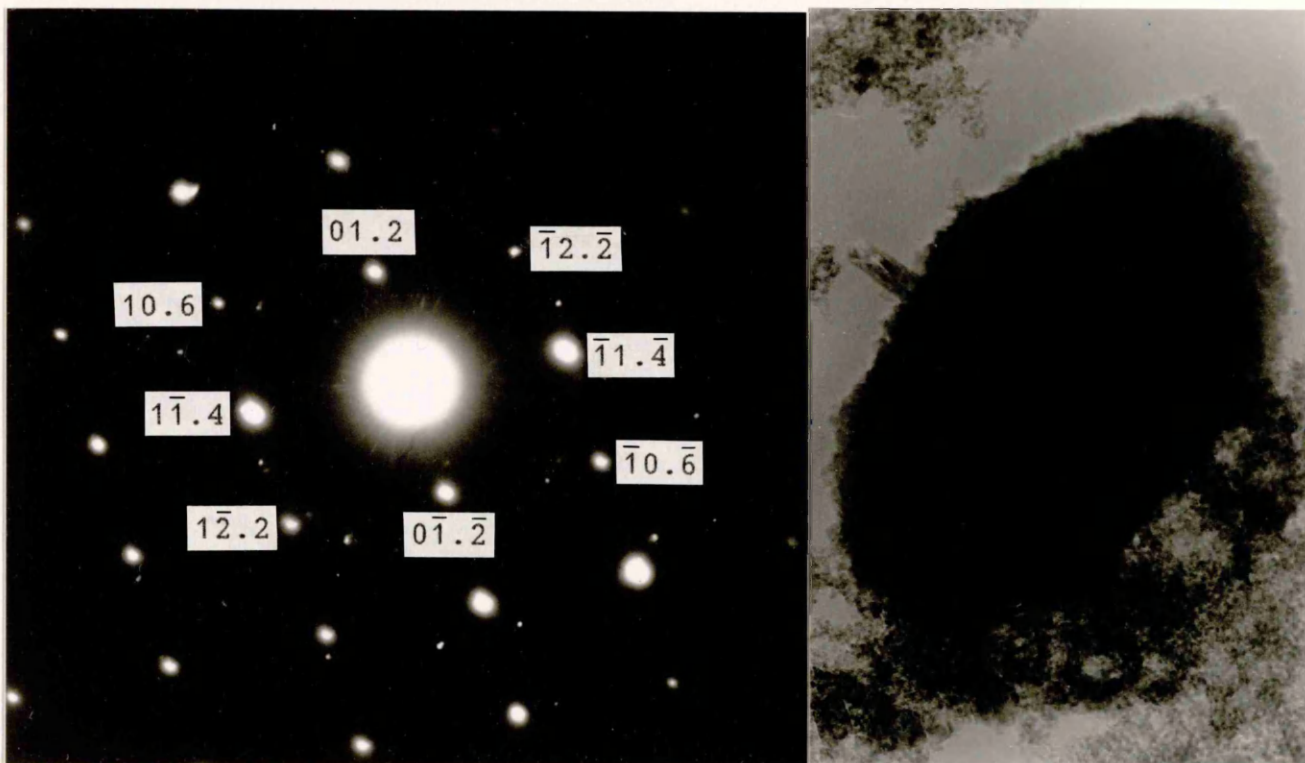


Plate 12:- Selected-area diffraction pattern for a singly-diffracting hematite crystal (inset).

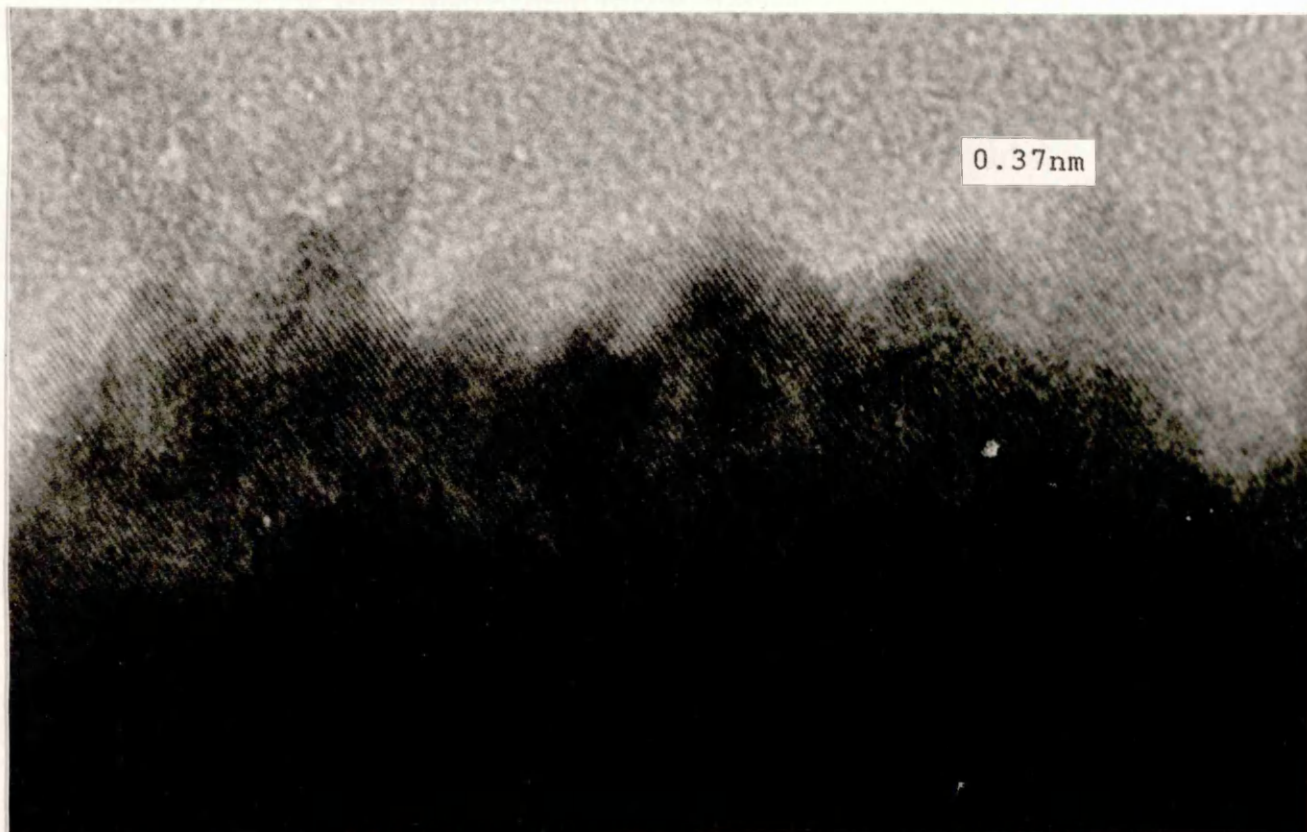


Plate 13:- High-resolution image showing an edge of the above crystal. The lattice fringes are essentially coherent. Scale bar represents 10nm.

selected-area diffraction patterns for crystal aggregates were consistent with values for the oxyhydroxide (Plate 15). In accord with XRD data, no obvious reflections corresponding to hematite were noted. It was observed that most crystals were not single-domain in nature but comprised several parallel intergrowths. However, diffraction patterns obtained for individual acicular crystals were generally found to be consistent with singly-diffracting particles, suggesting that the intergrowths were largely coherent. The most common zone axis was identified as [100] (Plate 16).

An enlarged area from the above acicular crystal is shown in Plate 17. Lattice fringes measured at 0.498 nm, 0.258 nm (at an angle of 58°) and 0.301 nm (at 90°) are indicated. These values are consistent with, respectively, (020), (021) and (001) reflections for a goethite crystal imaged in [100]. In accord with results obtained by Mann *et al* [64] lattice resolution over the grain boundaries between neighbouring intergrowths in these crystals generally appeared to be coherent, although (as in the above micrograph) areas containing dislocations were often observed. These regions may have arisen as a result of prolonged exposure to the electron beam or from misalignments inherent in the goethite structure (the effect of beam damage on the crystals is discussed further in Section 3.9).

Twinning of goethite crystals was not observed to any great extent at pH 12 in the absence of additive, although some twins, mainly of dendritic or "star-shaped" composite types, were detected.



Plate 14:- Goethite crystals formed at pH 12 in the absence of additive. Scale bar represents 200nm.

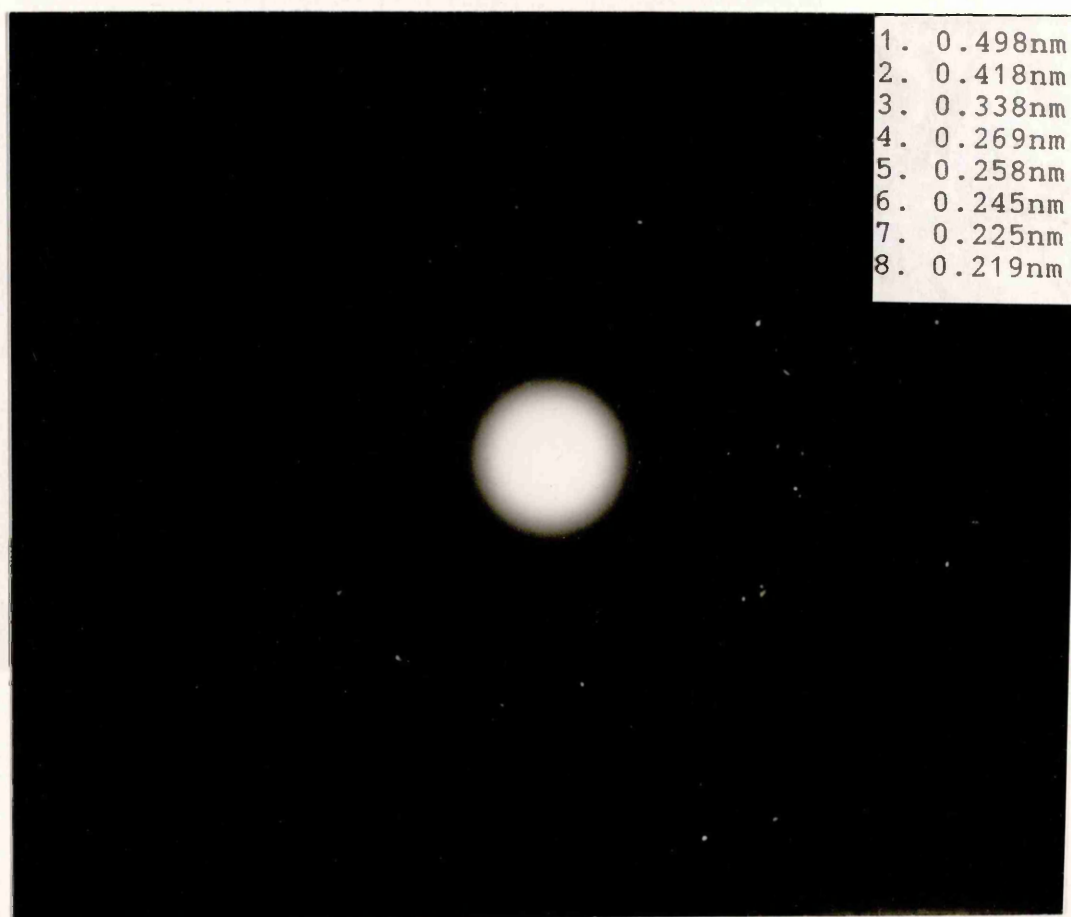


Plate 15:- Selected-area diffraction pattern obtained for the above product.

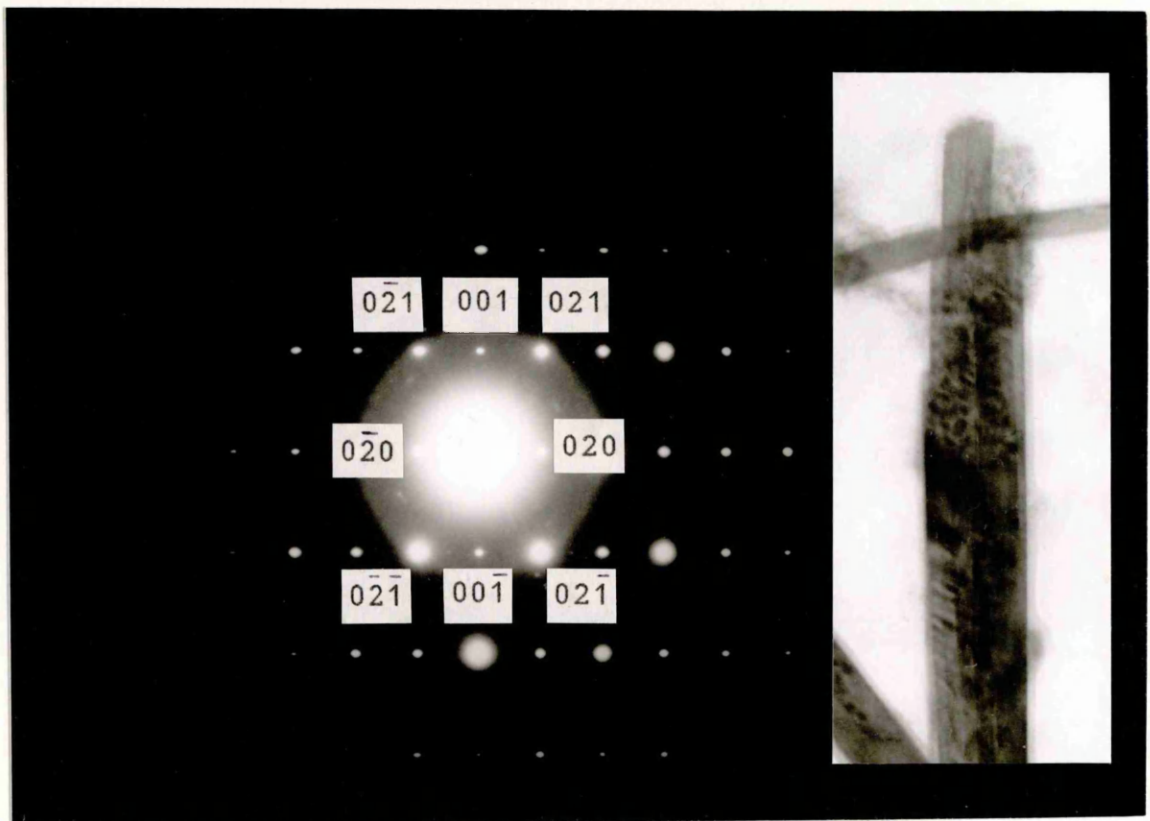


Plate 16:- Diffraction pattern for a single acicular crystal, indexed as goethite imaged in [100].

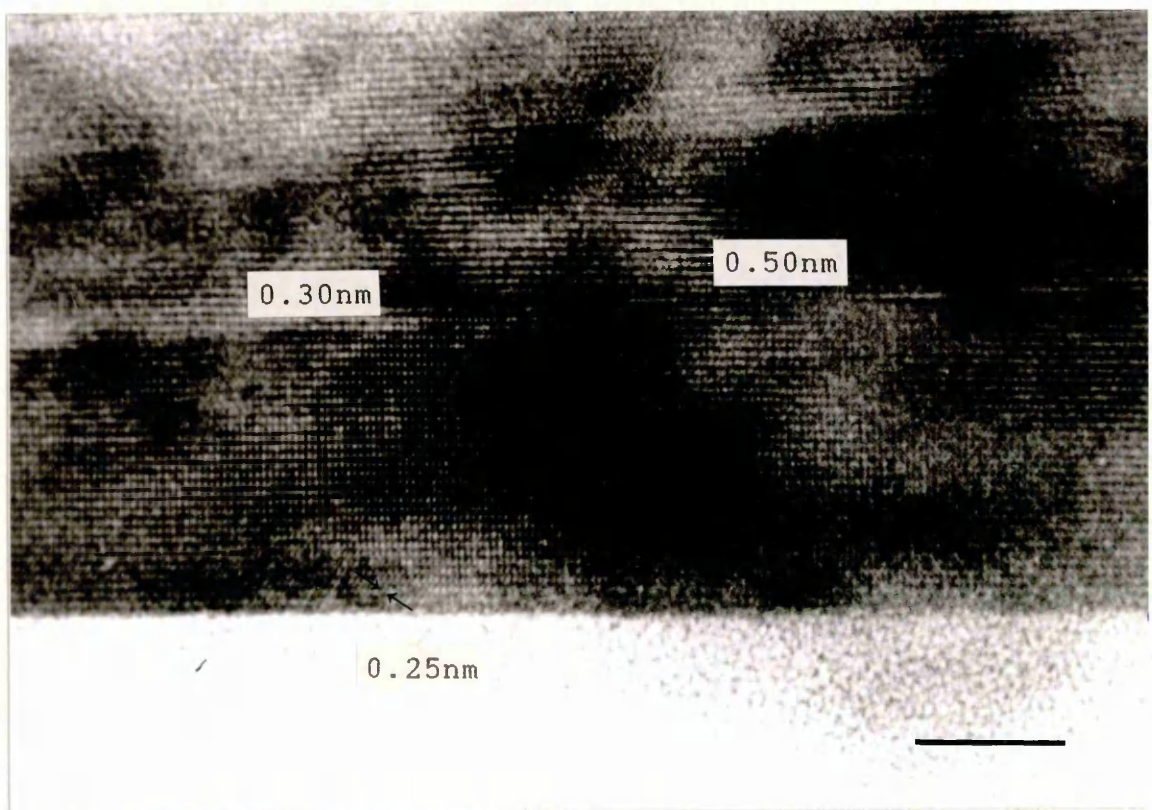


Plate 17:- Enlarged area from the above crystal showing resolution of (020), (001) and (021) spacings. Scale bar represents 10nm.

Control samples formed at pH 9 were found to consist of small hematite particles, usually exhibiting goethite outgrowths, and large numbers of the so-called "star-shaped" crystals quoted in previous studies [48,57]. These twins comprised a central region from which as many as six sets of arms had grown outwards, each at an angle of 60° relative to its neighbours (Plate 18). In contrast to single acicular crystals formed under similar growth conditions, the twin outgrowths were normally found to terminate in well-defined (021) faces. Many of the individual arms appeared to comprise several parallel intergrowths.

Plates 19 and 20 show, respectively, selected-area diffraction patterns for a star twin and an acicular crystal. Plate 20 is indexed in accord with singly-diffracting goethite imaged in [100]. One equivalent set of spots in Plate 19 is highlighted. The overall pattern for the twin can be generated by superimposing three such acicular crystals, so that each is set at 60° relative to the others.

It was commonly found that, in any one direction, several acicular outgrowths had developed. A high-resolution image showing one set of arms from a star twin is illustrated in Plate 21. Lattice fringes measured at 0.50nm (corresponding to d_{020} spacings for α -FeOOH) are resolved over the boundary between two outgrowths. There appears to be little or no incoherency where the (020) planes of these arms meet, suggesting that the outgrowths are in phase. Similarly, where two neighbouring sets of arms connected near the crystal centre there was little evidence of a mismatch. However,

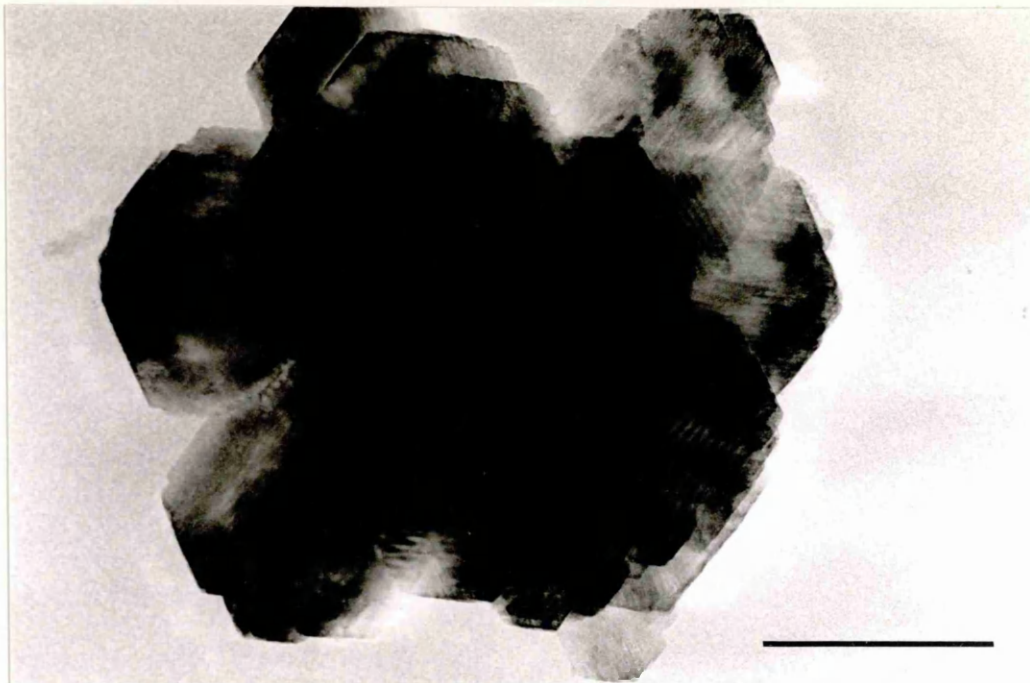


Plate 18:- Star twin formed at pH 9 in the absence of additive. Scale bar represents 200nm.

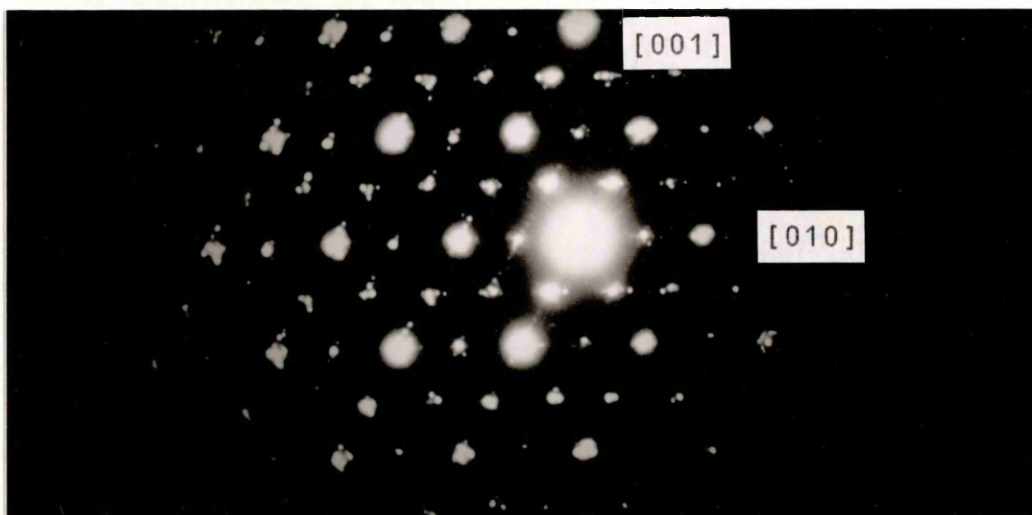


Plate 19:- Selected-area diffraction pattern obtained for the above twin. simply an ordered array within the twin.

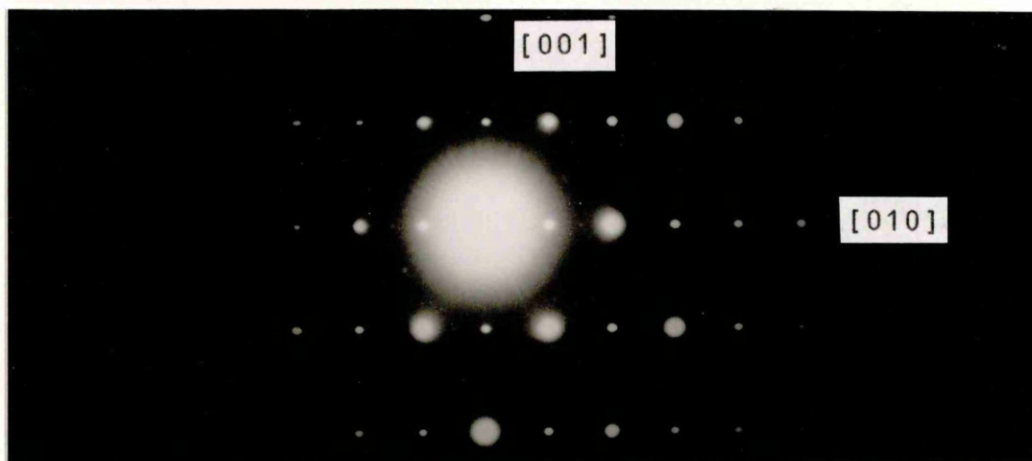


Plate 20:- Single crystal diffraction pattern, oriented to illustrate equivalence with highlighted spots in Plate 19.

diffraction patterns obtained for entire twins (Plate 19) showed that some degree of fine structural misalignment was present between the various sets of outgrowths. Preferential dissolution at the crystal centre on addition of 1M HCL gave further evidence for strain in this region.

The above results are in accord with a study by Atkinson *et al* [48], who found that the morphology of the individual twin arms was comparable to that of acicular goethite crystals, with extended growth occurring in the [001] direction. The outgrowths meet on (021) faces at the twin centre. However, the nature of the central area is ambiguous. The twins may be composite in nature (containing only goethite), or may show epitaxy with hematite. Examination of diffraction patterns could not show conclusively which was the case, and the crystals were found to be too thick to obtain lattice resolution over the central area.

Formation of this type of twin has previously been thought to occur via a mechanism in which either a hematite nucleus or simply an ordered region within the ferrihydrite precursor develops during the induction period. This nucleus will act as a template, allowing growth of goethite to occur [48,57]. The model is dependent on the similar hcp anion arrangement present in both the goethite and hematite structures. In goethite, the direction of stacking for close-packed anion layers is parallel to [100], while in the case of hematite the oxygen layers lie parallel to the c-axis (Section 1.1.2.). Table 3.5. shows a set of equivalent d-spacings for the two phases.

α -FeOOH		α -Fe ₂ O ₃	
(hkl)	d(nm)	(hkl)	d(nm)
(021)	0.258	($\bar{2}1.0$), ($\bar{1}2.0$)	0.252
(040)	0.249	(11.0)	
(002)	0.150	(30.0), (03.0)	0.145
		($3\bar{3}.0$)	

Table 3.5:- Equivalent goethite/hematite spacings.

For a twin diffraction pattern such as that shown in Plate 19, the [001] direction for each acicular arm is then parallel to one of [10.0], [01.0] or [$\bar{1}1.0$] directions for hematite in reciprocal space (Fig.3.7). The goethite (100) and (010) spacings are then associated with, respectively, [00.1] and one of [11.0], [$\bar{2}1.0$] and [$\bar{1}2.0$] reflections for α -Fe₂O₃.

Goldsztaub [104] found that on firing a sample of α -FeOOH the a-axis of goethite was transformed into the c-axis of hematite, while the oxyhydroxide c-axis became [12.0] for the oxide in real space. This equivalence is illustrated by Plate 22, which shows the diffraction pattern obtained for an acicular crystal (inset) from a sample of goethite (main zone axis [100]) which was fired at 250°. Indexing identified the crystal as hematite imaged in [00.1].

The above model can now be used to aid the indexing of diffraction patterns for twin crystals which were thought to show epitaxy. Many of the hematite crystals formed at pH 9 in the presence of zinc showed a number of quite short acicular arms growing outwards from the crystal body. Similar crystals have been observed in products formed in the presence of other additives (notably copper). It has been suggested that these outgrowths could comprise either goethite or hematite.

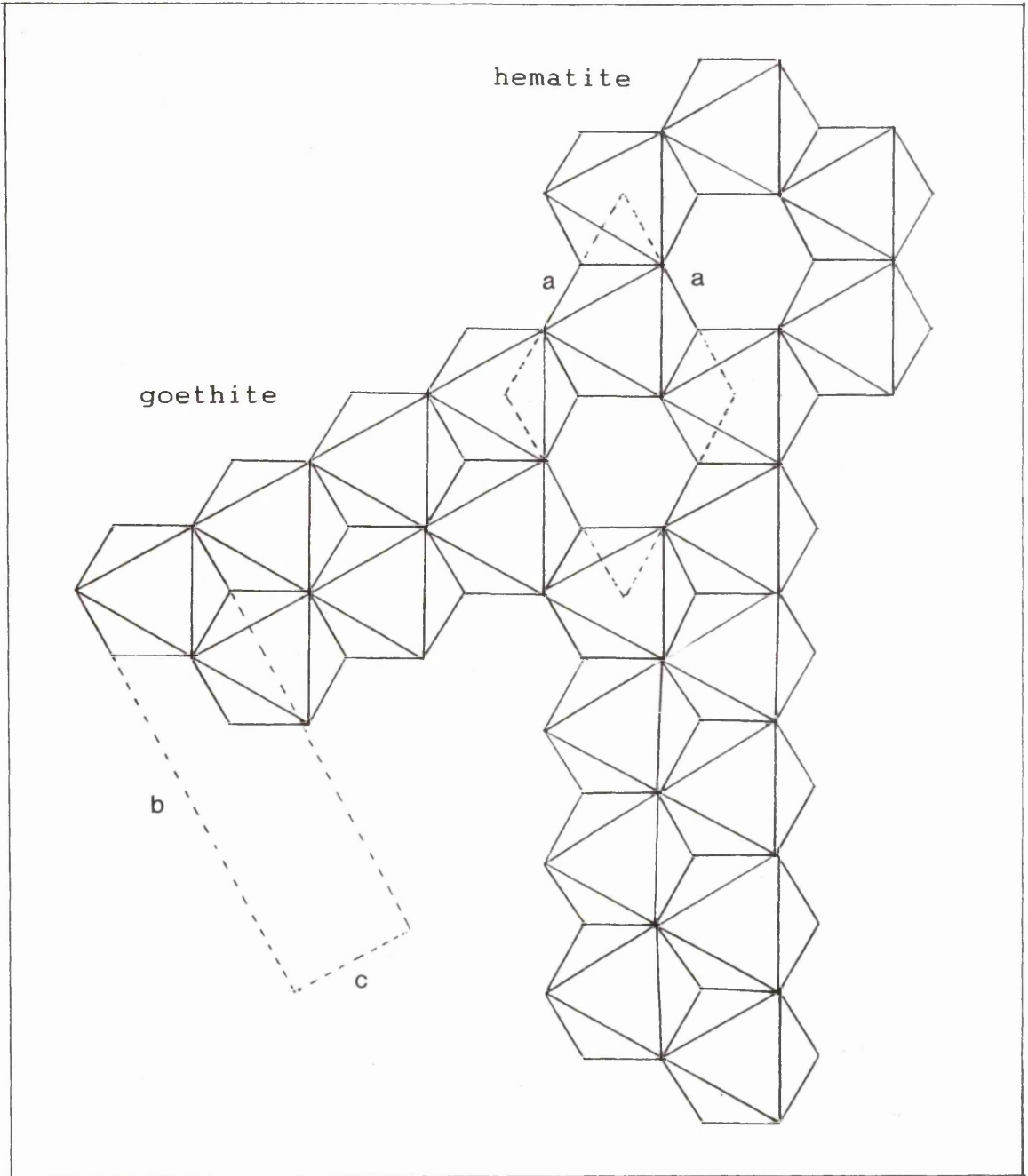


Fig.3.7:- Hematite structure projected onto [00.1] (upper half), showing potential for development of double chains leading to goethite formation in the presence of a high concentration of soluble ferric species. Unit cells are marked with dotted lines.

Plate 21 (over):- High resolution image of a star twin arm, showing resolution of 0.50nm lattice fringes corresponding to (020) spacings for goethite. Scale bar represents 10nm.

Plate 22 (over):- Goethite crystal fired at 250°C, together with corresponding diffraction pattern indexed as hematite imaged in [00.1].

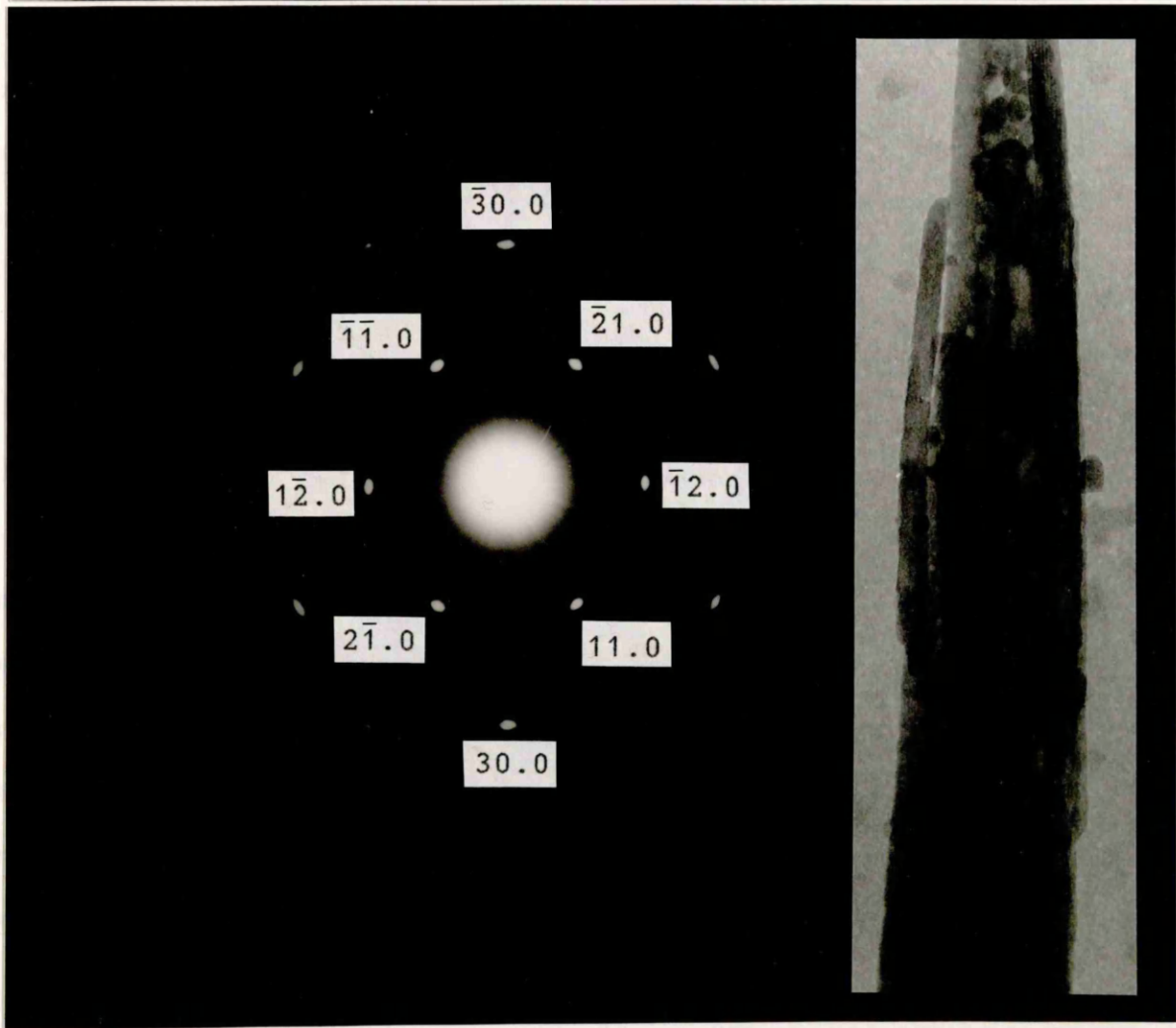
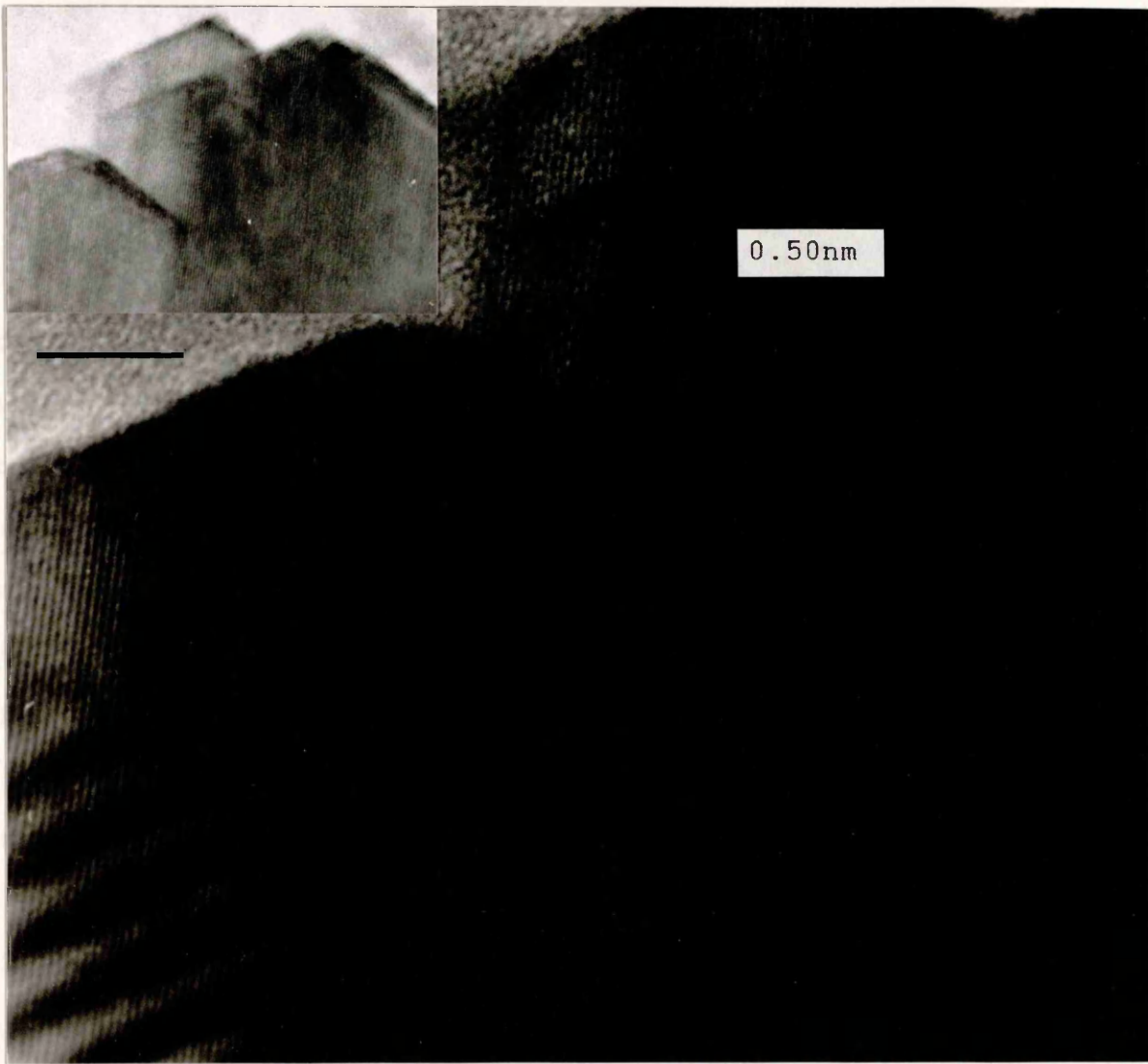
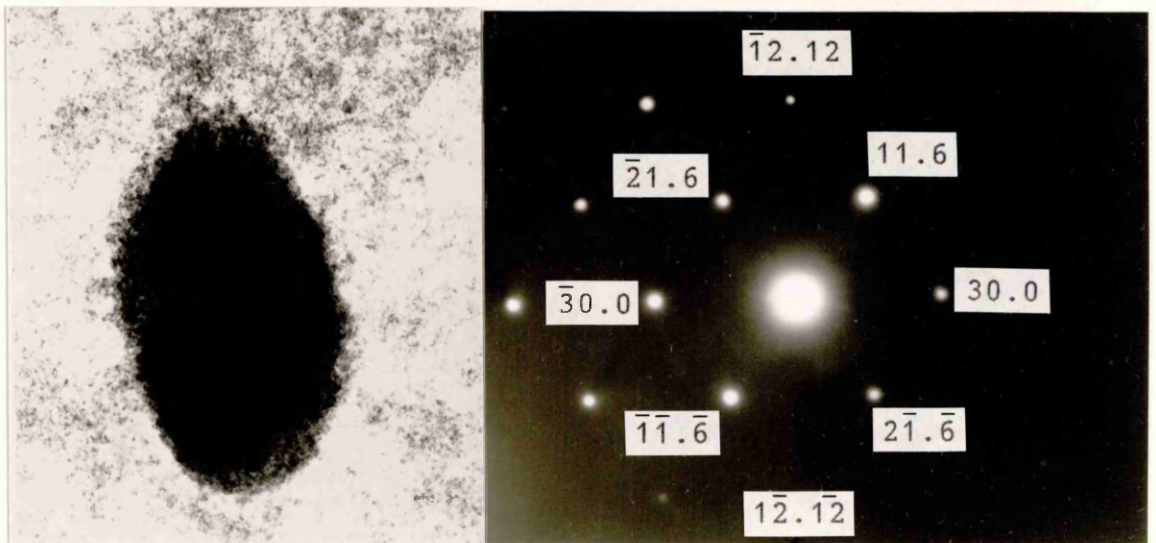


Plate 23a) shows a typical ellipsoidal hematite particle, which was produced at pH9 in the presence of 12.5 mol% zinc. The corresponding diffraction pattern (Plate 23 b)) is indexed in accord with a singly-diffracting oxide crystal imaged in [06.1]. Plates 24a) and 24b) show, respectively, a second crystal from the same sample (which exhibited several outgrowths), together with the corresponding selected-area diffraction pattern. Plate 24b) also exhibited a set of spots which were consistent with hematite imaged in [06.1]. However, a number of extra reflections were present which could not be accommodated. These spacings were measured at 0.418nm, 0.302nm (at 90°) and 0.245nm (at 47°). The above values and angles are consistent with goethite imaged in [110]. Lattice fringes running the length of the short outgrowths were measured at 0.42nm (consistent with d_{110} for goethite). If the [100] zone for α -FeOOH is again taken as equivalent to [00.1] for α -Fe₂O₃, consider tilting of the goethite unit cell to bring [110] into line with the electron beam. This angle was calculated at 65.1° . The angle between [00.1] and [06.1] zones of α -Fe₂O₃ is 65.3° . In this case, the outgrowths are more likely to comprise goethite.

At pH 12, products formed on ageing ferrihydrite gels containing up to about 10-15 mol% additive were found to comprise at least some proportion of goethite and hematite. The main effect of introducing low levels of zinc was to promote twin formation. If the level of additive present was restricted to 0.5-2.0 mol%, the products formed were found to comprise a mixture of single acicular crystals and twins.



Plates 23.a) and b):- Hematite crystal formed at pH 9 in the presence of 12.5 mol% zinc. The zone axis was identified as $[06.1]$.



Plates 24.a) and b):- Hematite crystal exhibiting outgrowths (also from the above sample). The diffraction pattern could be indexed as above, with extra spots consistent with goethite arms imaged in $[110]$.

Although typically comprising several intergrowths, the acicular crystals were usually found to be singly-diffracting. The main zone axis was again identified as [100] (c.f. control samples). If 5-7.5 mol% zinc was present in the initial precipitates, single goethite crystals were largely absent from the products. Other than promoting twin formation, the presence of low levels of zinc did not appear to modify the actual acicular goethite morphology to any extent.

In contrast to the twin crystals formed at pH 9 in the presence of zinc, which consisted of large hematite plates exhibiting short outgrowths, the twins which developed at high pH typically consisted of long goethite arms growing from a small central area which may or may not have comprised hematite. Most of the twin crystals observed in samples formed at very low levels of addition (<3 mol%) could be assigned to one of two characteristic types:-

a) twins exhibiting a morphology similar to that of an acicular crystal, but which were generally wider and contained a small dark central area which was completely enclosed by the crystal arm.

b) crystals comprising up to three parallel acicular arms growing from a plate-like or prismatic centre. This central component was usually elongated in a direction perpendicular to the length of the twin arms, and extended out with the width of the outgrowths. These crystals were similar in morphology to epitaxial twins grown in the presence of simple sugars [105]. Due to the effects of spot streaking and the presence of satellite spots, etc a high proportion of the diffraction

patterns obtained for this crystal type were too complex to index with any confidence.

A typical example of twin morphology "(a)" is illustrated by Plate 25, in which an acicular crystal is shown together with the corresponding selected-area diffraction pattern (inset). The measured spacings and angles were found to be consistent with goethite imaged in [100]. As described above, the difficulty in determining the nature of these twins lies in characterising the central area, which may comprise a hematite "nucleus" around which the acicular crystal has grown, or which may simply consist of a further overgrowth of goethite. If a model similar to that used for "star-shaped" twins is employed, the 0.25nm spacings in Plate 25 which correspond to, respectively, (040), (021) and $(02\bar{1})$ reflections for α -FeOOH, can also be assigned to $(\bar{1}2.0)$, $(\bar{2}1.0)$ and (11.0) spacings for hematite imaged in [00.1]. The central region of a similar crystal is shown in Plate 26. Lattice fringes measured at 0.50nm (corresponding to (020) spacings for goethite) are resolved over the grain boundary between the central area and the main crystal body. These fringes continue over this region with little or no incoherency, suggesting that the goethite arms had completely enclosed the centre. No evidence for the presence of hematite was observed. Although diffraction patterns often showed spot splitting, lattice imaging gave little evidence for the presence of pronounced defects in these crystals. However, irregularities such as etch pits were often found to have developed (Plate 25, arrowed). Such defects have previously been found to be associated with

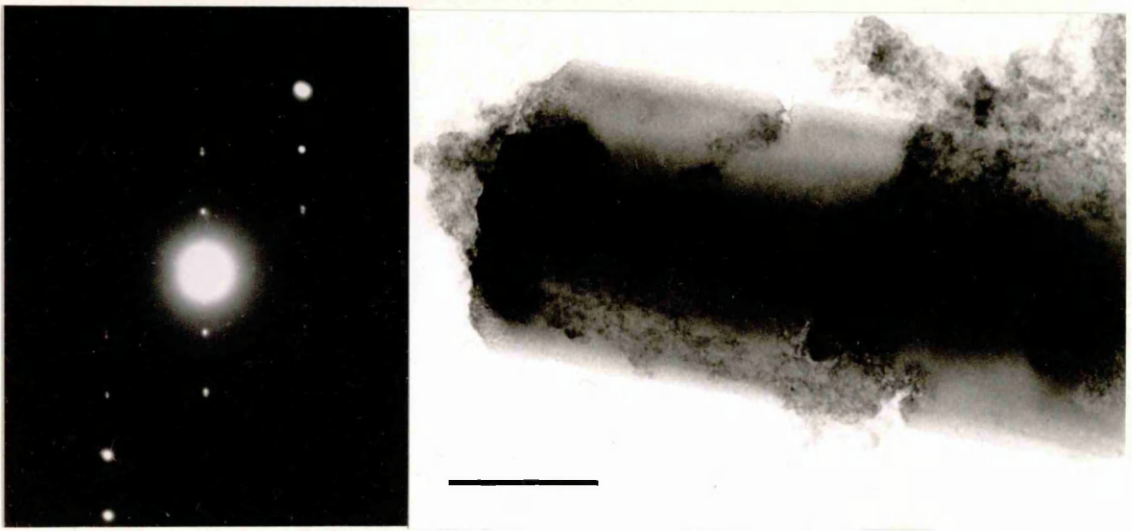


Plate 25:- Acicular crystal showing a dark central area. The diffraction pattern shown is consistent with goethite imaged in [100]. Etch pits in the sides of the crystal are arrowed. Scale bar represents 50nm.

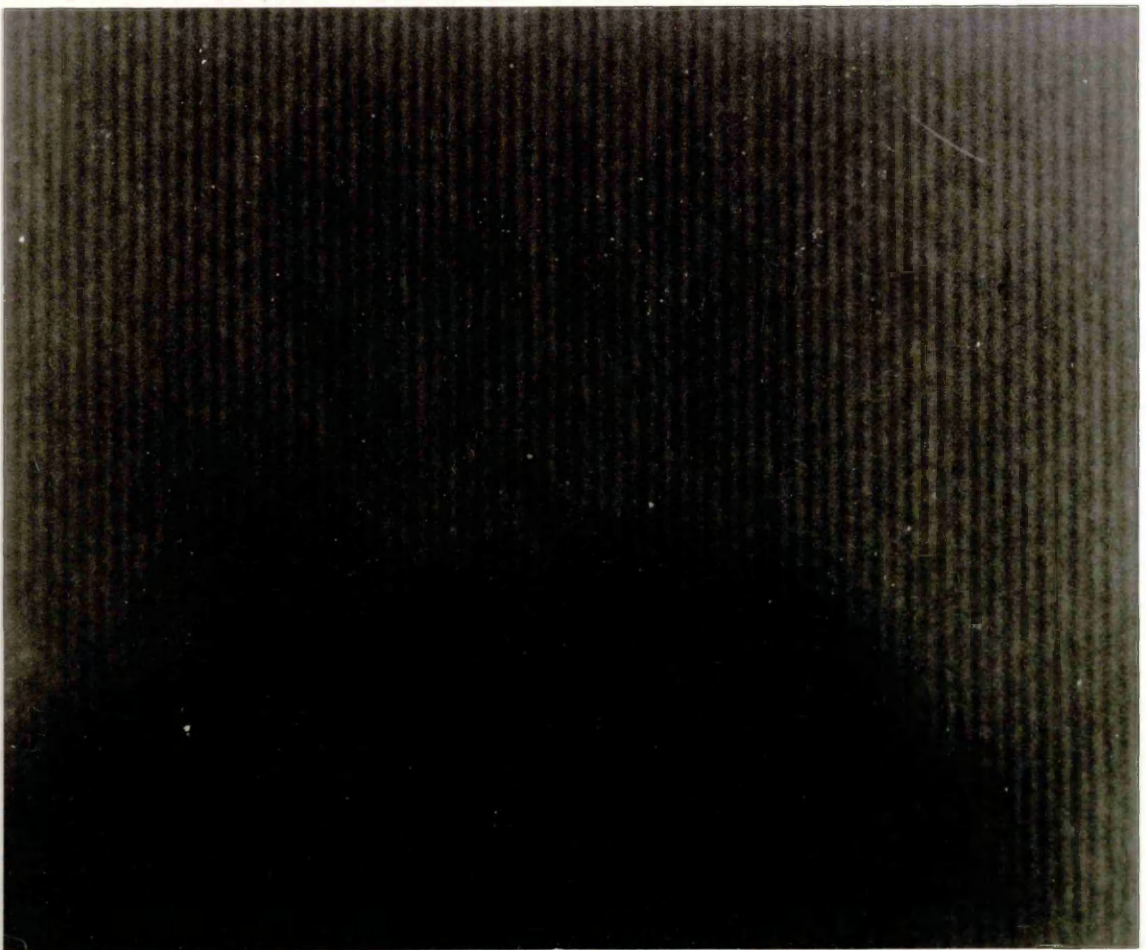


Plate 26:- High-resolution image showing the central area of the above crystal. Lattice fringes corresponding to goethite (020) spacings were resolved.

goethite produced in the presence of foreign cations [75]. This effect was thought to arise through direct interaction of additive species with the growing crystals. However, EDX analyses did not give any evidence that zinc was associated with the above particles.

Plate 27 (inset) shows an example of the second twin type described above (in this case formed at pH 12 in the presence of 2.5 mol% zinc). The corresponding selected-area diffraction pattern (main Plate) was indexed as goethite imaged in [210]. Again, the nature of the central area is ambiguous, since extra spots which would be inconsistent with a single goethite crystal were not observed. However, it was again possible to index certain of the spots in accord with hematite, using the model for epitaxial twinning. Plate 28 (inset) shows a single oxide crystal formed at pH 7 in the absence of additive. The diffraction pattern (main Plate) was indexed as hematite imaged in [03.1], which can be fitted to that for goethite imaged in [210] (highlighted spots in Plate 27). A tilt angle of 47.2° is required to bring the [210] zone of a goethite crystal imaged in [100] into line. The corresponding angle between [00.1] and [03.1] hematite zones was calculated at 47.4° .

The model for epitaxial twinning between goethite and hematite appeared to be consistent with the diffraction data for most of the crystals studied (this was especially obvious in products formed at pH 9). However, at high pH further evidence was obtained which pointed to the presence of short goethite overgrowths rather than obvious hematite centres in

Plate 27:- Hematite crystal (inset) formed at neutral pH in the absence of zinc. The diffraction pattern has been indexed, and the zone axis identified as [03.1].

Plate 28:- Twin crystal (inset) formed at pH 12 in the presence of 2.5 mol% zinc. The diffraction pattern is indexed in accord with goethite imaged in [210], but the crystal centre may comprise hematite. The pattern shown in Plate 27 can be superimposed, illustrating the [210]/[03.1] goethite/hematite equivalence allowed for the model used.

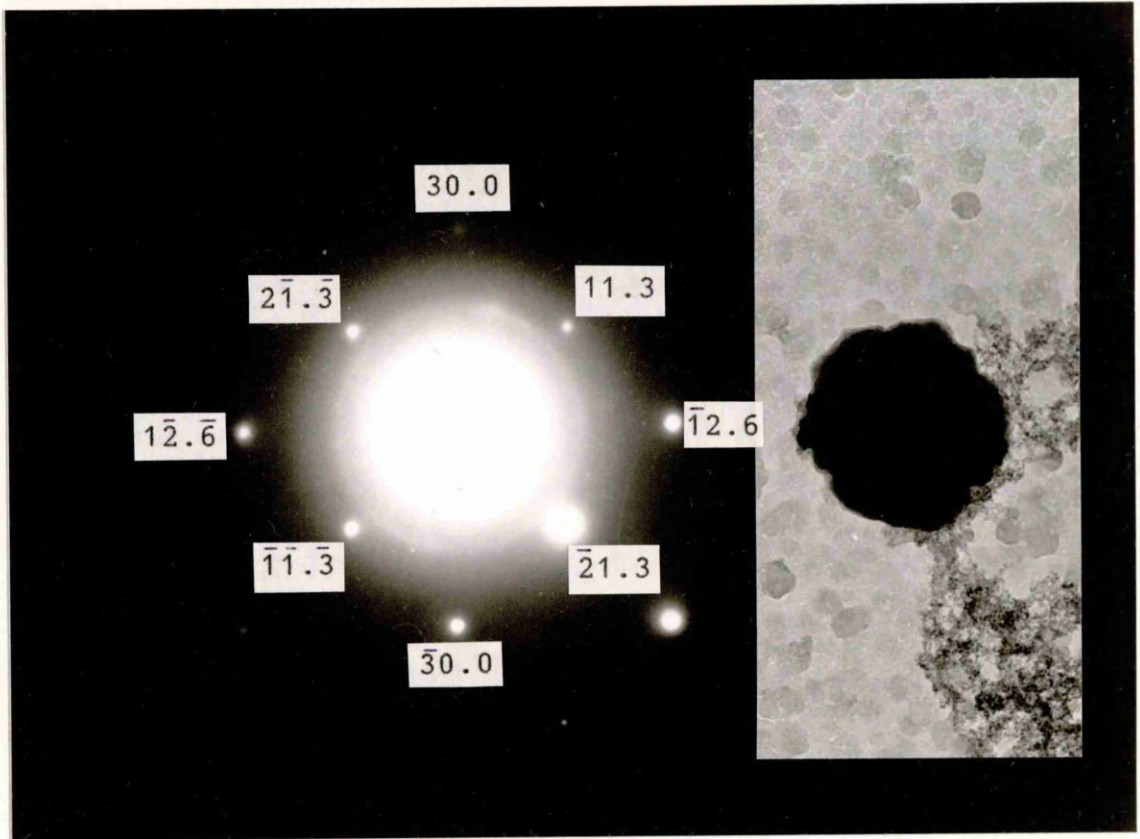


Fig. 1. Electron diffraction pattern of a spherical particle.

Fig. 2. Micrograph of a spherical particle.

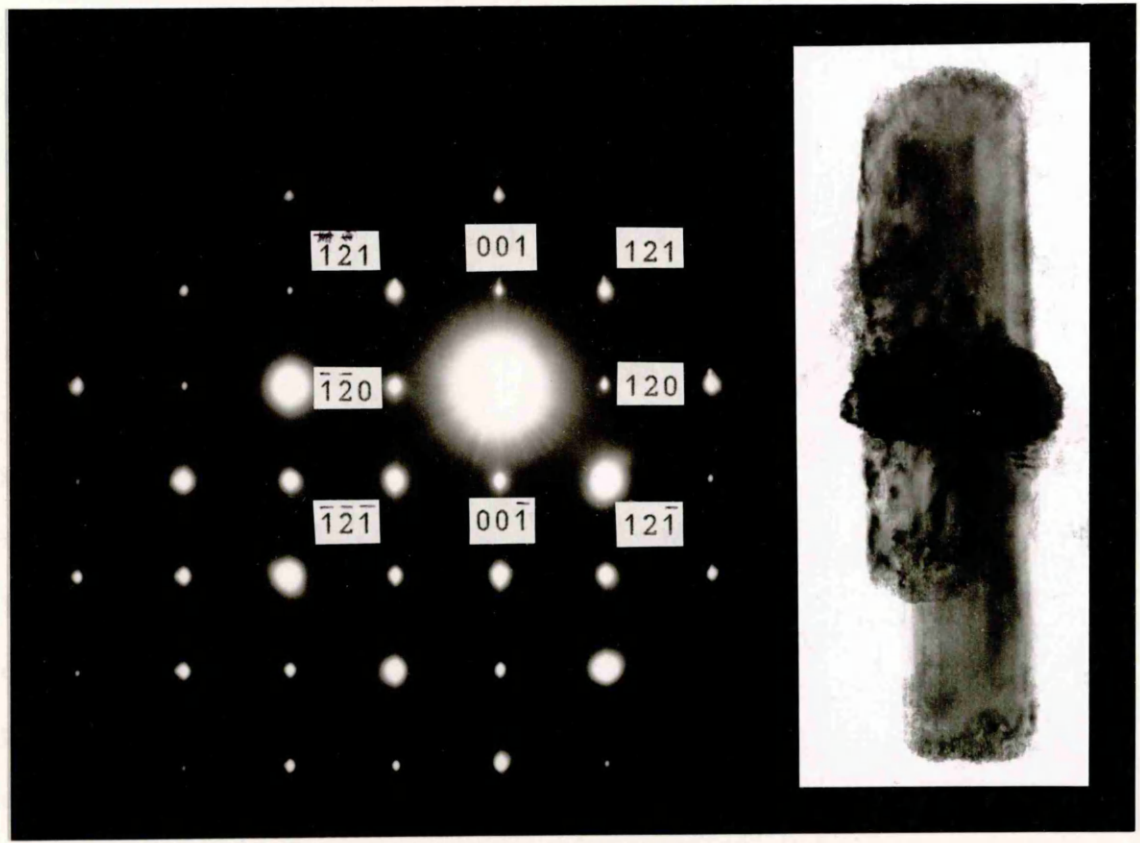


Fig. 3. Electron diffraction pattern of a cylindrical particle.

Fig. 4. Micrograph of a cylindrical particle.

many of the twin crystals. Plate 29 (inset) shows the central area of an acicular crystal formed in the presence of 5 mol% zinc at pH 12. Lattice fringes measured at 0.5nm and 0.25nm, corresponding to (020) and (021) goethite spacings, are indicated in the magnified area shown in the main Plate. The zone axis was identified as [100]. Over the boundary between the main acicular arm and the central area, the (020) lattice fringes appear to be coherent and continue over this region. Additional 0.5nm spacings were also resolved at 60° to those on the acicular arm (c.f. "star" twins). The centre is more likely to comprise an overgrowth of goethite rather than an area which could be identified as hematite.

If the level of zinc addition was raised to between 5 and 7.5 mol% or above, goethite was almost solely found to be present as twins, predominantly in the form of "star-shaped" crystals (Plate 30). These twins were similar in morphology to those observed in control samples formed at pH 9, although the crystals were often very thick and gave poor diffraction patterns. Fig. 3.8 shows a typical EDX profile obtained for one of the above twins. These results indicated that zinc had not been incorporated in either the arms or the central area of these crystals, but remained associated with the unconverted ferrihydrite. In addition to the twins described above, a proportion of long, thin crystals were also observed in these products (Plate 30, arrowed). Previous TEM studies carried out on goethite samples produced under unfavourable growth conditions (often in the presence of additive species) have shown a pronounced increase in the length:width ratio

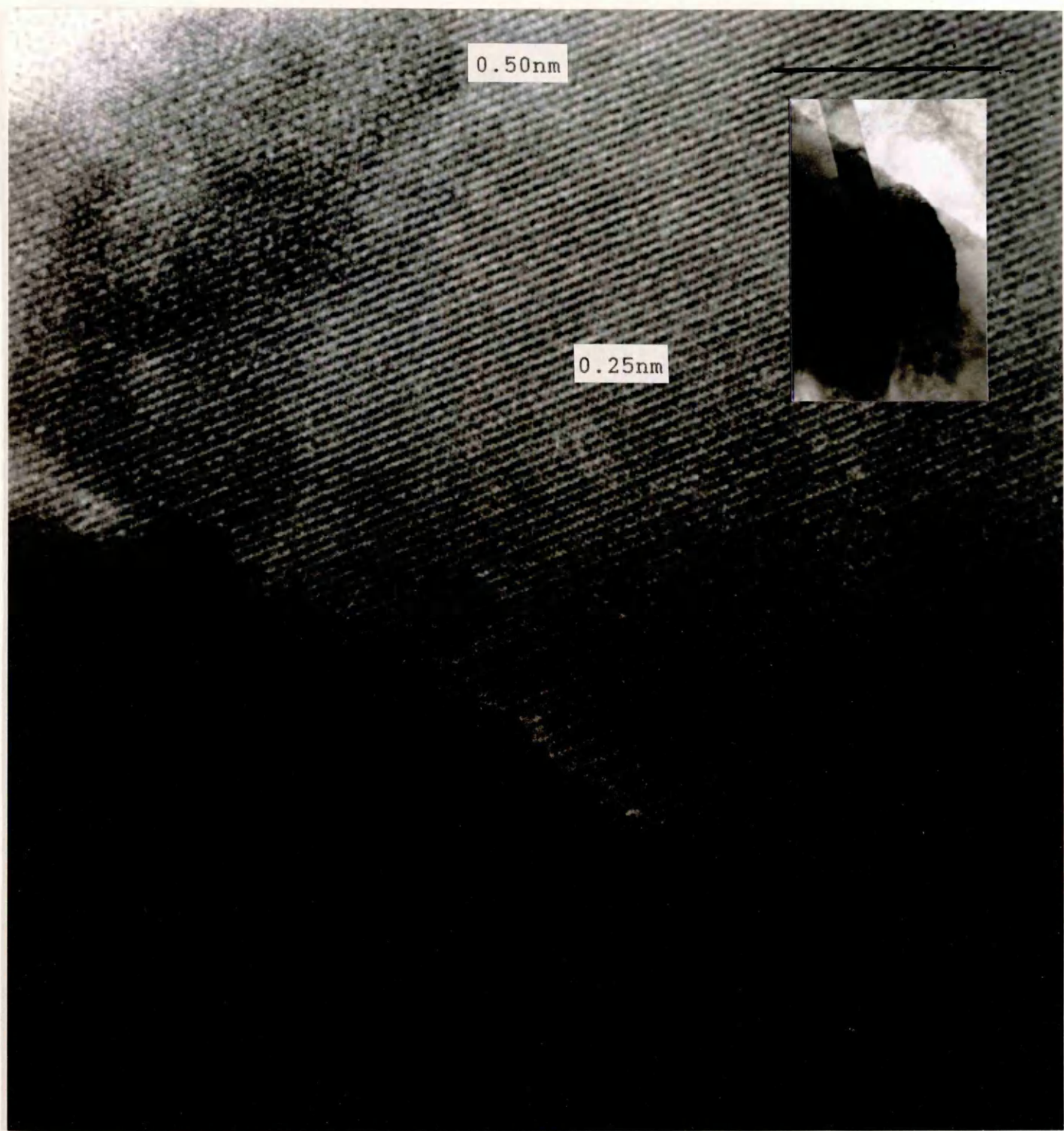


Plate 29:- Twin crystal, identified as goethite imaged in [100]. Lattice resolution over the central area suggested that this region comprised goethite rather than hematite. Scale bar represents 20nm.

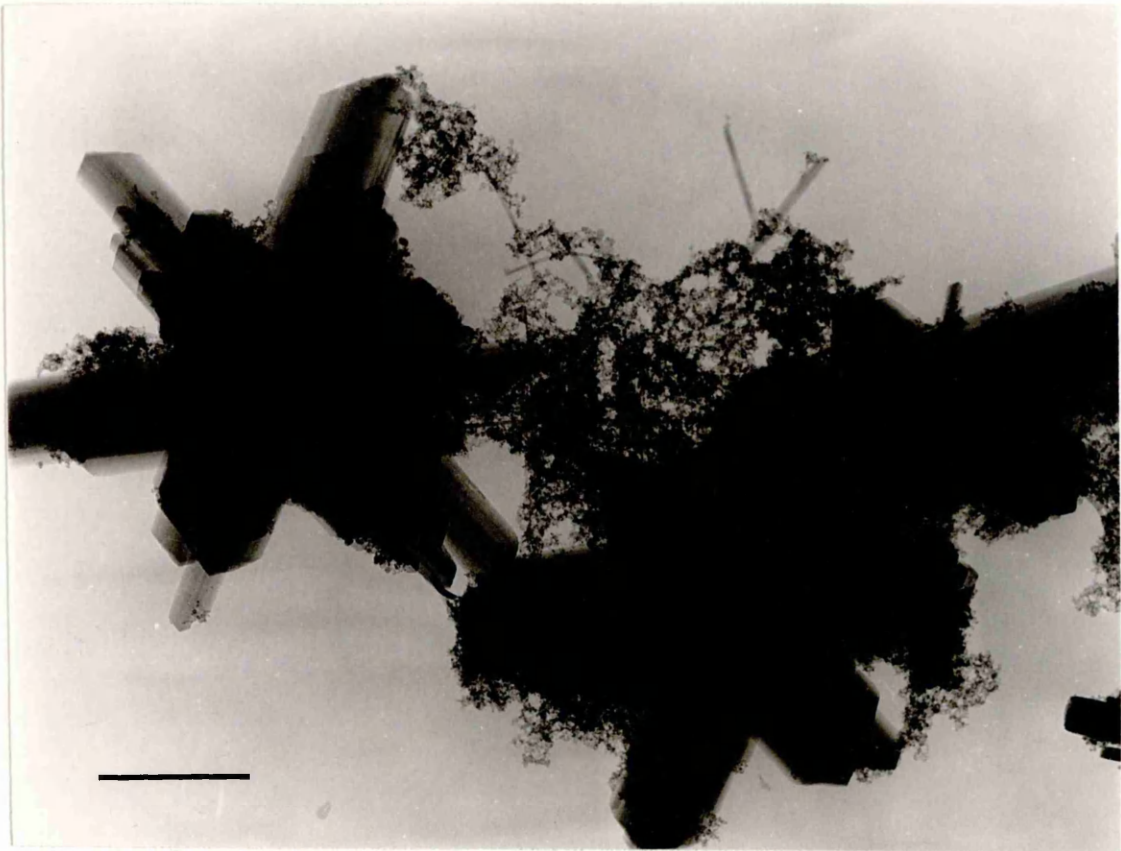


Plate 30:- Star twins formed at pH 12 in the presence of 7.5 mol% zinc, together with some long, thin needles and unconverted ferrihydrite. Scale bar represents 200nm.

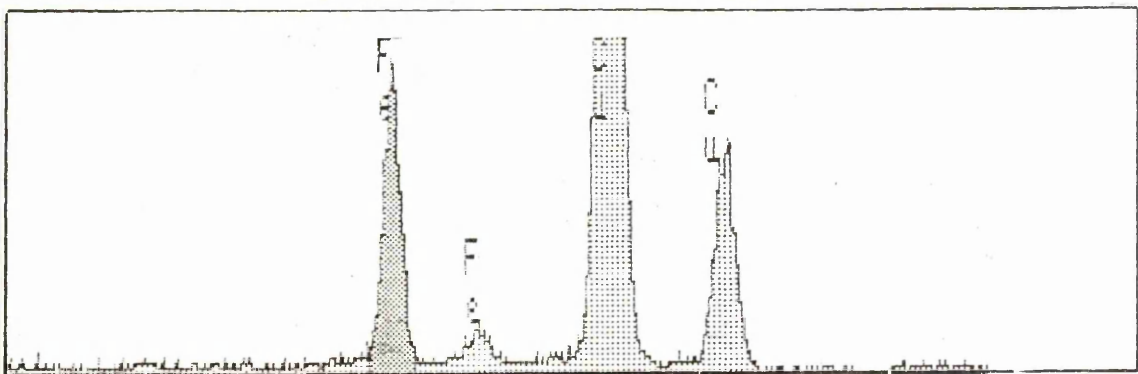


Fig.3.8:- EDX profile for one of the above twins.

relative to that observed in control samples [57,68]. However, in the present work, the above products are found to contain both very large star twins and more poorly-crystalline thin fibrils. This observation can be explained if the two morphologies are considered as arising via different mechanisms. Cornell and Giovanoli [57] suggested that twin nucleation was facilitated by the development of ordered regions within ferrihydrite. Formation of these "nuclei" will become competitive with that of single crystals (formed in solution) if dissolution of the precursor is sufficiently inhibited. In this study, it is the presence of zinc which strongly retards the transformation at pH 12. In the extended induction period during which crystal nucleation occurs, the reduced level of ferric species released into solution would inhibit formation of goethite nuclei and allow, either directly or indirectly, formation of "twin nuclei". During the subsequent growth stage there will therefore be fewer single crystals produced.

It has previously been suggested that the reduced width to length ratio often observed for goethite formed in the presence of certain cationic species may be caused by additive adsorption on the growing crystals. However, there is also evidence that increased width (and therefore number of intergrowths) is dependent on a high concentration of ferric species in solution, allowing secondary nucleation on [100] faces. In this case, the strongly-adsorbing zinc species may affect the morphology of single goethite crystals indirectly through inhibiting ferrihydrite dissolution, rather than

directly through interaction with the crystals. The level of zinc associated with unconverted ferrihydrite, and the absence of incorporated additive species in goethite, is in accord with this mechanism.

3.4. DEVELOPMENT OF ZINC-MAGNETITE.

As described in Section 3.2, the presence of a sufficient proportion of zinc (about 7-8 mol%) led to the formation of what would nominally be termed zinc-magnetite ($ZnFe_2O_4$) in products formed at pH 7 to 12. Samples shown by XRD to contain some proportion of the spinel phase were next prepared for further examination in the TEM, where the crystals were characterised using a combination of electron diffraction data, EDX analysis and high-resolution imaging.

Micrographs which showed resolution of lattice fringes were transferred to computer using a video camera, thus allowing processing operations to be carried out on the images using the SEMPER system. In order to increase the accuracy of measurement, d-spacings were determined from power spectra generated for each image.

Results indicated that spinel nucleation, growth and final stoichiometry were influenced by the proportion of additive present in the initial gels, and the pH at which the transformation was carried out. The following section is divided into two parts. The nature of the individual spinel crystals is first discussed, with respect to the levels of additive incorporated, morphology adopted, etc. Secondly, the "background" material present in the products is examined

in order to determine whether any obvious structural changes occurred in individual ferrihydrite platelets during ageing.

3.4.1. TRANSFORMATION AT pH 9-12

3.4.1.a) CHARACTERISATION OF SPINEL CRYSTALS.

Analysis of samples produced at pH 9 and 12 showed that, depending on the ageing conditions, goethite, hematite and the spinel phase were all potential products.

At pH 9, products formed in the presence of up to 15 mol% zinc were found to comprise what appeared to be unconverted ferrihydrite (Section 3.4.1.b), hematite, and (above 7 mol% addition) a proportion of spinel crystals which exhibited a characteristic cubic or rhombohedral morphology (Plate 31). These were found to be up to 40nm in diameter. If the level of zinc present was raised from 7 to 15 mol%, spinel twin formation appeared to become increasingly common. Many of the crystals examined were found to contain two or more twin planes (Plate 32, arrowed).

Fig.3.9 shows a typical EDX profile obtained for an individual spinel crystal (in this case formed at pH9 in the presence of 12.5 mol% zinc). The measured mass concentration ratio, $C_{Zn}/C_{Fe}=0.45$, corresponds to approximately 28 mol% substituent incorporation in the structure (5 mol% less than that required for the stoichiometry $ZnFe_2O_4$). Taking the accuracy of the analytical technique into account it cannot be stated with certainty in this case that the proportion of zinc present in the crystal is insufficient for full substitution. However, concentration ratios as low as 0.3,

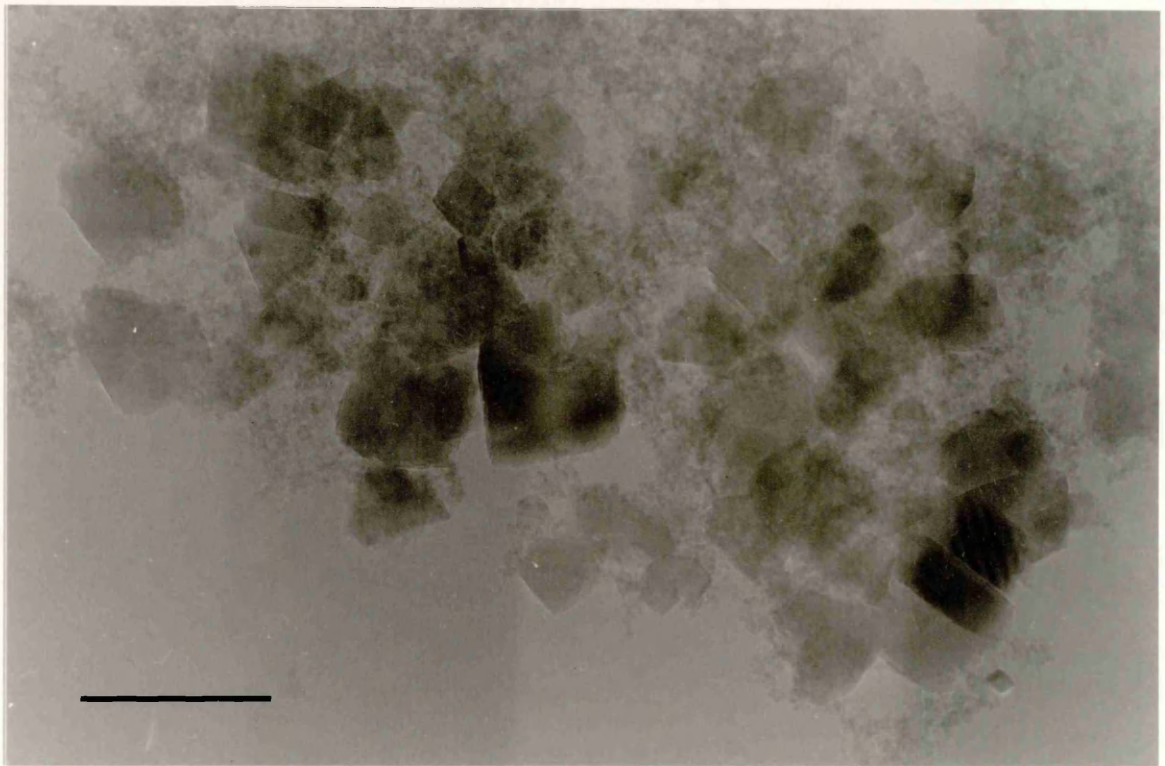


Plate 31:- Single spinel crystals formed at pH 9 in the presence of 7.5 mol% zinc. Scale bar represents 50nm.

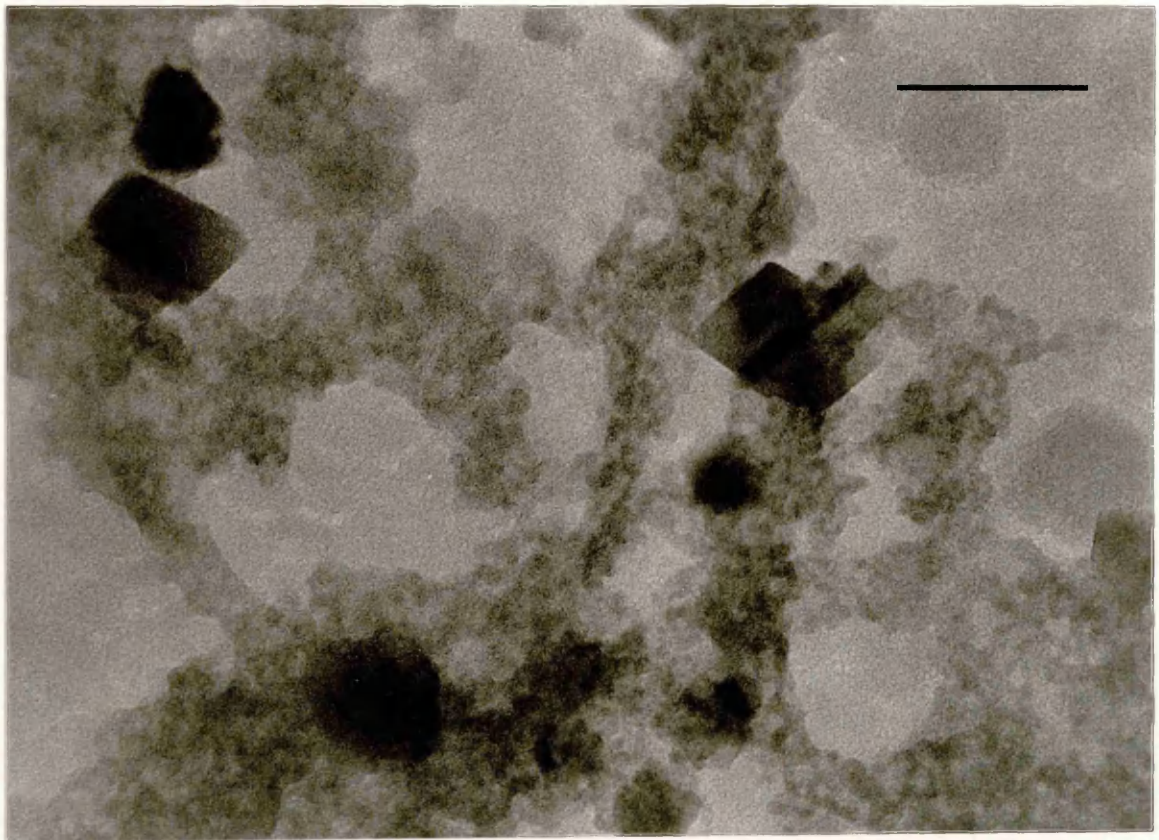


Plate 32:- Mixture of single and twin spinel crystals formed at pH 9 in the presence of 12.5 mol% zinc. Scale bar represents 50nm.

equivalent to 17 mol% additive incorporation, were obtained for individual crystals formed in the presence of up to 15 mol% zinc. These values are definitely consistent with a defect spinel structure. A full treatment of zinc distribution in the spinel phase is given in Section 3.5.

If the gel pH was raised to 12, the formation of zinc-magnetite appeared to be slightly less favoured; well-defined spinel crystals were observed in samples produced in the presence of about 8 mol% zinc (c.f. >7 mol% at pH 9). However, the spinel morphology in each subsequent product was found to be comparable to that observed in the corresponding sample produced at pH 9.

Raising the proportion of zinc in the precipitates above 10 mol% led to increased spinel nucleation. A subsequent reduction in the average crystal dimensions was observed in products formed at pH 9 and 12. Products formed on ageing ferrihydrite gels containing 25-50 mol% zinc were found to comprise only small spinel crystallites up to a maximum 10-15nm in diameter (Plate 33).

Plate 34 shows a typical selected-area diffraction pattern obtained for aggregated spinel crystals formed at pH 12 in the presence of 50 mol% zinc. In Table 3.6, the measured spacings are compared with available XRD data for zinc-magnetite. At lower levels of addition (up to about 20 mol%), the diffraction patterns exhibited a much wider range of spacings, suggesting that the particles became more uniform as the average size decreased. Plates 35 and 36 show, respectively, diffraction patterns obtained for products formed

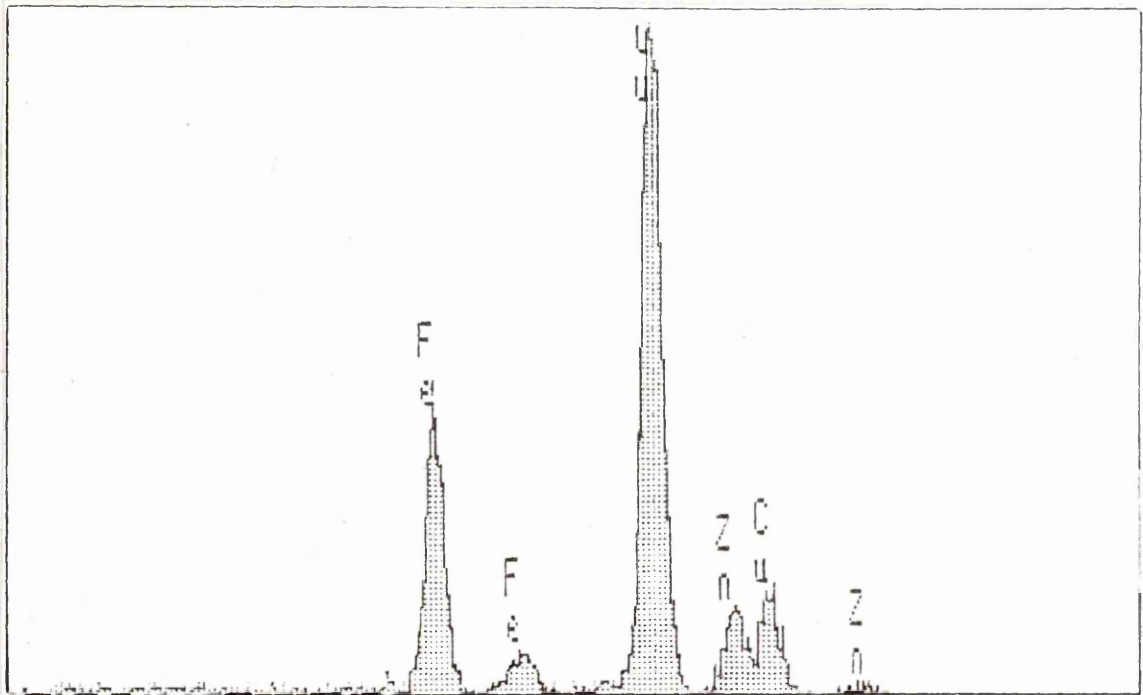


Fig.3.9:- EDX profile for arrowed spinel crystal shown in Plate 34.

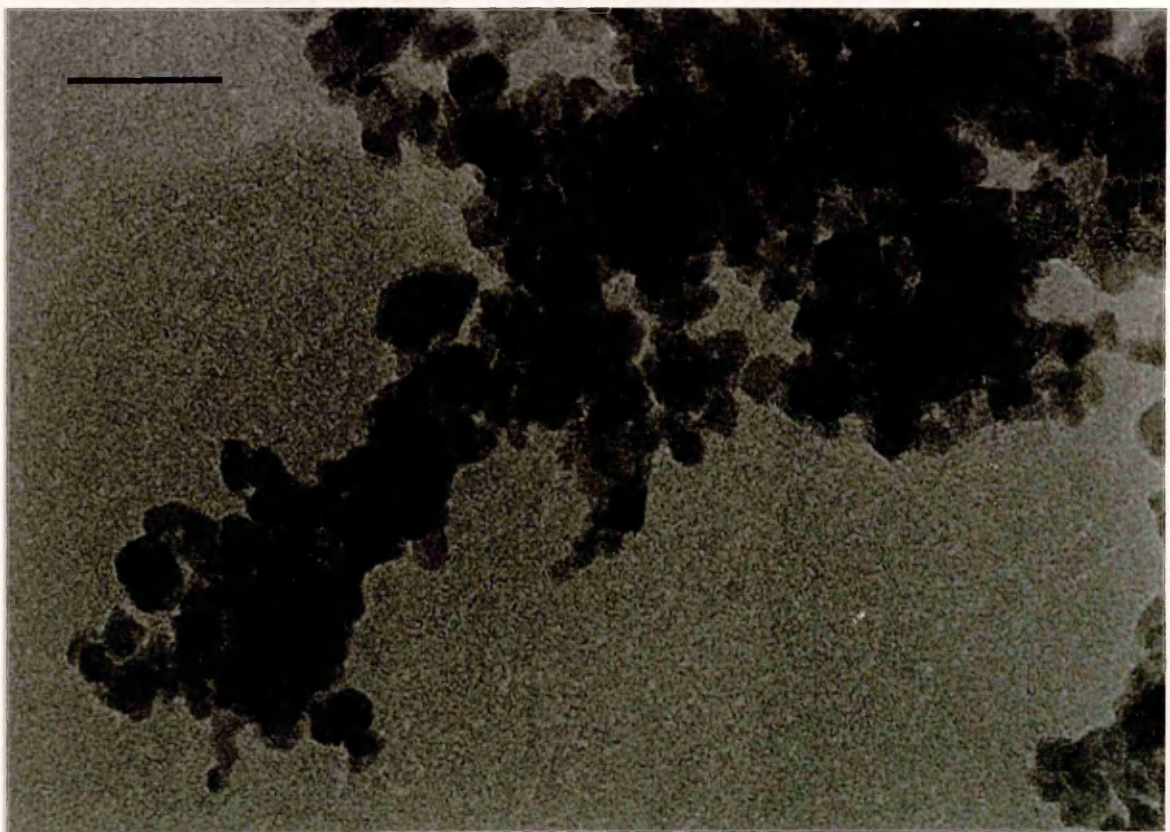


Plate 33:- Spinel crystals formed at pH 12 in the presence of 50 mol% zinc. Scale bar represents 25nm.

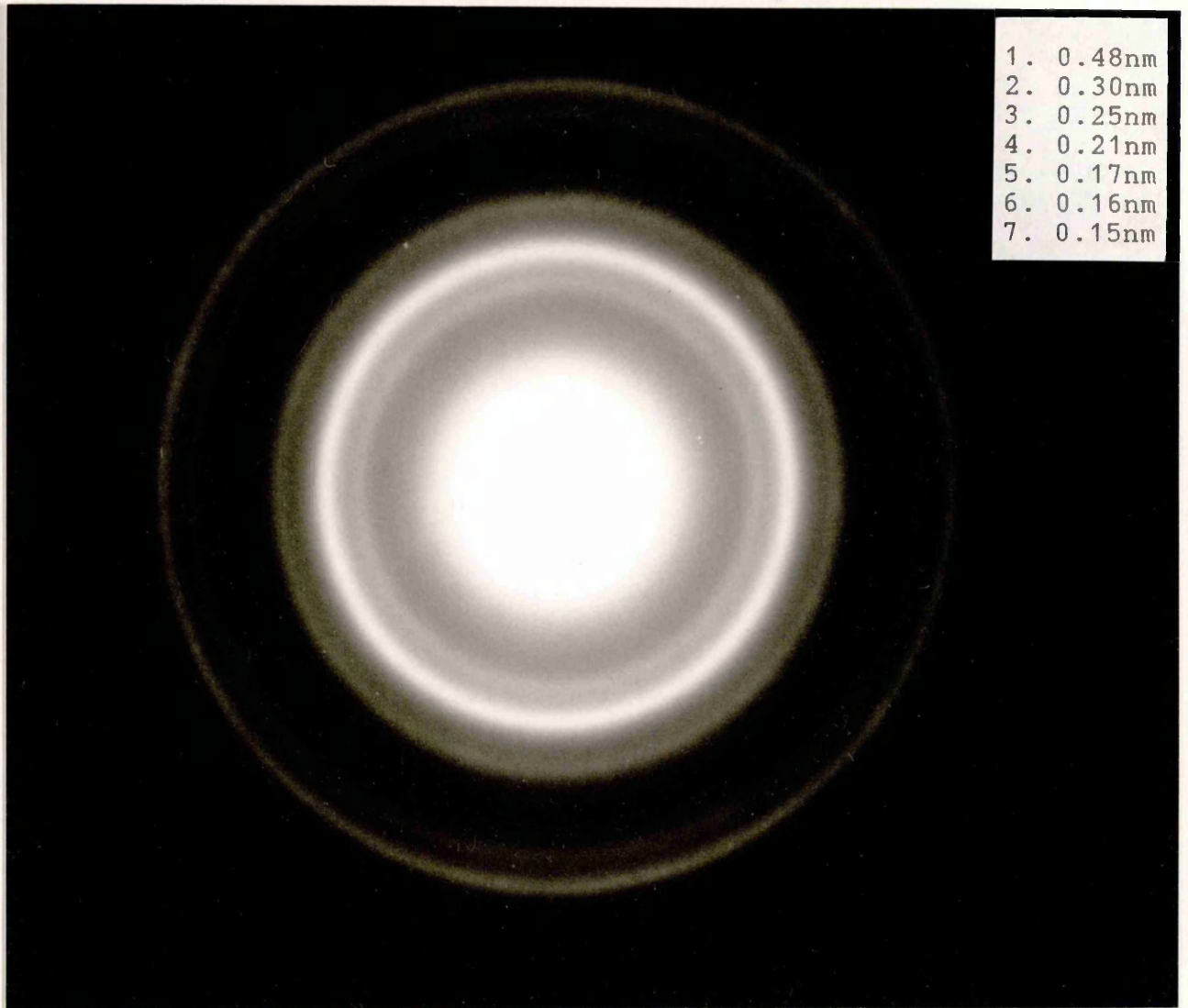


Plate 34:- Selected-area diffraction pattern obtained for the spinel sample shown in Plate 33.

ZINC-MAGNETITE			EXPTL VALUES
d (nm)	I/I ₀	(hkl)	d (nm)
0.485	20	111	0.48
0.299	50	220	0.30
0.254	100	311	0.25
0.243	10	222	
0.210	40	400	0.21
0.172	40	422	0.17
0.162	70	333	0.16
0.149	80	440	0.15

Table 3.6:- Comparison of measured d-spacings with expected values for zinc-magnetite.

at pH 9 in the presence of 12.5 and 15 mol% additive. In addition to the expected range of values, a number of extra spacings were observed which often appeared to be forbidden for the face-centred spinel phase ZnFe_2O_4 . The oxide belongs to the space group $O_h^7 \text{Fd}3m$, reflection conditions for which are shown in Table 3.7.

indices are permutable	General conditions
hkl	$h+k=2n$ and $h+l, k+l=2n$
0kl	$k+l=4n$ and $k, l=2n$
hhl	$h+l=2n$
h00	$h=4n$

Table 3.7:- Reflection conditions for the Space Group $O_h^7 \text{Fd}3m$.

Table 3.8 shows the range of experimentally-measured spacings obtained from Plates 35 and 36, together with all possible reflections for zinc-magnetite down to 0.14nm, including those arising from forbidden combinations of indices. Although the above electron diffraction data suggested that some deviation from the expected cubic symmetry may be induced in the spinel crystals under certain growth conditions, the origin of the extra reflections is not certain. The range of samples produced at pH 9 for which obvious additional spacings were observed consisted of hematite, spinel crystals and a very small proportion of goethite (mostly present as short outgrowths on the large hematite crystals). Some smaller hematite or goethite particles may also have been present, unnoticed, in the products. It is possible that inclusion of such crystals in the selected areas for which the diffraction patterns were

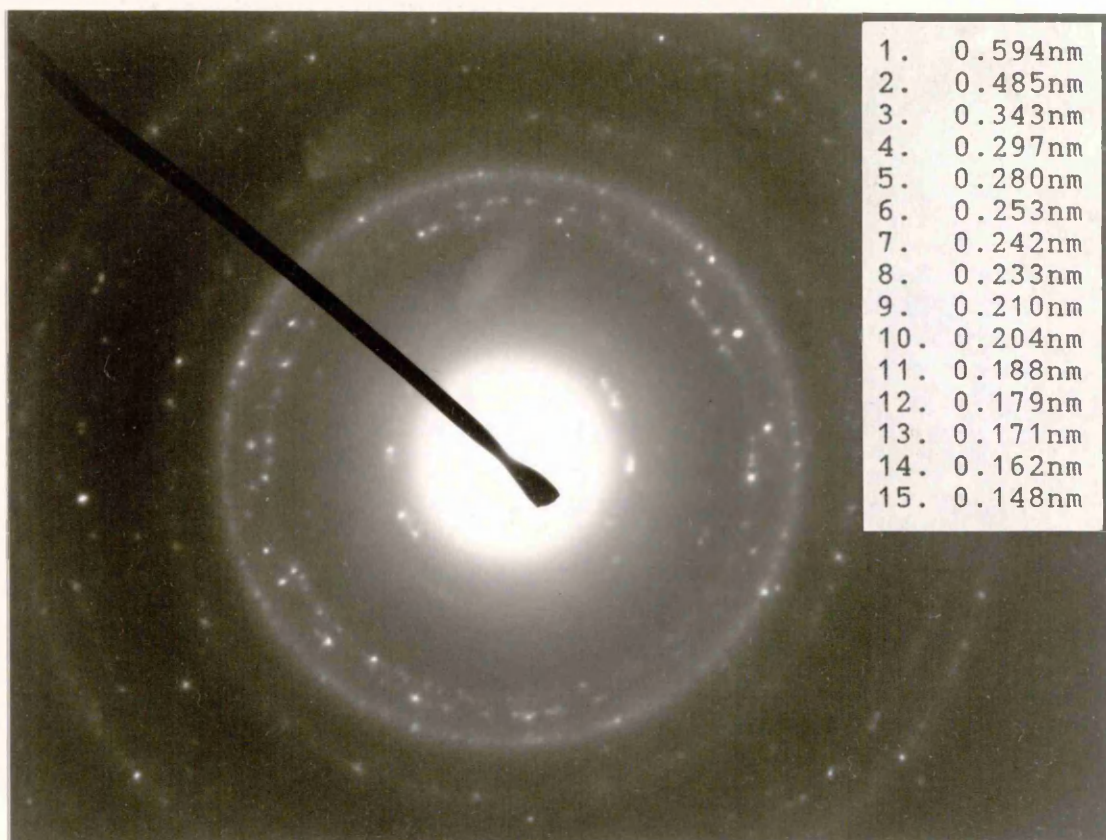


Plate 35:- Diffraction pattern obtained for aggregated spinel crystals formed at pH 9 in the presence of 12.5 mol% zinc.

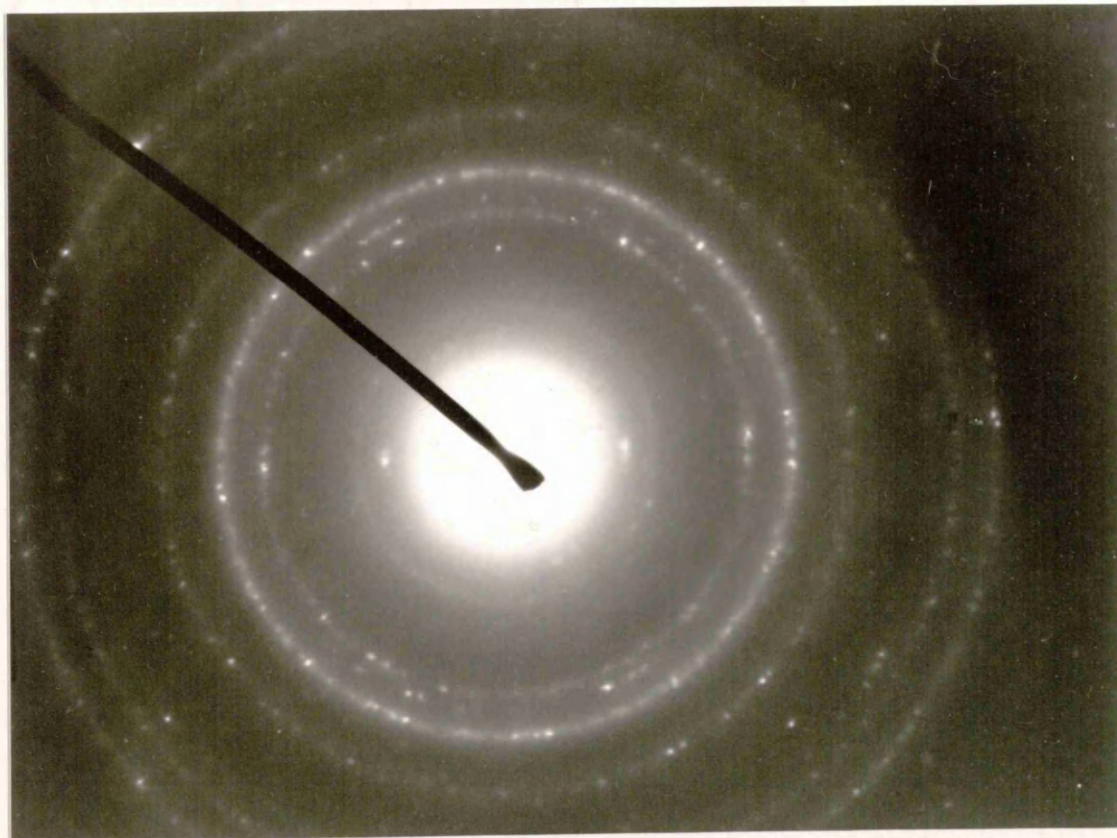


Plate 36:- Diffraction pattern obtained for spinel crystals formed at pH 9 in the presence of 15 mol% zinc.

(hkl)	d(nm)	EXPTL	(hkl)	d(nm)	EXPTL
100 *	0.84		400	0.21	0.21
110 *	0.594	0.59	410, 223*	0.204	
111	0.485	0.48	411, 330*	0.198	
200	0.42	0.42	331	0.193	
210 *	0.376		240	0.188	0.19
211 *	0.343	0.34	241 *	0.183	
220	0.297	0.30	233 *	0.179	0.18
221, 300	0.28	0.28	224	0.171	0.17
310 *	0.266	0.26	500 *	0.168	
311	0.253	0.25	510 *	0.165	
222	0.242	0.24	511, 333	0.162	0.16
230 *	0.233		520 *	0.156	
231 *	0.224		521 *	0.153	
			440	0.148	0.15

Table 3.8:- Comparison of d-spacings from Plates 35 and 37 with values for zinc-magnetite. Symmetry-forbidden reflections are marked with an asterisk.

obtained could explain the above results. However, many of the commonly-observed extra reflections (including 0.59nm, 0.35nm or 0.28nm) are not consistent with any of the possible spacings for either of the above phases. It is also conceivable that these spots could have arisen due to double diffraction. However, if the spacings were simply the result of geometrical effects then it would be expected that a similar range of spacings would be obtained for every spinel-containing product. This was not found to be the case. Lastly, since EDX data indicated that in each of these samples at least some proportion of the spinel crystals were deficient in zinc, there is the possibility that some degree of extended ordering is present, similar to the vacancy ordering in some unsubstituted maghemite preparations. The existence of a superstructure would be dependent on the fact that the spinel structure is not fully-substituted with respect to zinc since Zn^{2+} , as a d^{10} species, cannot exhibit a distorted co-ordination sphere. This is in contrast to Cu^{2+} which, as a d^9 species, is found to induce a tetragonal symmetry in stoichiometric $CuFe_2O_4$ [106].

In order to obtain more conclusive diffraction data, patterns were recorded (and corresponding EDX profiles taken in each case) for examples of individual spinel crystals formed at up to 15-20 mol% addition.

Results were difficult to obtain, partly due to the small particle sizes and degree of aggregation in the products, but mainly because the majority of crystals examined did not give a coherent set of diffraction spots from which a zone axis could be identified. Diffraction patterns recorded for the

singly-diffracting crystals were generally of poor quality but could still be indexed. However, in these cases little direct evidence was obtained to indicate the presence of symmetry-forbidden reflections. Plate 37 shows the diffraction pattern obtained for a spinel crystal (inset) which was formed in the presence of 12.5 mol% zinc at pH 9. This could be indexed in accord with ZnFe_2O_4 imaged in [110], which was found to be the most common orientation relative to the beam direction adopted by the singly-diffracting spinel crystals. The EDX profile obtained gave a mass concentration ratio $C_{\text{Zn}}/C_{\text{Fe}}=0.46$, corresponding to approximately 28 mol% zinc incorporation in the spinel structure.

Plates 38 and 39 show two further examples taken from the same sample. These patterns have also been indexed in accord with ZnFe_2O_4 crystals, imaged, respectively, in [112] and [332]. The corresponding EDX profiles gave ratios $C_{\text{Zn}}/C_{\text{Fe}}=0.44$ and 0.46 , corresponding to 27.2 and 28.4 mol% substituent incorporation in the crystals. It was found that reasonable diffraction patterns were generally obtained for those crystals containing the highest proportions of zinc.

In accord with the diffraction data described above, indexing of power spectra obtained from high-resolution images showing individual spinel crystals formed at pH 9-12 (see Fig. 3.10) gave no direct evidence for any deviation from cubic symmetry.

Although a large number of crystals were examined during the course of the work, clearly-resolved crossed lattice fringes were obtained only where the crystals were imaged in

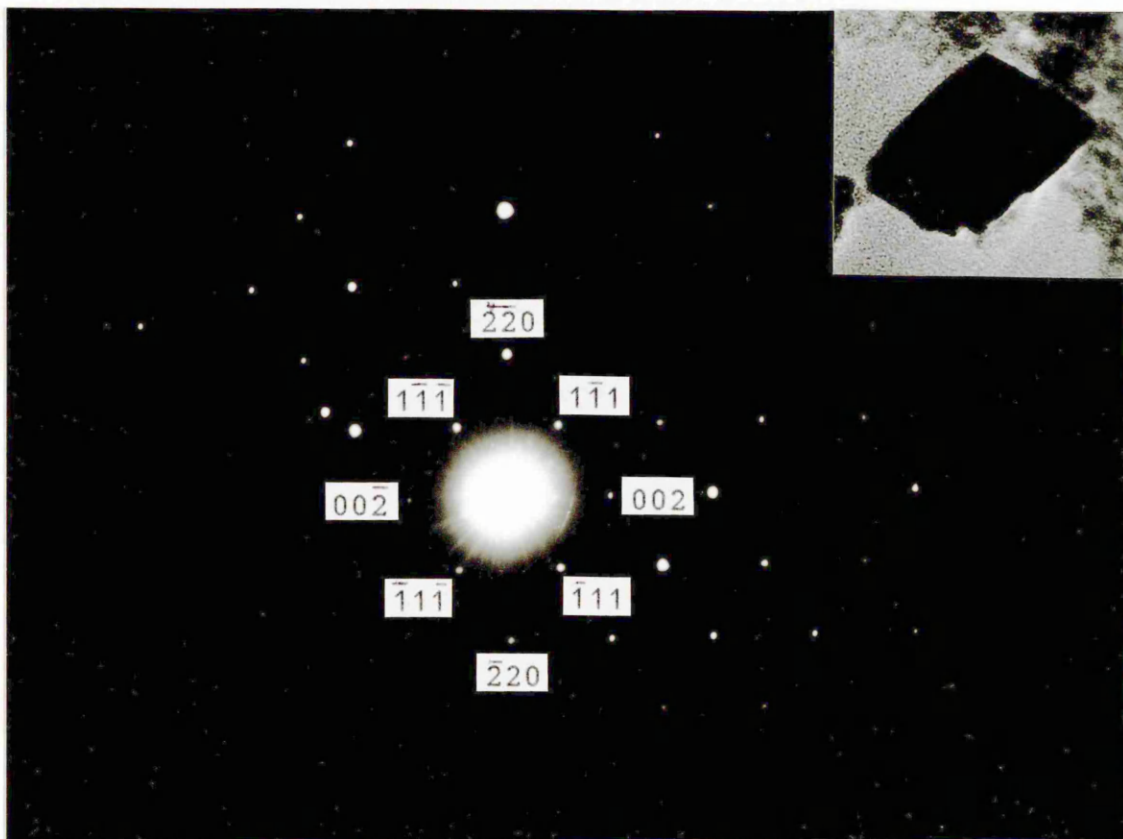


Plate 37:- Spinel crystal (inset) and corresponding diffraction pattern, indexed as zinc-magnetite imaged in $[110]$.

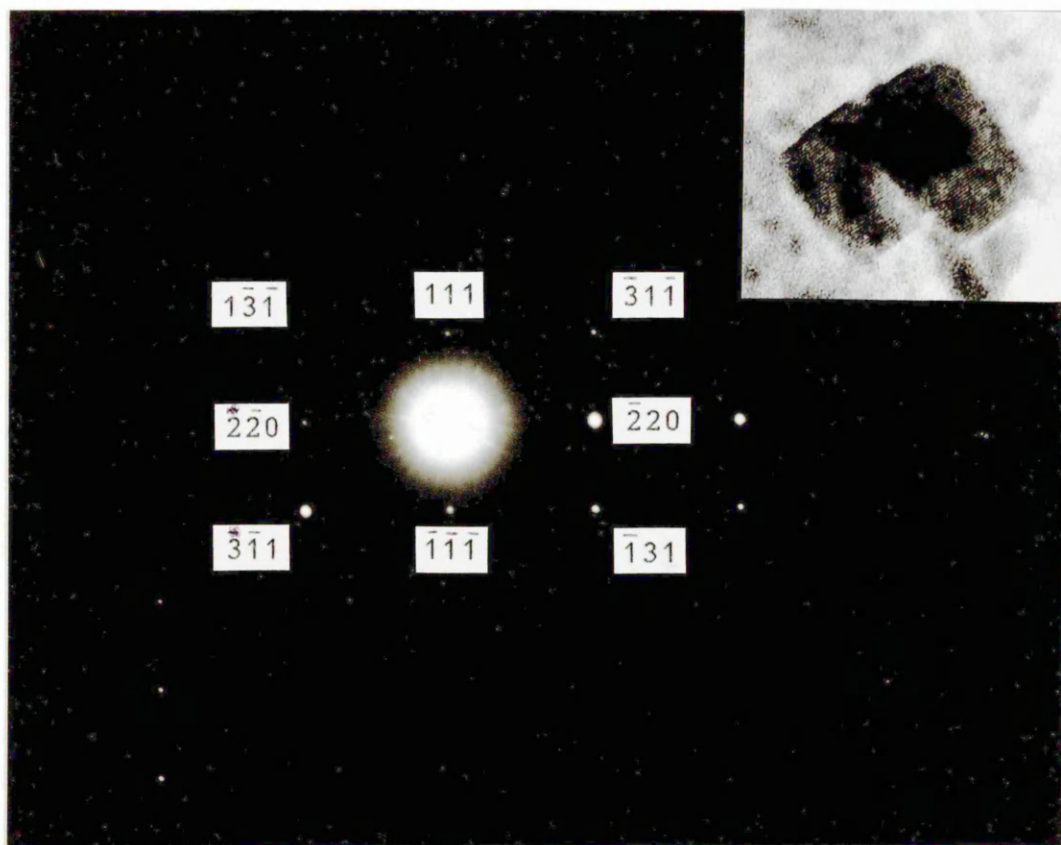


Plate 38:- Spinel crystal and corresponding diffraction pattern indexed as zinc-magnetite imaged in $[112]$.

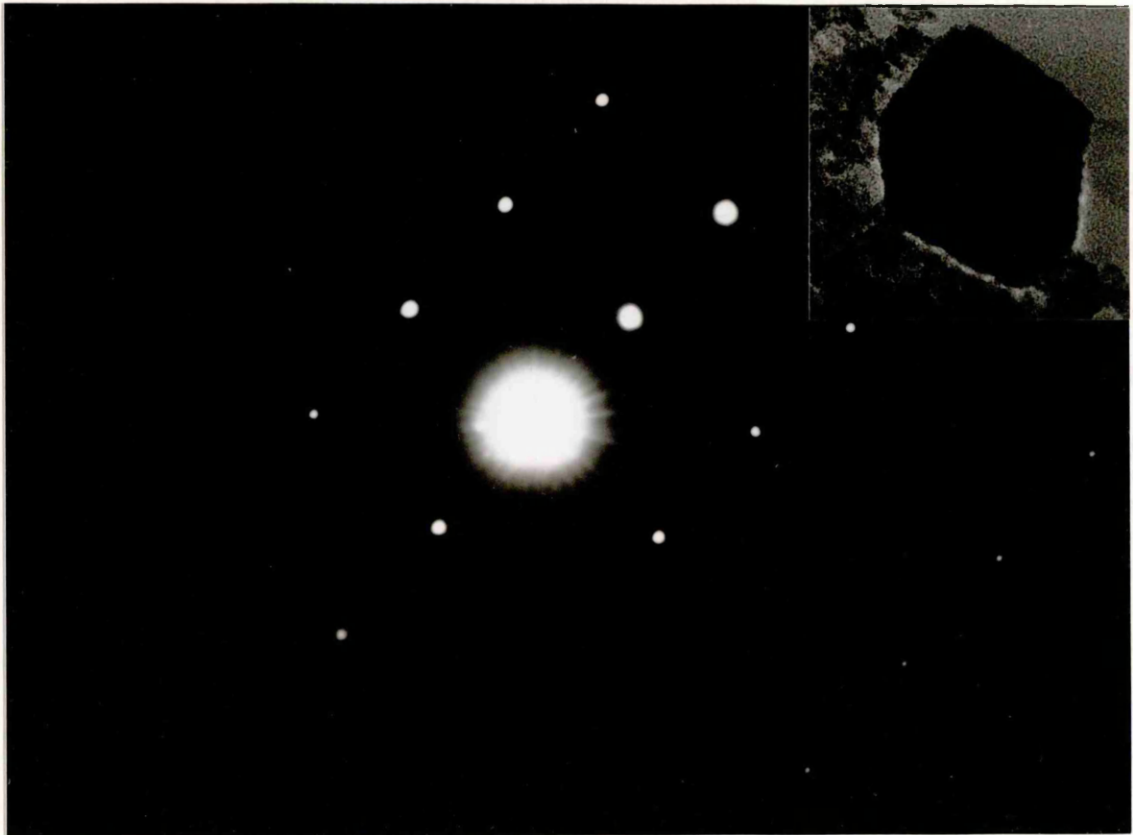


Plate 39:- Spinel crystal and corresponding diffraction pattern indexed as zinc-magnetite imaged in [332].

one of two zones. Plate 40 shows a single spinel crystal formed at pH 9 in the presence of 12.5 mol% zinc. Lattice fringes measured at 0.30nm, 0.48nm (at 35° to the 0.30nm spacing) and 0.42nm (at 90°) were obtained. These have been indexed as, respectively, (220), (111) and (002) reflections for cubic ZnFe_2O_4 imaged in [110]. This was also the most common zone axis identified in the s.a. diffraction work.

A second crystal from the same sample is shown in Plate 41. In this case, the resolved lattice fringes were measured at 0.48nm, 0.25nm (at 54°) and 0.30nm (at 90°). These values are consistent with (111), (311) and (220) reflections for a cubic crystal imaged in [112]. In most cases, as illustrated by both of the above Plates, the spinel crystals did not exhibit a granular appearance, and were free from surface defects. The edges generally terminated in well-developed (111) faces.

Plate 42 shows a spinel crystal formed at pH 9 in the presence of 15 mol% zinc, and which contains a single twin plane. Lattice spacings for the left and right halves were measured at, respectively, 0.29nm, 0.48nm (at 35°), 0.41nm (at 90°) and 0.48nm (at 145°); and 0.29nm, 0.48nm (at 35°), 0.41nm (at 90°) and 0.48nm (at 145°). The power spectrum therefore consisted of two superimposed mirror-image patterns which could be indexed such that both sides of the crystal were imaged in [110]. The twin plane common to all of these crystals was found to be (111) (a twin law common to spinels). Plate 45 shows a typical selected-area diffraction pattern obtained for this twin type.

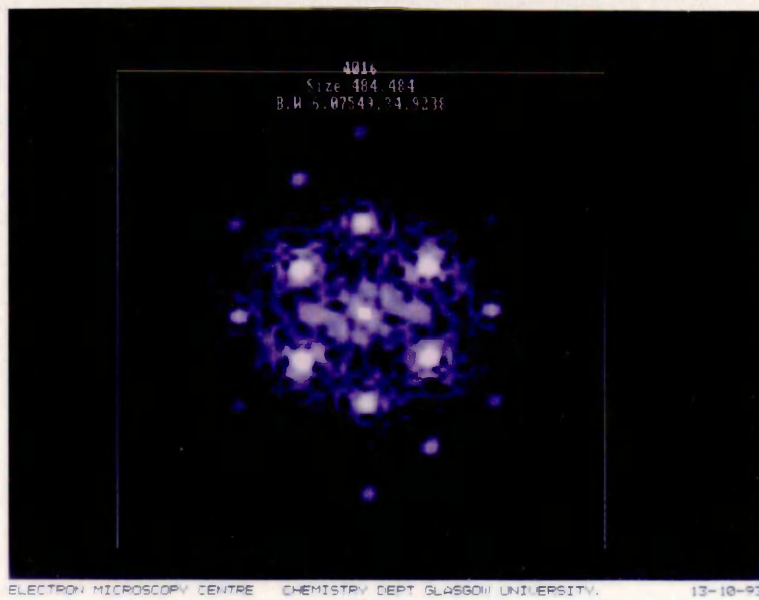


Fig.3.10:- Typical power spectrum obtained from a high-resolution image of a spinel crystal (in this case consistent with zinc-magnetite imaged in [110]).

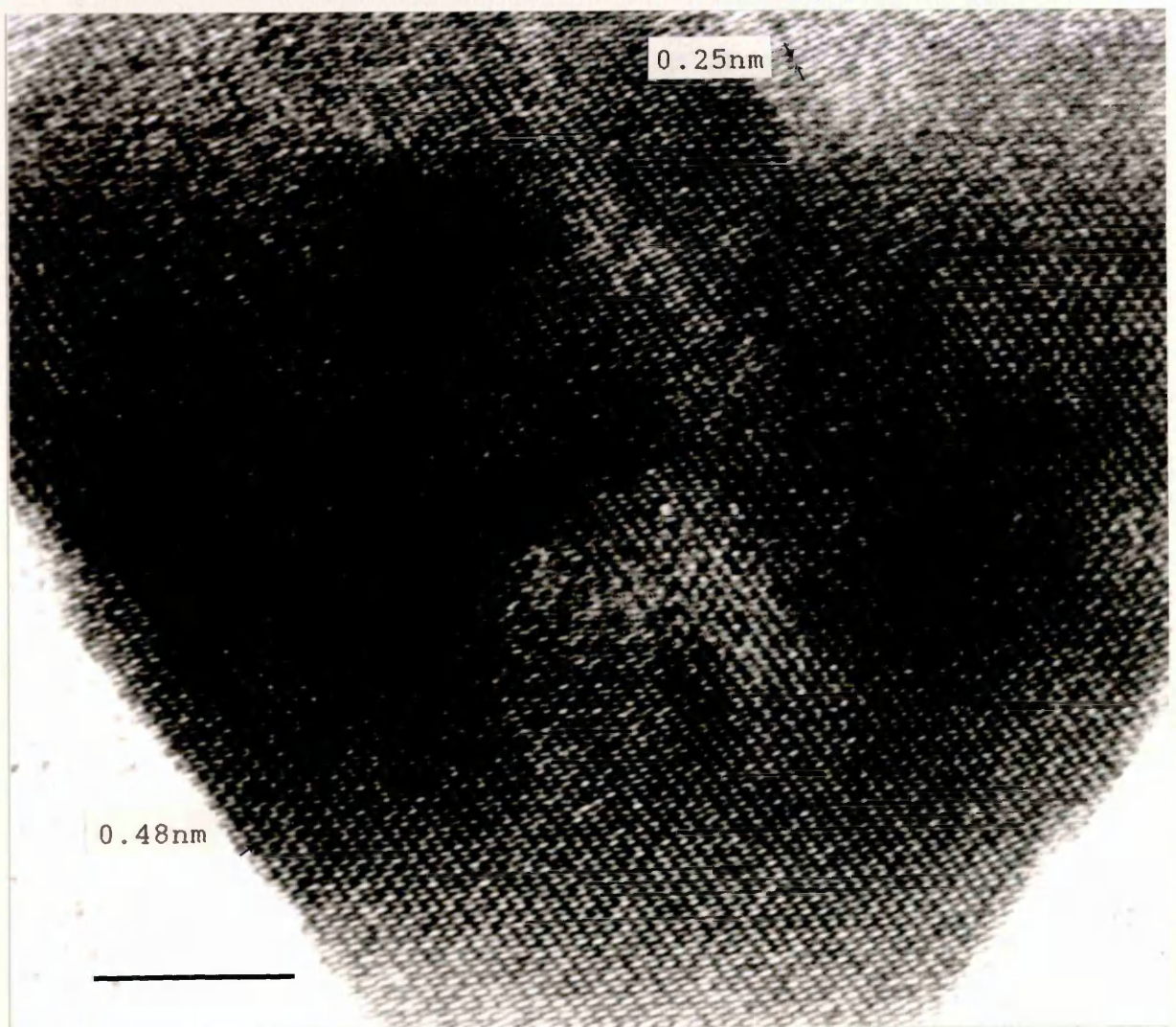


Plate 40:- Single spinel crystal formed at pH 12 in the presence of 10 mol% zinc. Lattice spacings and angles are consistent with imaging in [110]. Scale bar represents 10nm.

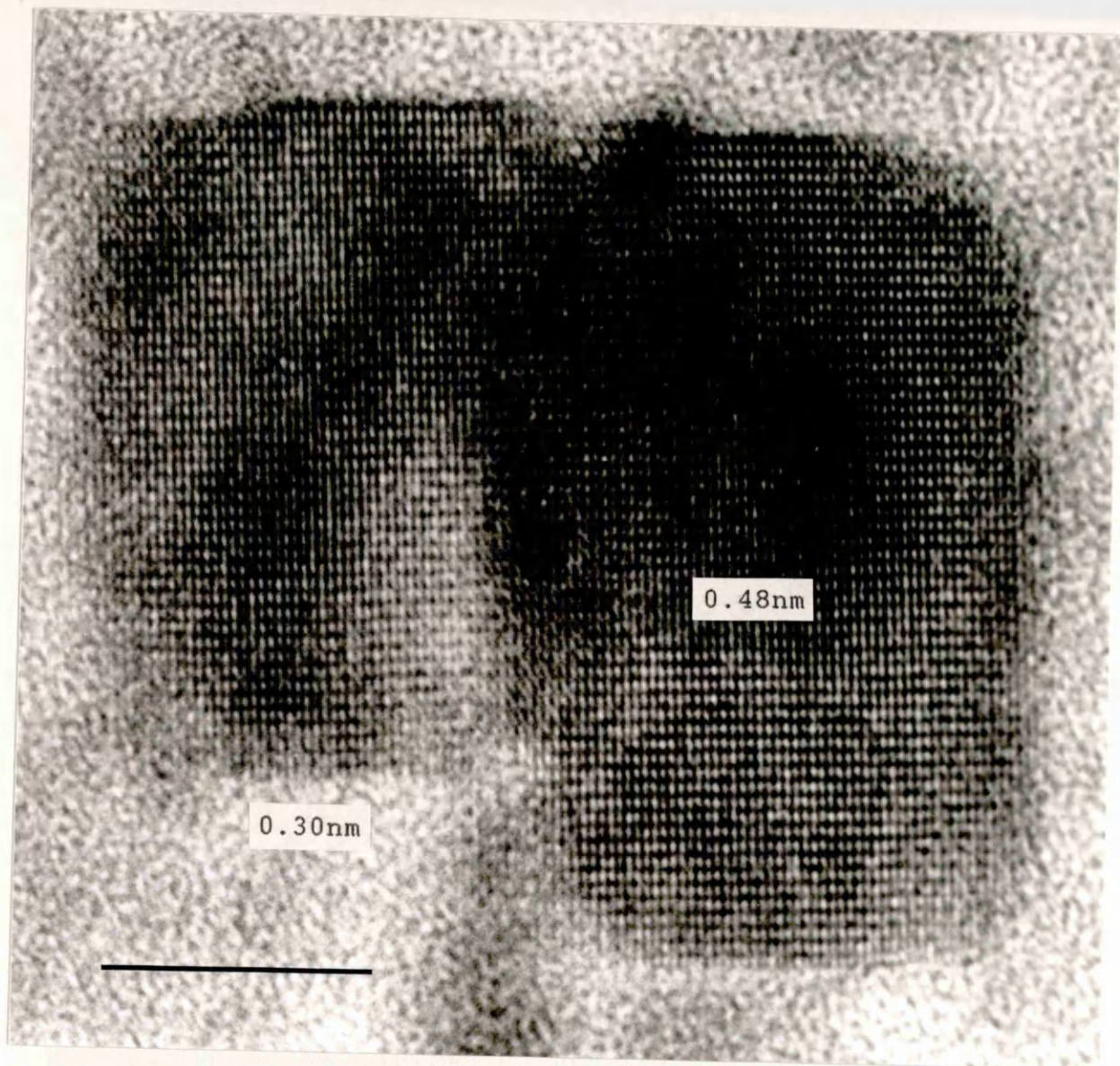


Plate 41:- Single spinel crystal formed at pH 12 in the presence of 10 mol% zinc. The zone axis was identified as [112]. Scale bar represents 10nm.

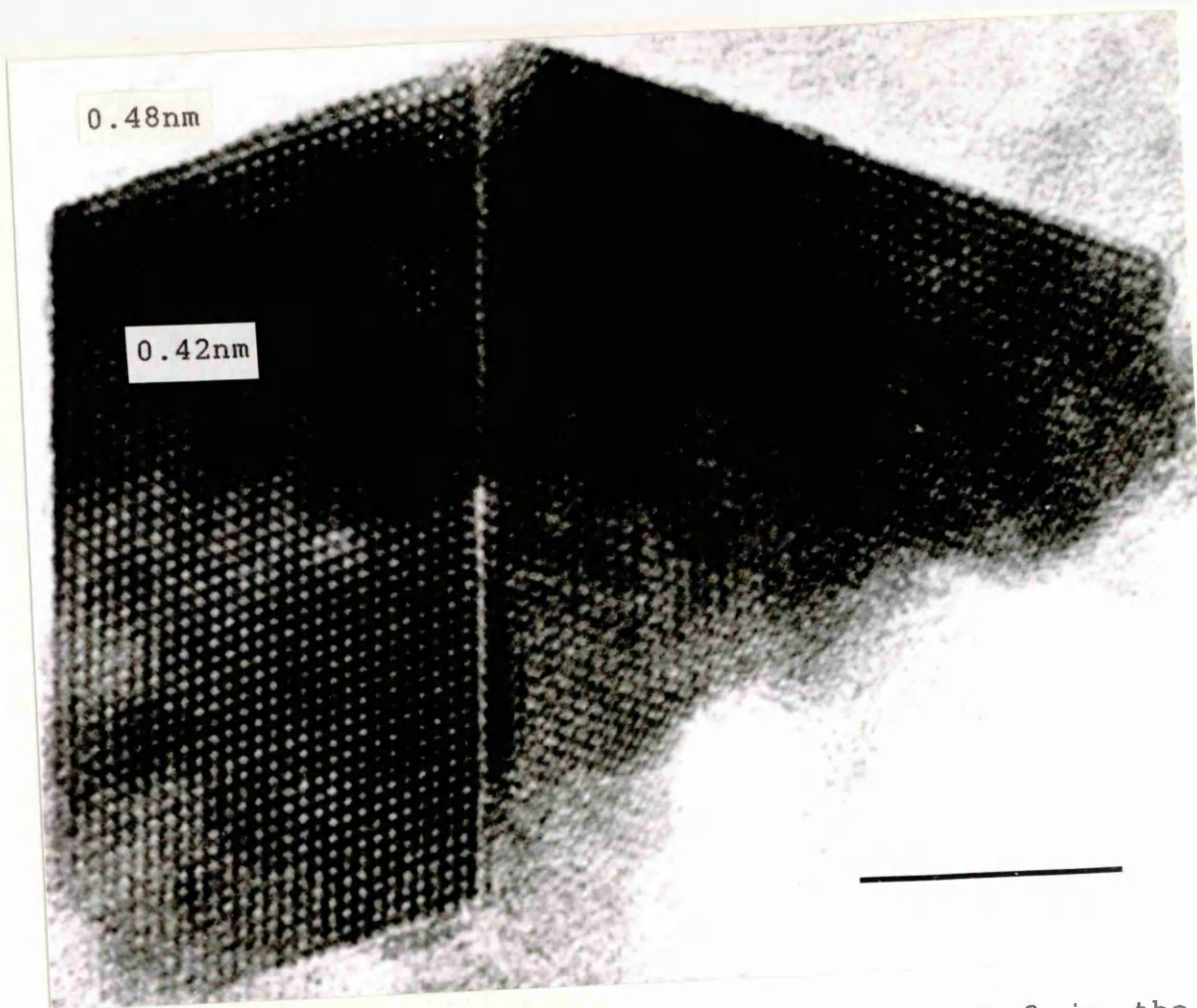


Plate 42:- Twinned spinel crystal formed at pH 9 in the presence of 15 mol% zinc. Scale bar represents 10nm.



Plate 43:- Typical selected-area diffraction pattern obtained for a twinned spinel crystal imaged in [110].

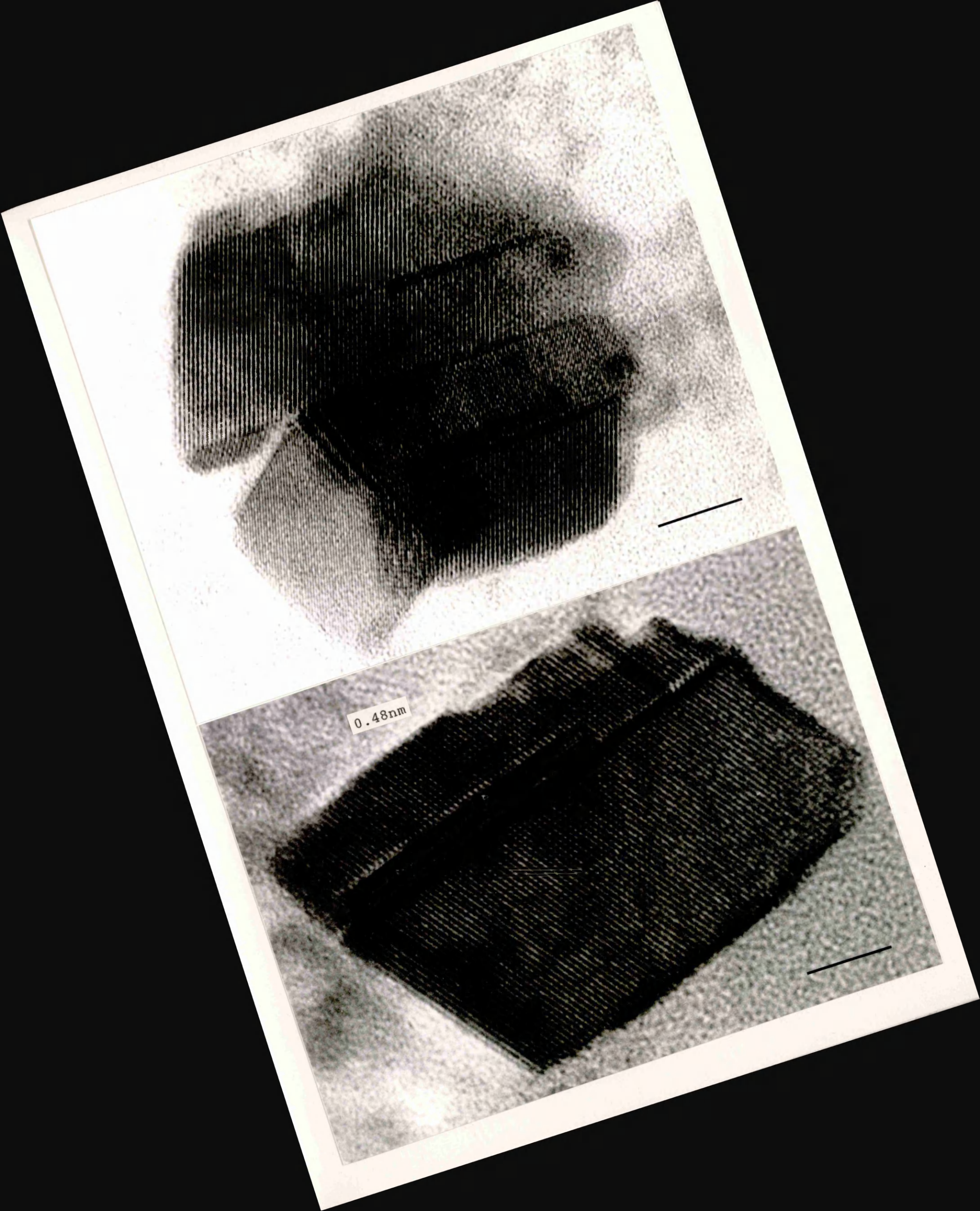
Individual crystals occasionally exhibited a higher degree of twinning than that shown above. An extreme example is shown in Plate 44, in which multiple planes are present. Each area of the crystal is again imaged in $[110]$. The presence of several thin twin bands over a small area in an essentially single crystal was also a commonly-observed feature (Plate 45). The edges of many of the particles imaged had in this way developed a "stepped" appearance.

The stacking sequence of oxygen layers in the neighbourhood of a twin plane will be ABCABACBA. The cation occupancy of the co-ordination polyhedra in and on either side of the plane can vary. In some spinel structures, twinning similar to that shown in Plate 45 (but extended over large areas) is carried out regularly, clockwise alternating with anticlockwise, so that a new structure is generated $[107]$.

The degree of accuracy in the measurement of lattice fringes (and associated angles) in high-resolution work must also be considered, if the above results are not to prove ambiguous. For an individual crystal, repeated analysis of any one power spectrum gave values for resolved spacings which were in agreement to within 0.003nm of each other. However, individual lattice fringes will not seem to be set apart at exactly uniform distance, and the accuracy of measured values will therefore be dependent on having large regions of uniform spacing available for analysis. In the present work, the largest spinel crystals studied were only 40nm in diameter, and even manual measurement showed a variation between equivalent spacings from one position to another over

Plate 44:- Twinned spinel crystal formed at pH 9 in the presence of 12.5 mol% zinc. Scale bar represents 10nm.

Plate 45:- Spinel crystal formed at pH 12 in the presence of 10 mol% zinc. Scale bar represents 10nm.



0.48nm

the surface of any one particle. The relationship between the measured spacings and the true values is further complicated by physical factors. If the area under examination contains no defects at all, changes in the observed orientation and spacing of fringes may still arise due to variations in specimen thickness and focus, as focal conditions will determine the value of the objective lens transfer function. In order to obtain a more accurate uncertainty, it is usually necessary to obtain a through-focal series. Tilting of the crystal away from the Bragg angle is also a factor which must be taken into account; a tilt angle of only 1° can affect results significantly (c.f. effect of tilt on single-crystal electron diffraction patterns, Section 2.2.4.).

The unit cell parameters of the spinel phase will also vary according to the degree of zinc incorporation in the structure. These values should lie between the limiting parameters for the unsubstituted oxide (maghemite) and fully-substituted zinc-magnetite. Table 3.9 shows the range of values obtained for (111), (220), (002) and (311) spacings measured from about 30 crystals imaged in [110], together with the expected values for a unit cell based on the above solution series. Comparison of these results showed a reasonable level of agreement, although many of the spacings were consistently lower than expected. Similar variations were observed in the measured angles between sets of lattice planes. The above deviations are most likely caused by slight tilting of the crystals such that the relevant zone axis was no longer exactly perpendicular to the beam direction.

Focusing effects were found to be small by comparison.

(hkl)	D-SPACING (nm)	EXPTL VALUES
(111)	0.481-0.486	0.462-0.485
(200)	0.417-0.421	0.406-0.425
(220)	0.295-0.298	0.284-0.299
(311)	0.251-0.254	0.246-0.248

Table 3.9:- Comparison of experimentally-measured spinel spacings with expected values for the maghemite-zinc magnetite system.

In conclusion, the measured lattice spacings could be expected have an accuracy of about 0.02nm. The largest deviation in the observed angles was a 1.5-2.5° shift. In this case, the degree of inaccuracy was not sufficient to affect the identification of a zone axis for the crystals, but it was not possible to draw any conclusions about variation in lattice parameter, etc.

3.4.1.b) CHARACTERISATION OF BACKGROUND MATERIAL PRESENT IN TRANSFORMATION PRODUCTS.

Although powder diffraction data had indicated that only goethite and hematite were present in products formed in the presence of less than 7 mol% zinc (Section 3.2), TEM showed that the transformed samples still contained a proportion of unconverted ferrihydrite. Plate 46 shows a selected area from a sample aged for three months at pH9 in the presence of 5 mol% zinc. The corresponding diffraction pattern (Plate 47) shows spacings measured at 0.25nm, 0.22nm and 0.15nm. These values are consistent with the expected reflections for a

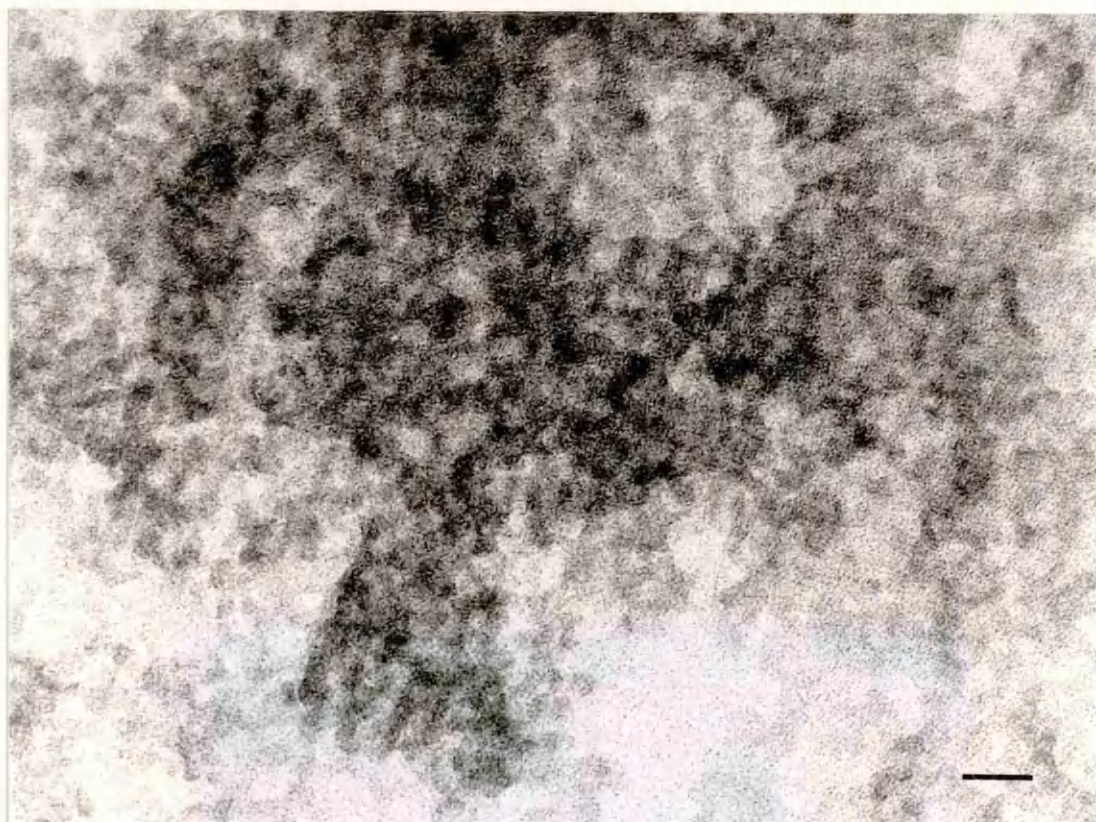


Plate 46:- Zinc-ferrihydrate aged three months at pH 9. Scale bar represents 10nm.



Plate 47:- Selected-area diffraction pattern obtained for the material shown in Plate 31.

fairly poorly-ordered synthetic "3-line" ferrihydrite. Although EDX data indicated that zinc was associated with the particles shown in Plate 46, extra spacings which would be consistent with zinc-magnetite were not observed. Similarly, additional reflections which would correspond to an obvious increase in ferrihydrite ordering (eg to a "6-line" structure) were absent.

The size and appearance of the ferrihydrite platelets appeared to remain largely unchanged, even after extended ageing. However, diffraction patterns observed for the aged solids were generally found to be stronger and less diffuse than those obtained for the fresh precipitates. Although the results did not show that individual platelets had become recognisably crystalline in nature (since conversion to hematite requires an aggregation step), some increase in ordering may have occurred.

Products formed at pH 9-12 in the presence of 10-15 mol% zinc at first appeared to contain a mixture of large (up to 40nm diameter) spinel crystals, hematite and unconverted ferrihydrite. However, closer examination of the background material in these samples showed that a proportion of the 5-10nm diameter particles were crystalline in nature.

Since selected-area diffraction patterns for individual crystallites could not be obtained due to the small particle size, the most convenient method by which the local structure could be examined was through high-resolution imaging. Plate 48 shows a typical area comprising background material present in a transformation product formed at pH 9 in the

presence of 15 mol% zinc. Measurement of d-spacings and corresponding angles for those particles which exhibited lattice fringes indicated that these were spinel crystallites. Since these are of a similar size to the original ferrihydrite platelets, it is possible that a direct transformation, induced by the adsorption of additive species, had occurred on individual platelets. The porous ferrihydrite "tunnel" structure could then allow rearrangement to fully cubic packing. Aggregation of the platelets does not appear to be necessary for nucleation to proceed.

Accurate EDX data for individual particles was difficult to obtain, but results indicated that the average additive incorporation levels were lower than those observed for the larger crystals. The crystallites therefore appeared to be quite deficient in zinc.

Assigning indices to the lattice fringes observed on these smaller spinel crystallites was difficult, due to the inevitable inaccuracy in measuring spacings on particles which were only 5-10nm in diameter. Fortunately, over the range in which the lattice planes were resolved (0.2 to 0.5nm) there are only six allowed spacings for the cubic zinc-magnetite structure (0.48nm, 0.42nm, 0.30nm, 0.25nm, 0.24nm and 0.21nm). In common with results obtained for the larger spinel crystals, the most common zone axis identified for these particles was [110]. However, a wide range of spacings was observed, and some lattice combinations appeared to be inconsistent with a cubic structure. The crystallites marked as 1 and 2 in Plate 48 show crossed lattice fringes measured

Plate 48 (over):- High resolution image showing small spinel particles present in a product formed at pH 9 in the presence of 12.5 mol% zinc. Crystallites which appear to be inconsistent with zinc-magnetite are numbered. Scale bar represents 10nm.

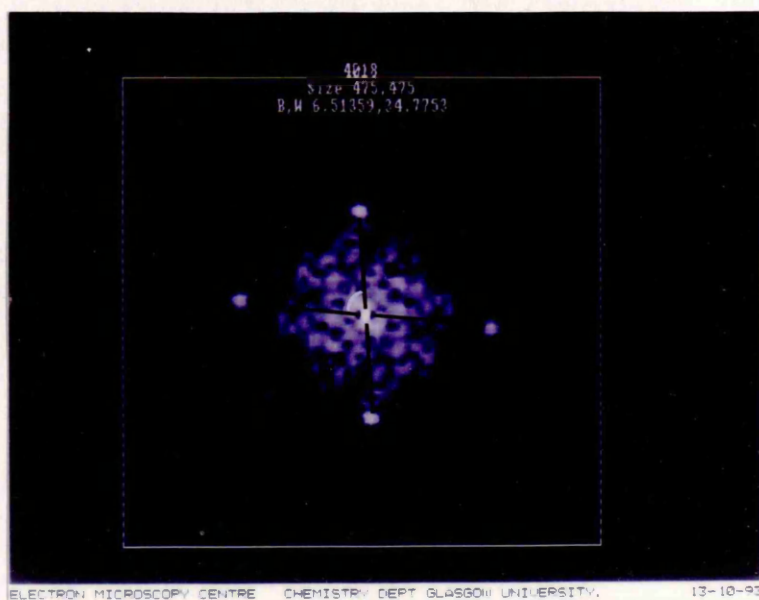


Fig.3.11:- Power spectrum obtained for the spinel particle numbered "1" in Plate 48.

0.25nm

0.315nm

2

0.30nm

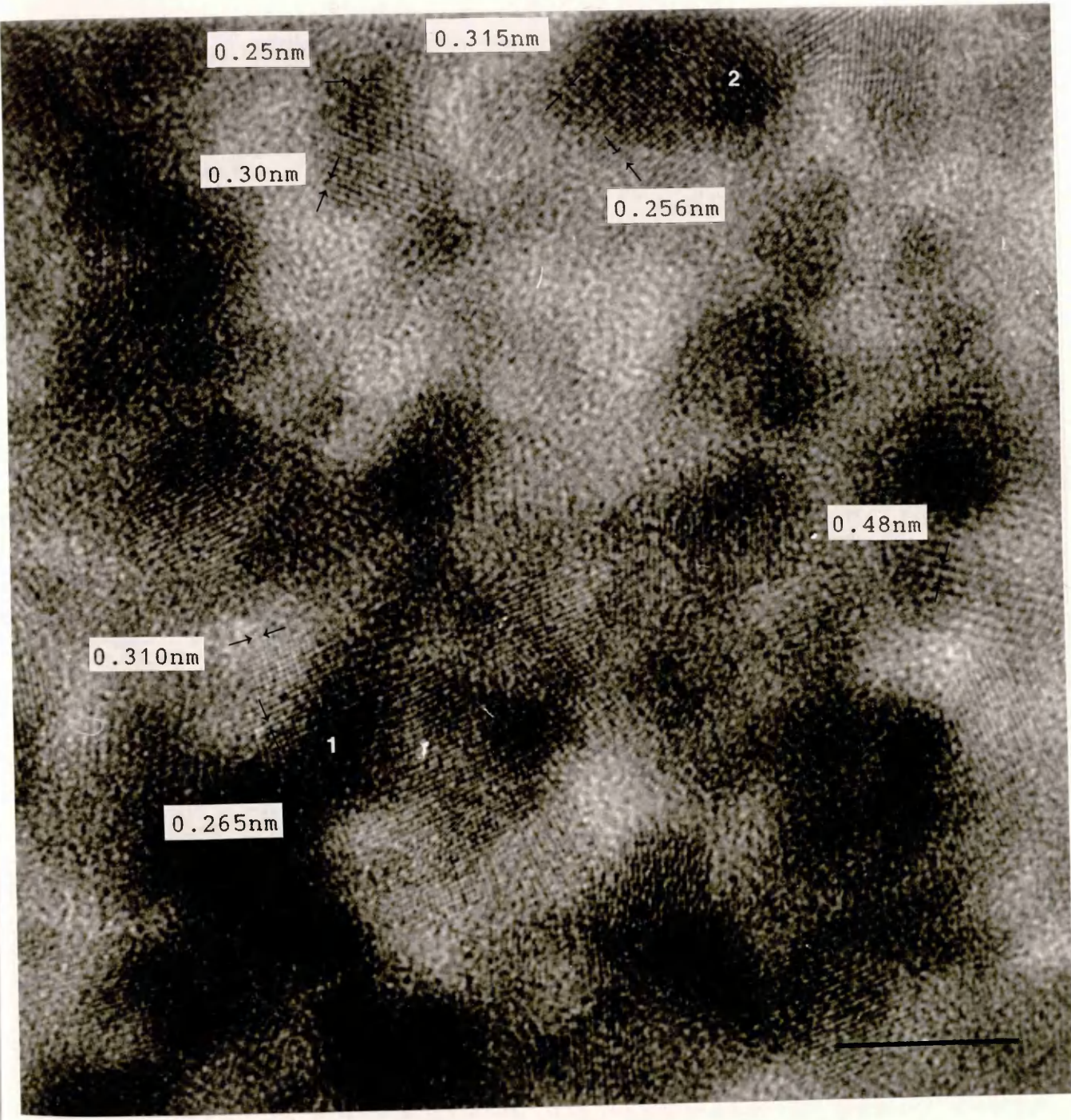
0.256nm

0.48nm

0.310nm

1

0.265nm



at, respectively, 0.256/0.315nm (at 83°) and 0.265/0.310nm (at 78°). The corresponding power spectrum for the former crystallite is shown in Fig.3.11. Allowing for the expected error in measured values of about 0.02nm, the spacings should lie in the range 0.28-0.32nm and 0.24-0.28nm. The only allowed reflections are then $d_{(220)}$ at 0.3nm and $d_{(311)}$ or $d_{(222)}$ at, respectively, 0.25nm and 0.24nm. Table 3.10 shows the range of calculated angles between the above planes.

ALLOWED SPACINGS			
(hkl)	(220)	(113)	(222)
d(nm)	0.298	0.254	0.243
ASSOCIATED ANGLES			
220/202 60°	220/2 $\bar{2}$ 0 90°	220/113 64.8°	220/1 $\bar{1}$ 3 90°
220/222 35.3°	220/2 $\bar{2}$ 2 90°	220/311 31.5°	220/3 $\bar{1}$ 1 64.8°
113/222 29.5°	113/2 $\bar{2}$ 2 58.5°	113/2 $\bar{2}$ 2 80.0°	113/1 $\bar{1}$ 3 35.1°
113/3 $\bar{1}$ 1 84.8°	113/1 $\bar{1}$ 3 50.5°	113/311 50.5°	

Table 3.10:- Possible spacings and angles for crystallites. For the approximately 80° angles to be accommodated, one spacing must correspond to $d_{(311)}$ (0.25nm), the other to $d_{(222)}$ (0.24nm). However, this would involve a consistent 0.05-0.06nm error in measurement of the 0.30nm spacing. This is far outside the degree of inaccuracy expected.

Although the above result appears to be inconsistent with data expected for a cubic spinel structure, it should be remembered that forbidden spacings which would suggest more

conclusively that extended ordering was present were not observed. Furthermore, identifying and indexing the observed spacings in terms of the measured angles is complicated by the fact that the number of unit cells which might be involved in any extended superstructure (so defining the value of c_0) is not known. All that can really be stated with any degree of confidence is that in some cases there appears to be a deviation from cubic symmetry.

3.4.2. TRANSFORMATION AT NEUTRAL pH

At pH 7, the transformation of ferrihydrite was found to be strongly retarded by the presence of zinc. In cases where the level of additive exceeded 30 mol%, the gels remained essentially unconverted even after months of ageing (cf a matter of days at higher pH). The final products were found to comprise a mixture of hematite or zinc-magnetite and unconverted ferrihydrite. Goethite was not observed in any of the products. Crystals of the spinel phase could be identified in products formed on ageing ferrihydrite gels containing more than 7 mol% zinc. This was comparable to the level required to induce spinel formation at pH 9. However, although spinel nucleation at neutral pH did not appear to be greatly inhibited, formation of the larger crystals present in products formed at pH 9-12 was found to be retarded.

Plate 49 shows a selected area comprising background material from a product formed at 8 mol% addition, chosen so as to avoid inclusion of hematite. The corresponding diffraction pattern (Plate 50) shows, in addition to spacings

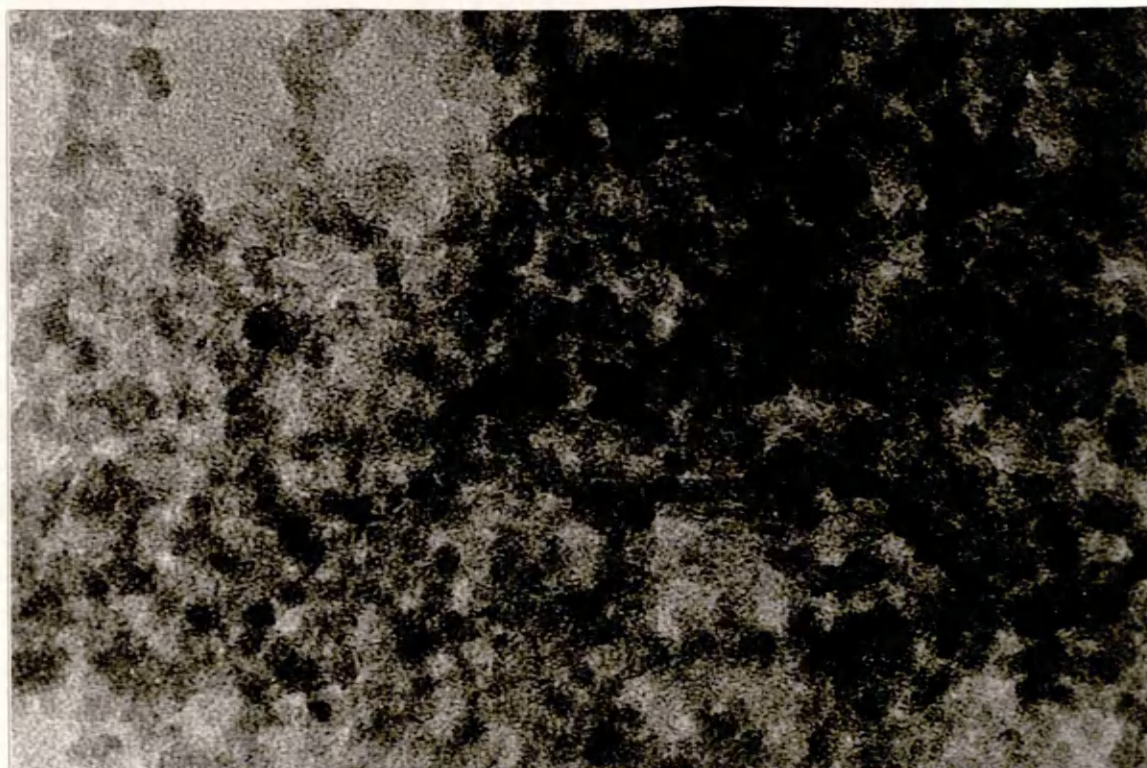


Plate 49:- Background material present in a product formed at neutral pH in the presence of 8 mol% zinc. Scale bar represents 20nm.

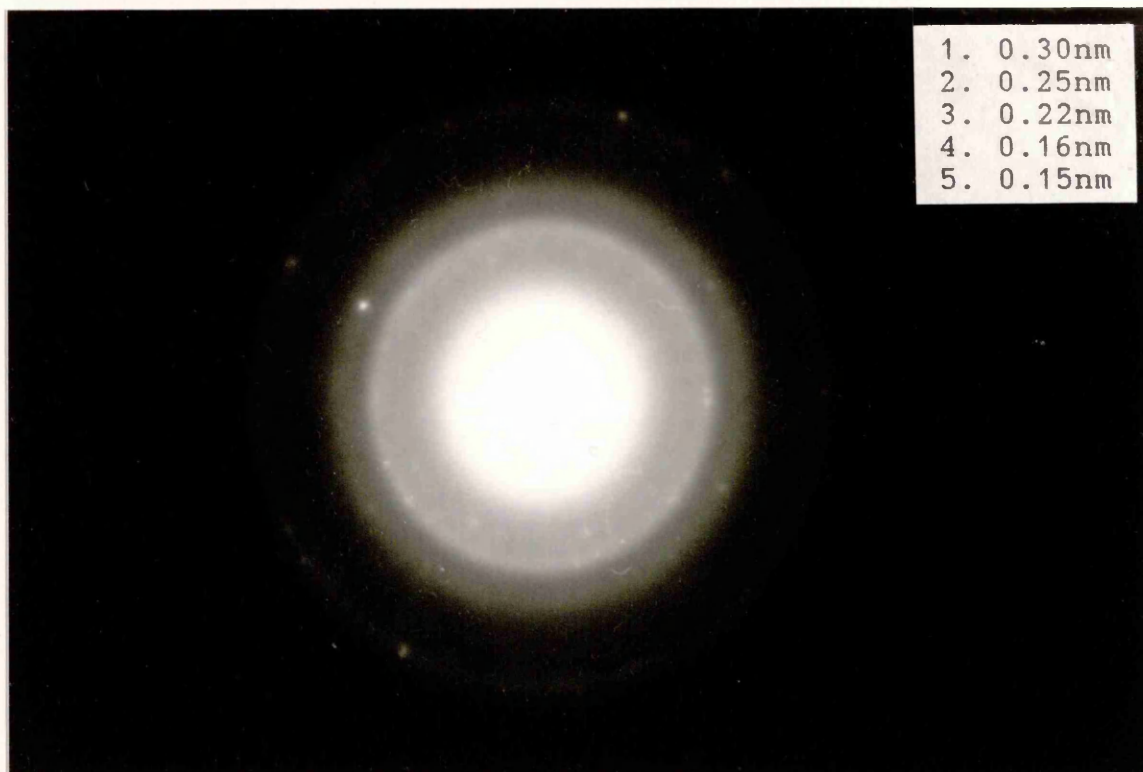


Plate 50:- Diffraction pattern obtained for the area shown in Plate 49.

at 0.25nm, 0.22nm and 0.15nm (corresponding to values for unconverted ferrihydrite), a few extra spots measured at 0.29nm and 0.16nm. These spacings are consistent with, respectively, (220) and (333) reflections for the spinel phase. Individual crystals were difficult to locate due to the small particle sizes. Plate 51 shows a similar area from a sample produced in the presence of 10 mol% zinc under identical growth conditions. In this case, the corresponding diffraction pattern (Plate 52) gave a wide range of spacings associated with zinc-magnetite. At this level of addition, individual spinel crystals lying amongst unconverted ferrihydrite platelets could quite easily be identified at high magnification where lattice fringes were resolved. Plate 51 (inset) shows a particle identified as zinc-magnetite imaged in [112].

A selected-area from a product formed at 15 mol% addition is shown in Plate 53. The corresponding diffraction pattern (Plate 54) gave a range of spacings which were consistent with values expected for zinc-magnetite. At neutral pH, no obvious evidence for the presence of extra symmetry-forbidden reflections was found for any of the products examined.

Accurate measurement of zinc incorporation in individual spinel crystals formed in these samples was restricted by the small particle sizes (up to a maximum of 15nm). In each case, an EDX profile was obtained by selecting what appeared to be a single spinel particle using an 8.8nm probe. In a product formed at 10 mol% addition, mass concentration ratios were

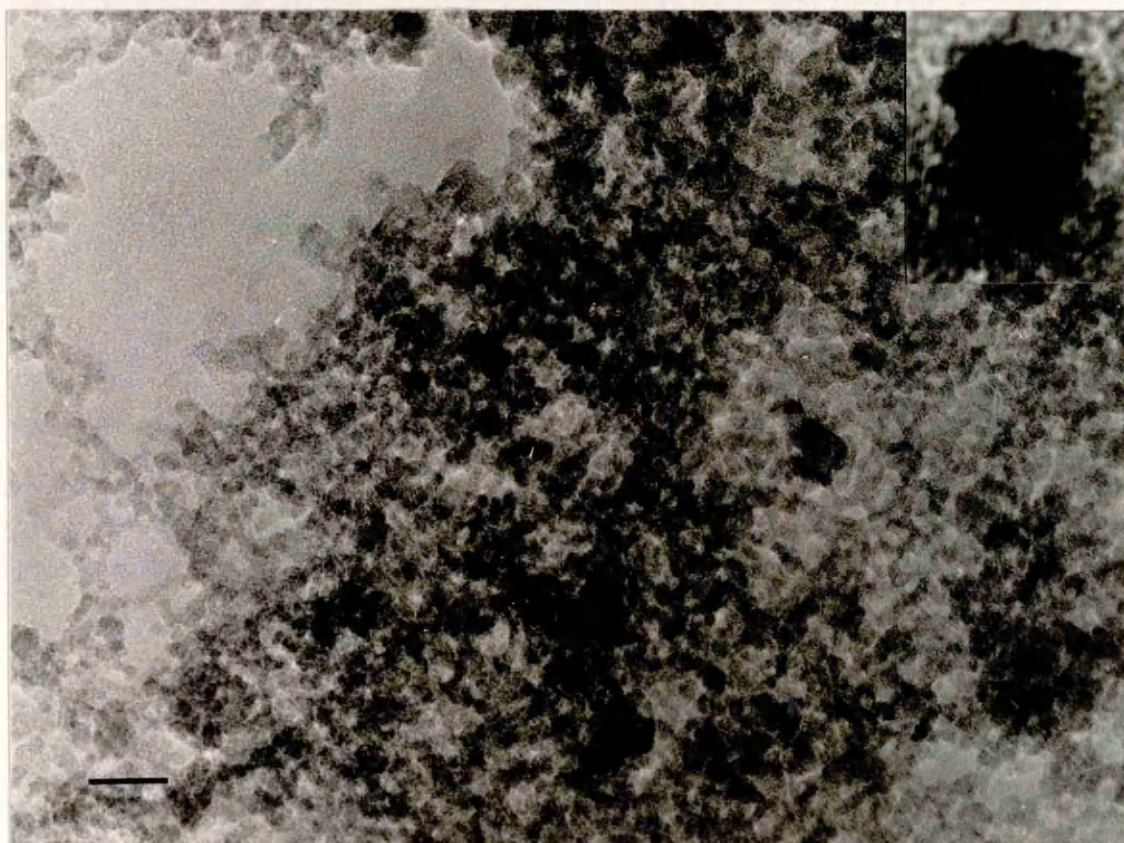


Plate 51:- Product formed at neutral pH in the presence of 10 mol% zinc. An enlarged spinel crystal is shown inset. Scale bar represents 20nm.

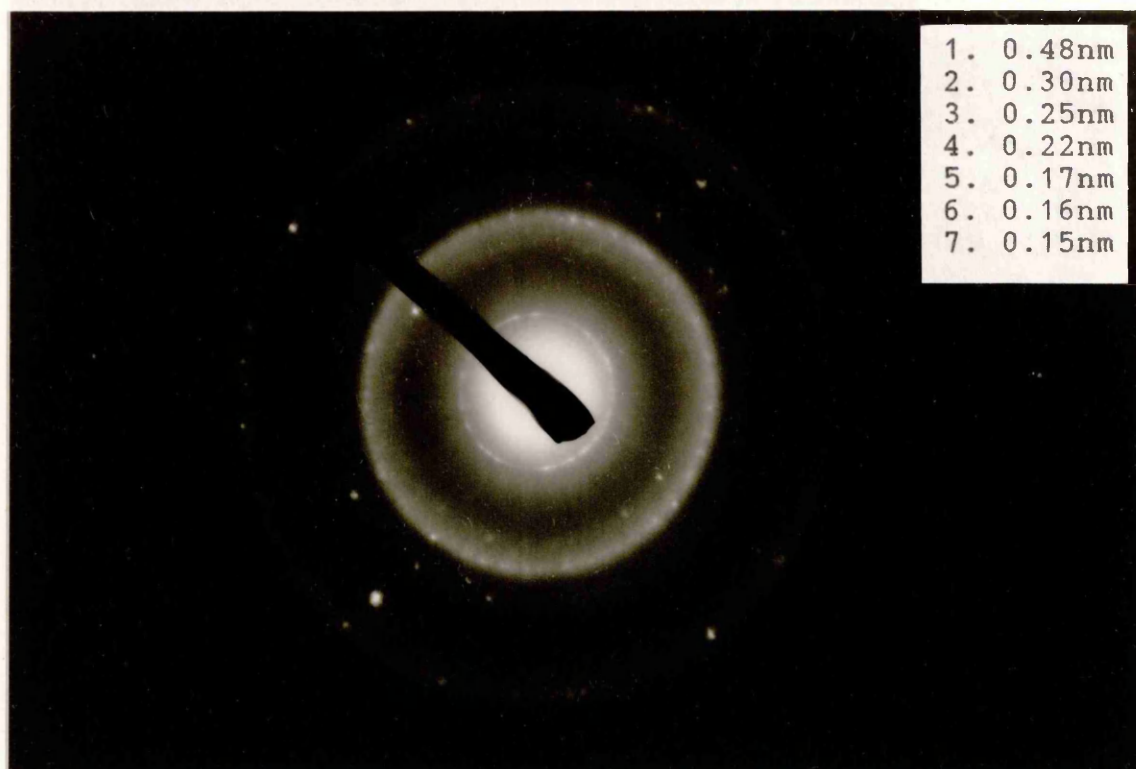


Plate 52:- Diffraction pattern obtained for the area shown in Plate 51.

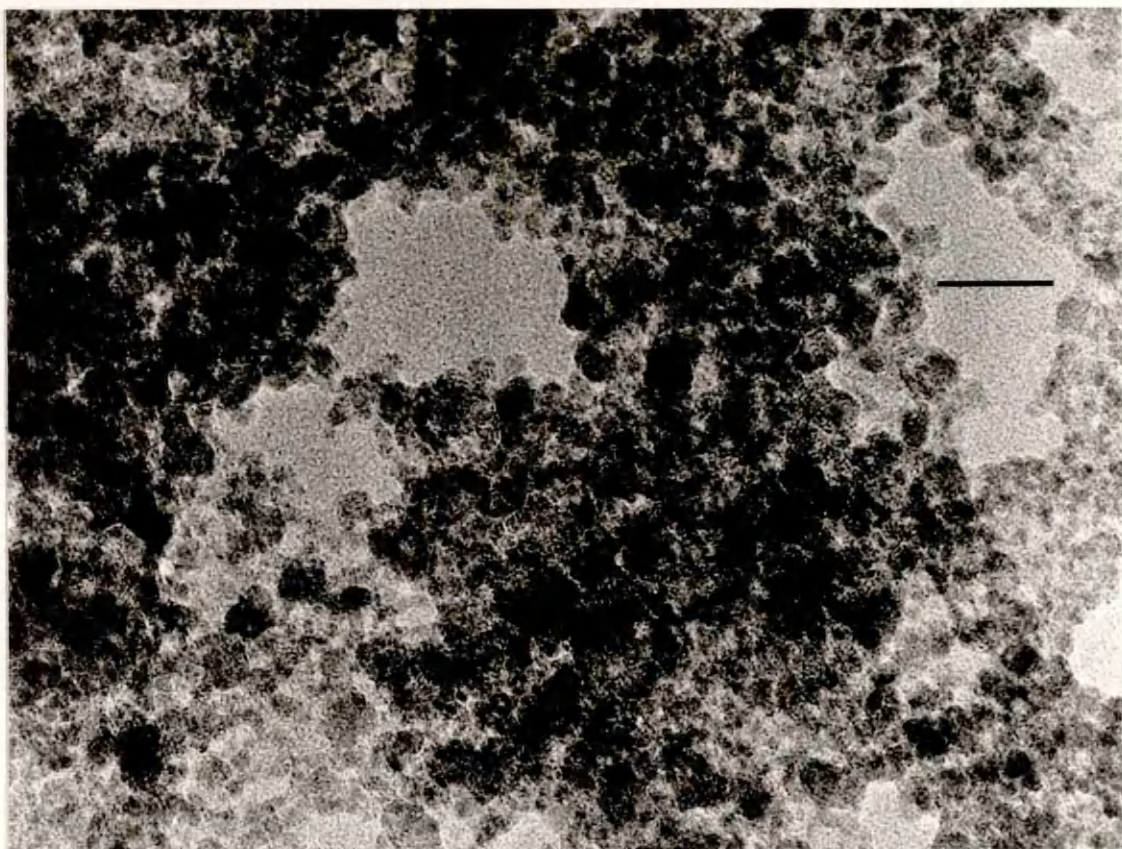


Plate 53:- Product formed at neutral pH in the presence of 15 mol% zinc. Scale bar represents 20nm.

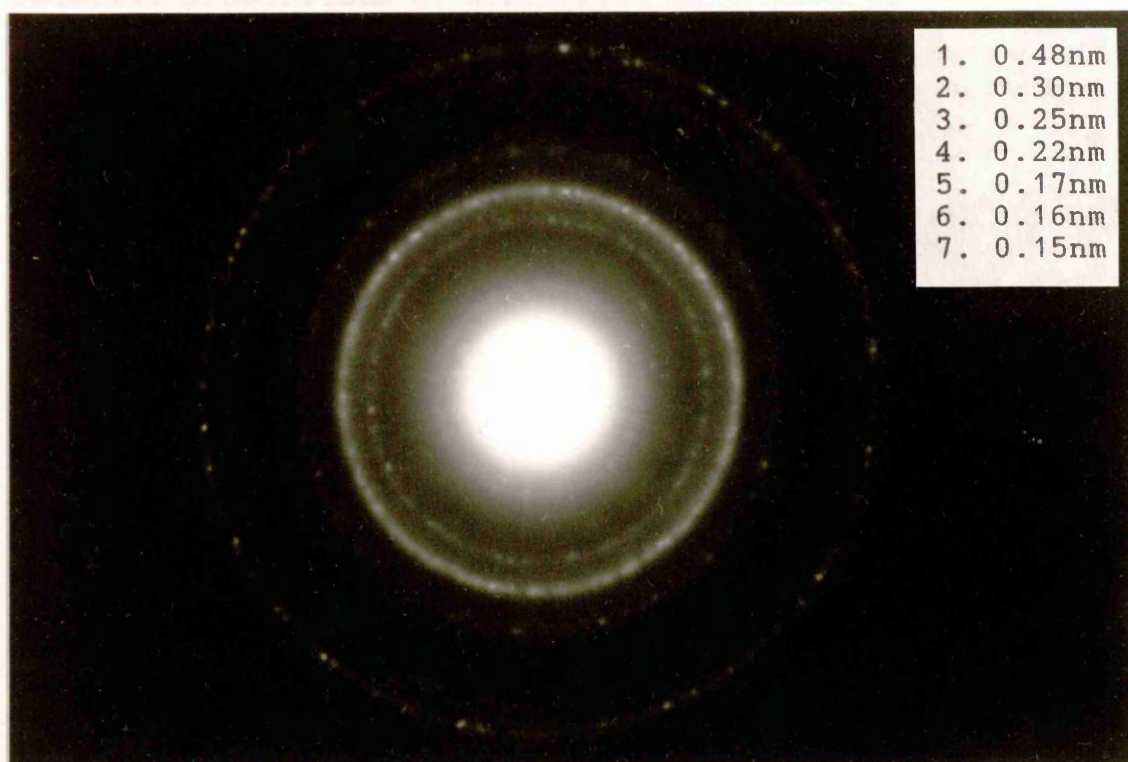


Plate 54:- Typical diffraction pattern obtained for the product shown in Plate 53.

measured at 0.15-0.40, corresponding to approximately 11-25 mol% additive incorporation in the spinel structure. The values obtained were generally lower than those obtained for similar crystals formed at higher pH.

3.5. ZINC DISTRIBUTION IN TRANSFORMATION PRODUCTS.

A combination of TEM and initial EDX data indicated that zinc was associated with, where present, hematite (Section 3.3), crystals of the spinel phase (Section 3.4), and any unconverted ferrihydrite remaining in the transformation products. Full EDX analyses were next carried out for each sample studied, in order to determine quantitatively the relative proportions of zinc taken up by each of the crystalline phases formed, and any variation in these values which might result from changes in growth conditions, eg varying the level of zinc associated with the initial precipitates and the pH at which the gels were held.

For each of the products, an average of 30-40 EDX profiles were obtained for a) general areas in the products using the maximum probe diameter available (56nm) to obtain average readings taken over all the phases present, and b) selected areas focussing only on one individual goethite, hematite or spinel crystal at a time, or on any unconverted ferrihydrite remaining. Total additive levels for the final products were found to be similar to values obtained for the initial precipitates. Experimentally-measured incorporation levels obtained for individual hematite and/or spinel crystals formed over the pH range 7-12 are shown in Table 3.11. The results for

crystals formed at pH9 in the presence of between 3.5 and 40 mol% zinc are shown in graph form in Fig.3.12.

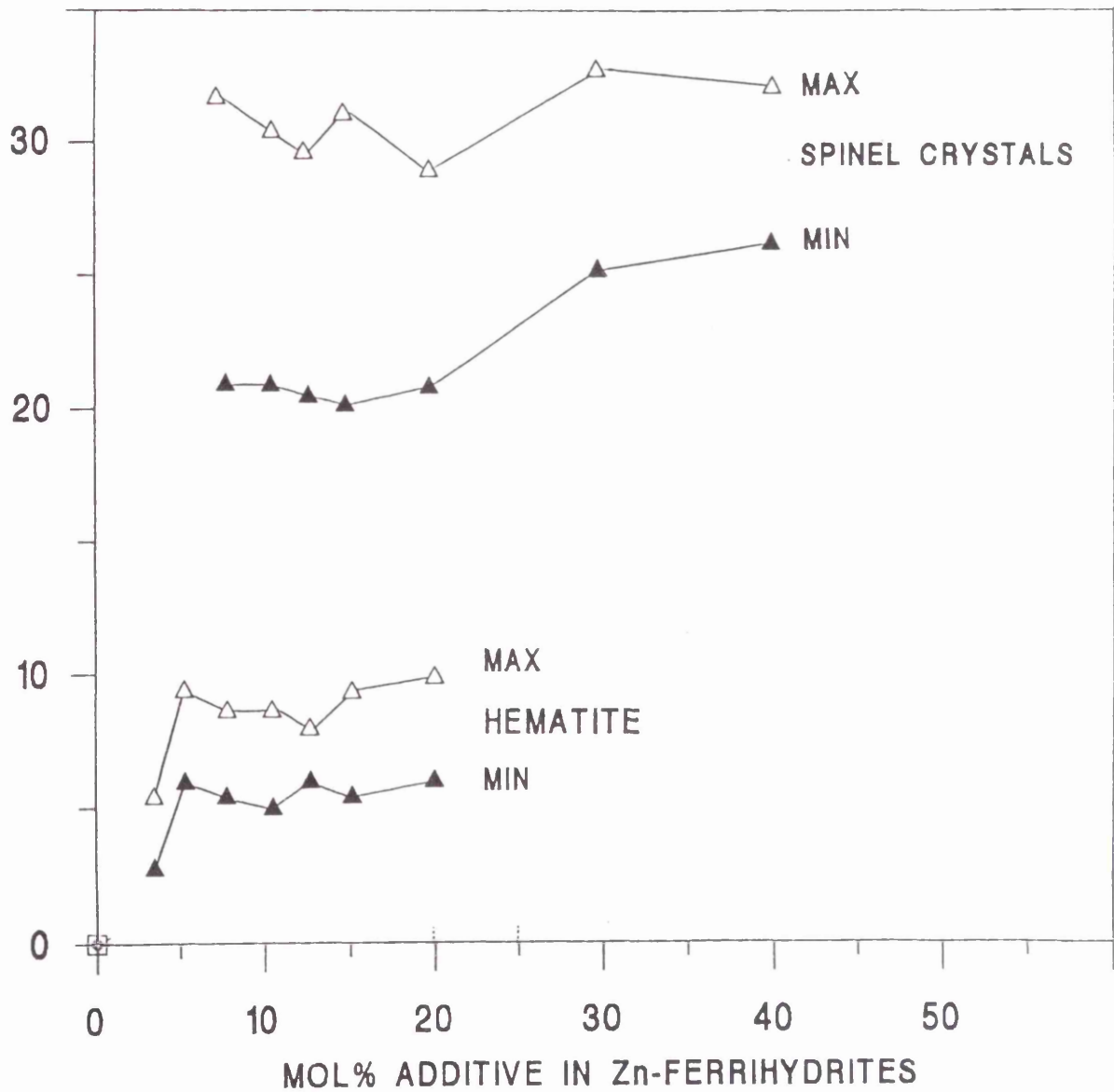
GEL pH	TOTAL Zn(mol%)	HEMATITE	SPINEL
9	3.5	2.5 - 5.6	N/A
	5	6.4 - 9.3	N/A
	7.5	5.6 - 8.6	21.5-32.4
	10	4.9 - 8.6	21.5-27.3
	12.5	6.4 - 7.9	20.9-29.1
	15	5.6 - 9.3	19.9-31.2
12	20	6.4 - 10	21.5-28.2
	8	N/A	19.9-25.5
	10	N/A	21.5-27.3
	15	4.1-7.9	20.4-30.0
	20	N/A	18.4-25.5
7	25	N/A	24.5-29.1
	8	6.4-9.3	11.4-18.7
	10	VERY LOW	10.7-22.5
	20	N/A	17.0-24.5

Table 3.11:- Additive incorporation levels in hematite and spinel crystals formed at pH 7-12.

At pH9, the degree of substituent ion incorporation in the hematite structure was found to be similar for crystals formed in the presence of anything between 5 and 20 mol% zinc (Fig.3.12). A limiting value of approximately 9-10 mol% incorporation was observed. The range of measured values was found to decrease only at very low levels of addition, in which case the distribution of zinc throughout the product made accurate measurement of additive incorporation difficult. The proportion of zinc associated with ferrihydrite in products which did not contain spinel crystals was found to be roughly

Fig.3.12:- Plot showing levels of zinc incorporation in hematite and spinel crystals as a function of the total proportion of additive species present in the initial precipitates.

MOL% DIST.
IN PRODUCTS



comparable to the level present in the initial precipitate.

If the total proportion of additive species exceeded 7 mol%, then formation of spinel crystals was induced at pH9. EDX data indicated that a highly disproportionate amount of zinc was taken up by the spinel phase when compared to the level taken over the product as a whole (for example, 21 to 32 mol% incorporation for crystals present in a gel containing a total of 7.5 mol% additive). In the above case, analysis of the initial precipitate gave little evidence for the presence of regions associated with such a high level of additive species. It might then be expected that a sufficient proportion of zinc would only be available if some release of the substituent into solution was involved in crystal growth. In cases where the spinel phase had formed, the proportion of additive which remained associated with unconverted ferrihydrite was barely detectable.

The above conclusion would appear to contradict the results described in Section 3.3, where EDX data suggested that zinc species would readsorb on ferrihydrite rather than enter solution. If the additive species were fully released from the solid they might easily become associated with goethite (since the oxyhydroxide shows a specific affinity for zinc [108]) and subsequently enter the crystal lattice. However, although the growing spinel crystals are likely to be fed by soluble ferric and zinc species released by the dissolution of ferrihydrite, it is not necessary for the ions to enter the bulk solution (where the goethite nuclei/growing crystals are thought to be located) if nucleation of the

spinel phase occurred on ferrihydrite.

Further evidence for the "mobility" of zinc species in the gels came from the range of incorporation values obtained for some samples which contained hematite. For example, many oxide crystals present in a 5 mol% gel were found to have taken up almost twice the average additive level distributed over the product as a whole (Fig.3.12). This suggested that adsorption and subsequent incorporation in the growing hematite crystals may have been favoured over readsorption on ferrihydrite.

Although a high proportion of the zinc species were incorporated into the spinel phase, in many cases there still appeared to be an insufficient level for a non-defect zinc-magnetite stoichiometry (the required Zn:Fe ratio is 1:2, equivalent to a mass concentration ratio $C_{Zn}/C_{Fe}=0.59$). EDX data obtained for a large number of the crystals examined gave values close to this, but the majority were found to contain significantly low levels of additive. Even taking into account the inaccuracies in the technique used, the crystals formed at up to 15 mol% addition generally appeared to be deficient in zinc. If we consider the spinel unit cell having 8 tetrahedral sites, 16 octahedral sites and 32 O atoms, with Zn occupying only tetrahedral positions (fully-substituted $ZnFe_2O_4$ having the normal spinel structure), then a range of possible stoichiometries for the spinel can easily be calculated. If the overall charges are balanced as required, the crystals could be described in the same manner by which the γ - Fe_2O_3 unit cell can be expressed as $Fe_8Fe_{13.33} \square_{2.67}O_{32}$.

The lower mass concentration ratios obtained for the spinel crystals lay in the region $C_{Zn}/C_{Fe}=0.30$, corresponding to approximately 20 mol% additive incorporation. This gives a stoichiometry $Zn_{0.58}Fe_{2.28}O_4$ and an average unit cell $Zn_{4.7}Fe_{18.2} \square_{1.1}O_{32}$. This is only an approximate value restricted by the accuracy of the quantitative calculations, but it shows that many of the crystals were significantly deficient in zinc and may contain some proportion of vacancies.

At initial levels of addition above 25-30 mol%, the more polycrystalline spinel material formed was associated with higher concentrations of zinc. If the samples were analysed before washing with acid to remove adsorbed zinc and any unconverted ferrihydrite, the Zn:Fe ratios calculated from EDX data were found to be approximately equal to the initial amounts present in the original precipitates. After washing, the additive levels were found to reach the limit for a non-defect $ZnFe_2O_4$ stoichiometry. Mass concentration ratios obtained for a transformation product formed at pH 12 in the presence of 50 mol% zinc, taken prior to washing, lay between 0.7 and 1.1; the higher level being the same as that measured in the unconverted zinc-ferrihydrite. After washing, values were obtained in the range 0.55-0.60, corresponding to 32-33 mol% incorporation of zinc in the spinel crystals.

3.6. THE EFFECT OF ZINC ON THE DEVELOPMENT OF CRYSTALLINE PHASES FORMED ON ADDITION OF EXCESS BASE TO PARTIALLY-HYDROLYSED FERRIC SOLUTION.

The results discussed so far have suggested that, on ageing zinc-ferrihydrate gels, the strongly-adsorbing additive species will block the release of ferric species into solution during the initial induction period, to the extent that the development of goethite is strongly inhibited at pH 9, and more mildly retarded at pH 12. This effect will then allow development of hematite to become competitive with the oxyhydroxide at higher pH. Examination of crystalline products formed on ageing zinc-ferrihydrates at pH 12 indicated that the presence of a relatively low level of additive (about 15 mol%) was sufficient to completely inhibit formation of goethite.

Initial data has also suggested that spinel nucleation requires a degree of interaction with the ferrihydrate precursor. If the subsequent growth stage involves dissolution/reprecipitation, there will be competition between the spinel and goethite crystals for uptake of soluble zinc and ferric species. In the samples discussed in sections 3.2-3.5, the spinel phase was generally observed in cases where goethite was largely absent. Further information on the parallel development of α -FeOOH and the spinel phase was next obtained using partially-hydrolysed gels in the transformation studies.

Ferric nitrate solutions were made up and allowed to age at room temperature for periods ranging from 24 hours to

several months. In order to enhance the rate of hydrolysis, a relatively low concentration of base ($\text{OH}:\text{Fe} = 3:4$) was added to the solutions prior to ageing. This amount was not sufficient to induce immediate formation of ferrihydrite. After the initial ageing period, the gel pH was quickly raised, and the resulting precipitates further aged in an oven at 70° .

The hydrolysis process will effectively "seed" the gels, either with polynuclear species capable of acting as nuclei for growth of goethite in solution [48] or, if the ageing period is extended for a sufficient period, goethite crystals. It is therefore possible to obtain further data on the mechanism by which zinc inhibits goethite growth in ferrihydrite gels by introducing the additive to aged solutions immediately prior to precipitation at pH 12, i.e. once hydrolysis had occurred and goethite "seeds" were already present in the gels. In this case, the spinel phase would have to compete directly with the oxyhydroxide for uptake of soluble growth species.

3.6.1. AGEING IN THE ABSENCE OF ADDITIVE

A number of ferric salt solutions were made up in the manner described above and left for hydrolysis to proceed. If the ageing time was restricted to between 25 and 50 hours at room temperature, TEM examination of sub-samples removed from the solutions indicated that, although there was a noticeable darkening in the colour of the gels, crystalline material had not been deposited from solution. However, small aggregates comprising amorphous particles 2-4nm in diameter had already

begun to develop (Plate 55). These are consistent with the polynuclear species quoted in previous studies [15,25].

Raising the pH of the above gels to 12 led to immediate formation of a red-brown precipitate giving s.a. diffraction spacings which were consistent with ferrihydrite. The samples were then transferred to an oven and left at 70°C. Plate 56 shows an area from a sample having undergone 50 hours hydrolysis in acidic media, examined by TEM 12 hours after precipitation. The small amorphous spherical particles shown in Plate 55 appear to have coalesced to form larger masses which then combine further, eventually assuming the shape of acicular crystals. 24 hours after precipitation, XRD profiles obtained for the final products indicated that the only crystalline phase which had developed was goethite. TEM imaging showed masses of acicular crystals about 100nm in length (Plate 57). Most of the crystals examined were singly-diffracting, and indexing of the patterns obtained showed that most were imaged in [110]. At high magnification, lattice fringes of 0.42nm, corresponding to (110) spacings for goethite, were often resolved running parallel to the extended crystal axis. The presence of intergrowths was not generally evident.

After 24 or more hours hydrolysis, the dimensions of the goethite crystals in the final products were much smaller than those observed in samples formed without first ageing the ferric solutions prior to precipitation. This is in accord with results obtained by Atkinson *et al* [48], who showed that the general effect of a short hydrolysis time was to induce



Plate 55:- Polynuclear aggregates formed on ageing ferric nitrate solution in acidic media for 50 hours. Scale bar represents 20nm.

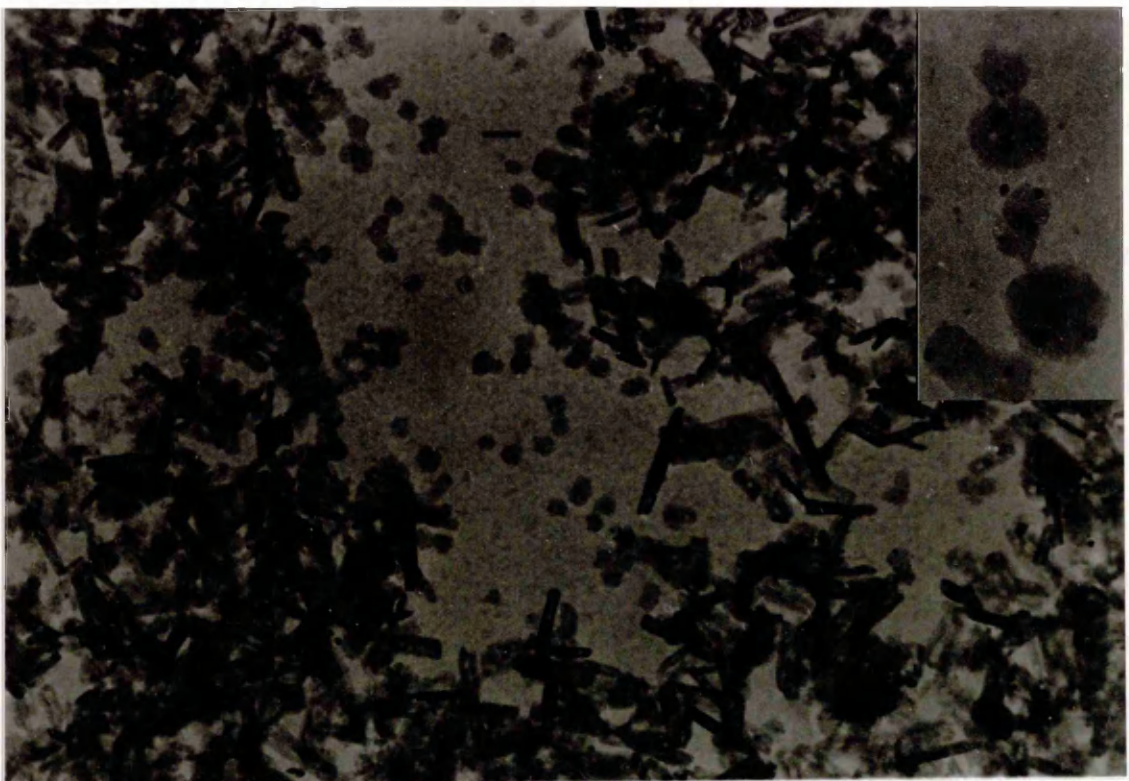


Plate 56:- Formation of acicular goethite crystals through further aggregation of polynuclear species (inset), after precipitation at pH 12. Scale bar represents 25nm.

a burst of growth in the precipitated gels, leading to more, shorter crystals.

If the ageing time prior to precipitation was increased to between 4 and 7 days, a yellow precipitate was gradually deposited from solution. After 4 days ageing this solid was shown by TEM to comprise short rafts of crystalline material, the lengths of which were seen to increase with the ageing time. After 7 days ageing, selected-area diffraction patterns gave spacings which could easily be identified as arising from goethite. TEM examination showed chains 100-200nm in length, which appeared to consist of individual flocculated particles (Plate 58). The structures observed in the final products, after precipitation and further ageing at pH 12, were of a similar length to those imaged in the hydrolysed gels. Further crystal growth appeared to have occurred preferentially along the length of each individual chain unit.

Plate 59 shows a high-resolution image of a chain structure, prior to precipitation at high pH, from a sample aged for 2 months. The spacings shown were measured at 1.0/0.50nm and 0.42nm, corresponding to, respectively, (020) (the 1nm spacing being caused by double diffraction) and (110) reflections for goethite. These values are consistent with a crystal imaged in [001]. Fig. 3.13 shows the structure as viewed along the c-axis. Plate 60 shows a single chain formed after 3 weeks ageing, taken 24 hours after precipitation at pH 12. Lattice fringes measured at 0.42nm, 0.34nm and 0.27nm are indicated. These spacings are consistent with (110), (120) and (130) reflections for α -FeOOH. The crystal is again imaged



Plate 57:- Final transformation product formed on precipitating a gel which had been aged for 50 hours in acidic media. Scale bar represents 100nm.

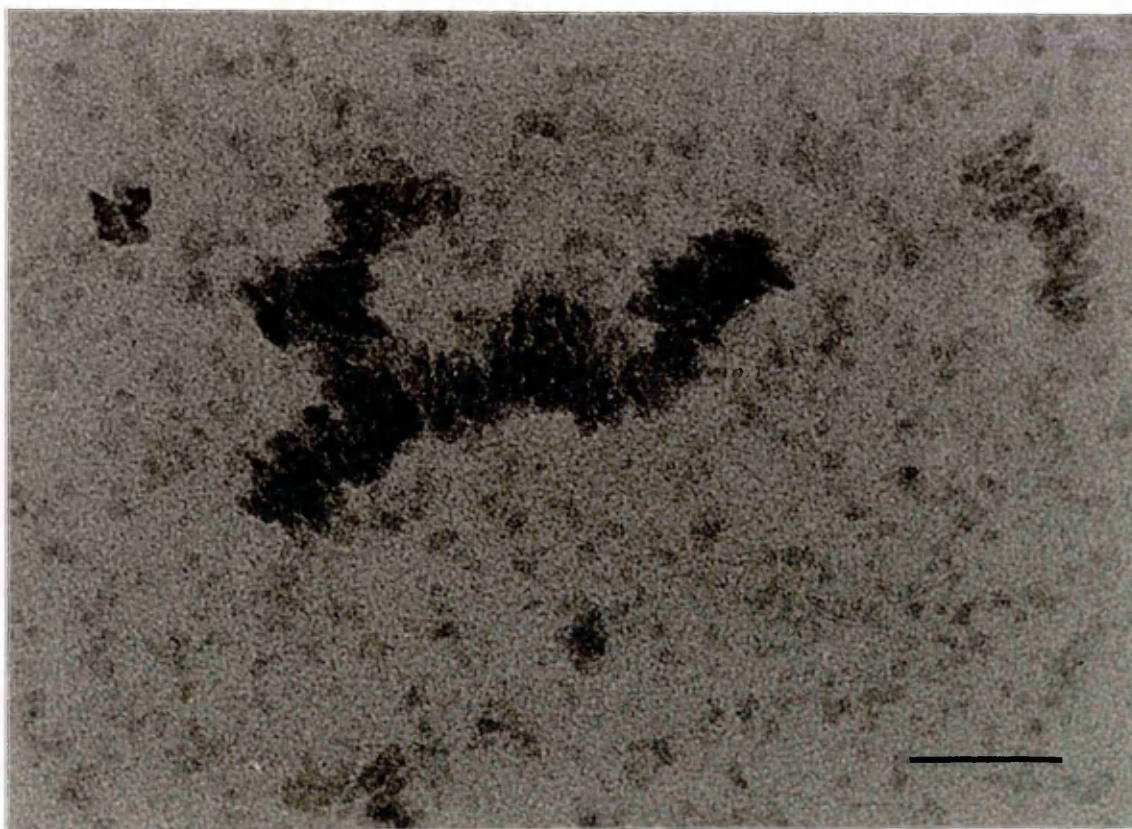


Plate 58:- Goethite chain formed on ageing ferric nitrate solution for 7 days in acidic media without raising the gel pH. Scale bar represents 50nm.

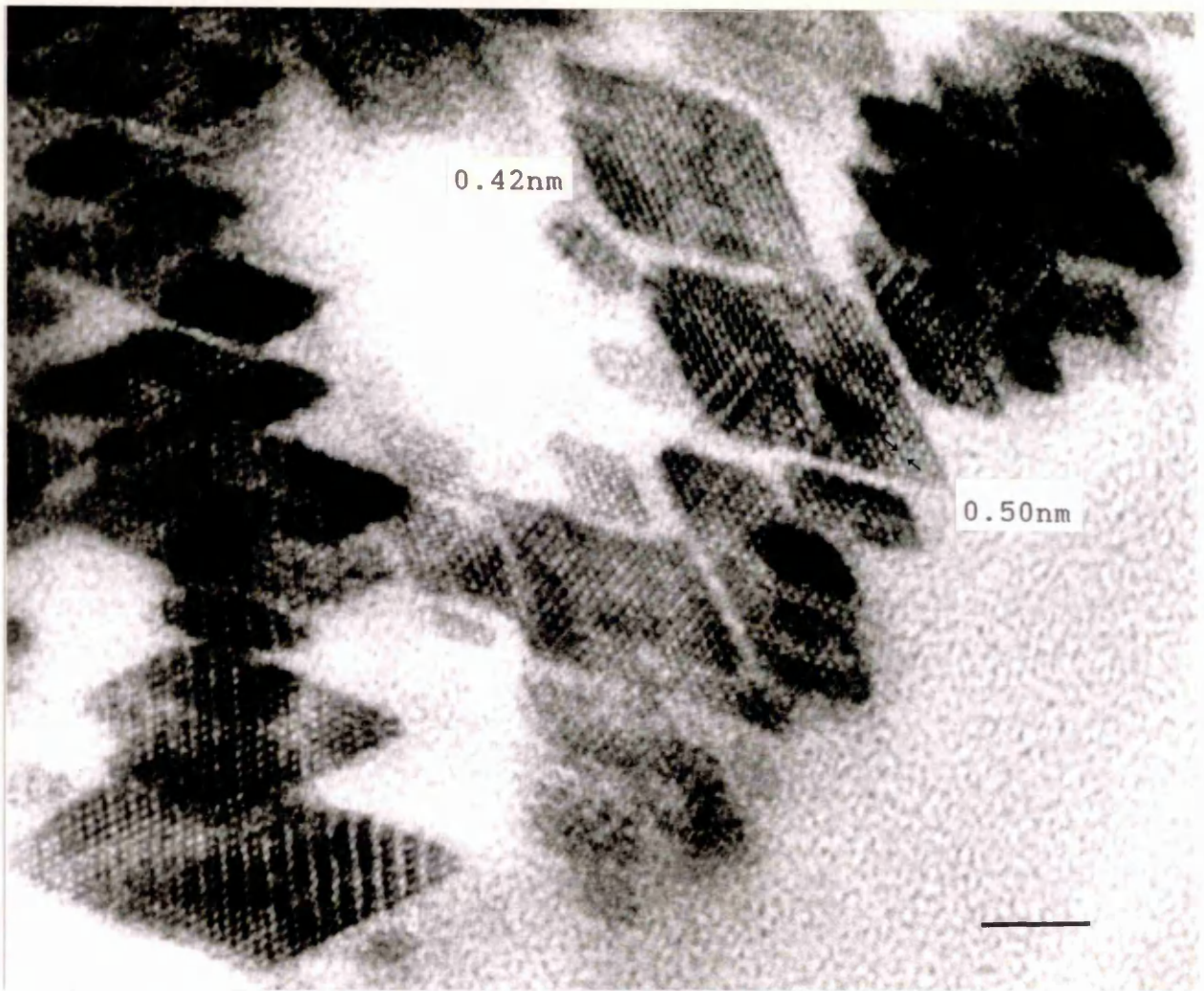


Plate 59:- Goethite chains formed on ageing ferric nitrate solution for 2 months in acidic media. Lattice fringes and associated angles are consistent with imaging in [001]. Scale bar represents 10nm.

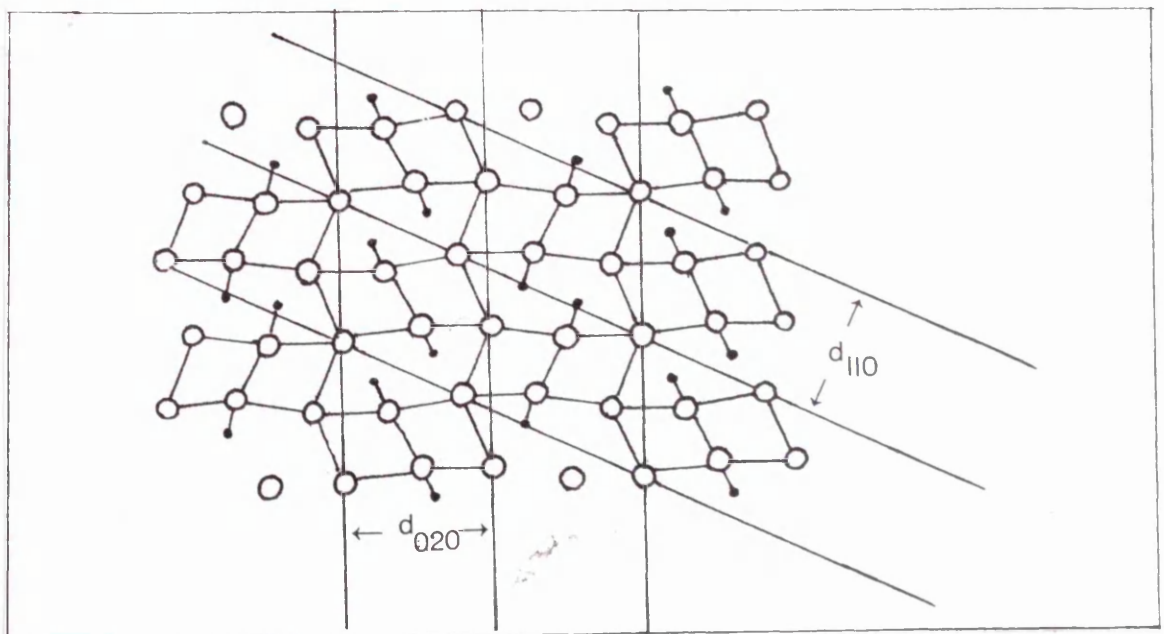


Fig.3.13:- Diagram showing goethite structure as imaged in Plate 59. (110) and (020) lattice planes are indicated.

Plate 60 (over):- Goethite chain structure observed in a final product formed on addition of excess base to a gel previously aged for 3 weeks in acidic media. Scale bar represents 10nm.

0.42nm

0.27nm

0.34nm



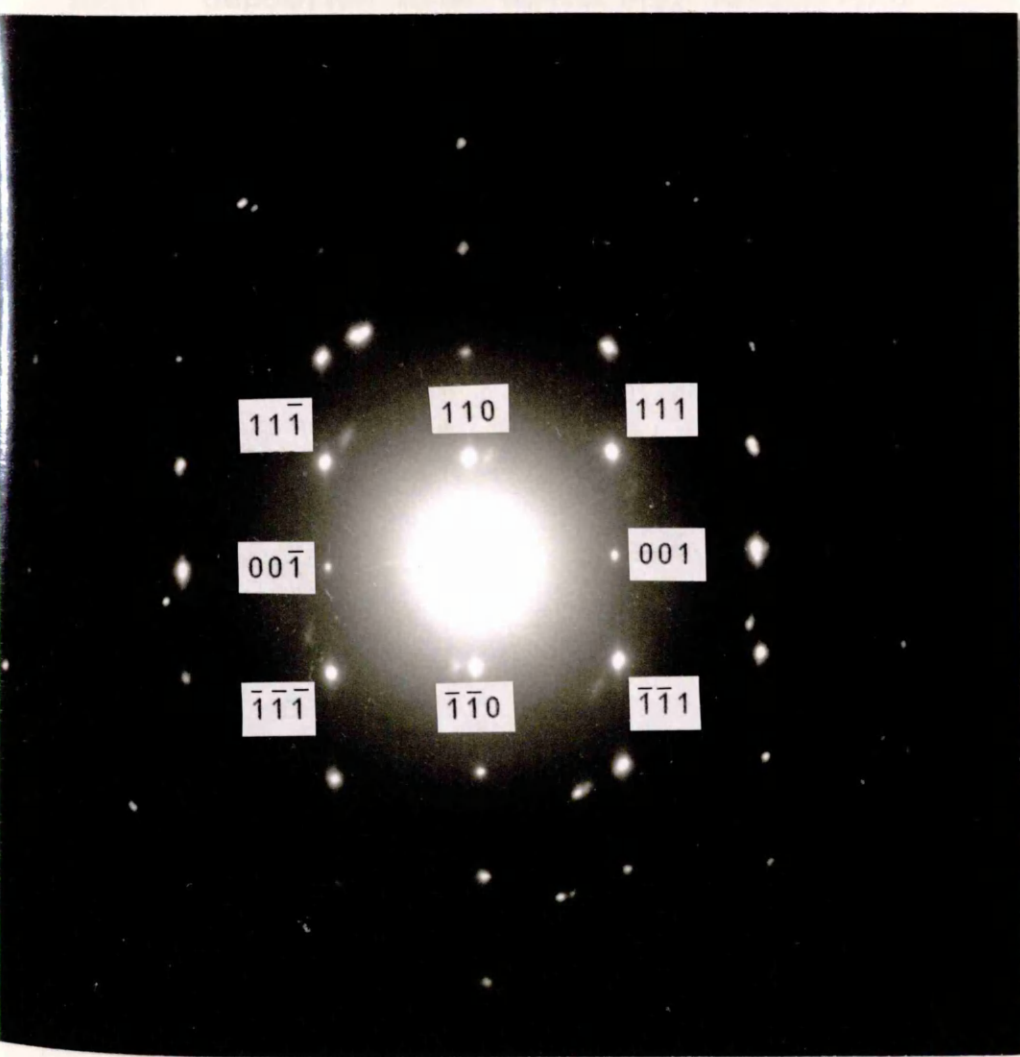
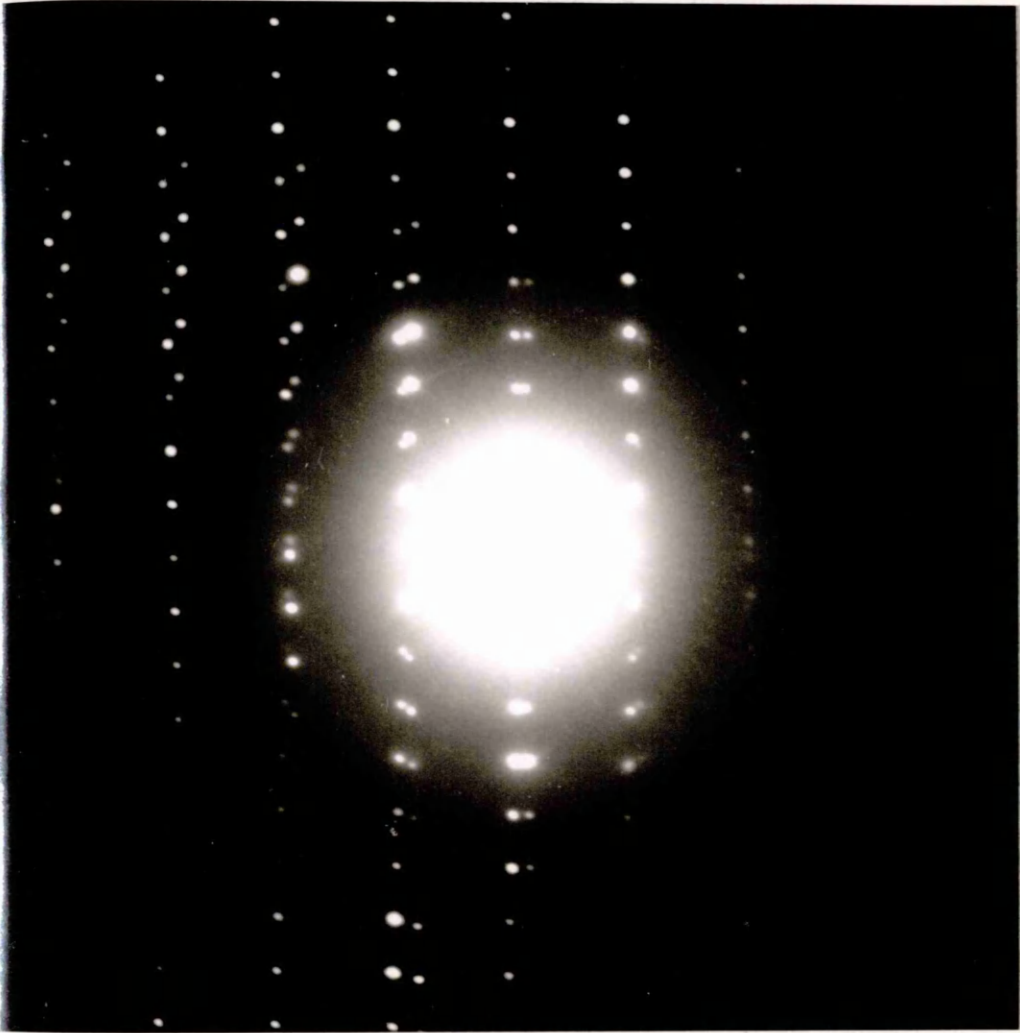
in [001]. In both of the above cases, there appeared to be only a slight incoherency in the lattice planes over the boundary between neighbouring chain units. However, in Plate 59 (arrowed), some of the aligned crystals hardly appear to be "connected". The alignment could be enhanced by H-bonding.

Many of the chains examined in these products gave essentially single-crystal diffraction patterns from which a zone axis could easily be identified. The two most common orientations adopted are illustrated by Plates 61 and 62. These patterns have been indexed, respectively, in accord with goethite imaged in [110] and [001]. The large number of extra spots in Plate 61 are caused by double diffraction (cf the lattice fringes shown in Plate 59). Some degree of misalignment was often evident in the diffraction patterns, although it could not be determined whether this was caused by inherent structural defects or through stress induced during sample preparation .

Imaging of the chain structures in [001] was found to be especially common where gels having undergone extended hydrolysis (>1-2 weeks) were examined prior to raising the pH. In this case, the c-axis of each individual unit in the chains was not likely to be elongated to any great extent relative to the other directions, since a large c-dimension would make adoption of the above orientation less likely on drying the samples down onto specimen grids. After further ageing at pH 12 the [110] zone was predominant, and most of the individual chain units exhibited the characteristic needle-like goethite morphology. A change was also observed

Plate 61 (over):- Goethite chain (inset), together with corresponding diffraction pattern. The zone axis was identified as [001].

Plate 62 (over):- Chain structure (inset), shown together with corresponding diffraction pattern indexed as goethite imaged in [110].



in the a and b directions. Preferential growth along the c-axis was also noted for goethite growth from ferrihydrite without an initial hydrolysis stage. No obvious increase was observed in the average chain lengths after precipitation.

3.6.2. GOETHITE AND SPINEL FORMATION IN THE PRESENCE OF ZINC.

The partially-hydrolysed gels used in these transformation studies can be divided into two categories: those in which the hydrolysis time prior to raising the pH was restricted so that only polynuclear species were present (up to about 3-4 days ageing), and those having undergone further hydrolysis, to the extent that goethite had already been deposited from the acidic gels.

Two ferric nitrate solutions were left to hydrolyse for 25 hours in the absence of additive. 5 mol% zinc was next added to one gel, and 10 mol% to the other. The pH of both solutions was then raised to 12. Electron diffraction patterns obtained for the resultant precipitates were found to be similar to those for ferrihydrite. Crystalline material was not found to have developed during hydrolysis. After a further 24 hours ageing at elevated temperature, XRD data for the final products showed that in both cases the only crystalline phase present was goethite. TEM imaging showed small acicular crystals of a similar size and morphology to the corresponding control sample.

Products formed at pH 12 in the presence of 5 mol% zinc without an initial hydrolysis stage mainly comprised "star" twins, while 10 mol% additive induced nucleation and growth

of the spinel phase, and inhibited goethite formation (Section 3.2). However, in the above products the development of zinc-magnetite was not favoured, and the presence of additive did not appear to strongly promote formation of goethite twin types. Little evidence for the association of zinc with goethite was obtained from EDX profiles of individual crystals. The additive appeared to remain associated with any unconverted ferrihydrite in the products.

Addition of 15 mol% zinc to a gel also having undergone 25 hours hydrolysis gave rise to a final transformation product comprising a mixture of long fibrils (up to 500nm in length) and masses of small platelets up to 15nm in diameter (Plate 63). The long crystals were identified from electron diffraction data as goethite. Lattice fringes measured at 0.42nm, corresponding to reflection by (110) planes, were resolved running the length of many of the fibrils. These were generally free from defects. Selected-area diffraction patterns obtained for the aggregated platelets gave spacings which were consistent with zinc-magnetite. Similar products formed in the presence of 25 and 50 mol% zinc were found to comprise zinc-magnetite and, in the case of the latter sample, long, well-formed acicular crystals of ZnO. Goethite crystals were not observed, even though goethite "nuclei" were certainly present in the gels.

Again, such a high proportion of goethite crystals was not observed in products formed in the presence of 15 mol% zinc where the ferric solutions had not been partially hydrolysed prior to precipitation. As described in Section

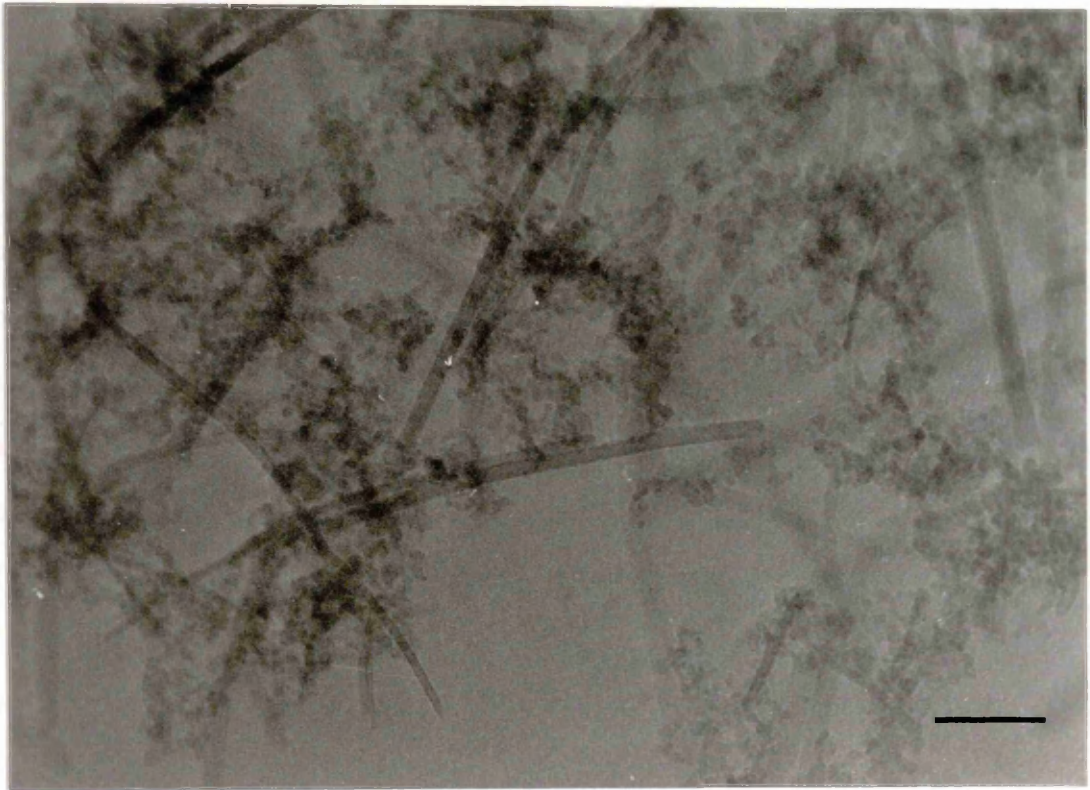


Plate 63:- Product formed on precipitating a gel (containing 15 mol% zinc) which had previously been aged for 25 hours. Scale bar represents 100nm.

3.6.1, restricted hydrolysis will seed the initial gels with polynuclear species which can act as nuclei for the growth of goethite crystals after precipitation. Since these nuclei are already present, the growth stage can begin immediately and the likelihood of hematite or spinel nucleation and growth becoming competitive with that of the oxyhydroxide is therefore reduced. This is in accord with the observation that in products formed from gels aged for 25 hours, spinel crystals were only observed at >12 mol% addition (cf 8 mol% at pH 12 in Section 3.2). Similarly, the twinned goethite crystals (thought to grow from small hematite "nuclei" formed during the induction period) were now absent. Increasing the level of zinc above 10 mol% led to a steady decrease in the proportion of goethite observed in the products. This would be expected if the higher additive levels inhibited release of ferric growth species into solution. The thin crystals shown in Plate 63 are similar in morphology to those observed together with "star" twins in Section 3.2. Again, the morphology can be explained in terms of the presence of a low concentration of ferric species in solution. Addition of growth units at the ends of the crystals (ie parallel to the c-axis) is favoured over secondary nucleation on the crystal sides (thus forming intergrowths) under these conditions.

If the ferric solutions were aged for slightly longer periods prior to precipitation (2 to 3 days) the extent of hydrolysis in the gels was increased, and formation of goethite was thus promoted in the presence of even higher levels of zinc. Plates 64 and 65 show, respectively, the

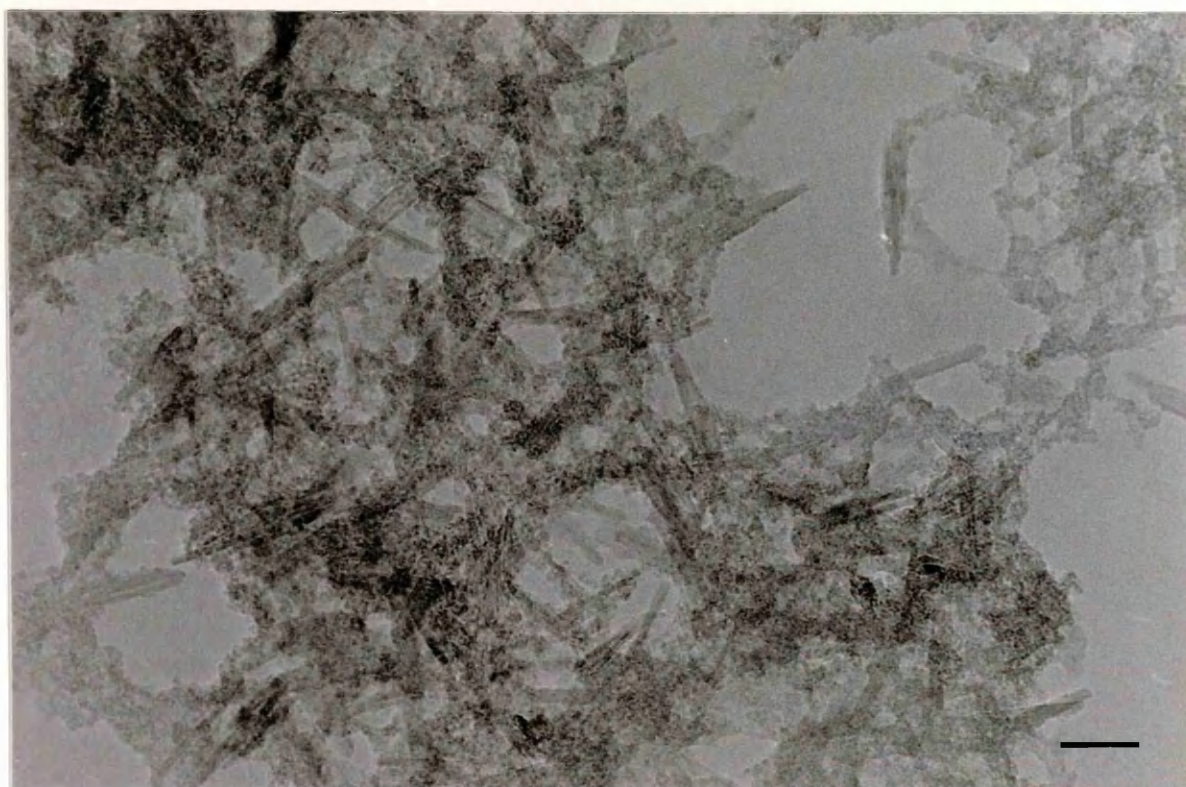


Plate 64:- Final product formed on precipitating a gel containing 15 mol% zinc which had previously been aged for 3 days in acidic media. Scale bar represents 50nm.

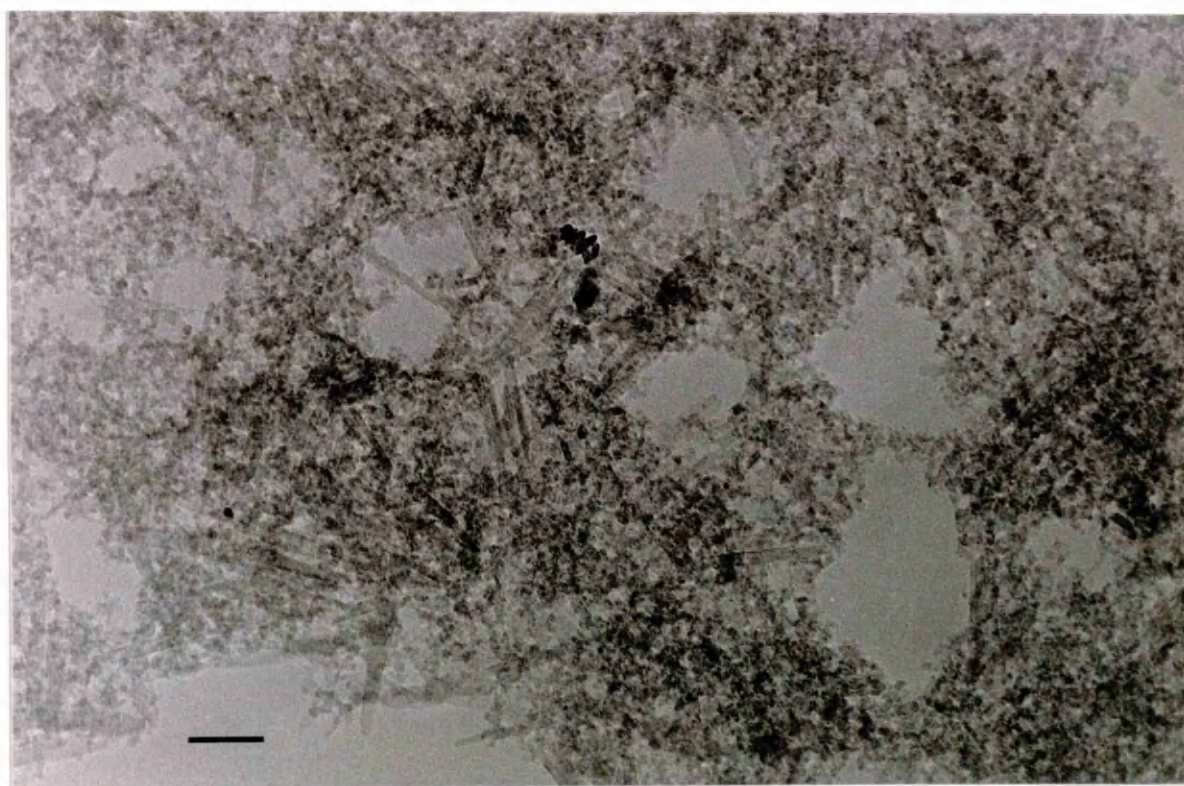


Plate 65:- Product formed under identical ageing conditions, but in the presence of 25 mol% zinc. Scale bar represents 50nm.

final products from gels which had been aged for 3 days prior to addition of 15 and 25 mol% zinc. Both were found to comprise zinc-magnetite and goethite. Although the goethite crystals in the former product exhibited a ragged appearance, they were better-defined than those formed in the corresponding product aged for only 25 hours. The proportion of goethite in the latter sample was smaller, but the crystals could still be easily identified. EDX data for the goethite crystals in the above samples gave occasional evidence for low levels of zinc incorporation.

If the initial ageing time was raised to 4 days or more, short rafts of material were deposited from solution (ie "crystalline" goethite precursors were now present). After precipitation, chains of flocculated acicular crystals were observed to some extent at all levels of zinc addition.

Plate 67 shows goethite chains present in one of two identical gels aged for 12 days in acidic solution. 50 mol% zinc was then added to one of the gels and the pH of both was raised to 12. After the samples were further aged at elevated temperature, the control was found to comprise goethite, while the crystalline phases present in the transformation product formed in the presence of 50 mol% additive were identified from XRD, electron diffraction and EDX data as goethite, zinc-magnetite and zinc oxide, ZnO. The XRD profiles are shown in Figs. 3.14 and 3.15. TEM observation showed the overall lengths of the chains to have changed little in both cases. Plates 68 and 69 show both samples 48 hours after precipitation. While extensive length-wise (c-direction) growth of the chain units

had occurred in the control product, the presence of zinc (Plate 69) appeared to have completely inhibited growth.

Lastly, a series of samples were prepared by adding various proportions of zinc species to ferric nitrate solution prior to the initial ageing stage, in order to examine the effect of the additive on goethite nucleation in solution. However, the results obtained were ambiguous. As expected, goethite chains soon developed in the gels. Electron diffraction patterns obtained for individual chains were often essentially single-crystal in nature (cf control samples), and could be indexed as goethite typically imaged in [110] or [001]. The presence of zinc did not appear to modify the morphology of goethite to a great extent, although high-resolution imaging of the chains gave some evidence to suggest that pitting on the crystal surfaces was enhanced under these growth conditions.

Ageing of a ferric solution having $Zn/(Zn+Fe)=50\%$ and $OH:Fe=3:4$ for several months at room temperature without precipitation at high pH was found to produce a crystalline product comprising masses of material which could be identified by diffraction data as chains of $\alpha\text{-FeOOH}$. Crystalline material having a spinel structure appeared to be absent. Formation of zinc-magnetite appeared to require interaction with ferrihydrite.

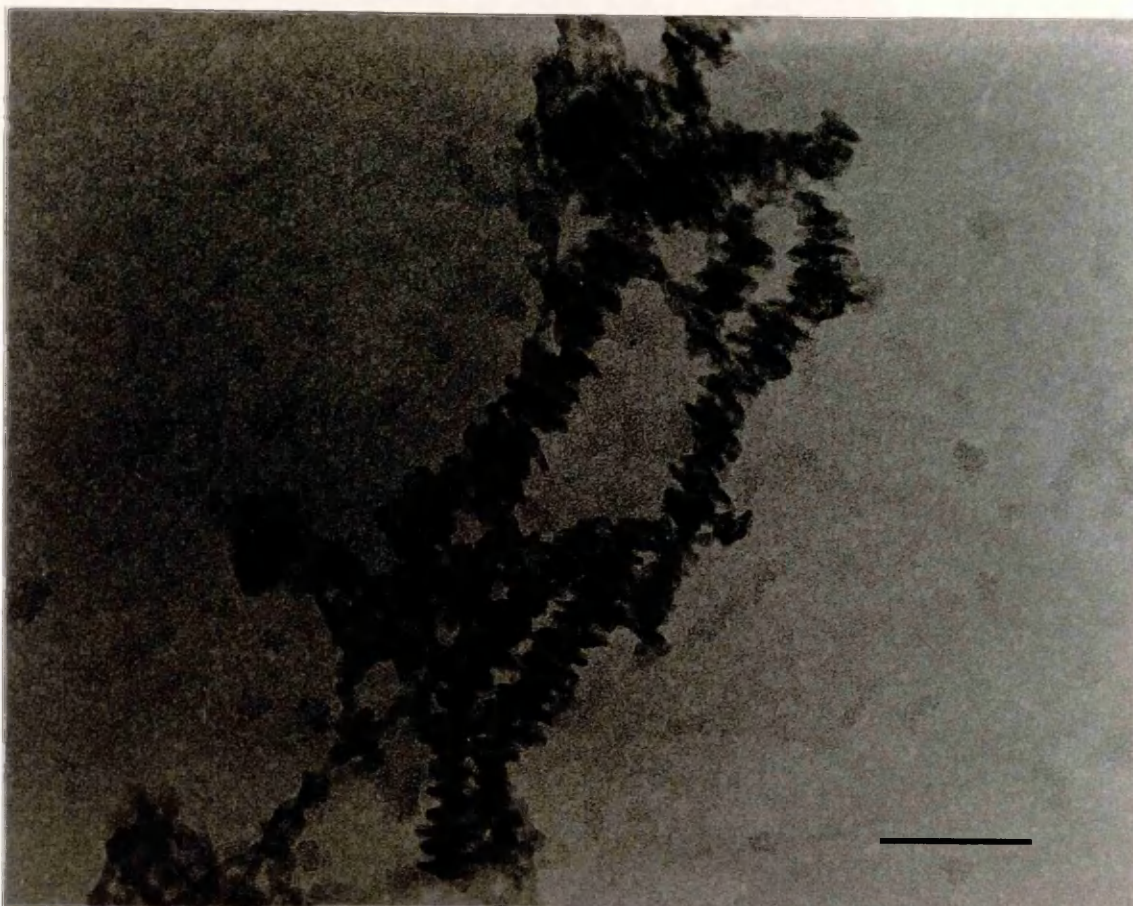


Plate 66:- Goethite chains present in an extensively hydrolysed gel after 12 days ageing in the absence of additive. Scale bar represents 50nm.

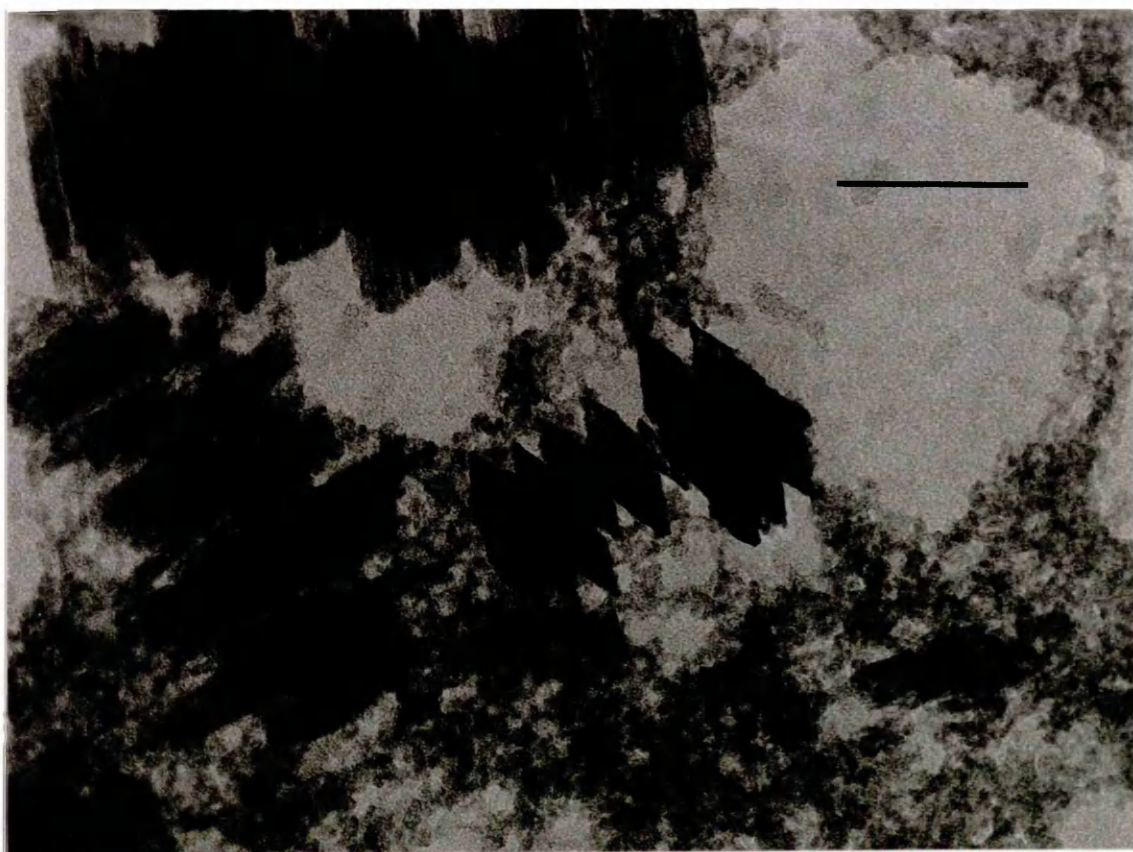


Plate 67:- Product formed on precipitating the gel shown in Plate 66. Scale bar represents 100nm.

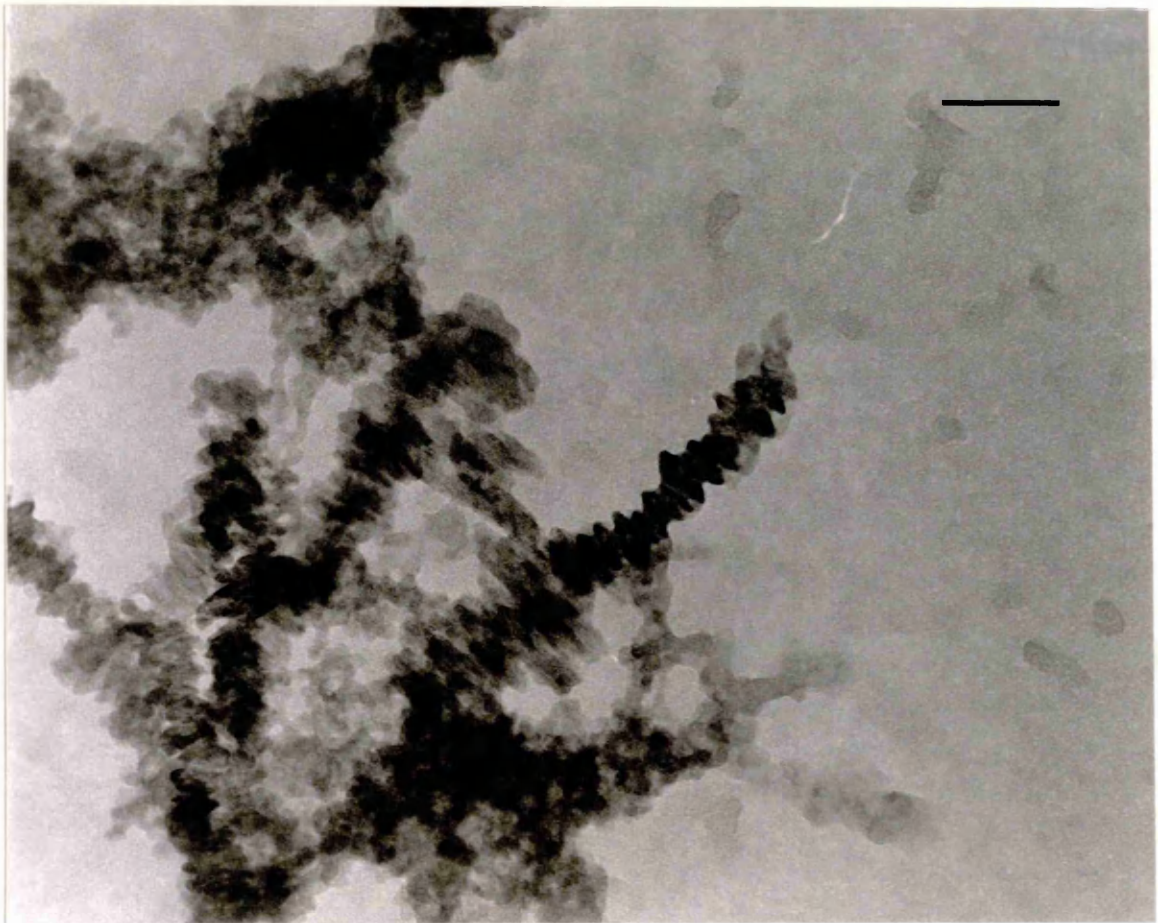


Plate 68:- Product formed on precipitating an identical gel, but in this case with 50 mol% zinc added immediately prior to addition of base. Scale bar represents 50nm.

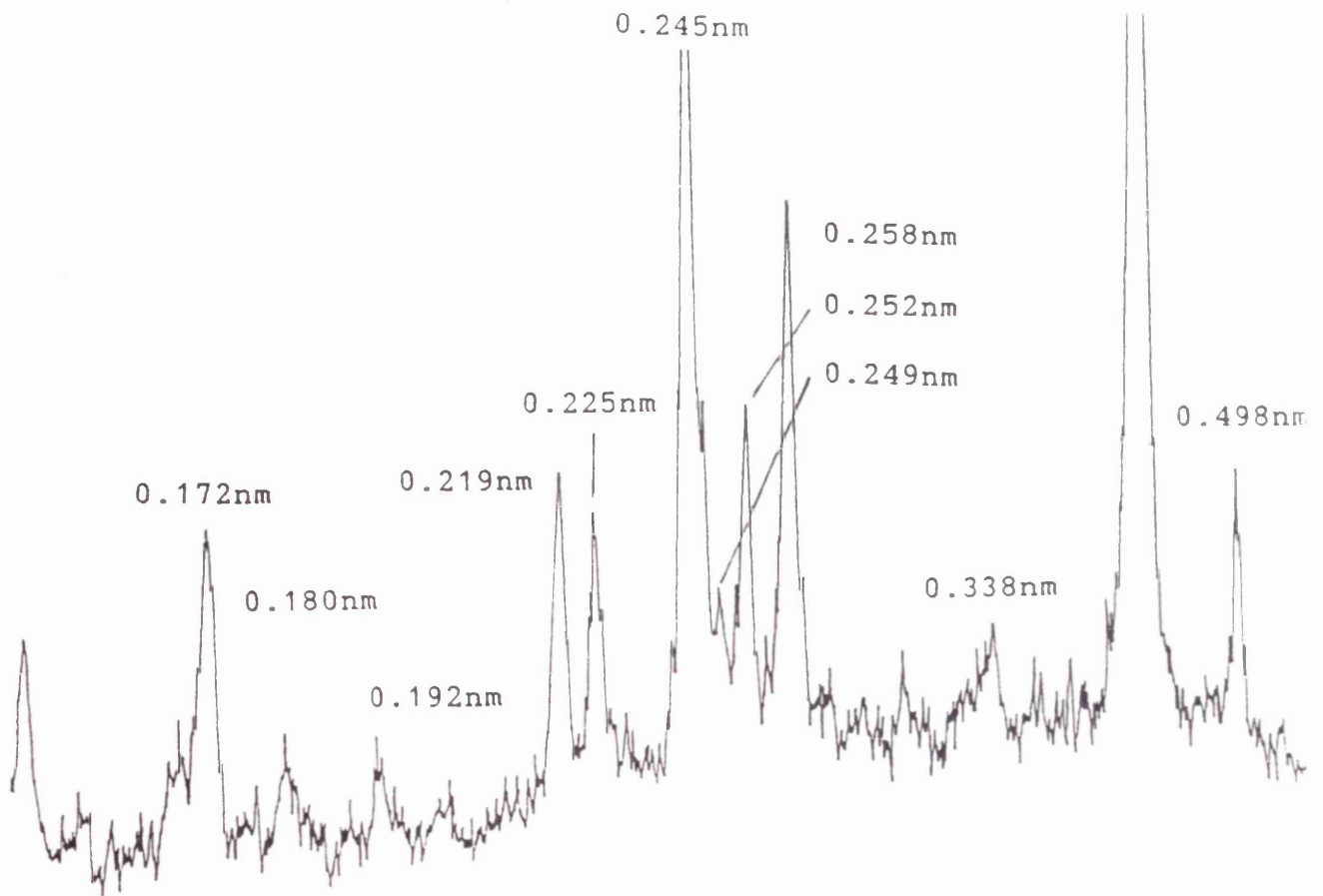


Fig.3.14:- XRD profile for goethite formed on precipitating a gel previously aged for 2 weeks in acidic media (Plate 67).

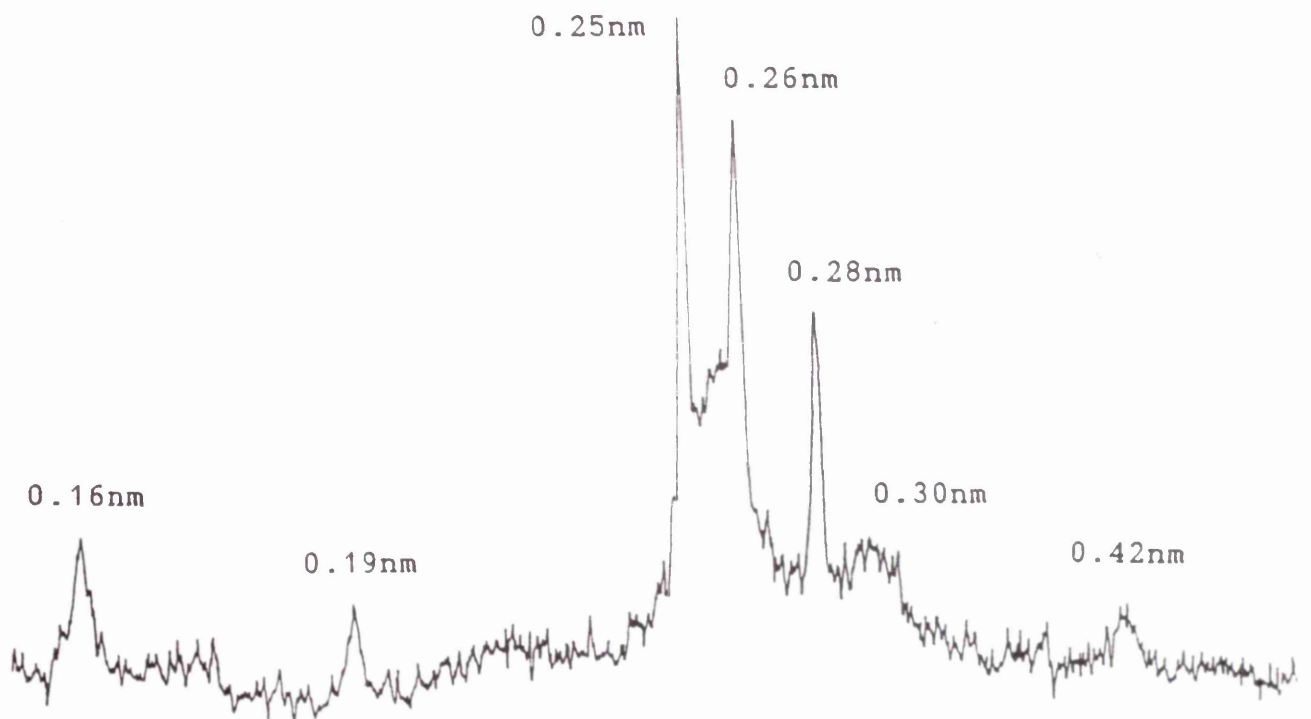


Fig.3.15:- XRD profile for a product formed on precipitating a gel identical to that described above, but with 50 mol% zinc added immediately prior to addition of base (Plate 69). The main spacings are consistent with ZnO. Goethite growth is suppressed.

3.7. THE EFFECT OF NICKEL (II) SPECIES ON THE NATURE AND MORPHOLOGY OF CRYSTALLINE PHASES PRODUCED FROM FERRIHYDRITE.

Ferric nitrate solutions containing between 5 and 40 mol% nickel (II) species were made up, and the pH quickly raised to either 7, 9 or 12 by addition of base. The resultant precipitates were then aged at elevated temperature (70°C) for periods of up to several months. The crystalline products which developed were characterised from TEM/EDX and diffraction data.

3.7.1. CHARACTERISATION OF PRECIPITATES

Raising the pH of solutions comprising a mixture of ferric and nickel nitrates led to immediate formation of a red-brown solid, the colour of which became darker as the proportion of nickel in the system was increased. TEM examination of these co-precipitates showed masses of small, poorly-defined platelets similar in morphology to the synthetic ferrihydrite observed in control samples. Selected-area diffraction patterns typically showed three broad bands which were consistent with spacings for the ferric oxide-hydrate. However, the presence of relatively low levels of nickel also led to the simultaneous formation of an amorphous sheet-like solid, the proportion of which was found to increase with the level of additive initially present. EDX data indicated that this was a separate nickel phase.

In the absence of ferric species, precipitation of nickel nitrate solution at pH 12 led to formation of a green hydroxide gel which was identical in morphology to the sheets

observed in the Ni-ferrihydrites (Plate 69, inset). If the precipitate was then aged at 70°C the gel quickly crystallised, forming a powdery green solid which could be identified from electron diffraction data (Plate 69) as crystalline nickel hydroxide, $\text{Ni}(\text{OH})_2$.

In order to determine whether any proportion of "free" additive was also directly associated with ferrihydrite, EDX data was obtained for selected areas from which the sheet-like hydroxide was absent. Fig. 3.16 shows a profile from a precipitate containing 10 mol% additive. Measurement of the relative integral areas gave $C_{\text{Ni}}/C_{\text{Fe}}=0.11$, corresponding to approximately 10 mol% nickel associated with the ferrihydrite.

3.7.2. TRANSFORMATION PRODUCTS FORMED ON AGEING Ni-FERRIHYDRITE PRECIPITATES AT HIGH pH

TEM examination of products formed in the presence of up to 15 mol% nickel indicated that the only crystalline ferric phase which had developed was goethite, observed as acicular crystals typically 300-500nm in length which often comprised several intergrowths (Plate 70). In the above products (and also the corresponding precipitates), only a small proportion of nickel hydroxide was found to be present. Selected-area diffraction data indicated that the background material observed in the above products mainly comprised unconverted ferrihydrite. Additional spacings consistent with either hematite or a spinel phase were not observed. Patterns obtained for individual acicular crystals could be indexed

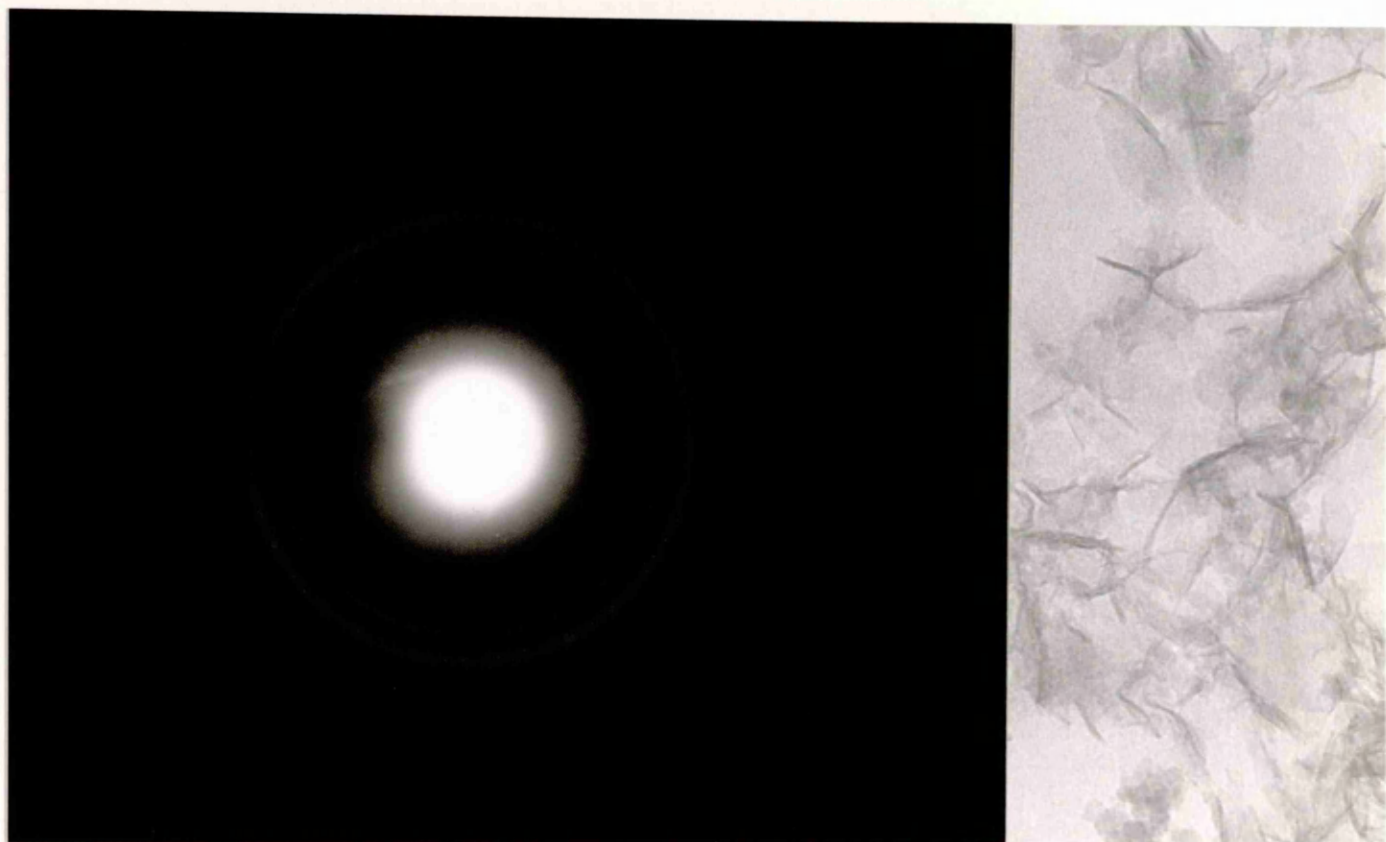


Plate 69:- Selected-area diffraction pattern for crystalline nickel hydroxide (inset).

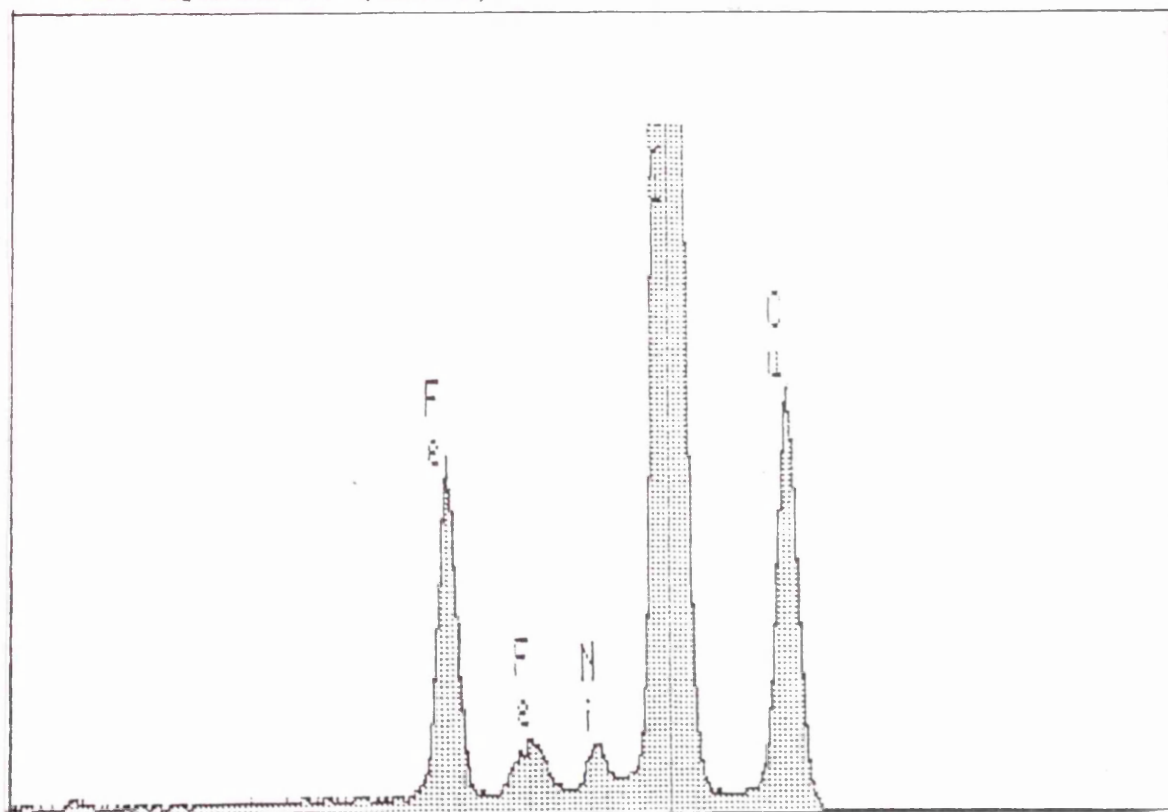


Fig.3.16:- EDX profile obtained for a ferrihydrite gel containing 10 mol% nickel (II) species.

as singly-diffracting goethite imaged in [100] or [110] (although the crystals appeared to adopt a wider range of orientations relative to the electron beam than was the case for control samples).

If the level of nickel present was increased further, it was found that the nucleation, growth and crystallinity of goethite was inhibited. Crystals produced in the presence of 20-40 mol% additive exhibited an increasingly ragged appearance (Plate 71), while a much higher proportion of $\text{Ni}(\text{OH})_2$ sheets was observed in the products. The development of irregularities such as etch pits (Plate 72, arrowed) also became common in the presence of higher levels of nickel. However, the effect of additive species on the local goethite structure was not investigated, since the crystals were very thin and unsuitable for high-resolution imaging.

Fig. 3.17 shows an EDX profile obtained for the crystal shown in Plate 72 (which had formed in a gel containing 30 mol% additive). In this case, the calculated nickel: iron mass concentration ratio, 0.08, corresponds to approximately 7 mol% additive incorporation in the crystal structure. Unlike goethite formed in the presence of zinc, the crystals examined here were all found to have taken up some proportion of additive species during growth. The influence of nickel (II) in directing goethite formation is therefore certain to involve some interaction with the crystals in solution. A full summary of incorporation values obtained for individual goethite crystals formed in the presence of between 10 and 40 mol% nickel is shown in Table 3.12. The maximum proportion

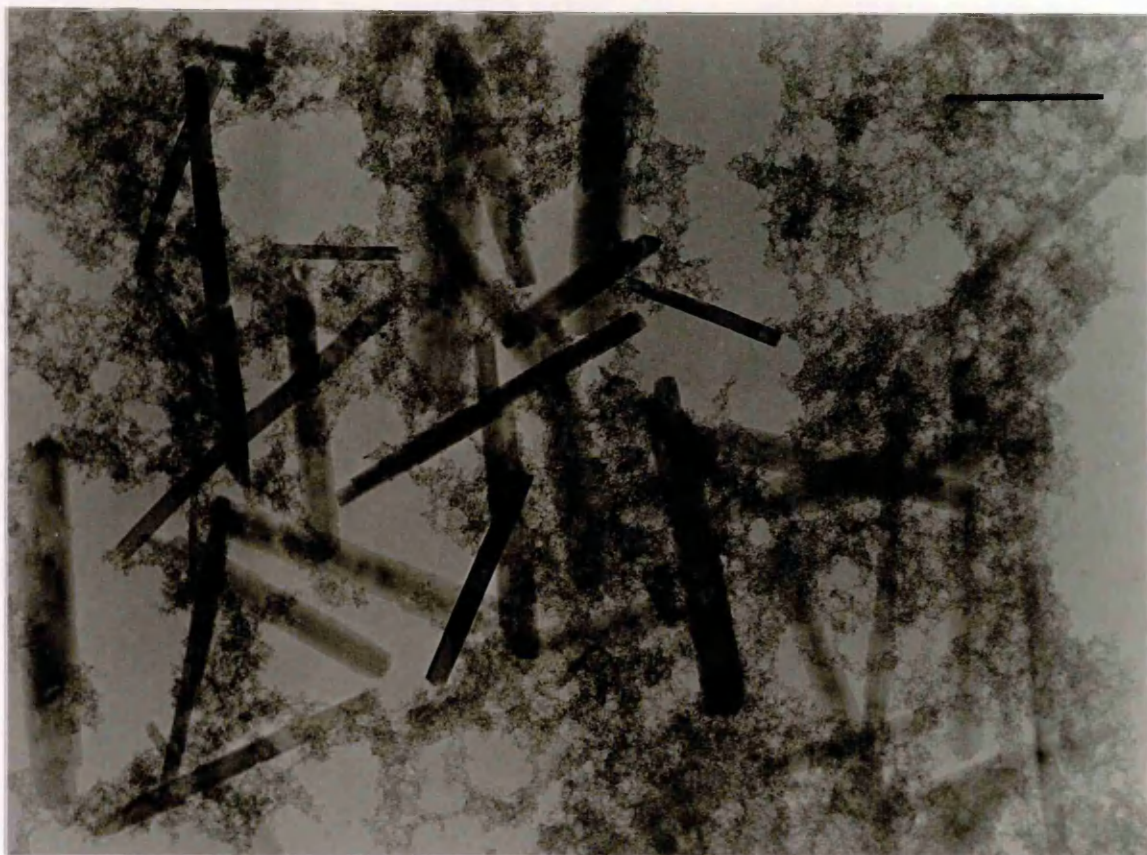


Plate 70:- Transformation product formed on ageing ferrihydrite at pH 12 in the presence of 10 mol% nickel. Scale bar represents 100nm.



Plate 71:- Transformation product formed at pH 12 in the presence of 40 mol% nickel. Scale bar represents 100nm.



Plate 72:- Goethite crystal formed at pH 12 in the presence of 30 mol% nickel. Scale bar represents 50nm.

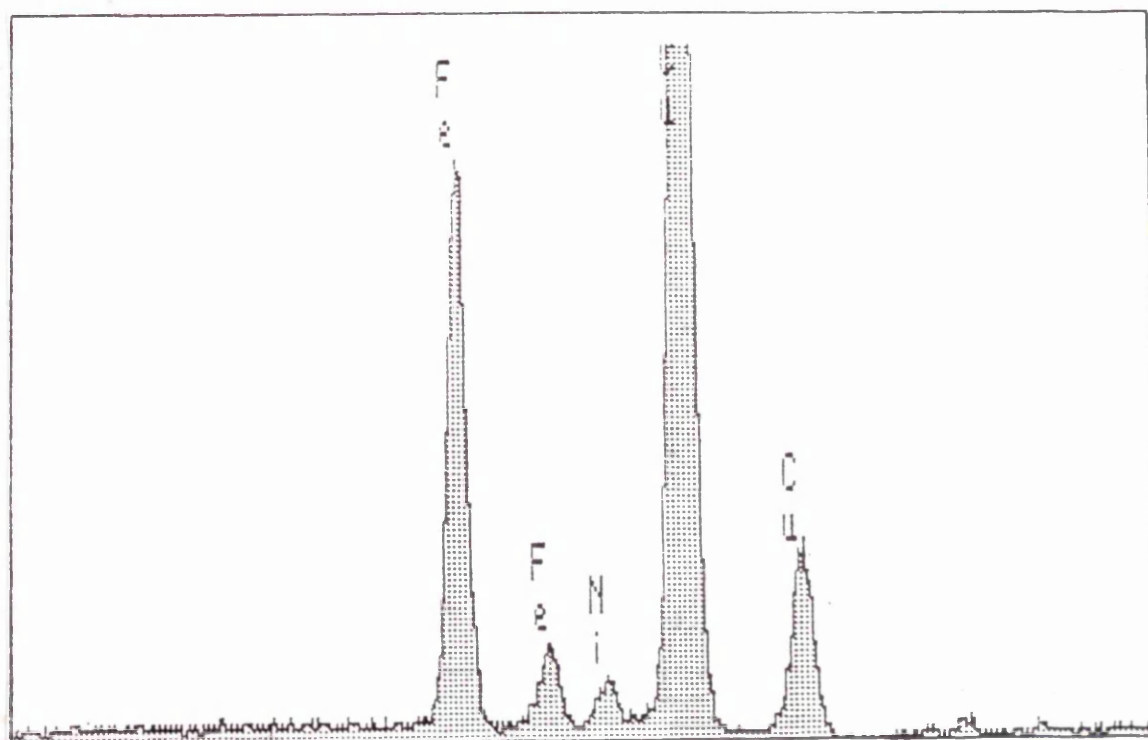


Fig.3.17:- EDX profile obtained for the goethite crystal shown above.

of additive taken up appeared to be in the region of 8-9 mol%. At high levels of addition, most of the nickel remained associated with the background material.

TOTAL Ni ADDED	GOETHITE pH 12 (mol%) 14nm PROBE	Ni-SPINEL pH 7 (mol%) 14nm PROBE
10 mol%	4.5-7.1	10.1-16.3
20 mol%	3.7-7.9	17.3-26.4
30 mol%	2.8-8.7	25.0-30.6
40 mol%	4.5-7.9	

Table 3.12:- EDX data obtained for nickel-ferrihydrites and corresponding transformation products formed on ageing at pH 7 and 12.

Results showed that the presence of nickel did not promote twinning of goethite crystals to any notable extent, even at high levels of addition. Epitaxial twinning was not observed since hematite was absent from the products, but some composite twins did form. These were mainly of dendritic type, and probably arose from the need to accommodate substituent cations in the crystal structure.

Diffraction data relating to the formation of a spinel phase at pH 12 in the presence of nickel (II) species was ambiguous. The larger spinel crystals produced at pH 9-12 from zinc-ferrihydrite gels containing 7.5-20 mol% additive were absent from each of the nickel-containing products, even after extended ageing. Selected-area diffraction patterns for background material, not including the separate nickel phase, from a sample produced in the presence of 20 mol% additive gave a range of spacings which were measured at 0.25nm, 0.21nm and 0.15nm. These results are consistent with the

expected reflections for ferrihydrite. Other than the above spacings, the only reflections observed were those corresponding to nickel hydroxide. The above data are inconclusive, but it might be the case that association of the insoluble additive hydroxide with ferrihydrite inhibited spinel formation.

3.7.3. TRANSFORMATION PRODUCTS FORMED ON AGEING Ni-FERRIHYDRITES AT NEUTRAL pH

A second set of nickel-ferrihydrite precipitates containing up to 40 mol% nickel were prepared and aged at pH 7 for up to several weeks at 70°C. Plate 73 shows a selected area of a product formed at 10 mol% addition. The corresponding diffraction pattern (Plate 74) shows spacings measured at 0.29nm, 0.25nm, 0.21nm, 0.16nm and 0.15nm. These values are consistent with reflections for nickel-magnetite, NiFe_2O_4 . Extra symmetry-forbidden spacings were not evident. Small spinel crystals up to 15nm in diameter could be identified lying amongst the unconverted ferrihydrite. Plate 73 (inset) shows lattice fringes measured at 0.30nm resolved on a crystallite. These are consistent with (220) spacings for nickel-magnetite.

TEM and electron diffraction data obtained for subsamples removed from the gels up to 2 months after precipitation indicated that the only crystalline ferric phase present in products formed in the presence of >10 mol% nickel was the doped spinel. Formation of $\alpha\text{-Fe}_2\text{O}_3$ had been completely inhibited by the presence of 10 mol% additive (cf

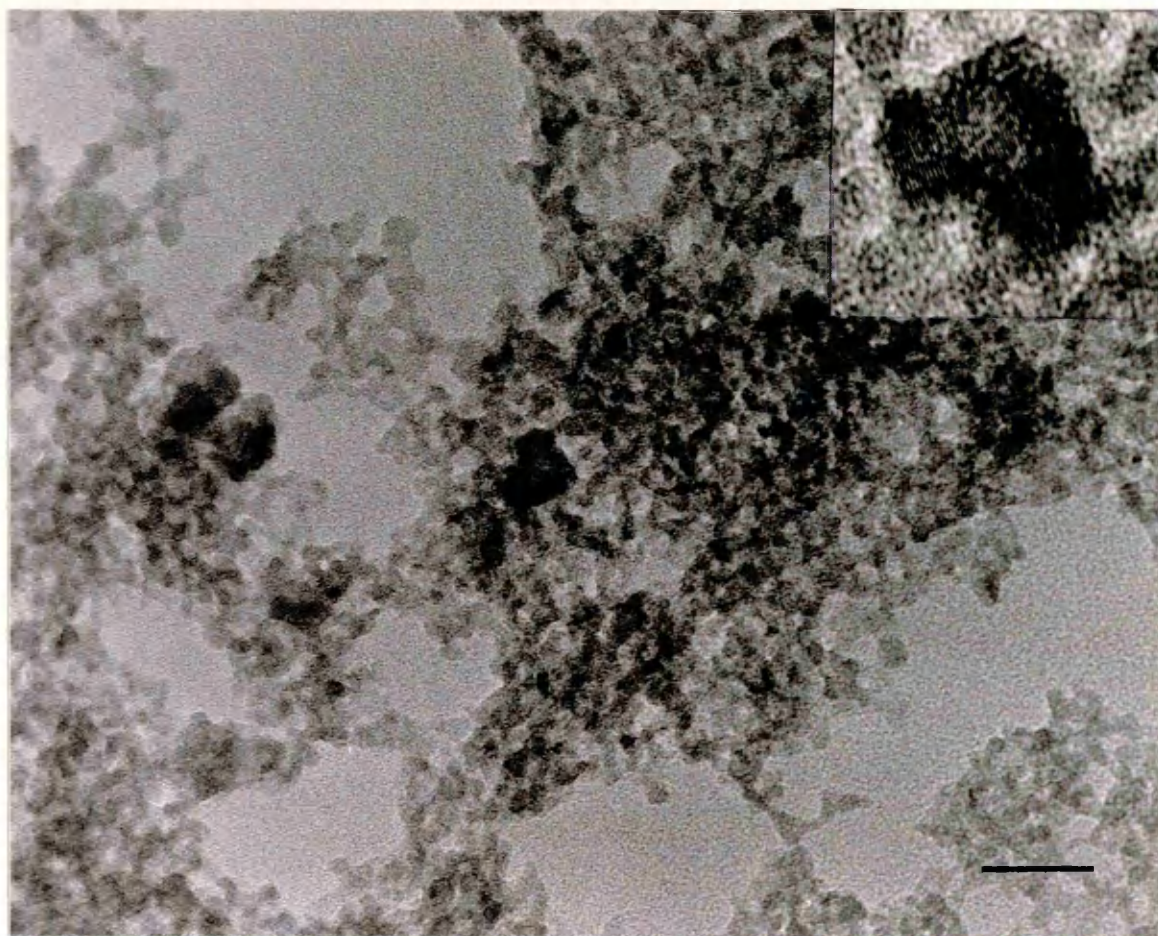


Plate 73:- Product formed at neutral pH in the presence of 10 mol% nickel. A spinel crystal is shown inset. Scale bar represents 20nm.



Plate 74:- Diffraction pattern obtained for the area shown in Plate 74.

similar products formed in the presence of 10 mol% zinc, Section 3.4.2). Products formed at up to 7 mol% addition comprised hematite crystals containing low levels of nickel species.

Further precipitates containing 10, 20 and 30 mol% copper (II) and cobalt (II) species were next made up and aged at pH7. After 3 weeks ageing at elevated temperature, and more than 6 months further ageing at room temperature, electron diffraction data indicated that the copper-ferrihydrites remained essentially unconverted. The cobalt-ferrihydrites had, after several weeks to months ageing, begun to transform. Diffraction data again showed that hematite was absent from the products. The only spacings observed were those consistent with cobalt-magnetite.

3.8. TRANSFORMATION PRODUCTS FORMED ON AGEING FERRIHYDRITE IN THE PRESENCE OF BOTH Zn(II) AND Ni(II) SPECIES.

Characterisation of transformation products formed on ageing nickel-ferrihydrites containing up to 40 mol% additive indicated that the development of well-defined Ni-magnetite was not favoured at high pH. By contrast, transformation of zinc-ferrihydrites yielded a high proportion of spinel crystals in the presence of only 8 mol% additive. In order to determine the necessary conditions for spinel nucleation, and also to compare the relative ease of uptake of the above additives into the crystal structure, a range of solutions comprising mixtures of zinc, nickel and ferric nitrates (containing a total of between 20 and 50 mol% additive) were co-precipitated at pH 12. The resultant ferrihydrite gels were then aged at elevated temperature for up to several weeks.

3.8.1. CHARACTERISATION OF TRANSFORMATION PRODUCTS

Samples produced in the above manner were found to comprise a mixture of small cubic crystals, unconverted ferrihydrite and (in the presence of more than 10 mol% nickel) a sheet-like material identified as crystalline nickel hydroxide. TEM examination did not suggest that either goethite or hematite was present in any of the products.

Plate 75 shows the product formed in the presence of 10 mol% each of zinc and nickel. The range of spacings measured from the corresponding diffraction pattern (Plate 76) was consistent with the cubic spinel phase $(\text{Zn}, \text{Ni})\text{Fe}_2\text{O}_4$. No evidence for the presence of symmetry-forbidden reflections

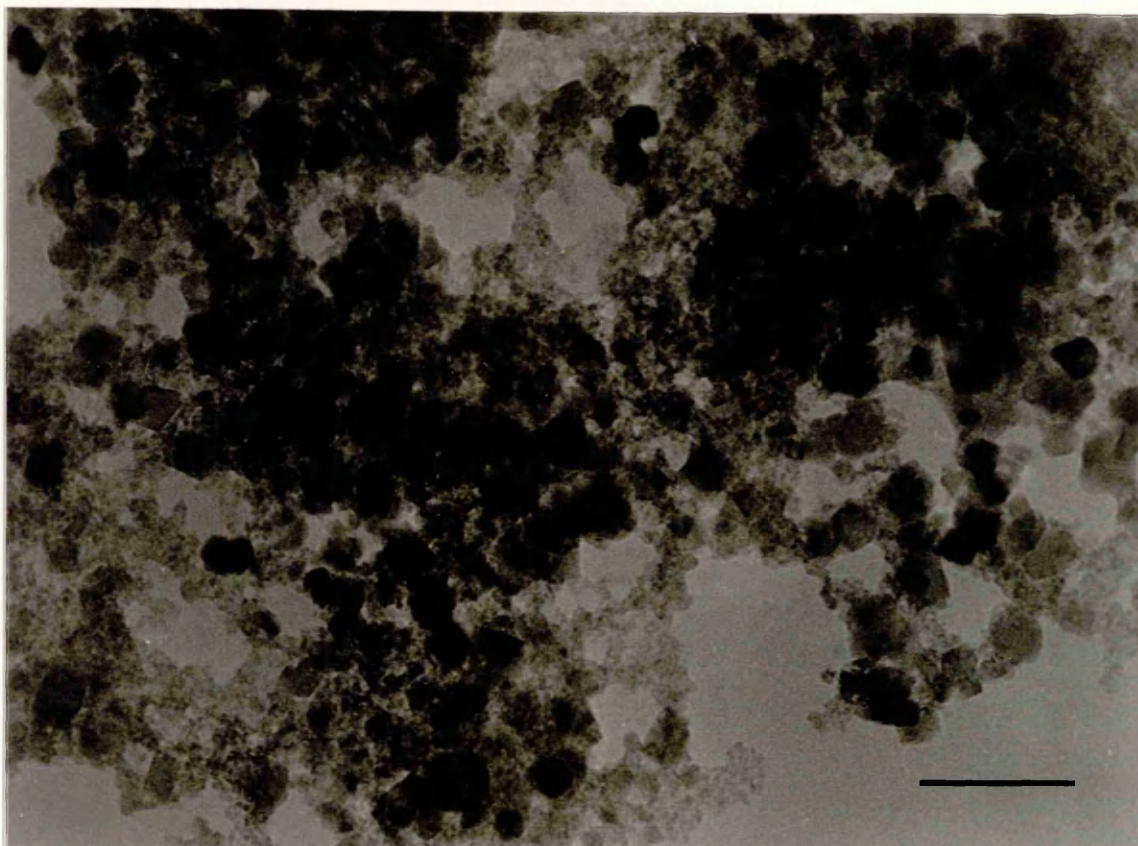


Plate 75:- Product formed at pH 12 on ageing a ferrhydrite gel containing 10 mol% zinc and 10 mol% nickel. Scale bar represents 50nm.

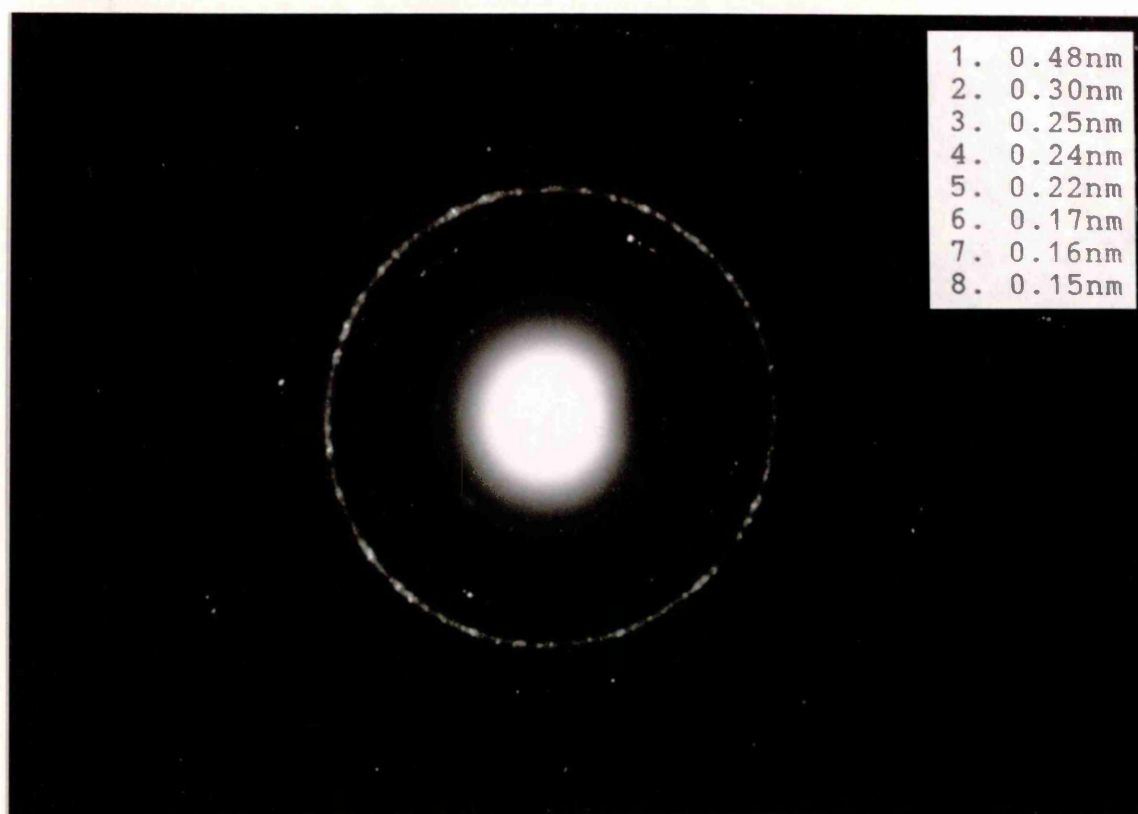


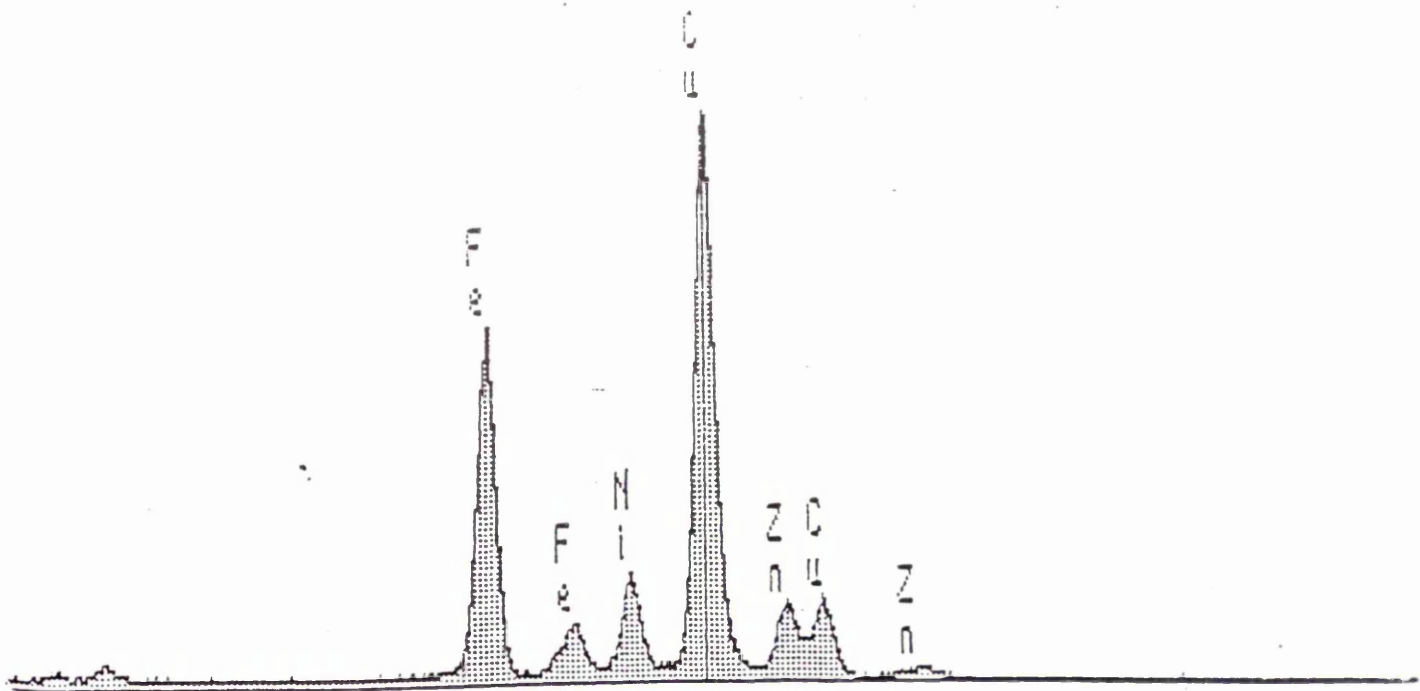
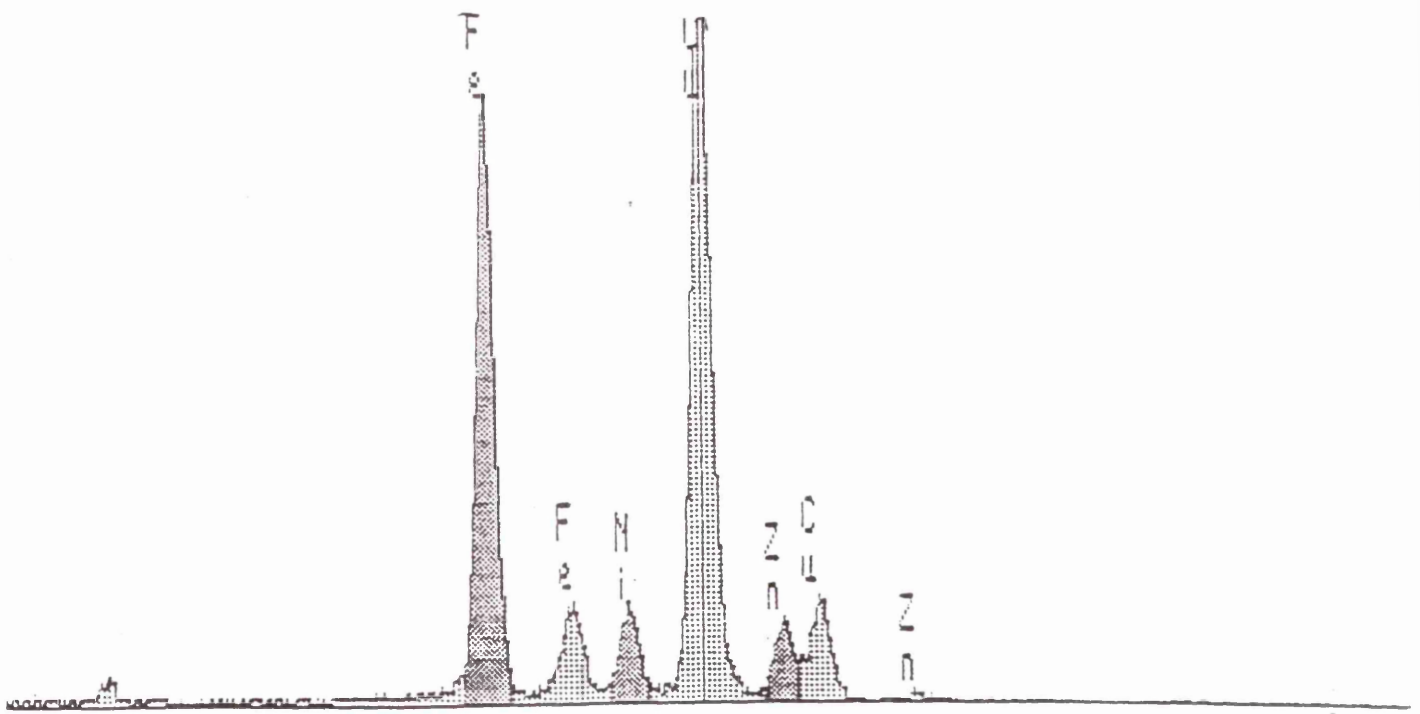
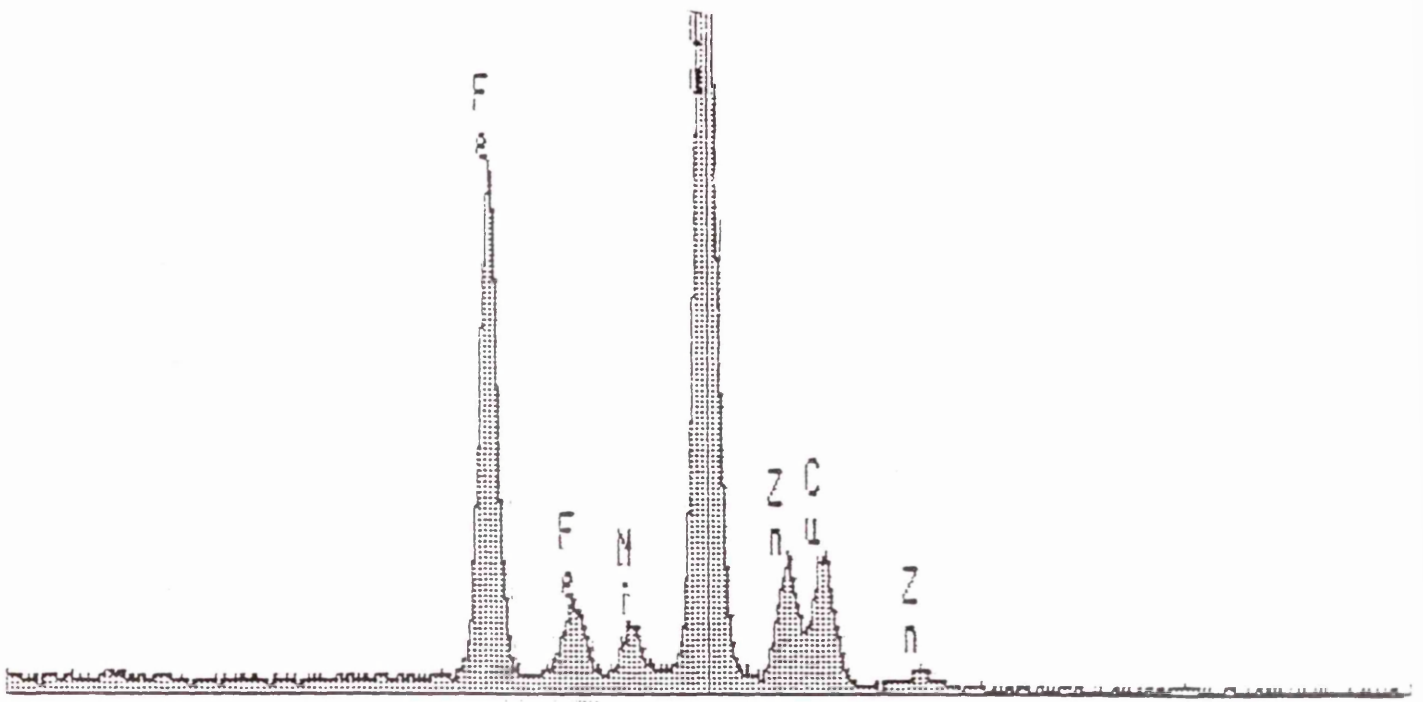
Plate 76:- Selected-area diffraction pattern for Plate 75.

was observed for any of the products examined. The diameters of the crystals shown in Plate 76 were found to lie between 10 and 25nm. If the additive levels were increased to 25 mol% zinc/25 mol% nickel, the observed dimensions decreased slightly to between 10 and 15nm.

3.8.2. ADDITIVE INCORPORATION IN THE TRANSFORMATION PRODUCTS

EDX data obtained for individual spinel crystals are summarised in Table 3.13. In almost every case, some proportion of both additive species had been taken up during growth. Fig. 3.18 a) shows a typical profile obtained for a particle formed in the presence of 10 mol% each of zinc and nickel. Integral measurement gave $C_{Zn}/C_{Fe} = 0.35$, corresponding to 23 mol% zinc incorporation. The corresponding ratio for nickel was determined at 0.085, giving approximately 7 mol% uptake of the additive. A large number of crystals examined in the above sample were found to contain a level of nickel which was broadly comparable to that added initially (10 mol%), while the level of zinc was often considerably higher (19-25 mol% being the average level detected). However, the additive distribution from crystal to crystal was not constant. The profile shown in Fig. 3.18 b) (taken from the same sample as Fig. 3.18 a)) gave $C_{Zn}/C_{Fe} = 0.16$ (12 mol% zinc) and $C_{Ni}/C_{Fe} = 0.13$ (11 mol% nickel). In this case, both additives are present in amounts close to those added to the system as a whole. In some other cases, the crystals under examination were found to contain more nickel than zinc (Fig. 3.18.c)). If the total additive level was raised to between 40 and 50 mol%, a

Fig.3.18 a),b) and c) (over):- Typical EDX profiles obtained for individual spinel crystals formed in the presence of 10 mol% each of zinc and nickel.



comparable proportion of each additive was found to be incorporated in the crystals.

TOTAL Zn AND Ni ADDED	SPINEL CRYSTALS Zn (mol%) 14nm PROBE	Ni (mol%) 14nm PROBE
10 mol% each	12.6-24.5	5.4-12.1
15 mol% each	10.0-27.3	9.5-17.0
20 mol% each	18.2-22.7	19.7-21.5
25 mol% each	17.4-26.4	15.3-27.0

Table 3.13:- Uptake of zinc and nickel species in individual spinel crystals formed during transformation of zinc/nickel-ferrihydrite gels.

In contrast to zinc-magnetite, $ZnFe_2O_4$, nickel-substituted magnetite adopts the inverse spinel structure. The lattice of the zinc/nickel spinel formed here is therefore likely to feature replacement of Fe^{3+} by Zn^{2+} in tetrahedral sites, with a proportion of Ni^{2+} occupying octahedral interstices. If the structure is based on the spinel unit cell (comprising 32 oxygen atoms, 16 octahedral and 8 tetrahedral sites), then, using the calculated ratios, the profiles shown in Figs. 3.18. a) and b) would give average unit cells calculated at, respectively, $Zn_5Ni_{1.4}Fe_{17}O_{32}$ and $Zn_{2.5}Ni_{2.3}Fe_{18.2}O_{32}$.

Again, the degree of accuracy available on applying EDX analysis limits the confidence with which these results can be stated. However, the data indicated that, in the above sample, the upper limit of zinc incorporation into individual spinel crystals was over twice the total level added to the system. This result is similar to that obtained for the spinel phase which had developed from ferrihydrite in the presence

of up to 20 mol% additive (Section 3.4). In the case of the zinc/nickel spinel phase, extra reflections forbidden for the face-centred unit cell (which were observed for some zinc-containing products) were not present. Similarly, indexing of lattice fringes resolved in high resolution micrographs gave results which were consistent with a face-centred structure. It is therefore unlikely that any extended ordering was present in the crystals.

3.9. EFFECTS OF BEAM DAMAGE ON TEM OBSERVATION AND CHARACTERISATION OF FERRIC OXIDES AND OXYHYDROXIDES

3.9.1. BEAM DAMAGE IN GOETHITE (α -FeOOH)

The damaging effect of prolonged exposure to the electron beam was found to be most evident for crystals of goethite. The excess loss of H_2O and subsequent structural modifications were reflected in the development of characteristic surface pitting and loss of spacings in single-crystal electron diffraction patterns. High-resolution micrographs occasionally often showed the presence of dislocation faults (Section 3.3).

Mann *et al* [64] also quoted frequent dislocations and areas of irregularity in high resolution micrographs showing the local domain boundary structure in synthetic acicular goethite crystals. Whether these faults are inherent or promoted by beam interaction is not clear. As in the present study EDX data did not show the presence of impurities which might have promoted fault formation in specific areas. Many

regions of strain, observed as extinction and bend contours on large acicular crystals grown at high pH have also previously been quoted [69], but these effects may also have been caused by localised heating during TEM observation. Mann concluded that the development of domain boundaries was highly coherent during growth, although inherent regions of disorder could be induced at high pH through competition between OH^- and $\text{Fe}(\text{OH})_4^-$ at the crystal surface.

3.9.2. BEAM DAMAGE IN SPINEL CRYSTALS.

High resolution imaging has been applied to an examination of the local structure in spinel crystals which were found to develop in ferrihydrite gels. In most cases, the particles under examination were found to be consistent with the expected cubic structures. However, care must be taken that beam damage did not create artefacts from which spurious results were derived.

During routine TEM imaging of spinel crystals, major structural phase modifications were not observed. Prolonged exposure to a high beam intensity often resulted in a breakdown in periodicity, which was reflected in the transformation of single-crystal diffraction patterns and the loss of lattice fringes during high resolution examination. David *et al* [109] found that $\gamma\text{-Fe}_2\text{O}_3$ prepared by reduction of Fe_3O_4 under wet conditions using a variety of routes always included appreciable quantities of water, which could not be removed without destroying the spinel structure and forming the alpha oxide. In addition, the diffusion of cations/cation

sites on heating magnetite/maghemite samples has been widely documented. Gallagher [110] concluded from XRD and kinetic measurements that reduction of Fe_3O_4 was controlled by outward diffusion of Fe cations to the surface.

In the present work, high resolution micrographs showing individual spinel crystals for which diffraction patterns had already been obtained showed no change in periodicity unless the structure broke down completely. If a number of images were taken for a single spinel crystal, and the corresponding power spectra were carefully measured and compared, it was found that the spacings were all similar, each being in accord with the diffraction data. No obvious extra spacings were observed after exposure to the beam.

CHAPTER 4:- DISCUSSION

4.1. INFLUENCE OF FOREIGN CATIONS ON THE DEVELOPMENT OF GOETHITE AND HEMATITE FROM FERRIHYDRITE.

4.1.1. CHANGES IN PRODUCT COMPOSITION.

Previous studies concerning the influence of divalent transition metal cations in directing the transformation of ferrihydrite have found that most will stabilise the solid against dissolution, and so retard the subsequent transformation to crystalline ferric oxide/oxyhydroxide phases [73-80]. Kinetic data on the effects of Mn(II), Co(II), Ni(II), Cu(II) and Zn(II) species on the rate of transformation of ferrihydrite at pH 12 [80] have shown that, while zinc and copper extended the induction period during which nucleation of ordered phases occurred and also retarded the subsequent growth stage, the influence of nickel and cobalt only became important in the last 30-40% of the reaction. Only manganese species did not influence the reaction kinetics to any great extent. The additives studied can then be placed in the order Zn, Cu >> Ni > Co >> Mn with respect to their stabilising abilities. This corresponds to the Irving-Williams Series [111] for the expected strength of interaction with ligands (in this case O^{2-} and OH^- on ferrihydrite).

The surface of freshly-precipitated ferrihydrite is well known to contain highly active sites which are capable of immobilising ionic species [112]. The extent of adsorption of each additive on the initial precipitate is of major importance in directing the course of the subsequent transformation to crystalline phases.

The series shown above also reflects the relative ability of each additive to suppress the formation of goethite, thereby promoting hematite development at a higher pH. At pH 12, products formed in the absence of additives were found to be effectively hematite-free. Under similar conditions, Cornell and Giovanoli [79] found that the presence of only 9 mol% copper(II) species inhibited goethite formation to the extent that the presence of the oxyhydroxide could no longer be determined by powder diffraction analysis. The present work has shown that, in accord with kinetic and XRD data obtained by Cornell and Giovanoli [80], zinc also strongly retarded the transformation of ferrihydrite and promoted formation of hematite at pH 12 (although not to the same extent as copper). If the gel pH was lowered to 9, the control samples already contained a substantial proportion of hematite. In the presence of zinc, goethite formation was suppressed much more quickly than at pH 12.

Further results obtained in the present work have shown that the presence of nickel species, like manganese and cobalt [75,113], did not retard the transformation sufficiently to promote formation of hematite in products formed at high pH. Increasing the level of additive was, however, found to gradually suppress goethite formation. At pH 12, the only identifiable crystalline ferric phase produced in the presence of up to 40 mol% nickel was goethite. In contrast to results obtained for samples formed in the presence of zinc, well-defined spinel crystals were not observed.

The above data are in accord with the competing mechanisms by which goethite and hematite are thought to nucleate and grow. At pH 12, the rate of dissolution of ferrihydrite is at a maximum, and only those additives which are sufficiently capable of blocking the release of soluble ferric species (Cu and Zn) will allow hematite formation to become competitive. This is not to say, however, that these additives do not also inhibit hematite formation. The development of goethite may simply be hindered to a greater extent.

At pH 7, ferrihydrite transformed to hematite in less than 2-3 days at elevated temperature. The presence of additive species was found to retard the transformation for more prolonged periods. Addition of 15-20 mol% copper to the gels was found to inhibit formation of crystalline phases almost indefinitely. Zinc species also strongly retarded the reaction, but after periods of ageing ranging from weeks to months, gels containing about 25 mol% additive yielded products containing zinc-magnetite. Addition of 10 mol% copper, zinc, nickel or cobalt was found to strongly inhibit the development of hematite. At low levels of addition, products were found to comprise hematite and/or the corresponding spinel phase, which in each case began to develop in the presence of about 7-8 mol% additive.

Results have shown that, although a limited increase in ordering may have occurred with time, more extensive changes in the structure of individual ferrihydrite platelets did not proceed, even after extended ageing. Unless an additive such

as oxalate is present, the nucleation of hematite requires an aggregation step during the induction period. The presence of the cationic additives described here will inhibit dissolution, but these are also likely to inhibit hematite nucleation or growth (hence the suppression of hematite in favour of the spinel phase at pH 7).

Goethite was not formed at pH 7 in the absence of additives, and was not promoted where any of the above species were introduced. However, Cornell and Giovanoli [75] obtained results which suggested that the presence of manganese (II) had inhibited hematite formation in favour of goethite in the pH range 8-10. This effect might be expected where an additive had accelerated the rate of dissolution, but kinetic data in the same study showed that the cation had slightly hindered the reaction. However, an investigation of the transformation of β -FeOOH to α -FeOOH and α -Fe₂O₃ in the presence of Mn(II) [114] showed that the additive did not suppress hematite formation in this system. It was therefore suggested that Mn destabilised ferrihydrite due to structural effects. The hydrous oxide surface is reactive in terms of chemical oxidation and reduction. If a proportion of Mn(II) (d^5) was oxidised to Mn(III) species (high spin d^4), a Jahn-Teller distortion would be induced in the manganese co-ordination sphere. However, a comparable effect was not observed where Cu(II) species were associated with ferrihydrite [79].

A further factor which may play a part in affecting the development of hematite is the relative solubility of the additive hydroxide. A solid such as Mn(OH)₂ is only slightly

amphoteric. If this material is directly associated with ferrihydrite, the ease of aggregation during the induction period could be reduced. Similarly, nickel hydroxide is insoluble, and Ni(II) species, although quite strongly adsorbing, did not promote hematite formation.

4.1.2. ADDITIVE INCORPORATION IN GOETHITE AND HEMATITE.

In contrast to the majority of organic ligands, the metal cations discussed here have the ability to become incorporated in the lattices of crystalline ferric oxide and oxyhydroxide phases. The degree of isomorphous substitution of foreign species in the transformation products will be dependent on a number of factors, including the nature of the additive species present in solution, their adsorbing ability, and subsequent charge/radius effects. As an example, goethite is thought to nucleate in solution, with crystal growth proceeding by addition (via adsorption at the solid-solution interface) of soluble ferric species released through dissolution of ferrihydrite. These growth units can then be incorporated into the bulk crystal structure. The likelihood of a high proportion of additive species being incorporated in the solid is dependent on competitive adsorption between the substituent and the corresponding ferric species (thought to be $\text{Fe}(\text{OH})_4^-$ at up to pH 12). Subsequent incorporation of the foreign cation into the crystal lattice will then be dependent on the number of charge units which must be lost, the ease of orientation at the surface, and the difference between the radii and charges on the ferric ion and those on the

additive. It is not possible to formulate a simple quantitative relationship to determine whether or not incorporation will occur, but the Hume-Rothery Rule can be used qualitatively. This states that, in cases where the atomic sizes differ by more than 15%, formation of a solid solution comprising the two species is not possible [115].

In the present work, hematite was found to form in the presence of zinc over the entire pH range studied (7-12). EDX profiles obtained for individual crystals showed that in each case some proportion of the additive had been incorporated into the hematite structure during crystal growth. For hematite formed at pH 9, quantitative calculations indicated that the degree of substituent incorporation reached a ceiling value of about 9 mol%. The maximum incorporation levels did not then vary significantly where the proportion of additive present over the product as a whole was anything from 5 to 20 mol%. In the presence of nickel (II) species, individual hematite crystals were not observed in any of the products formed at higher pH. At pH 7, products formed from gels containing up to 8 mol% nickel were found to contain hematite crystals where up to about 6-7 mol% additive was incorporated. Formation of goethite from zinc-ferrihydrates was restricted to the pH range 10-12 and at less than 15 mol% addition. EDX analysis of individual crystals gave no indication of zinc incorporation in the oxyhydroxide structure. Nickel-containing ferrihydrates were found to yield goethites containing 6-8 mol% additive at up to 40 mol% addition.

Maximum incorporation levels previously quoted in the literature for Al, Mn, Co, Ni and Cu uptake in goethite and hematite, together with a summary of the ionic radii, charges on the substituents when incorporated (and those species which will induce a Jahn-Teller distortion in lattice sites) are shown in Tables 4.1 and 4.2. In the present work, the maximum proportion of zinc taken up in hematite (compared to values for Cu) and nickel present in goethite are in good accord with the data shown. Although a figure of 8 mol% is quoted for copper substitution in goethite, Cornell and Giovanoli [79] found that additive incorporation in synthetic goethites grown from copper-ferrihydrate could not be determined by EDX. A similar result has been noted for zinc in the present work.

The general trend for cation incorporation in synthetic goethites formed from ferrihydrate is $\text{Al}^{3+} \gg \text{Mn}^{2+} \gg \text{Co}^{2+}, \text{Ni}^{2+} \gg \text{Cu}^{2+}, \text{Zn}^{2+}$. The highest degree of incorporation is for aluminium (33 mol%). The next highest level (for manganese) is less than half this value, while goethite can only accommodate levels of cobalt and nickel up to 25% that observed for Al.

The incorporation of aluminium is relatively easy. The active hydroxide is amphoteric [40], and is soluble in alkaline solution according to the equilibrium



The above species is monovalent, and should be competitive with $\text{Fe}(\text{OH})_4^-$ for adsorption on the surface of the growing crystals. In addition, it need only lose one unit of charge on incorporation. The radius of the Al^{3+} cation, 0.50 nm, is also

ADDITIVE SPECIES	α -FeOOH	α -Fe ₂ O ₃
Al ³⁺	33	15
Mn ²⁺	15	5
Co ²⁺	7	nd
Ni ²⁺	6-8	nd
Cu ²⁺	8	9
Zn ²⁺	nd	nd

Table 4.1:- Maximum levels for substituent incorporation previously quoted for goethite and hematite (nd=not determined).

SPECIES ADDED	CHARGE UPON INCORPORATION	IONIC RADIUS	TETRAGONAL DISTORTION (Y/N)
Al ³⁺	3+	0.50Å	
Mn ²⁺	3+ (d ⁴)	HS 0.79Å	YES
Co ²⁺	3+ (d ⁶)	LS 0.53Å	NO
Ni ²⁺	2+ (d ⁸)	0.70Å	NO
Cu ²⁺	2+ (d ⁹)	0.73Å	YES
Zn ²⁺	2+ (d ¹⁰)	0.74Å	NO

Table 4.2:- Charges on substituents present in goethite and hematite, together with corresponding ionic radii.

quite near to that of Fe^{3+} .

By comparison, manganese hydroxide is only slightly amphoteric, and dissociates in basic solution according to



As the proportion of additive present increases, the probability of a separate insoluble hydroxide phase forming together with Mn-ferrihydrite is higher (c.f. nickel in the present work). The proportion of ions released into solution may then be inhibited. However, as with adsorbed aluminium, the manganese species need only lose one negative unit of charge to enter the crystal lattice. Schwertmann [76] showed that the measured unit cell parameters of manganese-goethites obeyed Vegard's Law over the composition range $\alpha\text{-FeOOH}$ to $\alpha\text{-MnOOH}$, indicating that the substituent cation was present in the trivalent oxidation state. Similarly, comparison of Mn(II) and Mn(III) radii (0.96\AA and 0.79\AA respectively) with that of Fe(III) (0.78\AA) suggested that the additive was present in the trivalent form (bearing in mind the relative ease of incorporation). However, the substituent does not fit as easily into the goethite structure as does Fe(III), due to the electronic configuration of Mn(III). This d^4 species will exhibit a distorted octahedral co-ordination sphere in the lattice sites [75].

In the present work, ageing of nickel-ferrihydrite gels precipitated at high pH was found to yield products comprising nickel-goethite (containing a maximum of 6-8 mol% additive), and crystalline nickel hydroxide (in products containing in excess of 10 mol% nickel). In samples produced on

ageing zinc-ferrihydrites, formation of substantial levels of a separate zinc phase was not observed below about 30 mol% addition. The formation of a nickel phase at relatively low levels of addition is to be expected, since the hydroxide does not exhibit amphoteric behaviour. In alkaline media, Gayer and Garrett [42] found that the solubility was so slight that only estimates of its value could be made, even up to a hydroxyl concentration of 15M. However, since EDX analysis of individual goethite crystals showed some incorporation of the additive at all levels of addition, a proportion of "free" nickel species must be available in the gels.

The proportion of nickel taken up by goethite was found to be comparable to that of cobalt. Nickel is present in the divalent form [116], and, since Co(II) is oxidised to Co(III) at the oxide-solution interface prior to incorporation [113], charge effects would appear to favour the latter additive. However, the low spin cobalt radius (0.53\AA) is smaller than that of Fe(III) (the difference being about 17%), while the Ni(II) radius (0.72\AA) is of a similar size. If the above factors go some way towards cancelling each other, then the observed result can be explained.

The uptake of zinc (in the present study), and copper [79] has not been observed in goethite crystals grown from ferrihydrite gels. Grimme [117] showed that the ability of metal species to adsorb on goethite in solution was in the order $\text{Cu} > \text{Zn} > \text{Co} > \text{Mn}$. Since both zinc and copper hydroxides are readily soluble at high pH, and these additives are the most strongly interacting with goethite, it might be expected

that incorporation of these substituents in the oxyhydroxide would be favoured. However, the relative abilities of the species released into solution during the transformation to readsorb on unconverted ferrihydrite must also be taken into account. Cornell and Giovanoli studied the relative uptake of additives by goethite from precipitates containing low levels of divalent manganese, cobalt and nickel species [115]. Where all three additives were present, uptake of manganese and cobalt was favoured. The smaller proportion of nickel incorporated was thought to be consistent with readsorption on ferrihydrite, since this is the most strongly-adsorbing species of the three. In the present work, an appreciable proportion of goethite has been found to form in the presence of up to 10-15 mol% zinc (at pH 10-12). Since zinc has been shown to adsorb strongly on goethite and can become incorporated in the structure, the lack of substitution probably arose due to readsorption. The likelihood of zinc species reattaching to ferrihydrite would outweigh the chances of finding a growing goethite crystal.

Breuwsmas *et al* [118] proposed that the surface of hematite in solution was hydrated, slightly porous and permeable for cations having a radius similar to that of Fe(III). The model used was of a double layer where surface charge was not confined to the surface proper, but was distributed within some depth. Ion uptake will depend on geometric penetrability and the affinity towards the oxide. If the surface is very porous, then the former effect predominates. However, increased ionic radius decreases penetrability. Hematite was found to

exhibit especially strong specific adsorption of bivalent cations.

In contrast to the case for goethite, it might be expected that additive incorporation in hematite would be highest where the cation present was strongly-adsorbing, since interaction with the growing crystals would not necessitate release into the bulk solution. However, this was not found to be the case, since incorporation appeared to reach a ceiling value of 8-10 mol% for most of the additives studied.

The mechanism for hematite formation is thought to proceed largely through aggregation/internal rearrangement. Since this process involves interaction of ferrihydrite particles, rather than individual molecular growth units, a relatively low uptake of foreign species might be expected in the bulk crystals when compared to maximum values for goethite. Alternatively, structural factors may limit the degree of substituent incorporation.

4.1.3. THE EFFECT OF ADDITIVES ON THE FINAL MORPHOLOGY OF GOETHITE AND HEMATITE.

The morphologies of the crystalline phases described in the present work are dependent on both the intrinsic structure and the conditions under which the particles have grown. Variations in morphology are of interest, since these can provide information about the mechanisms by which the crystals are formed. In the following section, the influence of foreign cations in directing final goethite and hematite habits is discussed.

4.1.3.a) GOETHITE AND TWIN CRYSTALS.

The presence of an additive can influence the crystal morphology of goethite in four ways; by modifying the actual shape, by altering the length to width ratio, by inducing intergrowth formation, or by promoting twin formation. Previous studies on the transformation of ferrihydrite [73-80] have noted that the presence of foreign transition metals will normally promote the formation of twin crystals relative to control samples produced under equivalent conditions. These crystals can be classed either as epitaxial twins, comprising a hematite centre (including some star-shaped crystals), or as composite twins such as dendrites, stars and twin pieces. The presence of these cationic species has also often been found to induce development of long, thin acicular goethite crystals. This effect was thought to arise due to temporary adsorption of the additives.

At pH 12, copper-ferrihydrites have been found to yield twin crystals comprising a large prismatic or ellipsoidal hematite centre with occasional goethite outgrowths [79]. In the present work, zinc was not found to inhibit goethite formation to the same extent as copper, but did promote development of epitaxial twins at pH 9-12 under conditions where the induction period was extended, but the level of additive present was insufficient to induce extensive development of the spinel phase (<8 mol% zinc). Twins formed at pH 9 in the presence of zinc were found to be comparable in morphology to crystals observed in copper-containing products formed at pH 12 (which were quoted by Cornell and Giovanoli [79]).

Similarly, the presence of cobalt species in gels held at pH 10.5 [113] has been found to promote epitaxial twinning.

These results are in accord with a mechanism by which the retarding effect of the above additives allowed aggregation of ferrihydrite and subsequent nucleation of hematite to proceed during the extended induction period, while release of ferric species capable of forming critical goethite nuclei in solution was inhibited.

Cornell and Giovanoli [69] suggested that twin formation was limited to the induction period. Crystal nucleation occurred in ferrihydrite, but unlike the model proposed by Atkinson *et al* [48] a tiny nucleus of $\alpha\text{-Fe}_2\text{O}_3$ was not required. In this case, only an ordered region a few unit cells across needed to develop during the aggregation step. The essentially hexagonal close-packed anion array in the precipitate would then allow growth to proceed in up to three directions. In the absence of additives at lower pH (or in this work in the presence of zinc at higher pH) the ordered region will transform to hematite. At high pH, such a region can act as a seed for goethite twins. This would explain the observation that, in the presence of zinc, epitaxial twins grown at pH 12 generally comprised a small, poorly-defined centre and long (up to 500nm) outgrowths of goethite, while at pH 9 (where dissolution of ferrihydrite is retarded to a greater extent, whether or not additive species are present) only short outgrowths on large ellipsoidal or prismatic crystals of $\alpha\text{-Fe}_2\text{O}_3$ were observed. At pH 7, near the point of zero charge for ferrihydrite, the oxide crystals did not exhibit any out-

growths at all.

However, the structural model for ferrihydrite proposed by Manceau [51] suggests that the octahedra are joined through edge, corner and face-sharing, with both hexagonal and cubic fragments present. The hematite structure comprises exclusively edge and face-shared $[\text{FeO}_6]$ units, while the chains present in goethite are linked solely through edge and corner-sharing. If the transformation is carried out at high pH, a high concentration of soluble ferric species are available once the induction period is over. If there is a plentiful supply of "twin nuclei" in the gels, then development of chains leading to goethite outgrowths can be envisaged. However, whether the particles acting as twin nuclei comprise fully-ordered hematite or not, there will be a mismatch going from a structure involving face-shared octahedra to one exclusively involving edge and corner-sharing. In addition, both the hematite and goethite structures are distorted from their idealised arrangements (Section 1.1.2 and Fig.4.1).

It has been suggested that promotion of twinning, especially dendrite formation, may be facilitated by the accommodation of impurities during crystal growth [119,120]. This study has shown that, for goethite grown in the presence of zinc, the proportion of dendritic twins was far outweighed by stars and epitaxial crystals. Although crystals produced in the presence of low levels of zinc were often found to exhibit what appeared to be short overgrowths of goethite at the centre (Section 3.3.2), these may arise due to the presence of "twin nuclei" rather than the uptake of zinc. Simil-

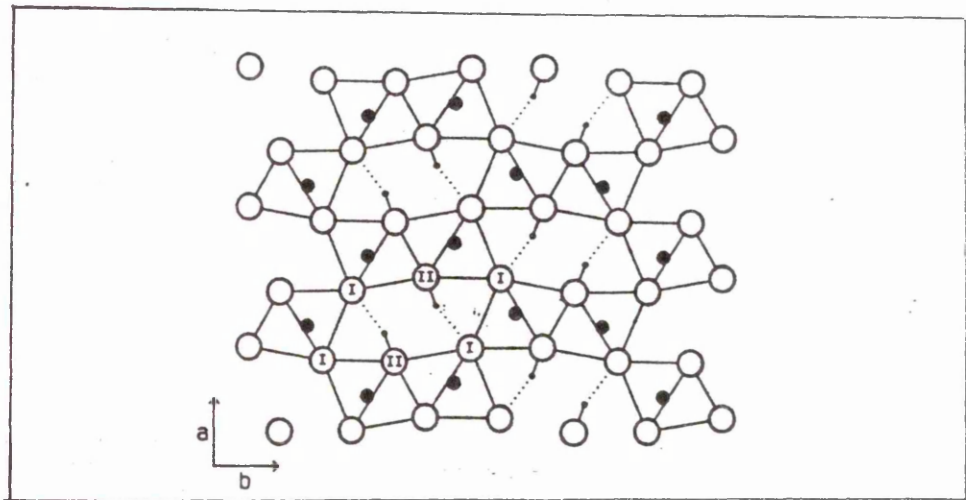


Fig.4.1:- Goethite structure projected onto [001], showing distortion of $(\text{Fe}, \text{O}, \text{OH})_6$ octahedra. Oxygen atoms are represented by large circles, H atoms by small circles. Hydrogen bonds are indicated by solid and dotted lines.

arly, EDX analyses did not indicate that the additive species were incorporated in the structures of either acicular or twin crystals, although zinc has previously been shown to adsorb strongly on goethite.

Crystals, especially twins, grown in the presence of zinc were often found to exhibit more extensive development in the b-direction than those grown in control samples under equivalent conditions. Many of these, mainly stars grown at 5-8 mol% addition, terminated in well-developed (021) faces (the outgrowths on obviously epitaxial twins usually showed rounded ends). Two possible mechanisms have been suggested by which an increase in crystal width can be accounted for [69]. In the first case, during the induction period where twins predominate, the "twin nuclei" are never as numerous as those of acicular crystals and a high local concentration of growth species is available. Alternatively, the size of the actual nucleus may be responsible for crystal width. In the case of epitaxial twins the hematite substrate is much larger than the acicular nucleus.

Cationic additives have also previously been associated with enhanced development of (021) faces at the ends of goethite crystals [75, 113]. It was proposed that this effect arose due to preferential adsorption on these planes. In the present work, the presence of very low levels of zinc (< 5 mol%) did not promote such an enhancement in either acicular or epitaxial twins formed at pH 12. However, at 5-8 mol% addition, the arms of star-shaped twins exclusively terminated in well-defined (021) faces. These crystals were of similar mor-

phology to twins grown at pH 9 in the absence of any additive species. The growth conditions for these twins, rather than adsorption effects, are therefore more likely to control the crystal development.

In the present work, the presence of nickel was not found to promote twin formation at high pH to the same extent as that induced by zinc. This is in accord with the lower stabilising ability of nickel. The acicular Ni-goethite crystals which developed did not terminate in well-defined ends, and were often poorly-crystalline in character. Similar results have been observed for goethite grown in the presence of divalent Co and Mn species [75, 113]. The reduced crystal width and the presence of irregularities such as etch pits is also thought to arise through additive adsorption. However, the presence of copper [79] and zinc is also found to induce formation of long, thin crystals. Results have indicated that these additives are more likely to influence the goethite morphology indirectly by restricting the release of ferric species into solution, rather than by interacting directly with the growing crystals. There will then be a balance between the extreme behaviour of strongly-adsorbing ions such as copper and zinc, and more weakly-adsorbing species such as Mn which are more easily released into solution.

4.1.3.b) HEMATITE CRYSTALS.

In the absence of additive species, plate-like crystals of hematite were found to develop in gels held at neutral pH. The presence of strongly-retarding additives such as copper

or zinc will promote nucleation of hematite in samples formed at high pH (probably by hindering goethite formation indirectly), and are also capable of influencing the eventual particle morphology. Additives such as nickel and cobalt, which only retard the reaction significantly in the later stages, and manganese (which effectively does not retard the transformation at all), will not induce nucleation and growth of hematite.

In the present work, zinc species did not appear to inhibit aggregation where hematite developed at pH 9 (reflected in the large crystal dimensions). However, as the additive level was raised, the internal structure of the crystals which developed became increasingly poorly-defined relative to oxide particles formed in the absence of zinc. Rather than exhibiting a relatively smooth, plate-like surface, these particles (which often appeared to be multi-diffracting) could clearly be seen to comprise masses of individual platelets. These results suggest that, although the aggregation stage did proceed and the ferrihydrite particles had become recognisably crystalline in nature, the stabilising effect of zinc was such that crystal growth was often inhibited to some extent. In the most recent structural study on ferrihydrite carried out by Manceau *et al* [51] results suggested that, since the oxide-hydrate contains both cubic and hexagonally-packed anion layers, it is unlikely that formation of hematite (strictly hcp) occurs solely via a solid state internal rearrangement mechanism, as was previously thought. It may be the case that after the aggregation step, some degree of

ferrihydrite dissolution is involved, where the platelets lose their individual character and lateral displacement of cubic layers to hexagonal packing can proceed. The presence of strongly stabilising species may hinder this transformation.

4.2. FORMATION AND COMPOSITION OF SPINEL PHASES INDUCED BY THE PRESENCE OF ADDITIVE SPECIES

4.2.1. PROBABLE MECHANISMS FOR SPINEL NUCLEATION AND GROWTH IN FERRIHYDRITE GELS

The mechanism by which crystalline spinel phases nucleate in ferrihydrite gels in the presence of divalent transition metal cations is not fully understood, but growth may involve a dissolution step. Crystal development could then proceed via the subsequent interaction of additive and ferric species with the solid precursor. Sidhu *et al* [121] suggested that magnetite was precipitated directly from solution in aqueous systems, while Schwertmann and Taylor [122] showed that formation of Fe_3O_4 in solutions containing a mixture of ferrous species and lepidocrocite ($\gamma\text{-FeOOH}$) appeared to involve dissolution of the initial solid phase. However, previous work carried out by Cornell and Giovanoli [75, 113] has suggested that ferrite phases formed via the transformation of ferrihydrite may nucleate on the water layer adsorbed on the surface of the solid precursor.

The proportion of any one divalent metal cation species which must first be present in order to induce formation of the corresponding spinel phase was found to vary with the

nature of the substituent present and, to a lesser extent, the transformation pH. In the present work, ageing of zinc-ferrihydrites precipitated at pH 11-12 was found to yield well-defined zinc-magnetite crystals in cases where the proportion of additive in the precipitates exceeded 7.5-8 mol%. Lowering the pH to 9 appeared to promote spinel formation, but only to a very slight extent (with a substantial proportion of zinc-magnetite formed at 7-7.5 mol% addition). If the level of zinc present was raised further, spinel formation became favoured over that of both goethite and hematite. TEM examination of products formed at pH 12 in which zinc had been replaced by nickel (II) indicated that formation of nickel-magnetite was not favoured to the same extent. In this case, little evidence for the presence of well-defined spinel crystals was observed.

Powder diffraction data previously quoted for transformation products formed at pH 12 in the presence of Mn, Co, Ni, Cu or Zn [80] indicated that the ability of these additives to induce spinel formation was in the order $\text{Cu, Zn} > \text{Co} > \text{Ni, Mn}$. This is quite similar to the ability of each species to promote hematite formation, suggesting that the conditions for spinel nucleation are similar to those required for hematite. If spinel nucleation occurred in solution, crystals might be expected to form more easily in the presence of less strongly adsorbing cations which were not bound to ferrihydrite. In this case, ferrite nucleation would have to compete directly with goethite.

In systems where both zinc and nickel species were precipitated together with ferrihydrite, the products formed on ageing were found to comprise well-defined (Zn,Ni)-magnetite crystals having a fairly wide range of composition, which contained substantial proportions of nickel. The presence of the strongly-adsorbing zinc species appeared to be necessary to induce spinel nucleation. This is in accord with a mechanism by which some degree of interaction with the solid precursor (or inhibited ferrihydrite dissolution) is required.

Initial results suggested that spinel formation at high pH will occur where ferrihydrite is stabilised against dissolution for a period which is sufficient for nucleation of goethite in solution to be restricted. Once the induction period is over, any ferric species released into the bulk solution by the dissolution of ferrihydrite would then be less likely to act as growth species for goethite, since formation of the necessary nuclei has been inhibited. However, further studies carried out on gels which were "seeded" with goethite nuclei (Section 3.6) indicated that the presence of these species retarded spinel formation, but only to a slight extent. In these samples, the presence of zinc appeared to have restricted the release of ferric species into solution to the extent that growth of the oxyhydroxide crystals was strongly inhibited, irrespective of the presence of goethite "nuclei".

Data from previous studies have suggested that the formation of jacobsite (MnFe_2O_4) involved interaction of dis-

solved Mn(II) species with ferrihydrite [75]. As was observed in the present work, reducing the gel pH to 7-8 did not promote spinel formation, which would have been expected if jacobite formed via an aggregation/rearrangement mechanism similar to that by which hematite develops. However, seeding the gels with spinel crystals also did not favour jacobite. This suggested that some interaction with ferrihydrite was necessary for nucleation to proceed.

In the present study, it was found that at higher pH, the average dimensions of ferrite crystals gradually became smaller with increasing zinc addition, until the particles were comparable in size to the original ferrihydrite platelets. As previously described, the nucleation of hematite requires an aggregation step, without which the individual ferrihydrite particles will not crystallise. It is possible that the larger (20-40nm) zinc-magnetite crystals could be formed by such a mechanism. However, high-resolution TEM examination of the local structure in these crystals gave no evidence for a granular character similar to that of hematite grown in the presence of zinc. Furthermore, since the smallest crystallites were similar in diameter to the precursor, it is unlikely that an aggregation step is necessary to induce spinel nucleation.

Products formed at neutral pH in the presence of various additive species were found to comprise unconverted ferrihydrite and small spinel crystals. Nucleation did not appear to be inhibited (in accord with the solid-interactive mechanism) but further growth of the particles was restricted, suggesting that dissolved species are involved at this stage. At

this lower pH, the formation of nickel-magnetite was not inhibited. It may be the case that the insolubility of nickel hydroxide affected spinel development at pH 12.

Specific adsorption is the most frequent explanation for the adsorption selectivity series of ionic species on metal oxides. Stumm and Morgan [123] quoted data for ion interaction with hydrous MnO_2 . This process appeared to involve proton exchange, via a stoichiometric reaction described by



This will result in the formation of oxo-linkages. Murray [81] showed that the metal species can penetrate into the surface layer and react with protonated sites on the hydrous oxide. These foreign ions may be associated with more than one surface group. Kinniburgh [124] obtained similar results for iron oxides. The above scheme may then reflect the reactions occurring on the surface of ferrihydrite which could lead to spinel nucleation. The porous nature of synthetic ferrihydrite and the tunnel structure proposed by Manceau [51] could also aid the diffusion of ionic species as the new crystalline phase developed on an individual particle.

4.2.2. COMPOSITION OF FERRITE PHASES.

A combination of X-ray diffraction, TEM, selected-area electron diffraction, High Resolution TEM and electron probe microanalysis has been used to determine the nature of spinel phases produced during transformation of ferrihydrite in the presence of additive species.

Quantitative EDX data for individual spinel crystals has indicated a variable stoichiometry for these phases. Crystals formed at pH 9-12 in the presence of up to 20 mol% zinc were found to have incorporated about 20-30 mol% additive species. A stoichiometry consistent with ZnFe_2O_4 was seldom observed in these cases, and calculations from the above data showed that, if the overall charge is to balance, some proportion of cation vacancies may be present in the structures (Section 3.5). Under such conditions, there is the possibility of preferential substituent ordering in the lattice sites, an effect which might lead to the development of an extended superstructure.

Since EDX data indicated that some proportion of zinc species was always substituted in the spinel phase, it is reasonable to assume that the actual stoichiometry of any one crystal would lie somewhere between the end phases $\gamma\text{-Fe}_2\text{O}_3$ and ZnFe_2O_4 . Powder diffraction data for the additive-free ferric oxide spinel phase, maghemite ($\gamma\text{-Fe}_2\text{O}_3$) has shown the presence of extra reflections which are associated with an extended tetragonal unit cell arising from vacancy ordering in the structure [125-128]. The forbidden reflections having highest-intensity were found at 0.595nm (corresponding to (110)/(103) planes, 60% intensity), 0.375nm ((106)/(203) planes, 100% intensity) and 0.342nm ((213)/(116), 65% intensity). In the present work indexing of powder diffraction profiles for the transformation products indicated that the spinel phases were consistent with face-centred MFe_2O_4 (where M was either Ni or Zn, or both species together). None of the above reflections

were observed for any of the samples studied. However, the dimensions of the spinel crystals observed by TEM (down to 5-10nm) were sufficiently small that XRD peaks were generally poorly-resolved. By contrast, symmetry forbidden reflections were observed where further electron diffraction data was obtained for some samples (Section 3.4). However, diffraction patterns showing only individual crystals were again found to be consistent with zinc-magnetite.

The structure proposed in previous studies for the unsubstituted ferric oxide, $\gamma\text{-Fe}_2\text{O}_3$, appear to have largely been dependent on the method of preparation used. Gallagher *et al* [128] oxidised Fe_3O_4 to $\gamma\text{-Fe}_2\text{O}_3$ by heating particles of size less than 0.2μ at temperatures greater than 250°C , and found that larger crystals were transformed to $\alpha\text{-Fe}_2\text{O}_3$. Smaller size preparations gave rise to $\gamma\text{-Fe}_2\text{O}_3$, XRD profiles for which showed extra reflections consistent with a tetragonal unit cell. At temperatures between 220°C and 240° XRD lines became broader as the transformation began, but vacancies moved about in disorder and no superstructure was present. Evidence for vacancy disorder in the final product was obtained by Takei [11] for large single crystals of $\gamma\text{-Fe}_2\text{O}_3$ epitaxially grown on the surface of MgO by halide decomposition. In this case, only reflections allowed for cubic symmetry were observed. The oxidation of Fe_3O_4 under wet conditions has generally been found to allow the conversion to $\gamma\text{-Fe}_2\text{O}_3$ to occur more easily, by stabilising the product either through adsorption of water or inclusion of protons in the vacant cation sites. Products formed in such cases always showed extra reflections which

were consistent with a tetragonal symmetry.

In the present study, well-defined 20-40nm spinel crystals were found to develop in the presence of relatively low levels of zinc species (about 7-8 mol%). As described in Section 4.2.1, nucleation is likely to proceed on individual ferrihydrite particles through the interaction of adsorbed additive species. However, although few Zn(II) species were present relative to Fe(III) in such a gel, it was not noted that further growth led to the development of crystals containing only low levels of additive species (ie nearer in composition to maghemite). The composition observed is in accord with the preferential readsorption of zinc species released into solution onto either undissolved ferrihydrite or growing spinel crystals. By contrast, ferric species are likely to pass directly into solution more easily.

A final factor which should be considered is the possibility of differences in the bulk and surface composition of the spinel crystals. Growing magnetite crystals may have the ability to specifically adsorb Co, Zn, Cu, Mn, etc [121]. These foreign species will be distributed evenly in the crystals only in cases where the ratio M:Fe is constant during growth, and where M can occupy lattice sites easily. In the present work, EDX examination of spinel-containing products before and after partial dissolution in acid gave little evidence for accumulation of either Zn or Ni species at the surface of the crystals. This is in accord with data for spinels grown in ferrous/ferric systems [121].

REFERENCES

1. Eggleton, R.A., *Am. Mineral.*, 60, 1063-1068 (1975).
2. Bragg, W.H. and Bragg, W.L., *X-Rays and Crystal Structure*, Third Edition, G. Bell and Sons, London (1918).
3. Pauling, L. and Hendricks, S.B., *J. Amer. Chem. Soc.*, 47, 781 (1925).
4. Blake, R.L., Hessevick, R.E., Zoltai, T. and Finer, L.W., *Amer. Mineralogist*, 51, 123 (1966).
5. Ewing, F.J., *J. Chem. Phys.*, 3, 420 (1935).
6. Christensen, H. and Christensen, A.W., *Acta. Chem. Scand.* A32, 87 (1978).
7. Ellis, R., Giovanoli, R. and Stumm, W., *Chimia*, 30, 194-7 (1976).
8. West, A.R., *Solid State Chemistry and its applications*, 569-75, J. Wiley and Sons (1987).
9. Goodenough, J.B. and Loeb, A.L., *Phys. Rev.*, 98, 391-408 (1955).
10. Ueda, R. and Hasegawa, K., *J. Phys. Soc. Jpn.*, Supp. B(11), 291 (1962).
11. Takei, H. and Chiba, S., *J. Phys. Soc. Jpn.*, 21, 1255 (1966).
12. Braun, P.B., *Nature*, 70, 1123 (1952).
13. Von Sinha, K.P. and Von Sinha, A.P.B., *Z. Anorg. Allg. Chem.*, 293, 229 (1957).
14. Blesa, M.A. and Matijevic, E., *Adv. Coll. Inter. Sci.*, 29, 173-221 (1989).
15. Flynn, C.M. Jr., *Chem. Rev.*, 84, 41-41 (1984).
16. De Bruyn, P.L. and Dousma, J., *J. Coll. Inter. Sci.*, 56, 527 (1976).
17. De Bruyn, P.L. and Dousma, J., *J. Coll. Inter. Sci.*, 64, 154

- (1978).
18. De Bruyn, P.L., Dousma, J. and Van der Hoven, T.J., *J. Inorg. Nucl. Chem.*, 40, 1089 (1978).
19. D. De Bruyn, P.L., Dousma, J. and Den Ottelander, D., *J. Inorg. Nucl. Chem.*, 41, 1565 (1979).
20. De Bruyn, P.L. and Dousma, J., *J. Coll. Inter. Sci.*, 72, 314 (1979).
21. Spiro, T.G., Allerton, S.E., Penner, J., Terzis, A., Bils, R. and Saltzman, P., *J. Am. Chem. Soc.*, 88, 2721 (1966).
22. Spiro, T.G., Allerton, S.E., Penner, J., Colt, S., Saltzman, P., *J. Am. Chem. Soc.*, 88, 3147 (1966).
23. Spiro, T.G., Brady, G.W., Kurkjian, C.R., Lyden, E.F., Robin, M.B., Saltzman, P. and Terzis, A., *Biochemistry*, 7, 2185 (1968).
24. Spiro, T.G., Sommer, B.A., Margerum, D.W., Renner, J. and Saltzman, P., *Bioinorg. Chem.*, 2, 395 (1973).
25. Quirk, J.P., Murphy, P.J. and Posner, A.M., *J. Coll. Inter. Sci.*, 56, 312 (1976).
26. Magini, M., *J. Inorg. Nucl. Chem.*, 39, 409 (1977).
27. Murphy, P.J., Posner, A.M. and Quirk, J.P., *J. Coll. Inter. Sci.*, 56, 270 (1976), b) *ibid.* 56, 284 (1976), c) *ibid.* 56, 298 (1976).
28. Hsu, P.H. and Ragone, S.E., *J. Coll. Inter. Sci.*, 23, 17 (1972).
29. Murphy, P.J., Posner, A.M. and Quirk, J.P., *Aust. J. Soil Res.*, 13, 189 (1975).
30. Murphy, P.J., Posner, A.M. and Quirk, J.P., *J. Coll. Inter. Sci.*, 52, 229 (1975).
31. Christoph, G.G., Corbato, C.E., Hofmann, T.A. and Tetenhors,

- R.T., *Clays Clay Miner.*, 27, 81 (1979).
32. Knight, R.J., Sylva, R.N., J. *Inorg. Nucl. Chem.*, 36, 591 (1974).
33. Post, J.E., Von Dreele, R.B., Buseck, P.R., *Acta Crystal.*, B38, 1056 (1982).
34. Mackay, A.L., *Miner. Mag.*, 32, 545-77 (1960).
35. Atkinson, R.J., Posner, A.M. and Quirk, J.P., *Clays and Clay Minerals*, 25, 49-56 (1977).
36. Feitknecht, W., Giovanoli, R., Michaelis, W. and Müller, M., *Helv. Chim. Acta.*, 56, 2847-56 (1973).
37. Matijevic, E. and Scheiner, P., *J. Colloid Interface Sci.*, 63, 509 (1978).
38. Hamada, S. and Matijevic, E., *J. Colloid Interface Sci.*, 84, 274 (1981).
39. Biedermann, G. and Chow, J.T., *Acta Chem. Scand.*, 20, 1376 (1966).
40. Baes, C.F. and Memer, R.E., *The Hydrolysis of Cations*, Wiley Interscience (1976).
41. Gubeli, A.O. and Ste. Marie, J., *Can. J. Chem.*, 45, 827-32 (1967).
42. Gayer, K.H. and Garret, A.B., *J. Am. Chem. Soc.*, 71, 2973 (1949).
43. Van der Geissen, A.A., *J. Inorg. Nucl. Chem.*, 28, 2155-9 (1966).
44. Towe, K.M. and Bradley, W.F., *J. Colloid Interface Sci.*, 24, 384-92 (1967).
45. Chukhrov, F.V., Chukhrov, A.I., Vermilova, L.P. and Balashova, V.V., *Intern. Geol. Rev.*, 16, 1131-43 (1973).

46. Schwertmann, U. and Fischer, W.R., *Geoderma.*, 10, 233-47 (1973).
47. Russell, J.D., *Clay Miner.*, 14, 109-14 (1979).
48. Atkinson, R.J., Posner, A.M. and Quirk, J.P., *J. Inorg. Nucl. Chem.*, 30, 2371-81 (1968).
49. Feitknecht, W. and Michaelis, W., *Helv. Chem. Acta.*, 45, 212 (1962).
50. Burns, R.G. and Burns, V.M., *Minerology*, pp 186-248, *In Marine Manganese Deposits* (ed G.P. Glasby), Elsevier New York (1977).
51. Manceau, A. and Drits, V.A., *Clay Minerals*, 28, 165-84 (1993).
52. Johnson, J.H. and Lewis, D.G., *Geochim. Cosmochim. Acta.*, 47, 1823-31 (1983).
53. Schwertmann, U. and Murad, E., *Clays and Clay Minerals*, 31, 277-84 (1983).
54. Fischer, W.R. and Schwertmann, U., *Clays and Clay Minerals*, 22, 33-7 (1975).
55. Schwertmann, U. and Fischer, W.R., *Z. Anorg. Allg. Chemie*, B46, 137-42 (1966).
56. Christensen, A.N., Convert, P. and Lehman, M.S., *Acta. Chem. Scand.*, A34, 771-6 (1980).
57. Cornell, R.M. and Giovanoli, R., *Clays and Clay Minerals*, 33, 424-32 (1985).
58. Schwertmann, U., *Z. Pflanzenernähr. Düng. Bodenkd.*, 105, 194-202 (1964).
59. Coombes, J.M., Manceau, A. and Calas, G., *J. de Phys.*, C8, 47, 2, 697-701 (1986).
60. Cornell, R.M., Giovanoli, R. and Schneider, P.W., *J. Chem. Tech. Biotechnol.*, 46, 115-34 (1989).

61. Cornell, R.M. and Schwertmann, U., *Clays and Clay Minerals*, 27, 402-10 (1979).
62. Lengweiler, H., Buser, W. and Feitknecht, W., *Helv. Chim. Acta.*, 44, 796-805 (1961).
63. Cotton, F.A. and Wilkinson, G., *Advanced Inorganic Chemistry*, 4th Edition, J. Wiley (1980).
64. Cornell, R.M., Mann, S. and Skarnulis, A.J., *J. Chem. Soc. Farad. Trans.*, 1, 79, 2679-84 (1983).
65. Schwertmann, U., Cambier, P. and Murad, E., *Clays and Clay Minerals*, 33, 369-78 (1985).
66. Torrent, J. and Guzmán, R., *Clay Miner.*, 17, 463-9 (1982).
67. Schwertmann, U., *Geoderma.*, 3, 207-14 (1969/70).
68. Cornell, R.M., *Clays and Clay Minerals*, 33, 1048-53 (1985).
69. Cornell, R.M., Giovanoli, R. and Schindler, P.W., *Clays and Clay Minerals*, 35, 21-8 (1987).
70. Anderson, P.R. and Benjamin, M.M., *Environ. Sci. Technol.*, 19, 1058-53 (1985).
71. Cornell, R.M. and Giovanoli, R., *J. Chem. Soc. Chem. Commun.*, 18, 412-14 (1987).
72. Cornell, R.M., *Z. Pflanzenernähr. Düng. Bodenkd.*, 150, 304-7 (1987).
73. Lewis, D.G. and Schwertmann, U., *Clay Miner.*, 14, 115-26 (1979).
74. Lewis, D.G. and Schwertmann, U., *Clays and Clay Minerals*, 27, 196-200 (1979).
75. Cornell, R.M. and Giovanoli, R., *Clays and Clay Minerals*, 35, 11-20 (1987).
76. Stiers, W. and Schwertmann, U., *Geochim. Cosmochim. Acta.*,

- 49,1000-11 (1985)
77. Fitzpatrick,R.W.,Le Roux,J. and Schwertmann,U.,Clays and Clay Minerals,26,189-201 (1978).
78. Inouye,K.,Ishii,S.,Kaneke,K. and Ishikawa,T.,Z. Anorg. Allg. Chem.,391,86-96 (1972).
79. Cornell,R.M. and Giovanoli,R.,Polyhedron 7,385-91 (1988).
80. Cornell,R.M.,Clay Minerals,23,329-32 (1988).
81. Murray,J.W. and Brewer,P.G.,Marine Manganese Deposits, Glasby,G.B. (ed.),Ch 10,297-327,Elsevier Sci. (1975).
82. Riley,J.P.,J. Colloid Interface Sci.,20,376-86 (1966).
83. Rubio,J. and Matijevic,E.,J. Colloid Interface Sci.,68, 408-21 (1979).
84. De Broglie,Phil. Mag.,47,446-58 (1924).
85. Davisson and Germer,Phys. Rev.,30,705-40 (1927).
86. Ahmed,H.,Proc. 25th Aniv. Meeting of EMAG,Inst. Phys. Con. Series No.30 (1971).
87. Lenz,EM and Analysis,Nixon,W.C. (ed.),224-9,IOP London (1971).
88. Boersch,H.,Phys.,B1,23,393-404 (1947).
89. Cowley,J.M and Moodie,A.F.,Acta. Cryst.,10,609 (1957).
90. Born,M. and Wolf,E.,Principles of Optics,5th Edition, Pergammon Press (1965).
91. Klug,H.P. and Alexander,L.E.,X-Ray Diffraction Procedures for Polycrystalline and Amorphous Materials,J. Wiley and Sons, New York (1974).
92. Brindley,G.W. and Brown,G.,Crystal Structures of Clay Minerals and Their X-Ray Identification,Mineralogical Society,London (1980).

93. Nemezc, E., Clay Minerals, Academiai Kiado, Budapest (1981).
94. Le Poole, J.B., Philips Tech. Rsch., 9, 33 (1947).
95. Andrews, K.W., Dyson, D.J. and Kedwin, S.R., Interpretation Of Electron Diffraction Patterns, Adam Higher, London (1968).
96. Beeston, B.E.P., Horne, R.W. and Markham, R., Practical Methods In EM (ed. A.M. Glavert), North-Holland, Amsterdam, Vol. 1 (1972).
97. Edington, J.W., Practical EM In Material Science, Macmillan Press, London (1975).
98. Vainshtein, B.K., Structural Analysis By Electron Diffraction, Pergamon Press, London (1964).
99. Hren, J.J., Goldstein, J.I. and Joy, D.C., Introduction To Analytical EM (1975).
100. Fitzgerald, A.G., Storey, B.E. and Fabian, D., Quantitative Microbeam Analysis, Proc. 40th Scottish Univ. Summer School in Physics, Dundee, IOP publishing (1992).
101. Carlson, L. and Schwertmann, U., Geochim. Cosmochim. Acta., 45, 421-9 (1981).
102. Fitzpatrick, R.N., Iron In Soils And Clay Minerals Ch.8.pp 165-201 (1983).
103. Cornell R.M. and Giovanoli, R., Clays and Clay Miner., 39, 144-50 (1991).
104. Goldsztaub, S., Bull. Soc. Franc. Miner., 58, 6 (1935).
105. Cornell, R.M., Clays and Clay Minerals, 33, 219-27 (1985).
106. Bertaut, E.F., J. Phys. Radium, 12, 252 (1954).
107. Andersson, S. and Hyde, B.G., J. Solid State Chem., 9, 92 (1974).
108. David, I. and Welch, A.J.E, Trans. Farad. Soc., 52, 1642

- (1956).
109. Gallagher, K.J., Feitknecht, W. and Mannweiler, U., *Nature*, 217, 1118 (1968).
110. Irving, M. and Williams, R.J.P., *J. Chem. Soc.*, 3192-3210 (1953).
111. Hem, J.D., *Geochim. Cosmochim. Acta.*, 41, 527-38 (1977).
112. Cornell, R.M. and Giovanoli, R., *Clays and Clay Minerals*, 37, 65-70 (1989).
113. Cornell, R.M. and Giovanoli, R., *Clays and Clay Minerals*, 39, 144-50 (1991).
114. Kitaigorodsky, A.I., *Mixed Crystals*, Ch9, p.181, Springer-Verloig (1984).
115. Cornell, R.M. and Giovanoli, R., *Clay Minerals*, 26, 427-30 (1991).
116. Cornell, R.M. and Giovanoli, R., *Clays and Clay Minerals*, 37, 65-70 (1989).
117. Grimme, H., *Z. Pflanzenernähr. Düng. Bodenkd.*, 121, 58-65 (1969).
118. Breuwsma, A. and Lyklema, J., *Disc. Farad. Soc.*, 52, 324-33 (1971).
119. Azaroff, L.V., *Introduction to solids*, McGraw-Hill, New York, 460pp (1960).
120. Maeda, Y. and Hirono, S., *Jpn. J. Appl. Phys.*, 20, 1991-2 (1981).
121. Sidhu, P.S., Gilkes, R.J. and Posner, A.M., *J. Inorg. Nucl. Chem.*, 40, 429-35 (1978).
122. Schwertmann, U., and Taylor, R.M., *Genesis and Use of Hydromorphic Soils*, *Proc. Int. Soc. Soil Sci. Trans.*, 45-54

Stuttgart, Germany (1972).

123. Stumm, W. and Morgan, J.J., *Aquatic Chem.*, Wiley Interscience New York, 583pp (1970).

124. Kinneburgh, A., PhD Thesis, U. Wisconsin, Madison, Wisconsin (1973).

125. Haul, R. and Schoon, T., *Z. Phys. Chem.*, 44, 216 (1939).

126. Van Oosterhaut, G.W., *Acta. Cryst.*, 3, 932 (1960).

127. Van Oosterhaut, G.W. and Roojimans, C.J.M., *Nature*, 181, 44 (1958).

128. Feitknecht, W. and Gallagher, *Nature*, 228, 549 (1970).